INVESTIGATIONS OF A DISCHARGE-EXCITED SHORT-PULSE XeCl LASER

by

ZHIMING XIA, B.Sc.

A Thesis

Submitted to the School of Graduate Study

in Partial Fulfilment of the Requirements

for the Degree

Doctor of Philosophy

McMaster University

May, 1993

INVESTIGATIONS OF

A DISCHARGE-EXCITED SHORT-PULSE XeCl LASER

To My Grandma, Zhang Ke-Rong

DOCTOR OF PHILOSOPHY (1993) McMASTER UNIVERSITY

(Physics) Hamilton, Ontario

Canada

TITLE: Investigations of a Discharge-Excited Short-Pulse XeCl Laser

AUTHOR: Zhiming Xia

B.Sc. (Beijing University, P.R. China)

SUPERVISOR: Professor E.A. Ballik

NUMBER OF PAGES: xviii, 188

ABSTRACT

Experimental and theoretical investigations have been carried out for a compact, UV-preionized, discharge-excited, short-pulse XeCl laser.

A comprehensive description of the molecular states and the potential-energy curves for XeCl is provided. The possible radiative transitions are determined according to the selection rules for electric-dipole transitions. An electron-jump model, based on the pseudo-crossings of the potential-energy curves of the ionic states and Rydberg states, is developed to calculate the formation rate-coefficient of the exciplex $XeCl^*$. The results from this model are in good agreement with the results of earlier models discussed in the literature. Furthermore, this model suggests two additional important channels for the formation of $XeCl^*$. As well, the model can be used to evaluate the rate-coefficients for each individual dissociative channel for $XeCl^*$.

The compact laser system has an active discharge volume of ≈ 1 cm^3, providing ≈ 1 mJ output energy in a pulse duration of ≈ 1 ns. This corresponds to a peak output power of ≈ 1 MW. Until very recently, this was the shortest duration pulse produced directly in a discharge-excited excimer laser. The typical operation of the laser employed a 0.8%Xe/0.3%HCl/He gas mixture at a total gas pressure in the range from 350 kPa to 450 kPa, and a capacitor charging voltage of 15 kV.

Discharge voltage waveforms were measured by using a fast-response Pockels cell. The time resolution for these measurements was better than 1 ns. Discharge current waveforms were measured using a fast-response Rogowski coil. These waveform data were used to evaluate

parameters such as inductance and resistance in the excitation circuit, and for comparison with the results from the model.

The model, which is self-consistent and concise, combines the models for both the kinetic processes and for the excitation circuit. In the kinetic model for the discharge, only 40 kinetic processes involving 13 chemical species, plus photons and electrons, are required. These 40 processes, chosen from a much larger number of possible processes, are the only ones with sufficiently large rate-coefficients to influence a short-duration discharge. For the model, use is made of the Boltzmann equation for a spatially-homogeneous medium to solve the electron energy distribution. The validity of the model is demonstrated by the good agreement between the calculated and measured waveform data for discharge voltage, current and resistance, and for laser output in terms of waveform, peak power, total energy, and delay time to the onset of laser emission. This model is very useful for the analysis of the kinetics for short-pulse XeCl lasers, and for optimizing the performance of these lasers.

ACKNOWLEDGEMENTS

I would like to extend my sincere gratitude to Dr. E.A. Ballik for his supervision and support throughout this research. I am also obligated to the members of my supervisory committee: Dr. D.P. Santry, Dr. G.J. Schrobilgen and Dr. W.Y. Lee for their interest and suggestions.

I am grateful to Dr. S.B. Hassal, Mr. A. Duft, and Mr. and Mrs. W.J. Corp for their encouragement, support and friendship.

The financial assistance from the Department of Physics and Astronomy, and the school of Graduate Studies of McMaster University are greatly acknowledged.

In addition, I must thank my parents for their love, encouragement and support.

Finally, I can not adequately express my appreciation and love to my husband, Weining, for his care, patience, encouragement, understanding and support during this study.

The initial phase of this research was supported, in part, by the Natural Sciences and Engineering Research Council of Canada.

TABLE OF CONTENTS

LIST OF FIGURES

LIST OF TABLES

LIST OF SYMBOLS

A	Einstein Spontaneous Emission Coefficient; Cross-Sectional Area of Discharge
$A^2\Pi_{1/2}$	(also $A^2\Pi_{3/2}$, $C^2\Pi_{3/2}$, $D^2\Pi_{1/2}$, $B^2\Sigma^+_{1/2}$ and $X^2\Sigma^+_{1/2}$) Molecular States of XeCl
b	Impact Parameter
c	Speed of Light
D_e	Dissociation Energy
e	Electron Charge
E_c	Energy Stored in a Capacitor
E, E_k	Kinetic Energy
$\overline{E}$	Electric Field Strength
g(v)	Lineshape Function
g	Gain
g_0	Unsaturated Gain
G_v	Vibrational Energy
h	Planck's Constant
I	Electric Current
J	Current Density
k	Wavenumber; Boltzmann Constant
K	Electric Dielectric Constant
l	Orbital Angular-Momentum Quantum Number; Length
L	Length; Inductance
L_1	Length of Active Medium
L_2	Length of Laser Cavity
m	Mass of Electron
M	Mass of Heavy Particle; Mutual Inductance
M_r, μ	Reduced Mass
n, n_0	Refractive Index
n_e	Electron Density
N	Total Density of Gas Mixture

N_i	Number of Incident Particles
N_j	Density of Chemical Species
N_p	Density of Photons
N_s	Number of Particles Scattered
$P_t(m,n)$	Probability of Transition From State m to State n
$P_L(t)$	Laser Output Power
Q	Electric Charge
r	Displacement
R	Internuclear Distance; Resistance
R_j	Rate Coefficient
R_∞	Infinite Internuclear Distance
R_e	Equilibrium Internuclear Distance
s	Spin Angular-Momentum Quantum Number
S_z	Spin Angular-Momentum Quantum Number along the Internuclear Axis of Molecule
t	Time
t_r	Round-Trip Time of an Electromagnetic Wave in the Laser Cavity
T	Temperature; Period of Waveform
T_c	Laser Cavity Lifetime
T_e	Electron Temperature
U(R), V(r)	Potential Energy
v	Vibrational Quantum Number; Velocity
V	Voltage; Discharge Volume
α_0	Absorption Coefficient
γ_{11}	Electrooptic Coefficient
δ	2m/M
δ_s	Density of a Chemical Specie as a Fraction of the Total Density of a Gas Mixture
δ_m	Fraction of Momentum Loss
δ_ε	Fraction of Energy Loss
ε_0	Vacuum Permittivity
η_p	Efficiency of Energy Deposition into a Discharge
η_q	Quantum Efficiency of a Laser
ε	Electron Energy

$\bar{\varepsilon}$, ε_e	Average Electron Energy
ε_j	Threshold Energy
Θ	Scattering Angle in Center-of-Mass Coordinate
θ	Scattering Angle in Laboratory Coordinates; Phase Shift in a Quartz Crystal
θ_1	Angle between Velocity and Electric Field
Λ	Orbital Angular Quantum Number along Internuclear Axis of Molecule
ϕ	Magnetic Flux; Irradiation Flux; Azimuth Scattering Angle
ϕ_s	Saturation Irradiance
$\Delta\phi$	Phase Retardness between Radiation Polarizations
Ψ	Wavefunction
λ	Wavelength
μ_e	Electric Dipole Moment; Electric Mobility
ν	Frequency
ν_m	Collision Frequency
ρ	Fraction of Amplified Spontaneous Emission
σ	Electric Conductivity
$\sigma_{e\text{-}e}$	Cross-Section for Electron-Electron Collisions
σ_j	Inelastic Scattering Cross-Section
σ_m	Momentum-Transfer Collision Cross-Section
σ_s	Elastic Scattering Cross-Section
σ_1	Stimulated Emission Cross-Section
σ_2, σ_3, σ_4	Cross-Sections for Photo Absorption
τ	Lifetime of a Molecular State
Ω	Total Angular-Momentum Quantum Number along Internuclear Axis of Molecule; Solid Angle

$\|u\rangle$, $\|l\rangle$, $\|v\rangle$, etc.	Dirac Operators
$[XeCl^*]$, $[Xe^*]$, $[He^*]$, etc.	Density of Chemical Species

Chapter 1

Introduction

1.1. General Properties of Excimer Lasers.

"Excimer" refers to an electronically excited molecular state, which can give rise to bound-bound or bound-free transitions, depending on whether the ground state is bond or repulsive, respectively. The term "excimer" is now usually used to describe a homonuclear molecule which has a strongly-bound excited state and a repulsive (or weakly-bound) ground state. Such bound-free molecules are generally formed from two closed-shell atoms with a $^1S_0$ ground state. However, the term "excimer" is often also used to describe a heteronuclear diatomic, triatomic or polyatomic molecule with molecular states having similar features. The "correct" term for this type of heteronuclear diatomic molecule, which is formed from a closed-shell atom and an open-shell atom (i.e., a ^2P ground state), is "exciplex". The ground state of an exciplex is either unstable, or bound by a weak van der Waals attraction. As is the current practice, this thesis will often use the term "excimer" instead of the proper term "exciplex". In general, excimers include diatomic rare-gases, rare-gas monohalides, triatomic rare-gas halides, rare-gas oxides, metallic Group II diatomic molecules and diatomic halogen molecules.

Historically, the first laser to use an excimer transition is the infrared nitrogen laser (Mathias and Parker, 1963). Extensive investigations of excimer lasers started after the first bound-free excimer laser system was observed (Koehler et al, 1972). Excimer lasers are capable of producing high output power with relatively-high quantum efficiency in the ultraviolet region

of the spectrum. These lasers have numerous scientific and technological applications, including photochemistry, material processing, excitation of dye- and solid-state lasers, isotope separation, and research into atoms and molecules. In addition, there are numerous medical applications.

Excimer lasers are usually based on radiative transitions from the bound excited states to the dissociative ground state. It is the combination of a strongly-bound excited state and dissociative ground state that provides the potential for high gain and for high laser efficiency. With proper excitation, a large population inversion can be achieved because the ground state is depleted rapidly.

A rare-gas excimer has a repulsive ground state, for which vibrational states do not exist. Consequently, the spectrum has a broad-band continuum. In contrast, a rare-gas monohalide laser ($B \rightarrow X$ transition) usually has a narrow-band spectrum containing a line structure because the transitions are between vibrational states in both the excited state and the weakly-bound ground state. Optical gain coefficients are inversely proportional to the spectral bandwidth. Consequently, the gain is generally higher for a rare-gas monohalide exciplex laser than for a rare-gas excimer laser at the same inversion density. For this reason, rare-gas excimer lasers generally operate at high gas pressures and are excited using electron-beam (e-beam) generators, which are expensive. Rare-gas monohalide exciplex lasers, which operate at relatively lower gas pressures, can be excited efficiently with simple capacitor-discharge circuits.

1.2. XeCl Excimer Lasers.

Since first demonstrated in 1975 (Searles and Hart, 1975; Ewing and Brau, 1975), there has been a rapid development of rare-gas halide lasers. Of the ten rare-gas-monohalide species

observed to date, only six have produced laser operation. Of these six, ArF, KrF, XeCl and XeF lasers are capable of operating with reasonably high efficiency. In particular, the XeCl excimer laser, operating at $\lambda=308$ nm, has attracted considerable attention because of its suitability for numerous industrial and medical applications. Furthermore, the XeCl system is the only important excimer laser capable of very long operating lifetime. XeCl laser performance is characterized by parameters such as peak output power, output energy, pulse duration, laser efficiency, pulse repetition rate, operating lifetime, and pulse-to-pulse stability.

Gas composition can dramatically influence the performance of any excimer laser system. Initially, the XeCl laser was not considered to be potentially important because the early research employed Cl_2 as the halogen donor and Ar as the buffer gas. Unfortunately, the laser radiation at $\lambda=308$ nm is highly absorbed by the Cl_2 and Ar_2^+, which are always present in the discharge, with the consequent reduction of output energy. Ewing and Brau (1975) suggested the replacement of Cl_2 with other chlorine-bearing compounds. Later research found that higher efficiency and higher energy can be achieved with a discharge-excited XeCl laser employing a Xe/HCl/He gas mixture, where the low-mass atom He is used as the buffer gas. Using this gas mixture, Burnham (1978) extracted an energy of 110 mJ with an electrical efficiency (conversion of electric energy into optical energy) of 0.8% from a self-sustained discharge-excited XeCl laser.

Neon is an important buffer gas that was used initially in e-beam excited XeCl lasers (Champagne, 1978). Neon is particularly useful for long-pulse high-energy systems (Osborne and Hutchinson, 1986; Champagne et al, 1987; Taylor and Leopold, 1988; Hasama et al, 1989). Furthermore, neon has higher X-ray absorption than helium (Steyer and Voges, 1987), and is therefore commonly used for X-ray preionized XeCl lasers (Bychkov et al, 1987; Champagne et al, 1987; Steyer et al, 1989; Gerritsen et al, 1990).

The halogen donors CCl_4, CF_2Cl_2, C_2F_5Cl, $CHCl_3$ and BCl_3 have been investigated (Ishchenko et al, 1977; Kudryavtsev and Kuz'mina, 1977; Bychkov et al, 1978), but have not provided benefits such as higher output energies. However, recent work by Peet et al (1991) indicates that the use of BCl_3 for the halogen donor provides a laser operating lifetime that is three times longer than with the HCl donor.

For the compact laser employed in this thesis, the usual gas mixtures were 0.8%Xe/0.3%HCl/He or 1.06%Xe/0.24%HCl/Ne.

Long-pulse operation usually reduces the peak output power, but provides higher output energy and efficiency in comparison with short-pulse systems. Large discharge volumes are usually required to produce high energy. Champagne et al (1987) reported the extraction of 66-J of output energy, in a 180-ns duration pulse, from an active discharge volume of 22 l. Hasama et al (1989) obtained 50-J energy, in an 85-ns duration pulse, from a large aperture discharge containing an active volume of 10 l. In order to achieve long-pulse high-efficiency laser operation, considerable effort has been made to obtain stable discharges. Osborne and Hutchinson (1986) obtained an output energy of 1 J in a pulse duration of greater than 250 ns, using X-ray preionization. An "ultralong" optical pulse (1-μs duration with an output energy of 100 mJ) was obtained by Taylor and Leopold (1989) using a simple corona preionization scheme together with the use of a magnetic spiker and pulse-forming technology. For some time, the most efficient discharge excited XeCl laser system was that of Long et al (1983) (4.2% conversion of electric energy to optical energy). More recently, Gerritsen et al (1990) obtained 5% efficiency from a XeCl laser using a magnetically-induced-resonant voltage-overshoot circuit.

In contrast to long-pulse systems, short-pulse XeCl lasers have high peak-power outputs, small discharge volumes, and relatively low efficiency. Pulse-shortening techniques to obtain

ultra-short pulse durations have been investigated. Employing a relatively complicated XeCl amplifier system, a 160-fs pulse duration with ≈ 100 GW peak power was reported by Glownia et al (1987). This pulse duration almost reaches the quantum limit for the XeCl B → X radiation. Using a relatively simple system to actively mode-lock a XeCl laser, Shay et al (1988) achieved 120-ps duration pulses with energies of 15 μJ.

To avoid the complexity inherent in systems employing pulse-shortening techniques, investigations have been carried out to develop simple, compact, short-pulse XeCl lasers. These lasers are important for a number of applications, including excitation for short-pulse dye lasers, remote sensing, reaction chemistry and spectroscopy. A particularly important application is for surgery, where short pulse durations minimize tissue damage. The miniature XeCl (1-cm^3 discharge volume) of Sze and Seegmiller (1981) provided 0.5-mJ output energy in an ≈4-ns duration pulse, with an electrical efficiency of 0.25%. Armandillo et al (1985) obtained 3-mJ output energy in a 15-ns duration pulse from a 19.6-cm^3 discharge volume.

One of major obstacles in the development of short-pulse laser systems is the difficulty of depositing high electrical energy into the discharge within a small time interval. Therefore, fast-risetime high-voltage excitation circuits are required. This requirement is satisfied for the compact discharge-excited XeCl laser used in this thesis. Based on design by Ballik (1981), the laser has a discharge current risetime of $0.3 \cdot 10^{13}$ A·s^{-1}, and is capable of producing 1-mJ energy in a 1-ns duration pulse. The electrical efficiency is 0.3%. Comparable direct short-pulse production had not been achieved until very recently (Rácz et al, 1992).

Kinetic modelling, based on computer simulations, remains an interesting and important topic in the study of excimer lasers, and is a very useful supplement to experimental investigations. For example, it is difficult to optimize or to change the laser output characteristics

experimentally because a large number of parameters can influence the laser performance.

In recent years, many attempts have been made to develop suitable kinetic models for discharge-excited XeCl lasers. This is a difficult problem because of the large number of chemical reactions occurring within the discharge. Kinetic models for long-pulse duration XeCl lasers (Lee, 1983; Hokazono et al 1984; Kannari et al, 1990; Turner and Smith, 1991; Letardi et al, 1992) include a large number of kinetic processes (>100) and chemical species. However, no other model in the literature is concerned with short-pulse duration XeCl lasers (<2 ns). In our model (Xia and Ballik, 1993), discussed in detail in Chapters 5 and 6, only 40 kinetic processes and 13 chemical species are found to be important for short-pulse duration XeCl lasers (for which the effective discharge duration is <10 ns). Many of the long-lived discharge species can be neglected in the calculations because both the discharge and output pulses have short durations. Compared to previous models, our model provides a better understanding of the fast kinetic processes, and of the development of species densities at the early stages of the discharge. In addition, the model provides a considerable simplification in the kinetic equations for the XeCl laser, thereby reducing computational time substantially. The validity of the model is verified by the good agreements between the calculated results and the measured data.

1.3. Organization of the Thesis.

In this thesis, both theoretical and experimental investigations have been carried out for a compact UV-preionized discharge-excited short-pulse-duration XeCl laser. The objectives of the research was to provide a comprehensive understanding of the $B \rightarrow X$ laser transitions and the kinetic processes in the discharge, and to optimize the laser system.

A study of the XeCl laser transition requires a knowledge of the basic structure of the XeCl molecule. The structure and spectroscopy of XeCl are discussed in Chapter 2. The experimental spectroscopic data of Sur et al (1979) are used to calculate the electronic potential-energy curves and their corresponding vibrational levels. Possible radiative transitions (including $B \rightarrow X$) from the ionic-bound excited states to the ground states are identified employing the selection rules for electric-dipole transitions. The lifetime and the emission cross-section of upper laser level, $XeCl^*(B)$, are calculated using the Franck-Condon factors. Based on the knowledge of the potential-energy curves for the XeCl molecule, an electron-jump model (Lee et al, in preparation) is developed to calculate the formation rate-coefficient for $XeCl^*$. Compared to previous models reported in the literature, the electron-jump model provides additional information for each individual channel in the formation and dissociation of $XeCl^*$.

Various excitation methods for excimer lasers are discussed in Chapter 3, followed by a discussion of the design and construction of the short-pulse-duration laser system used in the research. This system consists of several components, including a small UV-preionized laser body, a pulse-forming network to excite the discharge, a gas circulation system , and a high-voltage power supply. Chapter 3 also gives the results of experimental investigations of laser performance for a range of gas mixtures and pressures, and of discharge conditions.

Discharge voltage and current waveforms are important data for the study of energy flow in excimer laser systems, and for the verification of the kinetic model for the discharge. Chapter 4 presents the results of accurate measurements of these waveforms. Conventional high-voltage probes are unsatisfactory because these have a relatively-slow response time, and because these probes lack the ability to be electrically isolated from "ground" potential. Therefore, an optical technique, employing a fast-response Pockels cell, was used for observing fast changes

(~ 1 ns) in the discharge voltage waveforms. Current waveforms were measured using a fast probe employing a Rogowski-coil. The resulting experimental data were used in the development of the model for the excitation circuit.

Chapters 5 and 6 cover the development of a kinetic model to simulate the kinetic processes in the gain medium. Because of the short-duration discharge in our laser, it was possible to develop a concise model which includes only 40 processes involving 13 chemical species, plus electrons and photons.

Only electron-impact collision processes are discussed in Chapter 5. These processes include elastic, inelastic, superelastic and associative attachment collisions of electrons with other species in the discharge, and electron-electron collisions. In contrast to the Monte Carlo simulation of Lee (1983), a numerical code for the Boltzmann equation is developed to solve the electron energy distribution, and then to calculate the collision rate-coefficients and electron-transport parameters.

As mentioned, the electron-impact collisions are covered in Chapter 5. Other chemical reactions, and the photo-emission and -absorption processes are discussed in detail in Chapter 6. In particular, the formation channels are described for the upper laser-level species $XeCl^*$. In addition to the time-dependent densities of the various discharge species and the laser output, the calculations also provide data for parameters such as energy flow, laser efficiency, and optical gain. The validity of the model is verified by the good agreement between the calculated and measured data for the laser output waveform, peak power and energy, and for the discharge voltage, current and resistance waveforms.

The conclusions derived from this thesis are presented in Chapter 7. Also presented are the recommendations for future research on the short-pulse XeCl laser.

Chapter 2

Molecular Structure and Spectroscopy of XeCl

In order to advance the development of rare-gas monohalide UV laser sources, many studies have been carried out to examine molecular structure, molecular states and possible radiative transitions of these molecules (Sur et al, 1979; Dunning and Hay, 1978; Hay and Dunning, 1978; Brau and Ewing, 1975; Ohwa and Kushner, 1989). Because of the weak interaction between the closed shell of rare-gas atoms and the open shell of halogen atoms, the ground state of rare-gas halides are usually repulsive. In some cases, a weak bond is formed from a van der Waals attraction induced by charge-transfer mixing of the ground state and the ionic-bound excited states. However, the excited states formed from a positive rare-gas ion and a negative halogen ion are strongly bound by Coulomb attraction. It is this combination of an essentially repulsive ground state with a strongly-bound excited state that provides efficient gain production in rare-gas-halide lasers. The higher excited states have relatively weaker Rydberg covalent bonds between the excited rare-gas atom and the ground state halogen atom.

The electronic configurations of the molecular energy states are discussed in Section 2.1. Section 2.2 provides a description of the electronic potential-energy curves and vibrational states. In Section 2.3, the allowed emission spectra are introduced. Five emission bands are observed and identified as electronic transitions from ionic-bound excited states to the ground states. The Einstein spontaneous-emission rates and stimulated-emission cross-sections of the upper laser levels are determined from application of the Franck-Condon factors to the profiles of the emission bands. In section 2.4, an electron-jump model is developed to calculate the formation

rate of the upper laser level $XeCl^*$.

2.1. Electronic States

The potential-energy diagrams for all of the rare-gas monohalide molecules have characteristics similar to those for the XeCl molecule, shown in Fig. 2.1. These curves are based on experimental and theoretical data available in the literature (Sur et al, 1979; Hay and Dunning, 1978; Brau and Ewing, 1975). Applying the Wigner-Witmer correlation rules (Wigner and Witmer, 1928) for the addition of orbital momenta and spin momenta to the infinite internuclear separation limit (R_∞) for $Xe(^1S_0)+Cl(^2P)$, there arise two covalent molecular states, $X^2\Sigma^+$ and $A^2\Pi$. When the effect of spin-orbital coupling in the halogen atom is considered, the degenerate infinite-separation state splits into $Xe(^1S_0)+Cl(^2P_{1/2})$ and $Xe(^1S_0)+Cl(^2P_{3/2})$, with an energy separation of only 881.0 cm^{-1} (0.11 eV) (Moore, 1949, 1952 and 1958), which is the energy separation between $Cl(^2P_{1/2})$ and $Cl(^2P_{3/2})$. Both the $A^2\Pi$ and $X^2\Sigma^+$ states are either repulsive or only weakly-bound due to the weak interaction of the open-shell configuration of the halogen atom with the closed-shell configuration of the rare gas atom. The degree of repulsion for these states is approximately proportional to the number of $p\sigma$ electrons in the two atoms because the overlap of $p\sigma$ orbitals determines the strength of the covalent bond (Dunning and Hay, 1978). Therefore, the potential-energy curves for the $^2\Sigma^+$ state, which is formed from the doubly-filled $p\sigma$ orbital of Xe and the singly-filled $p\sigma$ orbital of $Cl(p\sigma)^1(p\pi)^4$, should be less repulsive than the curve for the $^2\Pi$ state, which is formed from the doubly-filled $p\sigma$ orbital of both Xe and $Cl(p\sigma)^2(p\pi)^3$. When the spin-orbital effects in the $X^2\Sigma^+$ and $A^2\Pi$ states are included, these split into three states, two with $\Omega=1/2$ and one with $\Omega=3/2$, where $\Omega=\Lambda+S_z$ is the total angular

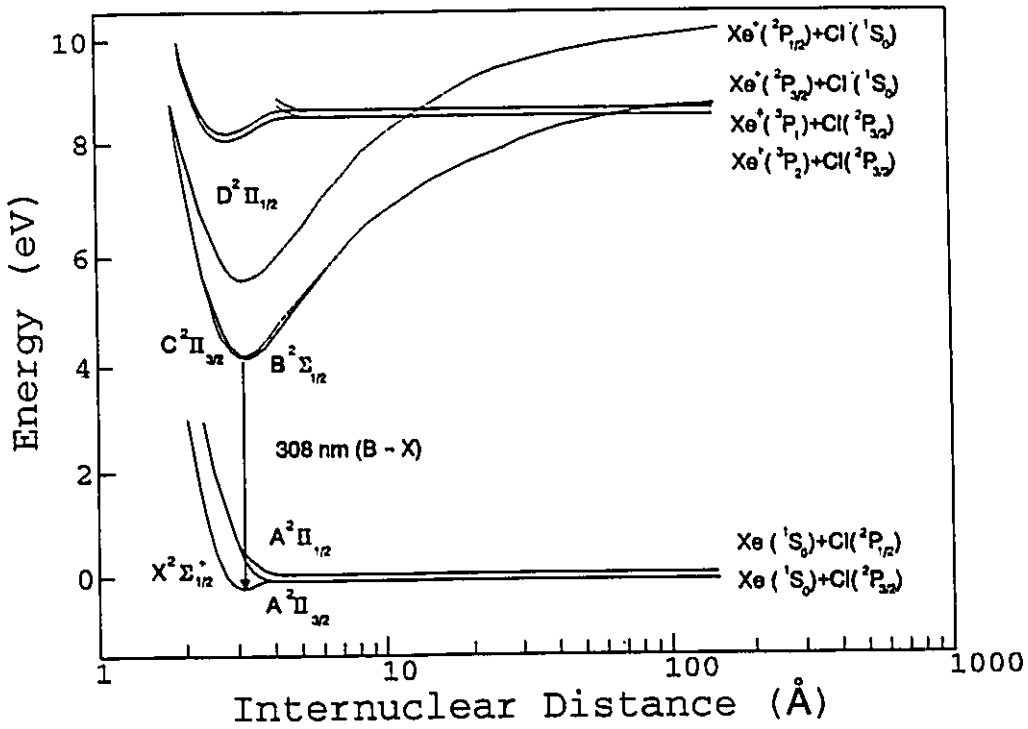

Fig. 2.1. Potential-energy diagram for the XeCl molecule.

momentum along the internuclear axis of the molecule. The state $A^2\Pi_{1/2}$ results from the $Xe(^1S_0)+Cl(^2P_{1/2})$ limit, and the $A^2\Pi_{3/2}$ and $X^2\Sigma^+_{1/2}$ states, which are degenerate at large internuclear distances, result from the $Xe(^1S_0)+Cl(^2P_{3/2})$ limit (Herzberg, 1950). At small internuclear distances, the energy between the $X^2\Sigma^+$ and $A^2\Pi$ states is greater than the energy between the $Cl(^2P_{3/2})$ and $Cl(^2P_{1/2})$ states. In addition, quenching of the atomic spin-orbit coupling causes states $A^2\Pi_{1/2}$ and $A^2\Pi_{3/2}$ to become nearly degenerate at small internuclear distances.

Similarly, the ionic-bond and charge-transfer states $^2\Sigma^+$ and $^2\Pi$, respectively, are formed from the ionic species $Xe^+(^2P)+Cl^-(^1S_0)$. When spin-orbit coupling is included, a total of three states are now produced, $B^2\Sigma^+_{1/2}$ and $C^2\Pi_{3/2}$ which correlate to $Xe^+(^2P_{3/2})+Cl^-(^1S_0)$ at R_∞, and $D^2\Pi_{1/2}$ which correlates to $Xe^+(^2P_{1/2})+Cl^-(^1S_0)$ at R_∞. The energy difference between the $Xe^+(^2P_{3/2})$ and $Xe^+(^2P_{1/2})$ states is 10,538 cm^{-1} (1.31 eV) (Moore, 1949), which is much larger than the difference between the $Cl(^2P_{3/2})$ and $Cl(^2P_{1/2})$ states of Cl. Consequently, the energy difference between states $C^2\Pi_{3/2}$ and $D^2\Pi_{1/2}$ is also much larger than that between states $A^2\Pi_{1/2}$ and $A^2\Pi_{3/2}$. The energies of the $Xe^+(^2P_{3/2})+Cl^-(^1S_0)$ and $Xe^+(^2P_{1/2})+Cl^-(^1S_0)$ states relative to the ground state are 68,670 cm^{-1} (8.51 eV) and 79,208 cm^{-1} (9.82 eV), respectively. These are equal to the ionization potentials of Xe to $Xe^+(^2P_{3/2})$ (97,834 cm^{-1}/12.127 eV) and $Xe^+(^2P_{1/2})$ (108,372 cm^{-1}/13.433 eV) (Moore, 1949), respectively, minus the electron affinity of Cl (29,164 cm^{-1}/3.615 ev) (Varshni and Shulka, 1950). The ionic states are strongly attractive because of the inverse Coulomb interaction between the positive and negative ions. States $B^2\Sigma^+_{1/2}$ and $C^2\Pi_{3/2}$ are nearly degenerate at all internuclear distances. In addition, employing the same arguments as were used above for the $p\sigma$ orbital interactions in the X and A states, the $B^2\Sigma^+_{1/2}$ state should be slightly lower in energy than the $C^2\Pi_{3/2}$ state. However, due to the ionic-covalent interaction of the two $^2\Sigma^+_{1/2}$ states at short internuclear distances (discussed in Section 2.2), the

energy of the $B^2\Sigma^+_{1/2}$ state becomes higher than that of the $C^2\Pi_{3/2}$ state.

Higher covalent excited states (Rydberg states) of XeCl are formed from metastable Xe and Cl atoms. From basic theoretical considerations of the Xe atom, the excitation of a 5p orbital electron to the 6s orbital gives four atomic states. Three of these states correspond to ^{3}P and one to ^{1}P. Because the 5p-subshell of the excited Xe atom is more than half-filled, the lowest energy term is the one with the largest total angular momentum (i.e., $^3P_2$). On the basis of the Wigner-Witmer correlation rules (Wigner and Witmer, 1928), the recombination of a ^{3}P Xe atom with a ^{2}P Cl atom gives rise to six doublet (three $^2\Sigma$, two $^2\Pi$ and one $^2\Delta$) and six quadruplet (three $^4\Sigma$, two $^4\Pi$ and one $^4\Delta$) Rydberg molecular states. As these molecular states are not directly related to radiative decay, the details are not shown in Fig. 2.1. At the separated-atom limit R_∞, states $Xe(^3P_2)+Cl(^2P_{3/2})$ and $Xe(^3P_1)+Cl(^2P_{3/2})$ are 67,081 cm^{-1} (8.315 eV) and 68,066 cm^{-1} (8.437 eV) above the $Xe(^1S_0)+Cl(^2P_{3/2})$ ground state, respectively. Both of these values are slightly below the ionic limit for $Xe^+(^2P_{3/2})+Cl^-(^1S_0)$ (68,671 cm^{-1}/8.512 eV). Therefore, at large internuclear distances, the ionic potential-energy curve crosses the covalent curves. The resulting diabatic interactions produce pseudo-crossings which contribute to the formation of the upper laser level ($B^2\Sigma^+_{1/2}$) via electron harpooning processes. These processes are discussed in Section 2.4.

2.2. Vibrational States and Electronic Potential-Energy Curves

Historically, the alkali-halide molecules were important in establishing the basic characteristics of the rare-gas halide molecules. The equilibrium internuclear separations (R_e) and the dissociation energies (D_e) of the B and D states (see Fig. 2.1) can be approximated by comparing the ionic rare-gas-halide molecule with the X state of the next higher alkali molecule

in the periodic table. Although the atomic configurations are slightly different, Hartree-Fock calculations (Fraga et al, 1971) demonstrate that the rare-gas/halogen-ion pair is analogous to the corresponding alkali halide. This is expected because the noble gas ion and the nearest alkali ion have approximately the same size. The potential-energy curves are similar, as are the vibrational spacings of 210 cm^{-1} for the XeCl B state (Brau and Ewing, 1975) and 214 cm^{-1} for CsCl (Dunning and Hay, 1978).

The potential-energy curves of the ionic and covalent electronic states can be characterized by theoretical *ab initio* configuration interaction calculations (Hay and Dunning, 1978). In these calculations, the atomic core orbitals are reduced to Hartree-Fock orbitals (single ζ function), and the valence orbitals are reduced to two functions (double ζ functions), using the general method of Raffenetti (1973). In addition, a single set of 2p-Gaussian functions is used to describe the negative halogen ion, and a single set of 3d-Gaussian functions is used to describe the polarization effects from all the atomic bases. The accuracy of the calculations for spectroscopic constants and emission wavelengths ($\sim 10\%$) is limited by the lack of a proper set of functions to describe the polarization effect of the halogen ion (Stevens and Krauss, 1979). Van der Waals attraction terms are not included in the calculations. As a result, a repulsive potential-energy curve is obtained for the covalent ground state where, experimentally, a the shallow well is observed.

From experimental measurements of the emission spectra of B → X and D → X transitions, Sur et al (1979) obtained more reliable molecular constants for the three states (X, B and D) by a simultaneous least-square fit of 41 vibrational band-heads in the B → X system and of 35 band-heads in D → X system. They also evaluated the potential-energy curves for all of these three states using Frank-Condon Factor (FCF) calculations, employing the vibrational energy levels (G_v) in an electronic potential well. These levels are generally approximated by the fourth-order

polynomials

$$G_\upsilon = \sum_{i=1}^{4} c_{\upsilon i}(\upsilon + \frac{1}{2})^i \quad . \tag{2.1}$$

or equivalently by

$$G_\upsilon = \omega_e(\upsilon + \frac{1}{2}) - \omega_e x_e(\upsilon + \frac{1}{2})^2 + \omega_e y_e(\upsilon + \frac{1}{2})^3 + \omega_e z_e(\upsilon + \frac{1}{2})^4 \quad . \tag{2.2}$$

For the $X^2\Sigma^+$ state of XeCl, the spectroscopic parameters are evaluated by a least-squares fit of Eq. (2.2) with the observed vibrational energy levels (Sur et al, 1979). The resulting constants are ω_e=26.22 cm^{-1}, $\omega_e x_e$=-0.321 cm^{-1}, $\omega_e y_e$=-0.0853 cm^{-1} and $\omega_e z_e$=0.00191 cm^{-1}. Note that $\omega_e x_e$ is generally positive for most diatomic molecules. Data calculated using these constants in Eq. (2.2) are plotted in Fig. 2.2. This anharmonic function is compared with a harmonic function having the same value of ω_e. There are 20 vibrational states in the shallow well of the $X^2\Sigma^+$ state because the vibrational energy spacings are very small. Long-range theory for a weak attractive potential between atoms (LeRoy, 1973) is employed to estimate the dissociation energy D_e. The estimated value of D_e is determined from

$$g(G_\upsilon) \equiv (dG_\upsilon/d\upsilon)^{3/2} = K_6^{3/2}(D_e - G_\upsilon) \quad . \tag{2.3}$$

Substitution of the theoretical value $K_6^{3/2}$=1.278 into Eq.(2.3) results in D_e=281 cm^{-1}. The turning points for each vibrational level, evaluated using Frank-Condon Factor calculations (Sur et al, 1979), are listed in Table 2.1, together with the equilibrium internuclear separation R_e. The potential-energy curve for the XeCl ground state is plotted in Fig. 2.3.

Based on the fact that the covalent $X^2\Sigma^+$ state has a negative $\omega_e x_e$, Lee (1983) proposed a potential function of the form

Table 2.1. Turning Points for the $X^1\Sigma^+$ Potential-Energy Curve.

v	$G_v(cm^{-1})$	$R_{min}(Å)$	$R_{max}(Å)$
-0.5	0.00	R_e = 3.23	
-0.4	2.63	3.1442	3.3363
-0.2	7.89	3.0944	3.4266
0.0	13.18	3.0645	3.4927
0.2	18.49	3.0422	3.5483
0.6	29.13	3.0091	3.6425
1	39.78	2.9843	3.7235
2	66.31	2.9400	3.8971
3	92.34	2.9089	4.0512
4	117.51	2.8853	4.1991
5	141.49	2.8664	4.3477
6	163.99	2.8511	4.5024
7	184.77	2.8385	4.6680
8	203.65	2.8281	4.8493
9	220.48	2.8195	5.0521
10	235.15	2.8124	5.2839
11	247.63	2.8066	5.5554
12	257.89	2.8019	5.8822
13	265.98	2.7982	6.2906

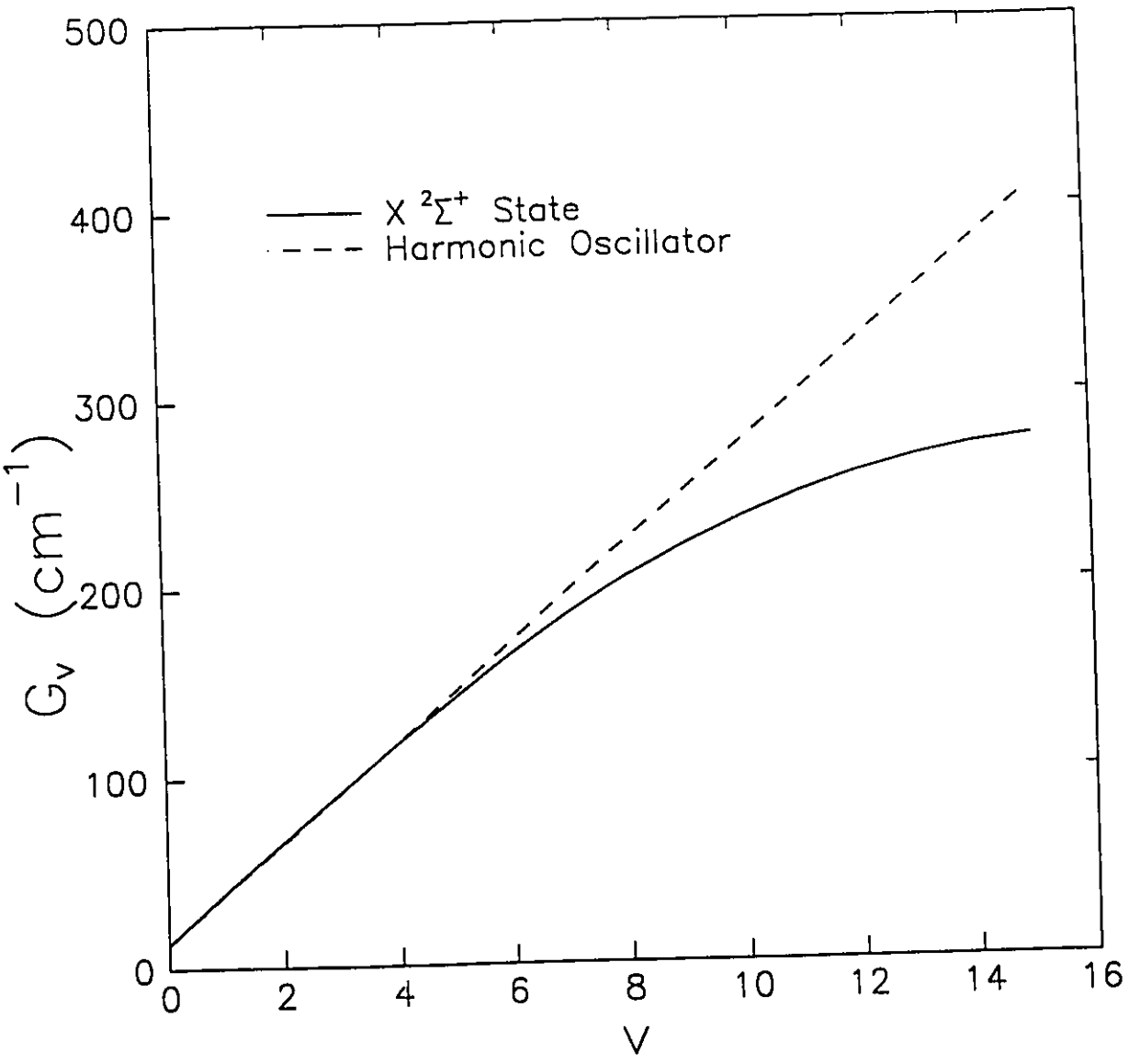

Fig. 2.2. Ground-state vibrational energy as a function of the vibrational quantum number. The harmonic oscillator is included for comparison.

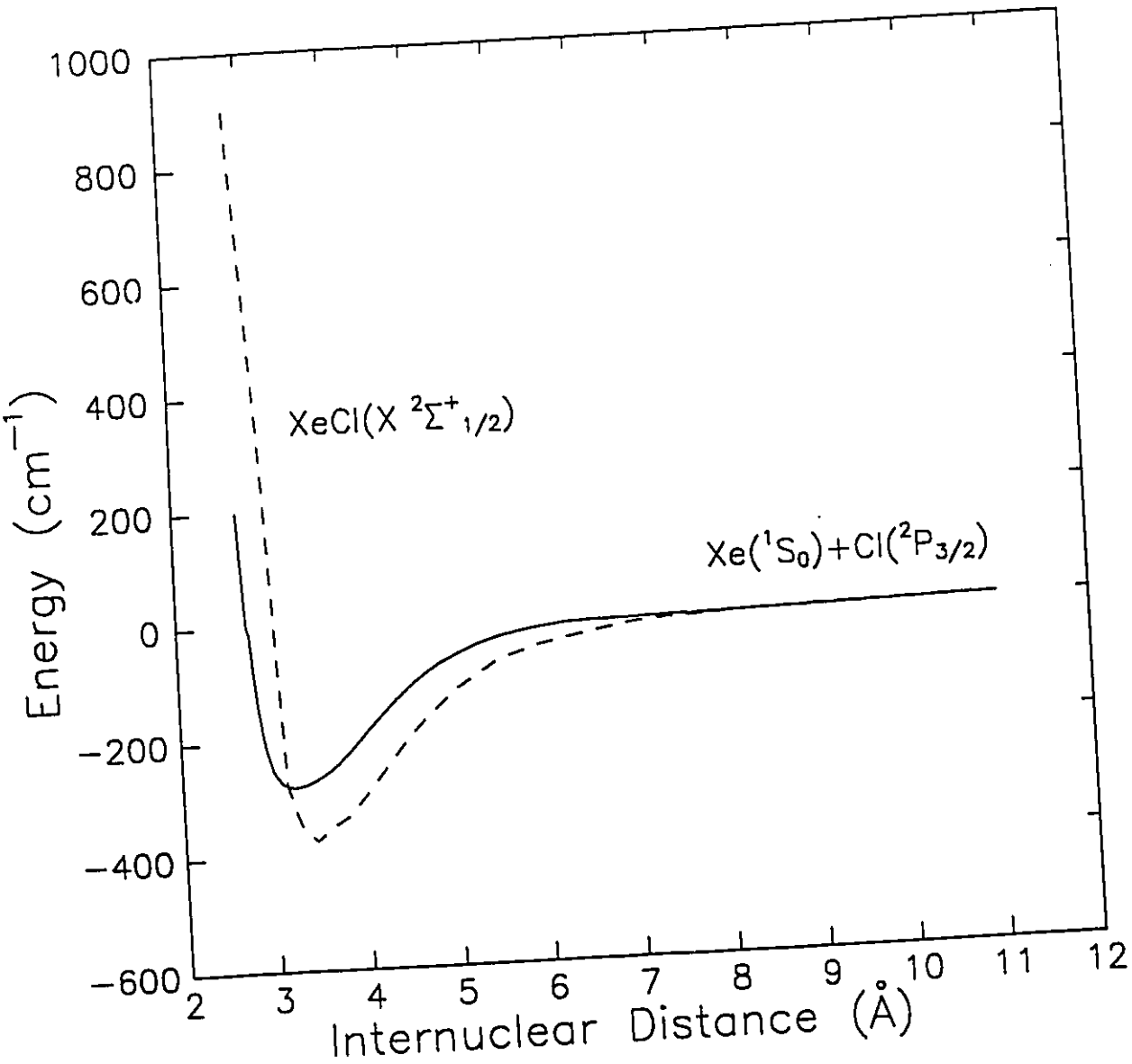

Fig. 2.3. The potential-energy diagram for ground state $X^2\Sigma^+$. The solid curve is based on the experimental data of Sur et al (1979). The dashed curve employs the data of Stevens and Krauss (1979).

$$V(R) = D_e \left[\frac{a \ln(y)}{y^n} + \frac{b \ln(y) - 1}{y^p} + 1\right] \quad , \qquad (2.4)$$

where $y = R/R_e$ (R is internuclear distance). Constants a, b, n and p are determined using a nonlinear least-squares fit of this function with the experimental data of Sur et al (1979), and the data in Table 2.1. This fit yields n = 6.973, p = 16.674, a = -13.176, and b = -3.498. It was suggested (Lee, 1983) that V(R) is a van der Waals (R^{-6}) potential distorted by a logarithmic-type (-ln(R)/R) field. The van der Waals interaction might originate from mixing of charge transfer ionic states (e.g., $B^2\Sigma^+$) with covalent states (e.g., $X^2\Sigma^+$). These interactions can have a substantial influence. In particular, the potential well of the ground state is deepened. Although this makes the $X^2\Sigma^+$ state less repulsive, the $B^2\Sigma^+$ state becomes more repulsive. As a result, the curve for the $B^2\Sigma^+$ state becomes steeper and crosses with the curve for the $C^2\Pi_{3/2}$ state at short internuclear distances. This effect increases with decreasing separation of the covalent and ionic curves. Therefore, the rare-gas-halide interaction increases in the sequence Ne < Ar < Kr < Xe. The corresponding rare-gas ionization energy decreases, causing a decrease in the ionic-covalent energy separations.

Detailed analysis of the electronic-vibrational spectra of the B → X and D → X transitions in XeCl shows that the D state curve is deeper and steeper than the B state curve, and that the former state also has slightly shorter equilibrium internuclear distance (R_e=2.922 Å for the D state compared to R_e=3.007 Å for the B state (Sur et al, 1979)). The dissociation energies (D_e) of the B and D states are 36,553 cm^{-1} and 37,148 cm^{-1}, respectively. The potential-energy curves for these two ionic states can be approximated by the truncated Rittner potential (Sur et al, 1979; Brumer and Kapplus, 1973)

$$U(R) = a + be^{-\beta R} - \frac{c_1}{R} - \frac{c_3}{R^3} - \frac{c_4}{R^4} \quad . \tag{2.5}$$

Parameter a is the asymptotic ionic energy. Parameters b and β are determined from the experimental value of D_e and ω_e. The c_1 term, which corresponds to the Coulomb interaction of the ion pair, dominates at large internuclear distances. At short distances, the exponential term dominates as a strong repulsive potential. The c_3 term corresponds to the ion-quadruple interaction. For the B state, $c_3=(e^2/5)<r^2>$, where $<r^2>$ is the average r^2 value of the p-valence electrons in the $Xe^+(^2P_{3/2})$ ion. For the D state, $c_3=0$ because the $^2P_{1/2}$ state of Xe^+ does not have a quadruple moment. Parameter c_4 relates to an ion-induced dipole interaction.

Molecular coefficients for the B, D and X states are given in Table 2.2 (Sur et al, 1979). The vibrational levels in the B and D potential wells were evaluated using a least-squares fit of the vibrational transition band-heads with Eq. (2.1), and from FCF calculations. In contrast to the X state, these two states are anharmonic states (i.e., $\omega_e x_e$ is positive). G_v as a function of v for the B and D states are plotted in Fig. 2.4. The potential-energy curves for the B and D states are given in Fig. 2.5 using data from Eq. (2.5). For comparison, Fig. 2.5 also includes the results of *ab initio* calculations (Hay and Dunning, 1978).

2.3. Spectra of XeCl

Spontaneous emission has been observed from a number of rare-gas halides, including NeF, ArF, KrF, XeF, ArCl, KrCl, XeCl, ArBr, XeBr and XeI. Of these, laser emission has been achieved only from ArF, KrF, XeF, KrCl, XeCl and XeBr. The emission spectra are similar because the molecular configurations of all the rare-gas halides are similar. As shown in

Table 2.2. Molecular Parameters for the X, B and D States (in units of cm^{-1}, except where indicated otherwise).

	X	B	D
D_e	281	36553	37148
$R_e(Å)$	3.23	3.007	2.922
T_e	0.0	32405.8	42347.9
$c_{v1}(\omega_e)$	26.22	194.75	204.34
$c_{v2}(-\omega_e x_e)$	0.321	-0.627	-0.682
$c_{v3}(\omega_e y_e)$	-0.0853		
$c_{v4}(\omega_e z_e)$	0.00191		
b		$1.7348 \cdot 10^7$	$2.1316 \cdot 10^7$
$\beta(Å^{-1})$		2.5637	2.7261
$c_3(cm^{-1}Å^3)$		$3.9 \cdot 10^4$	0.0
$c_4(cm^{-1}Å^4)$		$3.5 \cdot 10^5$	$3.5 \cdot 10^5$

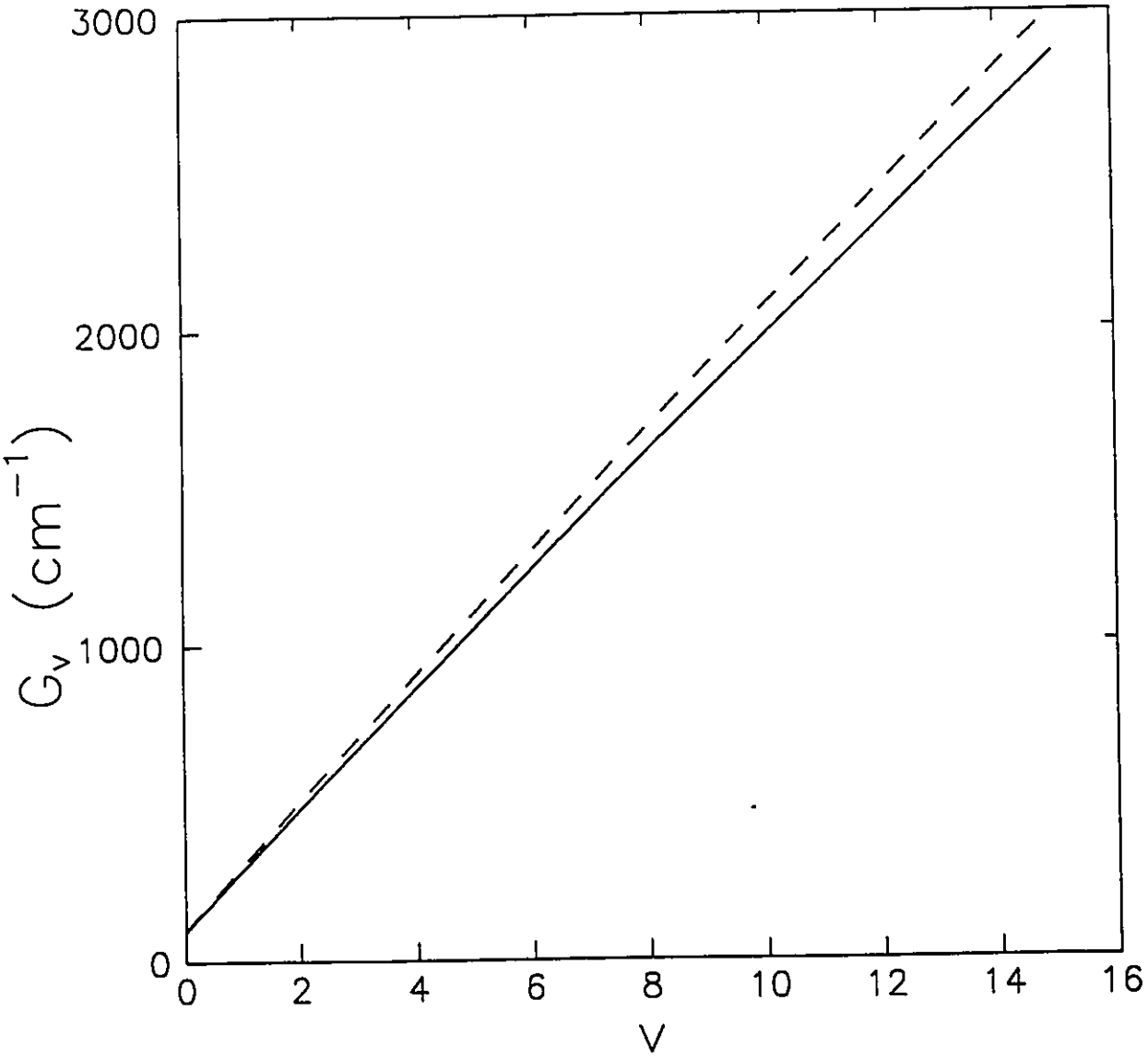

Fig. 2.4. The relationship between vibrational levels and energies for the excited states B (solid curve) and D (dashed curve).

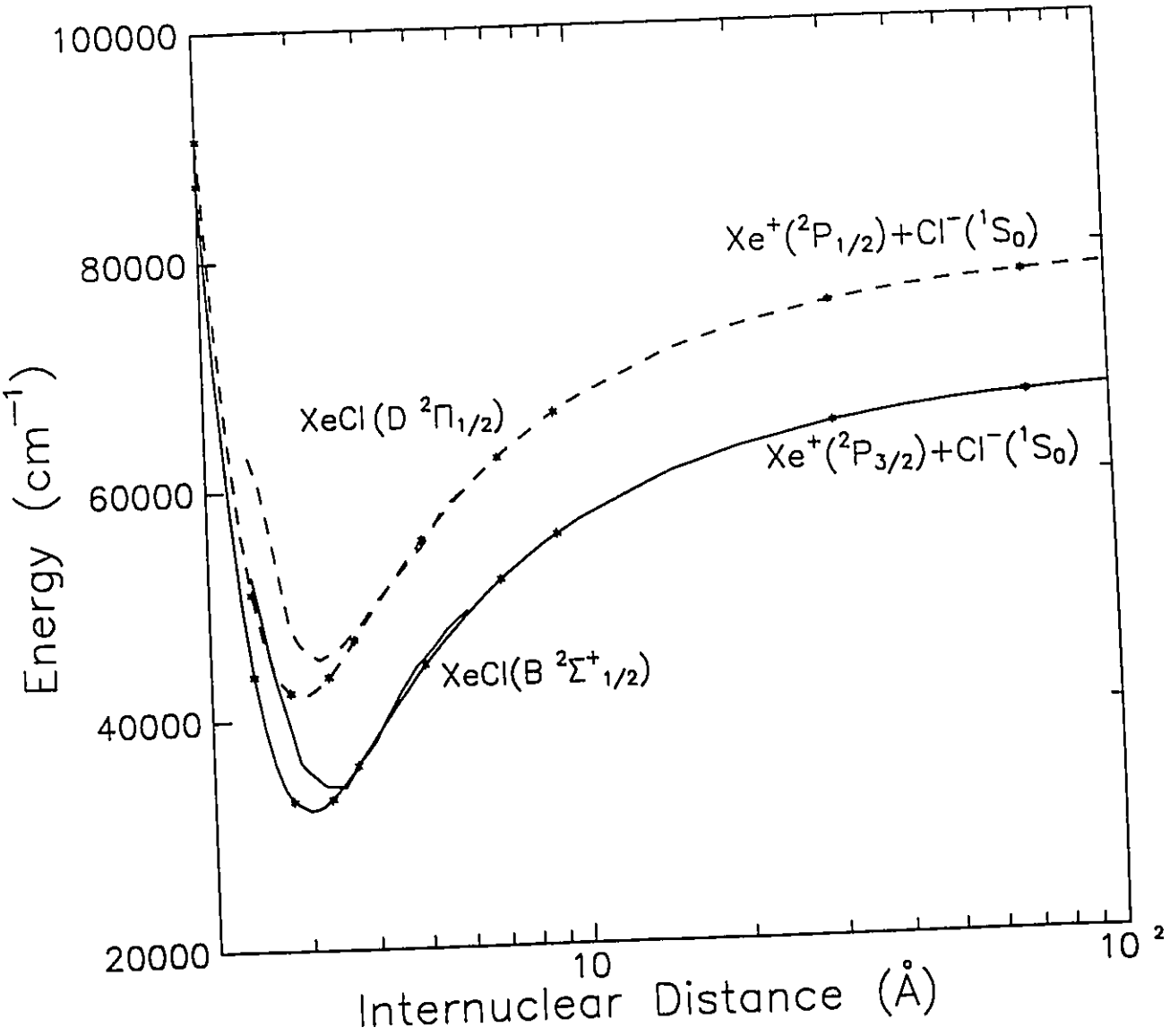

Fig. 2.5. The potential-energy diagram for the $B^2\Sigma^+$ states (solid curves) and the $D^2\Pi$ states (dashed curves). The two curves containing plotted points are based on the results from the experimental data of Sur et al (1979). The other two curves are based on the calculations of Hay and Dunning (1978).

Fig. 2.6, the spectrum for XeCl (Sur et al, 1979; Brau and Ewing, 1975) consists of several bands, with the strongest band arising from the $B^2\Sigma^+_{1/2} \rightarrow X^2\Sigma^+_{1/2}$ transition at high pressures. This transition has been observed to produce the most efficient laser emission from a rare-gas halide.

For XeCl, the $B^2\Sigma^+_{1/2} \rightarrow X^2\Sigma^+_{1/2}$ electronic-transition band has an intensity peak (band head) at $\lambda = 308$ nm. As the gas pressure is increased beyond 1 atm, successive vibrational-band heads appear as shorter wavelengths, with energy spacings of 195 cm^{-1} (Sur et al, 1979). These heads are identified as transitions from the lower vibrational levels of the upper electronic state (Brau and Ewing, 1975). At high pressures, collisions depopulate (quench) the higher vibrational levels by decays to the lower levels in the same $B^2\Sigma^+_{1/2}$ state. Consequently, only transitions from the lower vibrational levels are observed.

The strong emission at wavelength $\lambda = 308$ nm is the transition from $v' = 0$ ($B^2\Sigma^+_{1/2}$) to $v'' = 1$ ($X^2\Sigma_{1/2}$). At low pressures, where collisions are not a dominant factor in the quenching of levels, there is a diffuse spectrum extending to shorter wavelengths. In addition, there are some discrete bands within each of the main vibrational bands because the vibrational energy spacings in the $X^2\Sigma^+_{1/2}$ state are much smaller than those in the $B^2\Sigma^+_{1/2}$ state. These discrete levels correspond to transitions from the same vibrational level of the $B^2\Sigma^+_{1/2}$ state to several vibrational levels of the $X^2\Sigma^+_{1/2}$ state. The vibrational levels involved, together with the corresponding band heads, are listed in Table 2.3 (Sur et al, 1979). This table also includes the vibrational transitions in the $D^2\Pi_{1/2} \rightarrow X^2\Sigma^+_{1/2}$ electronic spectrum. This transition was also observed as a strong transition at low gas pressures (Hassal, 1991). The strongest transition is from $v' = 0$ ($D^2\Pi_{1/2}$) to $v'' = 3$ ($X^2\Sigma^+_{1/2}$), with an intensity peak at $\lambda = 236.0$ nm. The vibrational spectra of the $D^2\Pi_{1/2} \rightarrow X^2\Sigma^+_{1/2}$ transitions are similar to these of the $B^2\Sigma^+_{1/2} \rightarrow X^2\Sigma^+_{1/2}$ transitions. The latter have a slightly higher vibrational spacing of 204 cm^{-1} in the D state (Sur et al, 1979) because the

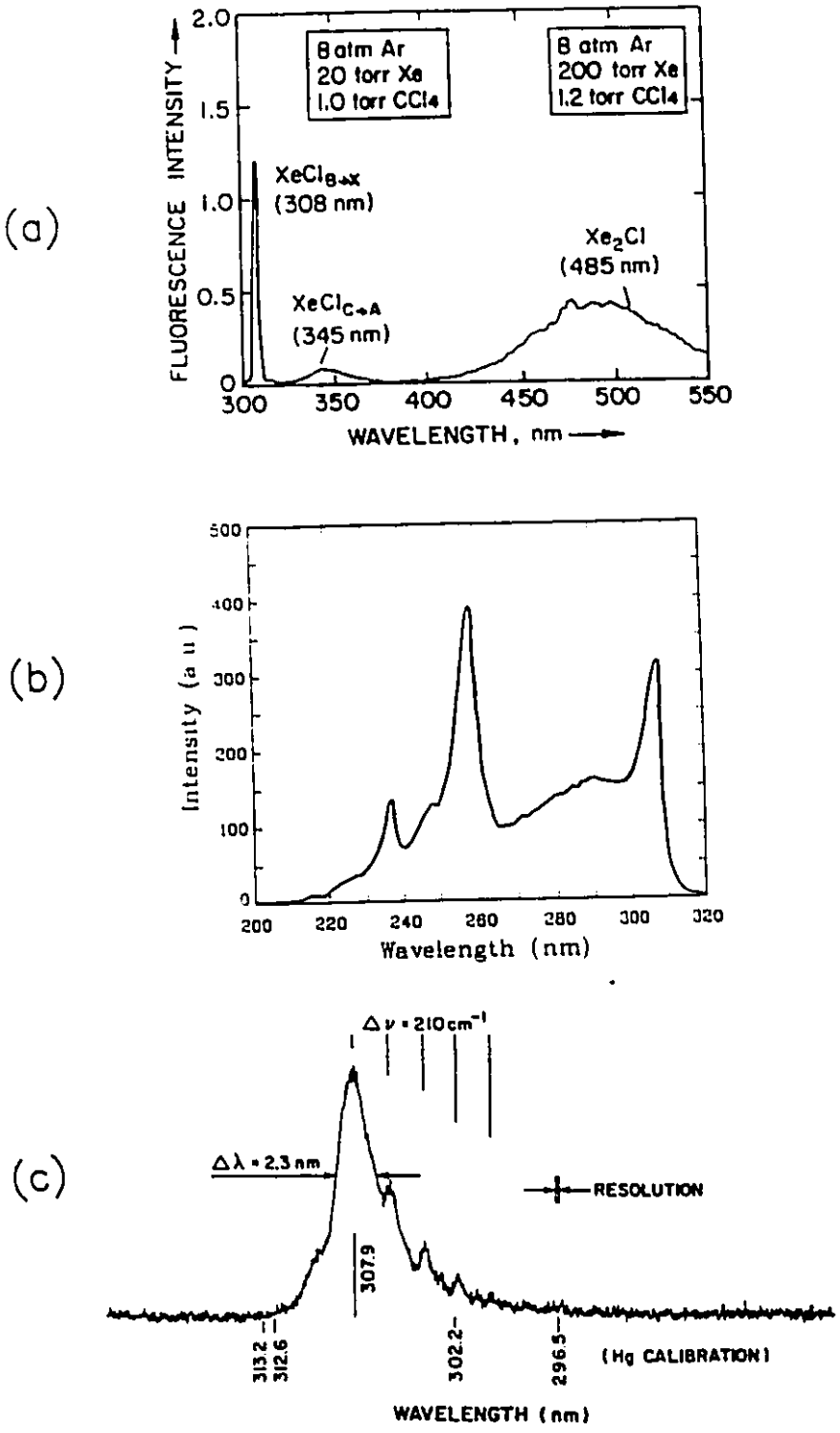

Fig. 2.6. The emission spectra of the XeCl molecule. (a) Electronic spectrum at a high gas pressure (Huestis et al 1984). (b) Electronic emission spectrum at a low gas pressure (Hassal, 1991). (c) The vibrational emission spectrum observed by Brau and Ewing (1975).

Table 2.3. Assigned Bandheads for XeCl

	B → X			D → X	
v'-v"	(Å)	(cm^{-1})	v'-v"	(Å)	(cm^{-1})
0-6	3091.37	32338.7	0-11	2368.74	42203.7
0-5	3089.21	32361.3	0-10	2368.07	42215.5
0-4	3086.90	32385.6	0-9	2367.31	42229.2
0-3	3084.50	32410.8	0-8	2366.35	42246.3
0-2	3082.04	32436.7	0-7	2365.30	42264.9
0-1	3079.53	32463.0	0-6	2364.13	42285.9
0-0	3076.98	32490.0	0-5	2362.87	42308.5
1-7	3074.91	32511.8	0-4	2361.54	42332.3
1-6	3072.97	32532.4	0-3	2360.15	42357.3
1-5	3070.83	32555.1	0-2	2358.69	42383.4
1-4	3068.55	32579.3	0-1	2357.24	42409.5
2-13	3064.46	32622.7	1-3	2348.84	42561.3
2-12	3063.75	32630.2	1-2	2347.44	42586.6
2-11	3062.76	32640.8	1-1	2345.99	42612.9
1-1	3061.26	32656.8	1-0	2344.52	42639.6
1-0	3058.75	32683.6	2-2	2336.40	42787.7
2-1	3043.35	32849.0	2-1	2334.92	42814.9
2-0	3040.89	32875.6	2-0	2333.47	42841.5
3-5	3035.17	32937.5	3-2	2325.50	42988.3
3-4	3032.91	32962.1	3-1	2324.05	43015.1
3-3	3030.55	32987.7	3-0	2322.63	43041.4
3-1	3025.80	33039.5	4-6	2320.06	43089.2
4-9	3024.97	33048.5	4-1	2313.37	43213.7
3-0	3023.30	33066.8	4-0	2311.93	43240.5
4-7	3021.68	33084.5	5-4	2306.95	43333.9
4-3	3013.26	33177.0	5-1	2302.86	43410.9
4-0	3006.07	33256.4	5-0	2301.41	43438.2
5-3	2996.21	33365.8	6-1	2292.52	43606.7

(Continued)

Table 2.3 (Continued)

5-2	2993.87	33391.8	6-0	2291.10	43633.8
5-0	2989.11	33445.0	7-3	2285.02	43749.8
6-0	2972.48	33632.1	7-0	2280.90	43828.8
7-2	2960.80	33764.9	8-0	2270.88	44022.3
7-0	2956.15	33817.9	9-3	2265.07	44135.1
8-0	2940.09	34002.7	9-2	2263.71	44161.7
9-0	2924.31	34186.1	9-0	2261.01	44214.4
10-1	2911.06	34341.7			
10-0	2908.80	34368.4			
11-1	2895.78	34522.9			
11-0	2893.55	34549.5			
12-1	2880.76	34702.9			
12-0	2878.60	34728.9			

potential well of the $D^2\Pi_{1/2}$ state is deeper than that of the $B^2\Sigma^+_{1/2}$ state.

A broad, smooth, relatively low intensity band is present near $\lambda=345$ nm. This band is identified as the $C^2\Pi_{3/2} \rightarrow A^2\Pi_{3/2}$ transition. Since $A^2\Pi_{3/2}$ is essentially repulsive and no vibrational states exist, the emission spectrum is a continuum. A transition from the $B^2\Sigma^+_{1/2}$ state to the $A^2\Pi_{1/2}$ state should also exist. However, this band is difficult to observe because the band is overlapped by the band from the $C^2\Pi_{3/2} \rightarrow A^2\Pi_{3/2}$ transition. The intensity peak at $\lambda=340$ nm is obtained from theoretical calculations.

At high pressures, there is another very broad emission band in the wavelength range from 450 nm to 550 nm, with an intensity peak at approximately 485 nm. This band is assigned to transitions from the triatomic rare-gas-halide Xe_2Cl to the corresponding ground-state atoms (Xe+Xe+Cl). The large band broadening results from a strongly repulsive ground-state potential-energy curve in the transition region, where the internuclear distance is small. Table 2.4 provides a summary of the band heads for XeCl. In the table, R is the rare-gas atom and X is the halide. The values in brackets are calculated. For comparison, band heads for other rare-gas halides are also included in the table.

From theoretical considerations, the emission intensity is determined mainly by the dipole moment for the transition. The upper and lower electronic states can be defined by $|u>$ and $|l>$, respectively. For a total dipole $-e\vec{r} = -e\Sigma\vec{r}_i$, the dipole moment is

$$\mu_e = \langle l| \, e\vec{r} \, |u\rangle \quad , \tag{2.6}$$

where μ_e is an implicit function of the internuclear distance R in the molecule. For ionic-covalent electronic transitions in rare-gas halides, strong transition probabilities exist only for those bands with a z component of dipole moment. These bands correspond to the $B^2\Sigma^+ \rightarrow X^2\Sigma^+$ and $C(D)^2\Pi \rightarrow A^2\Pi$ transitions with $\Delta\Lambda=0$. The (x,y) components of the dipole moments for the

Table 2.4. Wavelengths (nm) of the Intensity Peaks for the Rare-Gas-Halide Transitions.

RX	$B_{1/2}\rightarrow X_{1/2}$	$D_{1/2}\rightarrow X_{1/2}$	$C_{3/2}\rightarrow A_{3/2}$	$B_{1/2}\rightarrow A_{1/2}$	R_2X
NeF	108	(106)	(110)	(111)	(~145)
ArF	193	(185)	(203)	(204)	285±25
KrF	248	220	275	(272)	420±35
XeF	351	264	460	(410)	610±65
ArCl	175				245±15
KrCl	222	200	240		325±15
XeCl	308	236	345	(340)	490±40
KrBr	207		222	228	~318
XeBr	282	221	300	320	440±30
XeI	253	203	265	320	~375

$B^2\Sigma^+ \rightarrow A^2\Pi$ or $C(D)^2\Pi \rightarrow X^2\Sigma^+$ transitions are negligible (i.e., $\Delta\Lambda = \pm 1$). However, in all cases the spin-orbit corrections must be considered. Therefore, the five strongest transitions observed are those related to states with a z component of dipole moment, together with $\Delta\Omega = 0$. These transitions, shown in Fig. 2.7, are $B^2\Sigma^+_{1/2} \rightarrow X^2\Sigma^+_{1/2}$, $D^2\Pi_{1/2} \rightarrow X^2\Sigma^+_{1/2}$, $C^2\Pi_{3/2} \rightarrow A^2\Pi_{3/2}$, $B^2\Sigma^+_{1/2} \rightarrow A^2\Pi_{1/2}$ and $D^2\Pi_{1/2} \rightarrow A^2\Pi_{1/2}$.

Radiative decays in rare-gas halides are classified into bound-bound and bound-free transitions according to the shapes of the electronic potential-energy curves. Vibrational levels can only exist in a "bound" potential well. For bound-free transitions, the probability for spontaneous emission from a discrete upper vibrational state $|\psi_{v'}>$ to a lower continuous electronic state $|\psi_{\varepsilon''}>$, in an energy band $d(h\nu)$ with emission frequency ν, is defined as $g_{v'\rightarrow\varepsilon''}(h\nu)d(h\nu)$. The normalized continuum lineshape function is given by (Mies, 1973)

$$g_{v'\rightarrow\varepsilon''}(h\nu) = \frac{<v'|\mu_e(R)|\varepsilon''>^2}{<v'|\mu_e^2(R)|\varepsilon''>} \quad , \tag{2.7}$$

where $\mu_e(R)$ is the electric dipole moment at internuclear distance. For bound-bound emissions, discrete vibrational levels are involved in both the upper and lower states. In this case, the transition probability for emission from an upper level $|\psi_{v'}>$ to a lower level $|\psi_{v''}>$ is defined as $g_{v'\rightarrow v''}(h\nu)d(h\nu)$. The normalized lineshape function $g_{v'\rightarrow v''}(h\nu)$ is

$$g_{v'\rightarrow v''}(h\nu) = \frac{<v'|\mu_e(R)|v''>^2}{<v'|\mu_e^2(R)|v''>}/(\frac{dG_{v''}}{dv''}) \quad . \tag{2.8}$$

The variation of $\mu_e(R)$ is negligible over the internuclear distance R for which emission occurs. Consequently, the lineshape functions can be simplified to

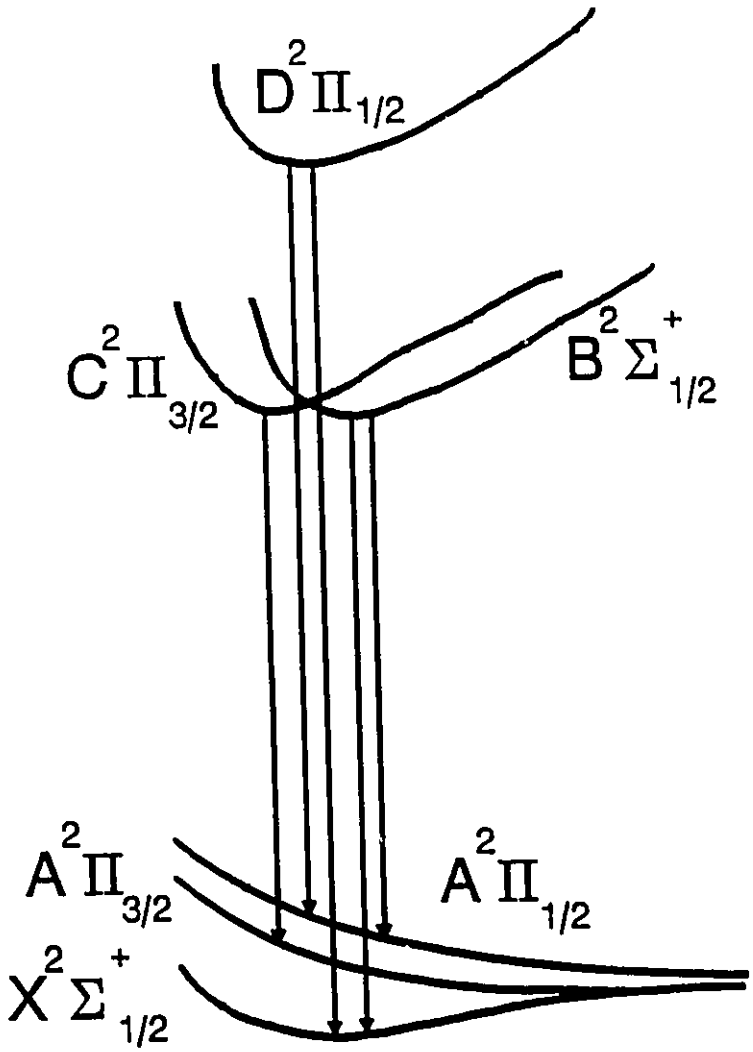

Fig. 2.7. Schematic of allowed transitions for the XeCl molecule.

$$g_{v'\to\varepsilon''}(h\nu) = \frac{\langle v'|\mu_e(R)|\varepsilon''\rangle^2}{\langle v'|\mu_e^2(R)|\varepsilon''\rangle} \approx \langle v'|\varepsilon''\rangle^2 \qquad (2.9)$$

for bound-free transitions and

$$g_{v'\to v''}(h\nu) = \frac{\langle v'|\mu_e(R)|v''\rangle^2}{\langle v'|\mu_e^2(R)|v''\rangle} / \left(\frac{dG_v''}{dv''}\right) \approx \langle v'|v''\rangle^2 / \left(\frac{dG_{v''}}{dv''}\right) \qquad (2.10)$$

for bound-bound transitions. Here $\langle v' \mid v'' \rangle$ is the Franck-Condon factor

$$FCF(v' - v'') \equiv \langle v'|v''\rangle = \int \psi_{v'}^{*}\psi_{v''}\, dR \quad . \qquad (2.11)$$

The FCF is actually the overlap integral between two vibrational functions in different electronic states. Therefore, the transition is strongest when the overlap is maximum. Such transitions can be represented by "vertical lines" of constant R. Values of the FCF for the B → X and D → X transitions, calculated by Sur et al (1979), are presented in Table 2.5. Note that the two strongest transitions for B → X are from $v'=0$ to $v''=1$ and $v''=2$.

The lineshape function given in Eq. (2.8), $g_{v'\to v''}(h\nu)$, is also called the Frank-Condon density (FCD). Calculated values of the FCD for the B → X transitions are shown in Fig. 2.8.

The Einstein spontaneous emission coefficient (A) and the cross-section for stimulated emission (σ) can be calculated from

$$A_{v'\to v''} = \frac{16\pi^3\nu^3}{3\varepsilon_0 hc^3} \langle v'|\mu_e^2(R)|v''\rangle \qquad (2.12)$$

and

$$\sigma_{v'\to v''}(h\nu) = \frac{c^2}{\nu^2}\frac{A_{v'\to v''}}{8\pi} g_{v'\to v''}(h\nu) \quad . \qquad (2.13)$$

Table 2.5. Frank-Condon Factors ($x10^3$) for the B-X (first row) and D-X (second row) States.

v″	v′=0	1	2	3	4	5
0	121	84	105	93	93	82
	29	41	56	66	73	77
1	218	65	60	20	8	0
	73	70	74	60	45	29
2	234	10	6	5	13	32
	114	67	48	20	5	0
3	186	7	4	43	32	36
	139	41	15	0	5	17
4	115	58	16	52	14	8
	142	13	0	10	22	30
5	57	114	12	30	0	1
	128	0	4	26	27	20
6	21	140	2	8	10	10
	105	5	14	31	17	6
7	5	131	2	0	28	13
	79	19	18	25	6	0
8	0	103	14	1	35	7
	57	33	17	15	0	2
9	0	71	29	2	31	1
	39	44	12	7	1	6
10	1	45	41	2	22	0
	26	47	7	2	4	9
11	2	26	45	1	14	2
	17	45	3	0	6	8
12	2	15	42	0	8	4
	11	39	1	0	7	7
13	2	8	35	0	4	5
	7	31	0	0	6	5
14	2	4	26	0	2	5
	4	23	0	0	5	3

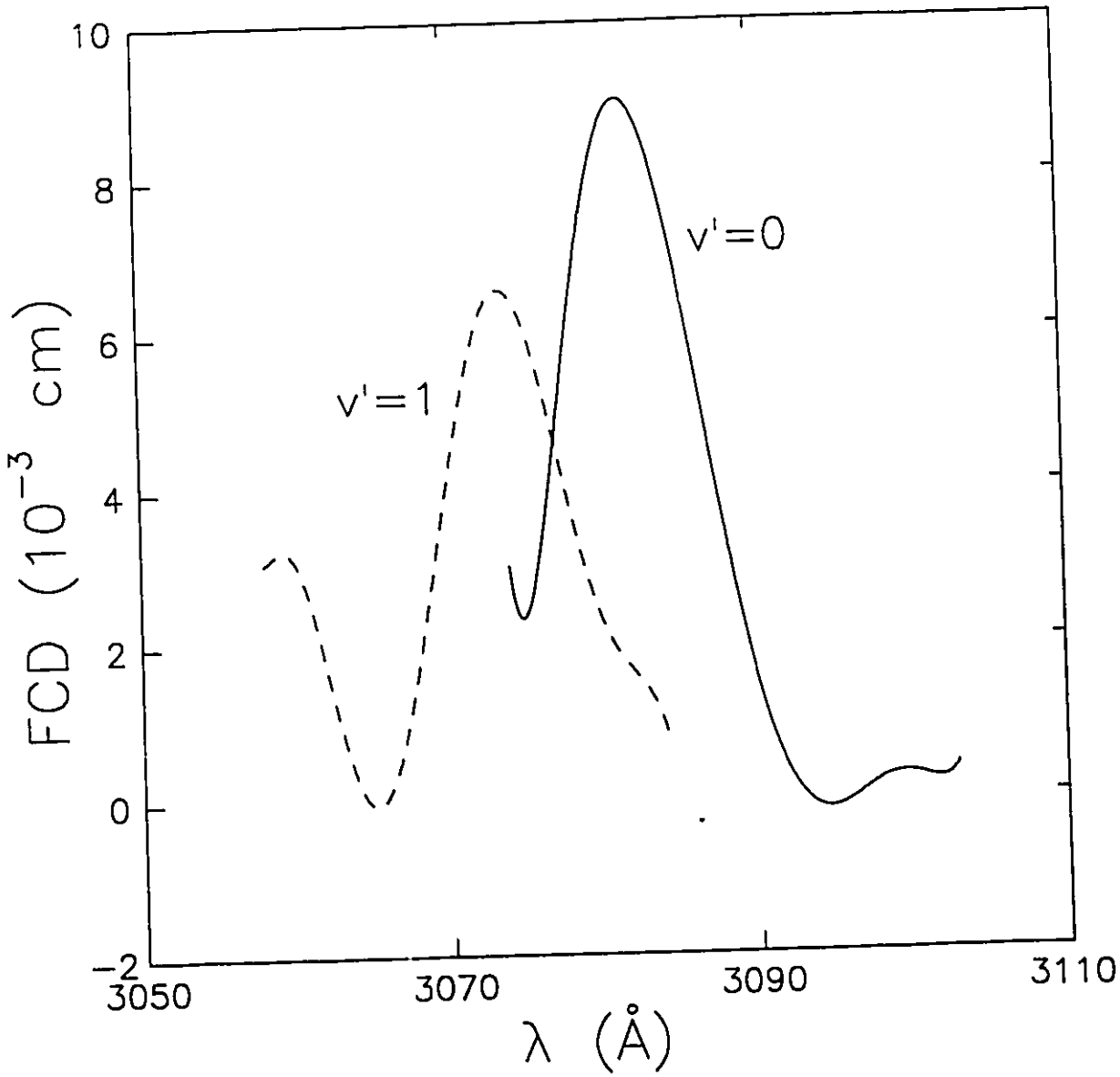

Fig. 2.8. Franck-Condon density for the transitions from state B(v'=0,1) to state X(v"=0).

Since only these transitions with small quantum number v′ are important, the R-dependent dipole moments can be approximated by the values at the equilibrium internuclear distance R_e. Therefore, Eqs. (2.12) and (2.13) become

$$A_{v'-v''} = \frac{16\pi^3\nu^3}{3\varepsilon_0 hc^3}\,\mu_e^2(R_e)FCF(v'-v'') \tag{2.14}$$

and

$$\sigma_{v'-v''}(h\nu) = \frac{c^2}{\nu^2}\frac{A_{v'-v''}}{8\pi}FCD_{v'-v''}(h\nu) \quad . \tag{2.15}$$

The stimulated-emission cross-section depends not only on the spontaneous emission rate, but also on the spectral width of the lineshape function. For transitions with a wide spectrum range (e.g., transitions to a repulsive ground state A), the stimulated-emission cross-sections are very small. If it is assumed that the band profile near the intensity peak can be approximated by a Gaussian, then the product of cross-section and lifetime may be estimated from (Bhaumik et al, 1976)

$$\sigma\tau = \frac{1}{4\pi}\left(\frac{\ln(2)}{\pi}\right)^{1/2}\frac{\lambda^4}{c\Delta\lambda} \quad . \tag{2.16}$$

If the spontaneous-emission rates for each vibrational level are found using Eq. (2.14), then the lifetimes of the radiative transitions from the upper electronic states B and D can be calculated using

$$\tau = \left(\sum_{v'}\sum_{v''} A_{v'-v''}\right)^{-1} \quad . \tag{2.17}$$

Based on the experimental value of $\Delta\lambda$=2.3 nm (Brau and Ewing, 1975), the stimulated-emission cross-section σ can be obtained from Eqs. (2.16) and (2.17). The calculated lifetimes, total spontaneous-emission rates, stimulated-emission cross-sections and the emission wavelengths for

the B and D transitions are given in Table 2.6.

Table 2.6. Emission Parameters for B → X and D → X Transitions of XeCl

	λ(nm)	μ_e(D)	A(sec^{-1})	τ(ns)	σ(cm^2)
B → X	308	2.76	$9.5x10^7$	10.5	$4.5x10^{-16}$
D → X	236	1.94	$1.0x10^8$	10.0	$1.6x10^{-16}$

The dipole moments in Table 2.6 are taken from Hay and Dunning (1978). Note that the real lifetimes of the upper electronic states are less than the values determined from the radiative lifetimes because of collisions between gas molecules. At the usual gas pressures (> 1 atm), the D state is actually quenched very fast. In part, this explains why the D → X emission is observed to be much weaker than B → X emission at high gas pressures.

2.4. Formation Rate of $XeCl^*$ Using the Electron-Jump (Harpooning) Model.

The accuracy of kinetic models for the XeCl laser relies on a knowledge of the rate coefficients for producing the upper laser level $XeCl^*$. As discussed in Section 6.1.2, the most important mechanism for $XeCl^*$ formation is three-body ionic recombination. At a total pressure of 350 kPa, our calculations show that more than 95% of the $XeCl^*$ is formed via this process. The two-body harpoon process (Reaction 15 in Table 6.1) contributes only 5%.

Although the formation rate of $XeCl^*$ has not been measured, various theoretical calculations provide reliable and consistent data. A review of previous models is given by Flannery (1972, 1982). These range from the early simple models of Langevin (1903), Thomson (1924) and Natanson (1959), to the more recent quasi-equilibrium statistical models of Bates and

Flannery (1968), the Monte-Carlo simulation of Bardsley and Wadehra (1980), the universal plots of Bates (1980), and the basic microscopic theory of Flannery (1982). In all of these models, Xe^+ and Cl^- form $XeCl^*$ only via the three-body ionic recombination process. It is assumed that other molecular states do not contribute to $XeCl^*$ formation. However, our electron-jump model (Lee et al, in preparation) suggests that two additional channels are important in the formation of $XeCl^*$. These channels, discussed in Section 2.4.1, are produced by the pseudo-crossings of two Rydberg-state energy curves with the ionic curve.

2.4.1. The Electron-Jump (Harpooning) Model.

As shown in Fig. 2.9, the separated-atom limits of the two lowest Rydberg states are $Xe(^3P_2) + Cl(^2P_{3/2})$ and $Xe(^3P_1) + Cl(^2P_{3/2})$. The corresponding energies are 8.315 eV and 8.437 eV above the ground state $Xe(^1S_0) + Cl(^2P_{3/2})$. Both of these limits are slightly less than the ionic limit (8.512 eV) for $Xe^+(^2P_{3/2}) + Cl^-(^1S_0)$. Therefore, pseudo-crossings of the Rydberg-state curves with the ionic curve are estimated to occur at the large internuclear distances of 137 a_0 and 353 a_0 (a_0 is the Bohr radius). The electron-jump (harpooning) model is based on the reactions

$$Xe(^3P_2) \cdot Cl(^2P_{3/2}) \rightarrow Xe^+Cl^-(B,C) \qquad (2.18a)$$

and

$$Xe(^3P_1) \cdot Cl(^2P_{3/2}) \rightarrow Xe^+Cl^-(B,C) \quad . \qquad (2.18b)$$

These reactions correspond to the transition of a molecular state, in the vicinity of a crossing, from dominantly covalent for r larger than the crossing radius to dominantly ionic for r smaller than the crossing radius. The transition represents the jump of an electron from $Xe(^3P_2$ or $^3P_1)$ to Cl at the crossings.

Although three-body ionic recombination is still the major channel for $XeCl^*$ formation in

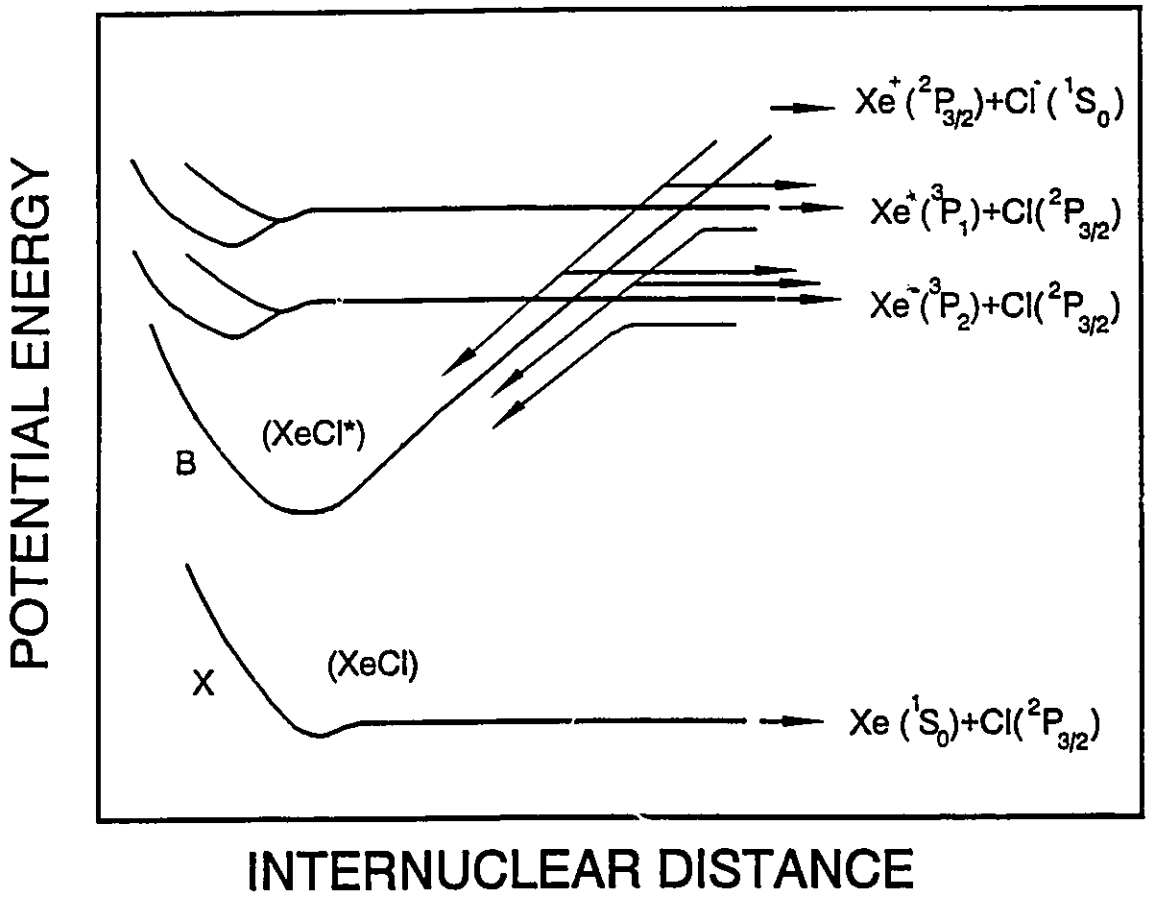

Fig. 2.9. Potential energy diagram for XeCl showing the formation channels for the $XeCl^*(B)$ exciplex. The various transformations are indicated by the arrows. The scales are arbitrary.

our model, this process can be highly affected by the transitions at the pseudo-crossings. The "complete" formation mechanism illustrated in Fig. 2.9 can be summarized by

$$Xe^+ + Cl^- + M \left\{ \begin{array}{l} \longrightarrow \\ \longrightarrow Xe(^3P_1) + Cl + M \left\{ \begin{array}{l} \longrightarrow \\ \longrightarrow Xe(^3P_2) + Cl + M \end{array} \right. \\ \longrightarrow Xe(^3P_2) + Cl + M \end{array} \right\} XeCl^* + M \,, \quad (2.19)$$

where M represents the third light body (i.e., the buffer gas He). Compared to bimolecular reactions, these reactions proceed more favorably in the presence of the third light body. Energy transfer is much more efficient in a three-body collision process.

All of the processes in Reaction (2.19) are reversible. Therefore, in addition to formation, our electron-jump model also explains the loss mechanism due to predissociation of $XeCl^*$. After the exciplex $XeCl^*$ dissociates into the elemental atoms of the Rydberg molecule, the exciplex can be regenerated. Therefore, this loss channel only delays the formation of the ionic state $XeCl^*$.

2.4.2. Formation Rate Coefficients.

The procedure is generally known for the analysis of a two-body process which involves a single pseudo-crossing of two potential-energy curves (McDaniel, 1964). However, the complete set of formulae developed here for estimating the three-body rate-coefficients for the formation and dissociation reverse processes in Reaction (2.19), involving double crossings of potential-energy curves, is not available in the literature.

Consider a typical situation, shown in Fig. 2.10, where the potential-energy curve of an ionic molecule AB (state 0), correlating to the dissociation limit $A^+ + B^-$ (state 1), is "intersected" at two places, b and c, by the potential curves of the Rydberg states $A^* + B$ (state 2) and $A^{**} + B$ (state 3), respectively. Provided that the properties of the intersecting states

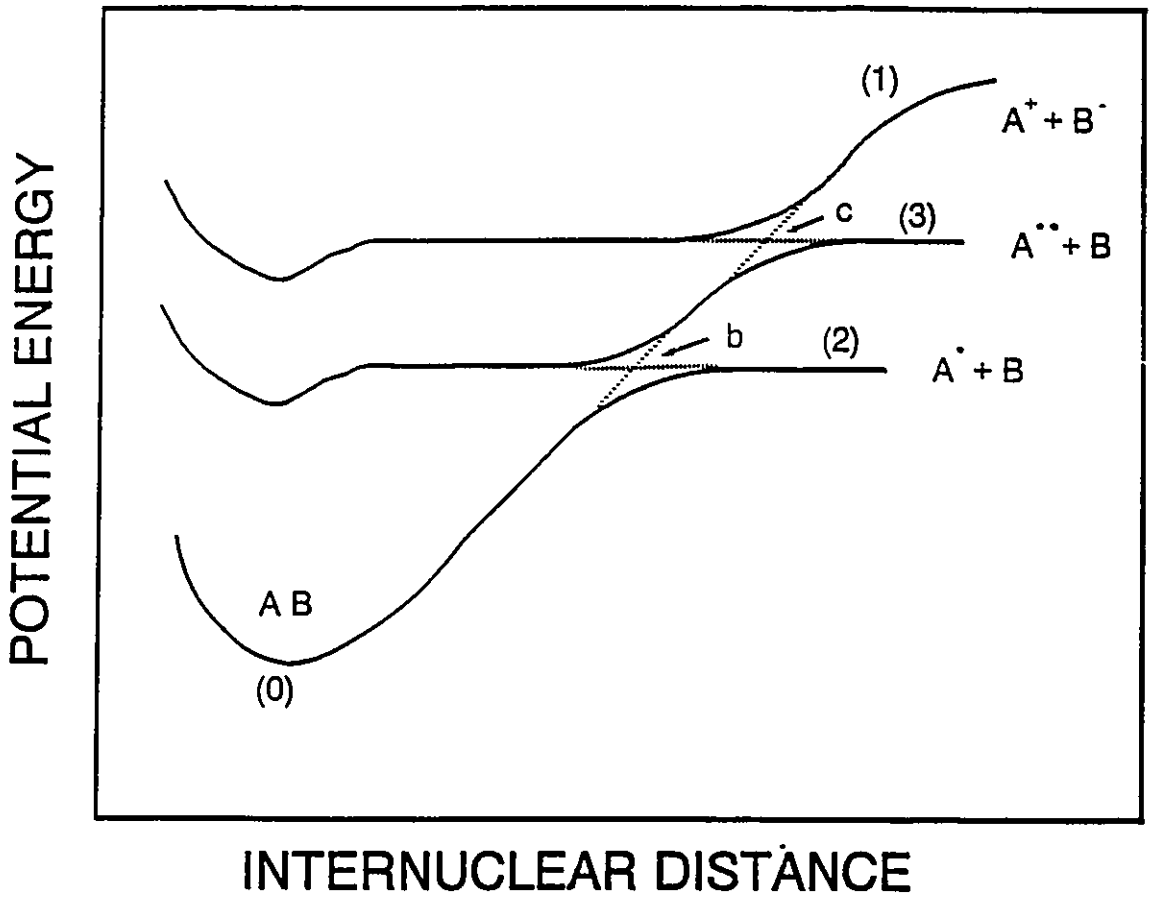

Fig. 2.10. Schematic diagram illustrating pseudo-crossings of the potential-energy curves. The scales are arbitrary.

permit pseudo-crossing, there is a finite probability, $P_l(m,n)$, for a transition from the initial state m to the final state n, which depends on the orbital angular-momentum quantum number l. According to Landau and Lifshitz (1977), the cross-section for this process is given by

$$\sigma(m \rightarrow n) = \left(\frac{\pi}{k^2}\right) \sum_l (2l+1)\, P_l(m,n) \quad , \tag{2.20}$$

where $k^2 = 2\mu E/\hbar^2$, and where μ is the reduced mass of the initial system and E is the relative kinetic energy of the two atoms or ions (A and B). Let P_b and P_c be the probabilities for the atoms or ions (A and B) to jump from one potential curve to the other at crossings b and c, respectively. The probability $P_l(m,n)$ is then determined by P_b and P_c. The derivations of P_b, P_c and $P_l(m,n)$ are given in the Appendix.

By definition, the rate coefficients for the processes shown in Fig. 2.9 can be evaluated by averaging the product of cross-section σ and relative velocity v over the energy distribution function of the atomic or ionic pairs (A and B). As an approximation, the Maxwell-Boltzmann statistics for a system in thermodynamic equilibrium can be used for the energy distribution. This quasi-equilibrium approach gives

$$\langle \sigma v \rangle = \left(\frac{\hbar^2}{2\mu}\right)\left(\frac{8\pi}{\mu kT}\right)^{\frac{1}{2}} \int_0^\infty \sum_l (2l+1) P_l \exp\left(-\frac{E}{kT}\right) d\left(\frac{E}{kT}\right) \quad , \tag{2.21}$$

where k is the Boltzmann constant and T is the gas temperature. When ionic-recombination is proceeding (especially in very high density discharge media), the relative motion of the ion-pairs are governed not only by the thermal motion, but also by diffusion and drift resulting from their mutual electrostatic field. However, the validity of quasi-equilibrium statistical theory for low and intermediate densities, such as those existing in our laser, has been demonstrated by Bates and Moffett (1966). Therefore, Eq. (2.21) provides a good approximation for our laser system.

Figure 2.11 shows the calculated rate-coefficients for the various kinetic processes involved in the formation and dissociation of the XeCl exciplex under typical laser discharge conditions. A He buffer was employed with the ratio of the electric field to the gas density fixed at $E_d/N = 15 \cdot 10^{-17}$ V·cm^2, and the temperature at T = 300 K. At low pressure (0.25 atm), $XeCl^*$ is formed primarily from $Xe(^3P_2) + Cl(^2P_{3/2})$ via the harpooning processes. However, at pressures greater than 0.25 atm, the formation of $XeCl^*$ through the ionic channel is dominant, even though the harpooning process from the Rydberg state $Xe(^3P_1) + Cl(^2P_{3/2})$ is also relatively important. Note that there is a high conversion of ions $Xe^+ + Cl^-$ into the Rydberg-state atoms $Xe(^3P_2) + Cl(^2P_{3/2})$ and $Xe(^3P_1) + Cl(^2P_{3/2})$. However, the subsequent transformation of these atoms back to the exciplex compensates for the reduced formation of $XeCl^*$ from $Xe^+ + Cl^-$.

The three-body ionic recombination rates as a function of gas pressure is shown in Fig. 2.12. At relatively low pressures (<3 atm), there is good agreement between the results from the electron-jump model and previous models (Flannery, 1982; Bates and Flannery, 1968). The other models predict that, at high pressures, there is a decrease in the rate coefficients with increasing pressure. However, the rate-coefficients from our calculations "saturate" to a constant value in this pressure range. A considerable additional effort would be required to modify our model in order to provide better data at high pressures. As the gas pressure rises, the ion-ion electric field increases. Therefore, the Maxwell-Boltzmann distribution used in Eq. (2.21) does not yield accurate ion velocities at the higher pressures.

In all of the models, ionic recombination is considered as the primary channel for the formation of the $XeCl^*$. However, our electron-jump model suggests harpooning reactions also contribute to the ionic recombination process. In addition, this model makes it possible to evaluate the rate-coefficients for each individual formation and dissociation channel of $XeCl^*$.

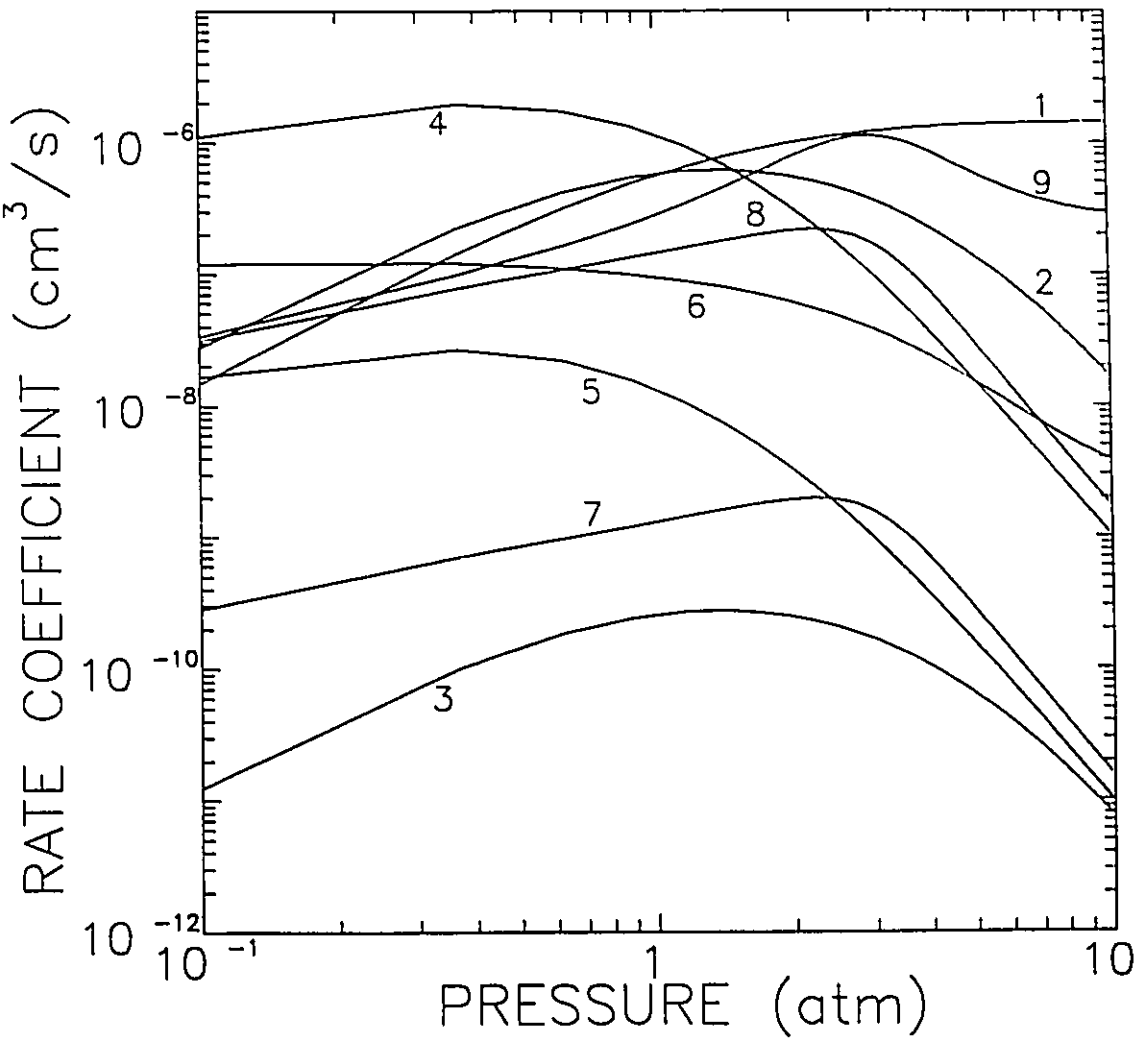

Fig. 2.11. Pressure dependence of the three-body rate-coefficients for the formation and dissociation of $XeCl^*$ at T=300 K.

1. $Xe^+ + Cl^- + He \rightarrow XeCl^* + He$
2. $Xe^+ + Cl^- + He \rightarrow Xe(^3P_2) + Cl + He$
3. $Xe(^3P_2) + Cl + He \rightarrow Xe^+ + Cl^- + He$
4. $Xe^+ + Cl^- + He \rightarrow Xe(^3P_1) + Cl + He$
5. $Xe(^3P_1) + Cl + He \rightarrow Xe^+ + Cl^- + He$
6. $Xe(^3P_2) + Cl + He \rightarrow XeCl^* + He$
7. $Xe(^3P_2) + Cl + He \rightarrow Xe(^3P^1) + Cl + He$
8. $Xe(^3P_1) + Cl + He \rightarrow XeCl^* + He$
9. $Xe(^3P_1) + Cl + He \rightarrow Xe(^3P_2) + Cl + He.$

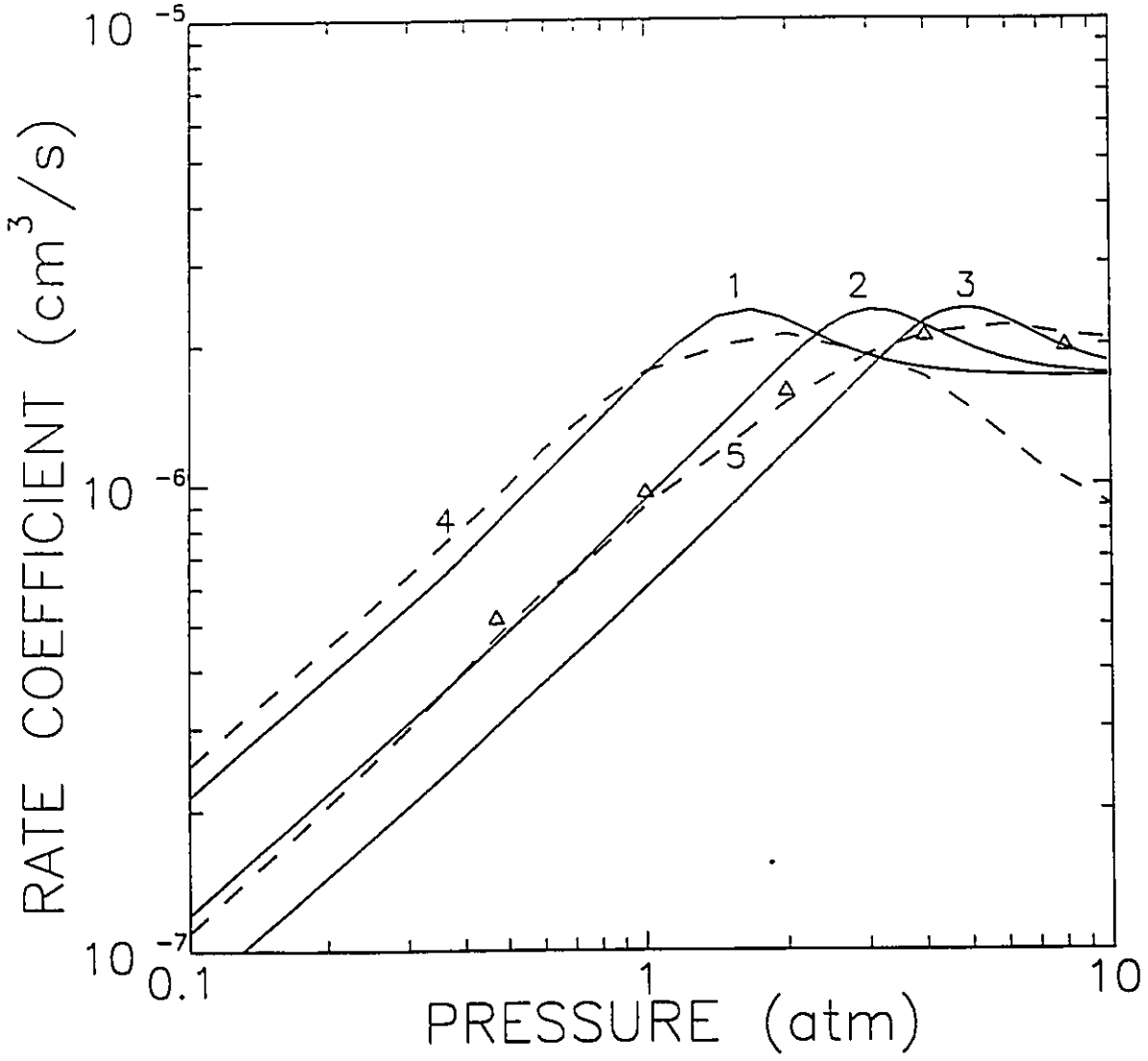

Fig. 2.12. Comparison of the three-body ionic recombination rates. The solid lines are obtained from our model employing different buffer gases (1. Ar, 2. Ne, 3. He). The dashed lines represent the data of Flannery (4. Ar, 5. Ne) (1982). The small triangles represent the data of Bardsley and Wadehra (1980).

Chapter 3

Experimental Investigations of a Compact Discharge-Excited XeCl Laser

In this chapter, the design and experimental investigations of a compact short-pulse discharge-excited XeCl laser system are presented.

In general, excimer laser excitation is provided using either electron beams or avalanche discharges. The most commonly used methods are described in Section 3.1. The physical details of the laser system used in the thesis research, including the excitation circuit, the gas handling system, and the optical components, are provided in Section 3.2. Experimental data are given in Section 3.3.

3.1. Excitation Methods.

Electron-beam (e-beam) generators are used to inject high-intensity, high-energy pulses of electrons into gas mixtures (Searles and Hart, 1975; Ewing and Brau, 1975; Ault et al, 1975). These generators can deposit very high power densities into high-pressure gas mixtures. Electron-beam excitation inherently provides much better discharge stability than avalanche discharges because the electron uniformity is relatively easy to control and arc formation does not occur. Furthermore, electron-beams are capable of faster deposition of energy.

Electron beams are particularly important for the excitation of high-pressure rare-gas excimer systems where high input power is needed. Unlike rare-gas halides, these excimer

systems have small stimulated-emission cross-sections. Electron beams are equally important for the excitation of long-pulse rare-gas-halide systems because these provide stable discharges. However, e-beam generators are complicated, large and expensive, and difficult to operate at high repetition rates.

Simple, economical and compact capacitor discharge excitation is usually employed for rare-gas halide systems (Burnham et al, 1976; Sze and Seegmiller, 1981; Miyazaki et al, 1985; Hiramatsu and Goto, 1986). The rare-gas-halide molecules have relatively larger stimulated-emission cross-sections than rare-gas molecules, and therefore can operate at relatively lower gas pressure. However, for reasons outlined below, discharges are most suitable for producing fast rise-time, short-duration excitation, as in our compact laser system.

In a discharge system, free electrons (always present as a result of cosmic radiation) obtain kinetic energy from the applied electric field. Secondary electrons and ions are produced when the gas atoms and the energetic free electrons collide. If the electric field is sufficiently high, then the number of free electrons increases very rapidly, the discharge impedance collapses, and an avalanche discharge occurs. Because the energetic electrons involved in ionizing collisions are concentrated in regions where the electric field is strongest, the density of electrons grows most rapidly in these regions. The resultant spatial non-uniformity of electrons causes instabilities within the discharge, which produces localized arcs and streamers. The presence of arcs in a discharge can destroy laser operation. Discharge stability can be greatly improved by the use of preionization, which produces a relatively large density of free electrons ($10^8 \sim 10^{10}$ cm^{-3}) prior to discharge breakdown. Preionization also reduces the breakdown voltage of a gas mixture.

Without preionization, the useful avalanche discharge current duration is limited to approximately 30 ns at "low" gas pressures (<0.5 atm) (Burnham et al, 1976). The useful

discharge duration (i.e., no arcing) decreases with increasing gas pressure (Christensen et al, 1976; McKee et al 1977). Two methods are generally used to suppress arc formation, X-ray preionization (Lin and Levatter, 1979; Forestier et al, 1981) and ultraviolet (UV) preionization (Miyazaki et al, 1985; Nassisi and Perrone, 1990). Compared to UV preionization systems, X-ray preionization systems are expensive and complicated, but can provide larger and more uniform initial electron densities. Therefore, X-ray preionization is employed primarily in large-volume, high-pressure, and high-energy rare-gas-halide laser systems. Ultraviolet preionization is particularly suitable for use in compact laser systems.

The seed electrons are produced by weak UV photoionization, which compensates for the loss of electrons by dissociate attachment to the halogen donors. This greatly increases the probability and rate of avalanche breakdown. The development of arcs is controlled, although not eliminated, by the uniform spread of seed electrons into the gas mixture.

Electron-beam discharge systems are much more sophisticated and expensive (Daugherty et al, 1976). In these systems, the discharge results primarily from electron-beam irradiation. Alternatively, a normal avalanche discharge is controlled and stabilized by the electron beam. In both cases, the electron density and electric field can be controlled separately. Therefore, a high degree of discharge stability can be achieved. However, these types of systems are not practical for compact lasers because of the complex construction required.

3.2. Laser Design.

A schematic diagram of our compact laser system is shown in Fig. 3.1. The basic design of this laser is similar to the system developed by Ballik (1981). The system includes a compact

UV-preionized laser assembly, a pulse-forming circuit for discharge excitation and a high-voltage power supply. The required gas handling system is not shown in the figure. Details of the various components are given in following section.

3.2.1. Mechanical Construction of the Laser.

Figure 3.2(a) shows the cross-section of the laser body. The main body component, constructed from KEL-F, is 16.5-cm long, 3.5-cm high and 3.35-cm wide at the ends. The sides are recessed to a depth of 0.56 cm in order to mount 14-cm long nickel-plated brass plates (0.6-cm thick), to which are attached the electrodes. Both electrodes, also of nickel-plated brass, are 10-cm long and 0.32-cm wide, separated by 0.47 cm. The active gain volume is ≈ 1 cm^3, compared to the total laser-body internal volume of ≈ 33 cm^3.

The main electrode (E1) is covered with $2.5 \cdot 10^{-3}$-cm thick tantalum foil. The active surface of the preionizer electrode, shown in Fig.3.2(b), is a mesh fabricated from the same thickness of tantalum foil. The quartz (fused-silica) tubing actually bends around both ends of the electrode base, and then passes through the side plate. Epoxy resin is used to provide a gas seal. The tungsten wires within the quartz tube are connected externally to the other plate in order to provide electrical contact with the other electrode.

After spark-gap breakdown, a high voltage develops rapidly between the tungsten wires and the tantalum mesh. Very rapidly, small sparks are formed in the vicinity of the holes in the mesh. This provides a uniform distribution, along the whole active surface of the electrode, of both electrons and high-energy UV radiation. The latter ionizes the gas between the electrodes, producing sufficient free electrons to initiate a reasonably-uniform discharge. Streamers are also present in the discharge. However, experience indicates that these streamers may be

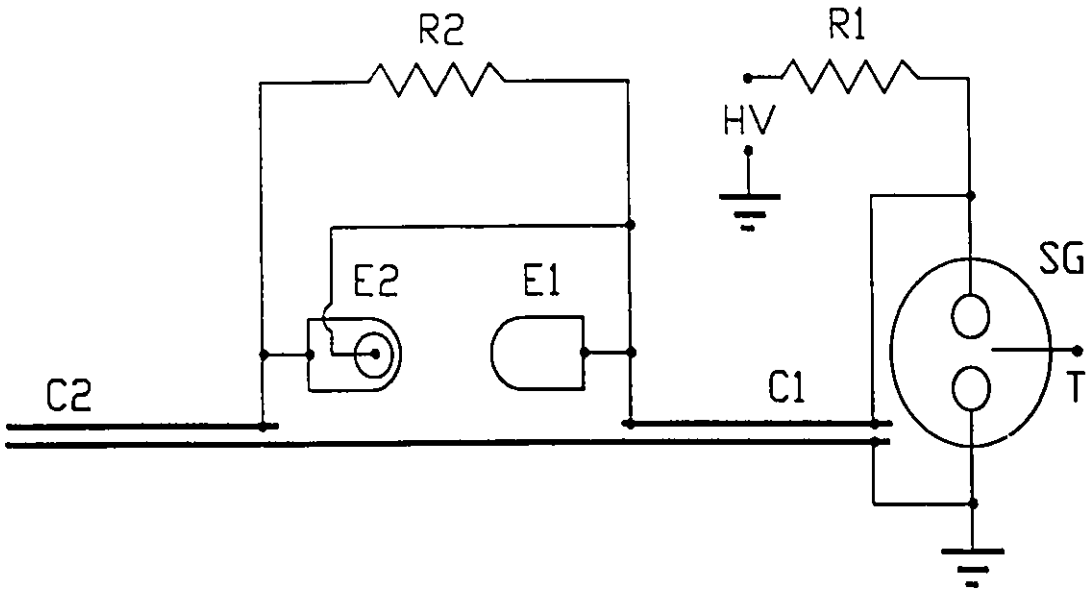

Fig. 3.1. Schematic diagram of the laser system. C1 and C2 are the energy storage capacitors, E1 and E2 are the laser electrodes, SG is the spark gap, R1 and R2 are large-value resistors for charging and isolation, respectively, and HV is the high-voltage power supply.

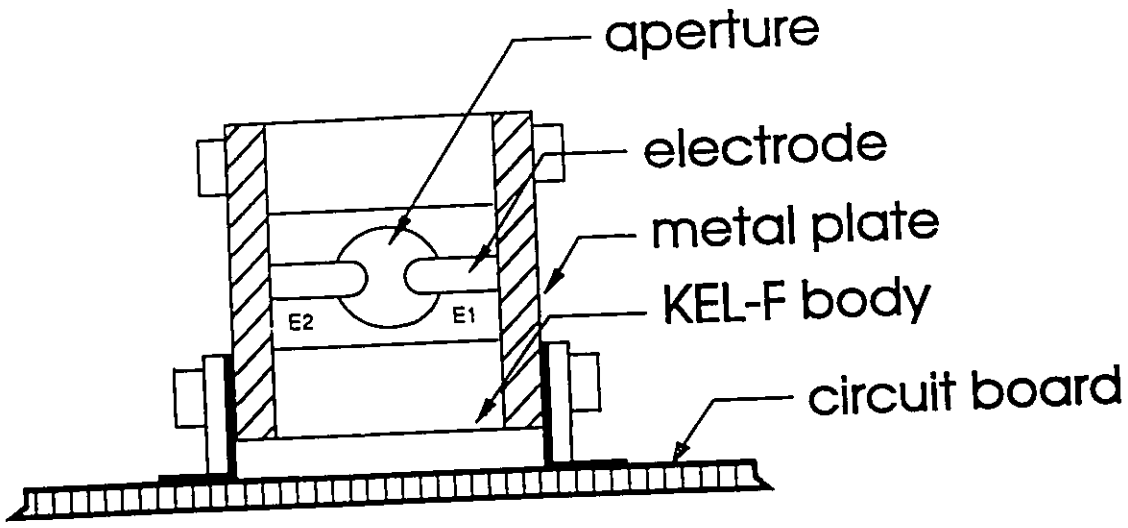

(a)

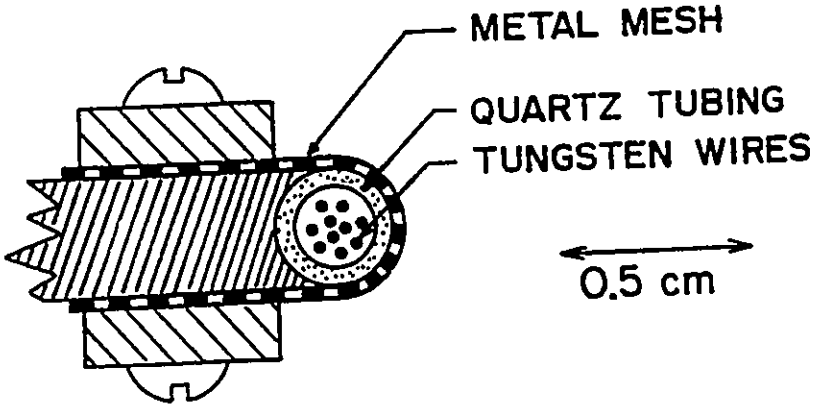

(b)

Fig. 3.2. (a) Cross-section of the laser body. Here E2 is the preionizer electrode. (b) Cross-section of the preionizer electrode.

beneficial for the production of gain.

The laser resonator consists of two fused-silica disks (0.32-cm thick) separated by the laser body length L = 16.5 cm. One disk (rear reflector) is externally aluminized, and the other (output reflector) is left uncovered, resulting in reflectances of $R_1 = 95\%$ and $R_2 = 7.5\%$, respectively. The round-trip time in the resonator is calculated from $t = 2nL/c$, where c is velocity of light, and n is the refractive index (≈ 1.0). For our laser, the pulse duration was usually less than the calculated round-trip time of 1.1 ns.

The construction of the spark gap (SG) unit is shown in Fig. 3.3. For convenience, the electrodes, which are separated by 0.47 cm, are made of brass. A standard automotive spark plug is used for the trigger electrode. During operation, the spark gap contains nitrogen gas at a pressure of approximately 1.3 atm.

The laser is mounted on the circuit-board capacitor (described in next section). Connections to the laser tube and to the spark gap employ short lengths of wide copper foil in order to minimize circuit inductance. The complete laser assembly (laser body, capacitors and spark gap) is supported on a stainless-steel optical table. To reduce electromagnetic interference (EMI) from the discharge circuit, the laser assembly is enclosed within a galvanized steel box, of dimensions 60-cm long, 25-cm wide and 20-cm high. All electrical connections into the box pass through filters and/or are shielded in order to reduce EMI.

3.2.2. Electrical Circuit.

The "Blumlein" type pulse-forming circuit is illustrated in Fig. 3.1. This type of circuit, which has also been used for short-pulse N_2 and CO_2 lasers, is relatively simple and inexpensive to construct. In our compact laser system, discharge current pulses less than 10-ns duration can

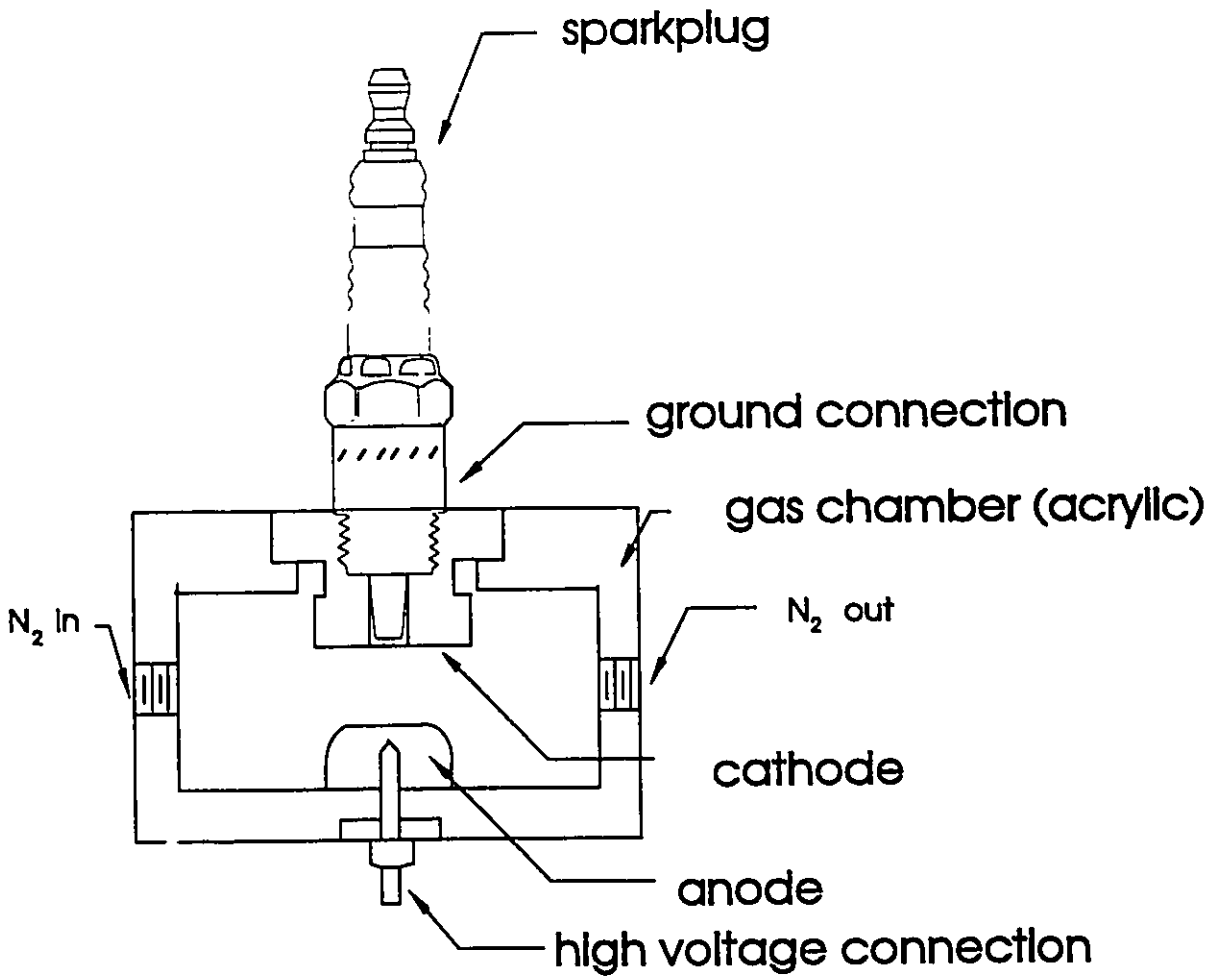

Fig. 3.3. Schematic of the spark gap. The metallic components are constructed of brass.

be produced.

Capacitors C1 and C2 are made on a single double-sided circuit board. These are formed from two parallel copper foils (26.7-cm long by 15.1-cm wide) separated by an epoxy/glass-fiber dielectric (0.098-cm thick) having dielectric constant K=4.3. The dielectric extends 2.5 cm beyond the upper foil in order to avoid breakdown of the dielectric. In addition, the lower foil extends 0.6 cm beyond the upper foil in order to reduce electric field gradients at the foil edges. Each capacitor has a value of 1.56 nF. Resistor R1 (1 MΩ) is used to limit the surge current when C1 and C2 are charged from the high-voltage dc power supply (Universal Voltronics BAL-50-16). Resistor R2 provides isolation between the capacitors during laser operation.

The equivalent circuit for the discharge excitation, shown in Fig. 3.4, consists of two basic circuits, the spark-gap circuit (C1, LSG, RSG and SSG) and the discharge circuit (C2, LD, RD, SD and C1). RSG represents the resistance of the nitrogen-filled spark gap. After the spark gap is triggered, the density of electrons increases very rapidly, causing RSG to decrease from ∞ to approximately 1 Ω within 1 ns. The value of RSG remains relatively constant for the duration of the active laser discharge. Resistance RD is the impedance of the discharge between the laser electrodes. This resistance is a function of the electron density in the discharge, as described in Section 3.3. Inductances LSG (27.6 nH) and LD (6 nH) are the total inductances in the spark-gap circuit and laser-discharge circuit, respectively. The values of these inductances can be evaluated from the measured current waveforms, as discussed in Section 4.3.

The high-voltage pulse used to trigger the spark gap is produced by the trigger unit shown schematically in Fig. 3.5. The pulse generator (Hewlett-Packard 3300A) provided a square-wave output pulse of >2 V. Components for the trigger unit include a standard automotive ignition coil, a SCR (2N688) and a HV power supply (Heathkit 1P-17). With a dc voltage of 100 V, the

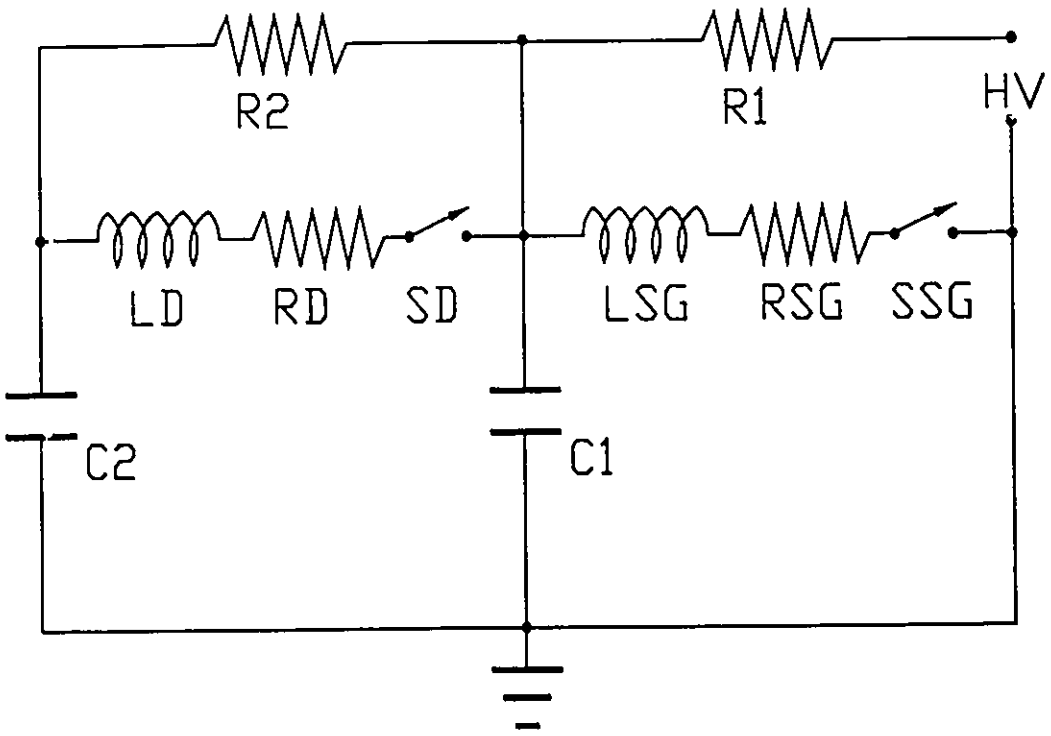

Fig. 3.4. Equivalent circuit for the discharge excitation.

peak magnitude of the output pulse from the ignition coil is approximately 15 kV.

3.2.3. Gas Handling System.

Figure 3.6 provides a schematic for the gas handling system. A two-stage mechanical vacuum pump (Sargent-Welch 8815) was adequate for evacuating both the laser body and the mixing chamber. These were evacuated to $< 10^{-1}$ Torr, as measured using a Pirani gauge (not shown), before introducing the gases. One of the gases in the laser mixture (HCl) is very corrosive in moist air, is toxic, and is capable of causing serious damage to the vacuum pump. Therefore, a liquid-nitrogen trap was used to condense gases such as HCl, Cl_2 and H_2O, which were later released in a fume hood.

Mixing the gas at a high total pressure ($\approx$ 800 kPa) made it possible to change the gas in laser body several times with each mixture. The gas pressure in the laser body was monitored using a small Bourdon gauge (Matheson 63-3112). The gas-mixture pressure in the mixing chamber was monitored using an accurate Bourdon gauge (U.S. Gauge 33022), which is calibrated from vacuum to 100 psig.

The laser operation has been investigated for gas mixtures consisting of Xe/HCl/He or Xe/HCl/Ne (He or Ne is the buffer gas) at various total gas pressures and capacitor charging voltages. Some results of these investigations are given in Section 3.3. Typical operation employs a gas composition of 0.8%Xe/0.3%HCl/He at a total absolute pressure of 450 kPa, and a 15-kV capacitor charging voltage. The gas mixtures at various composition were prepared from high purity xenon, helium or neon, and 5 to 10% hydrogen chloride in helium or neon (all supplied by Matheson). These were mixed in a 0.6-l stainless-steel chamber, and then released into the pre-evacuated laser body. Where possible, pre-mixed, such as 0.8%Xe/0.3%HCl/He, were

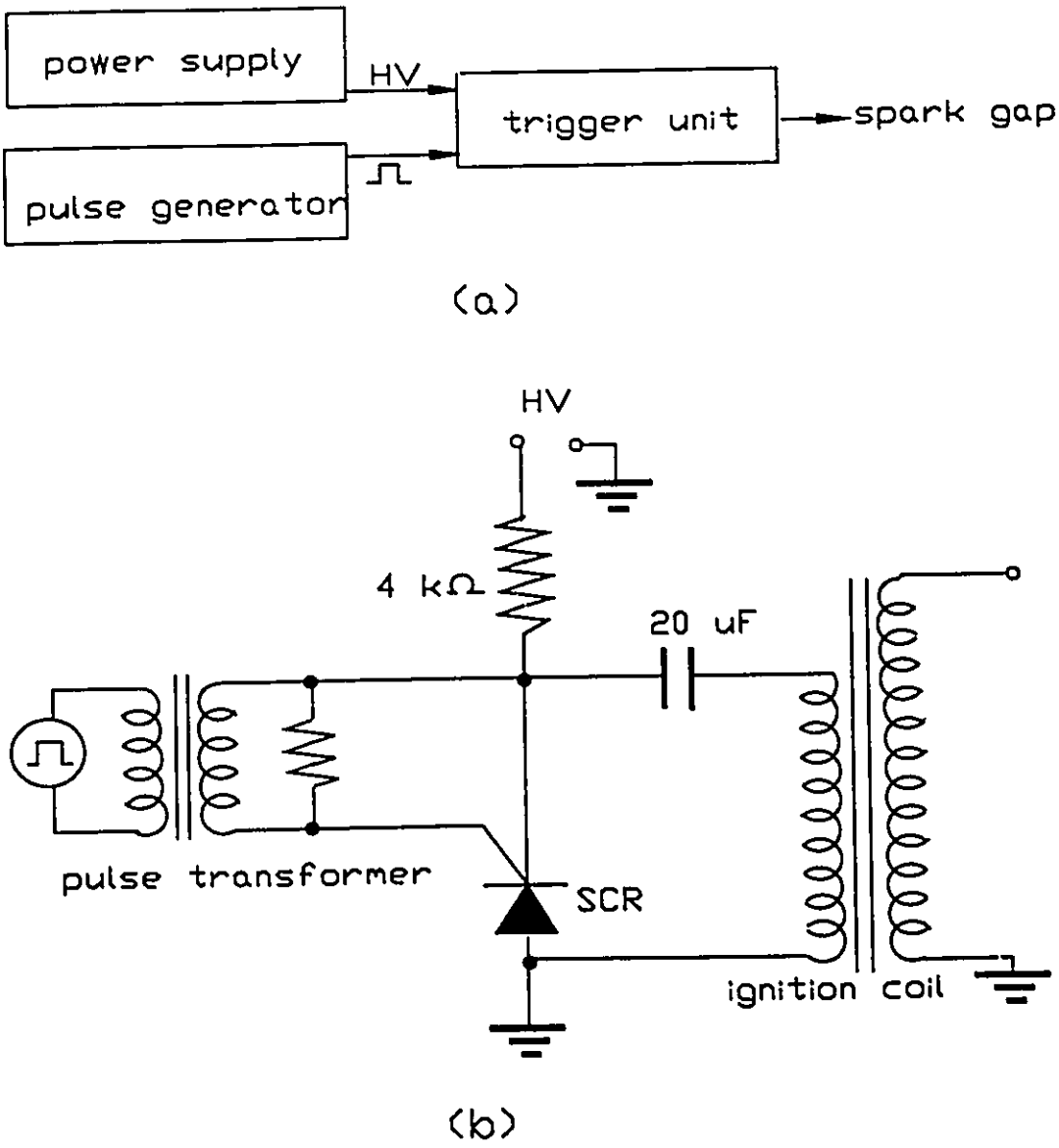

Fig. 3.5. (a) Block diagram for the spark-gap trigger unit. (b) Equivalent circuit for the trigger unit.

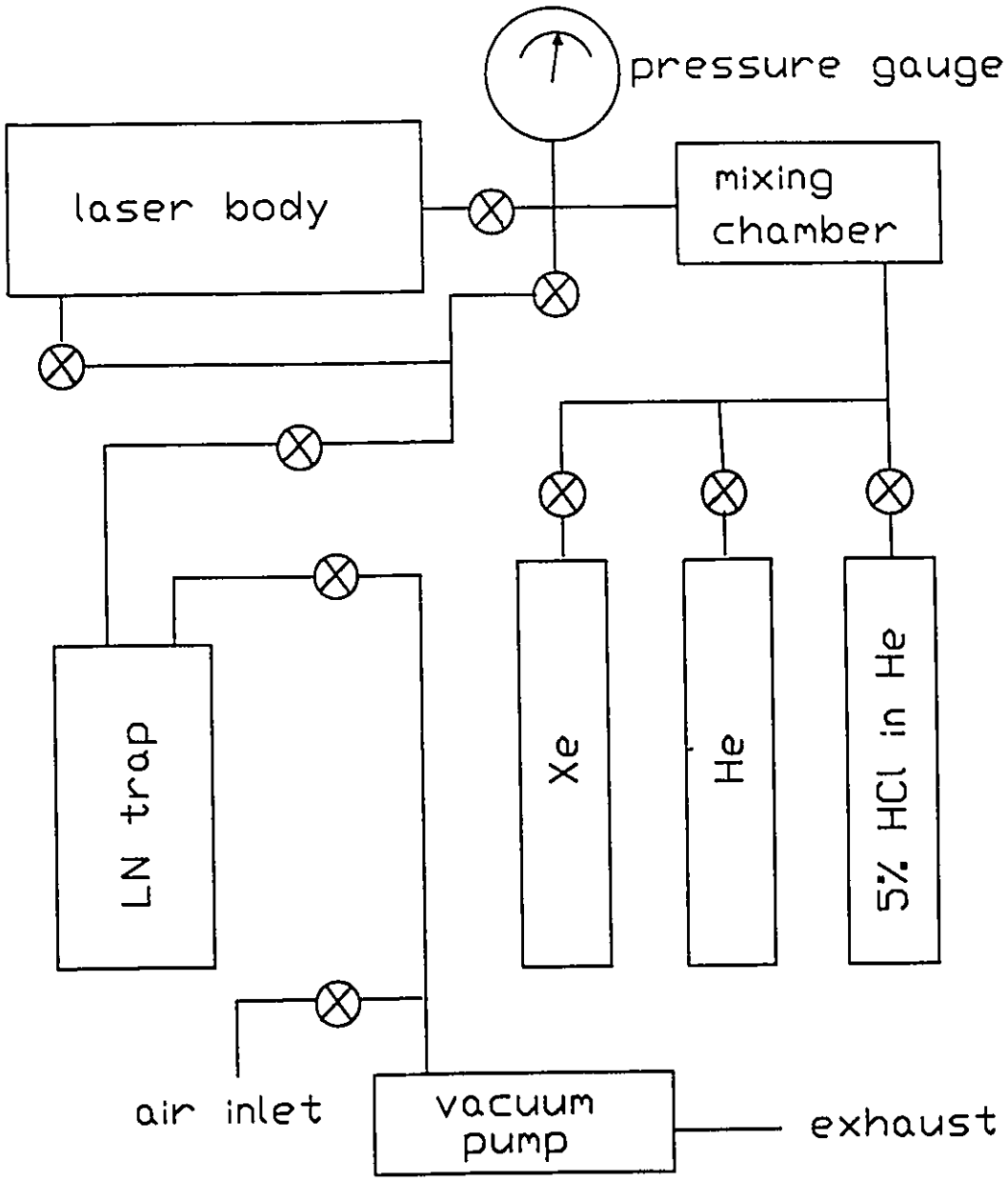

Fig. 3.6. Schematic of the gas handling system. Valves are indicated by ⊗.

employed (purchased from Matheson).

3.3. Laser Performance.

Excimer laser performance is characterized by peak output power, pulse duration, output energy, laser efficiency and operating lifetime. Section 3.3.1 provides a discussion of the physical properties of the compact XeCl laser system. Typical operating parameters for the system are listed in Table 3.1. Section 3.3.1 also describes some of the precautions necessary to optimize laser performance. Experimental results relating to laser output as a function of capacitor charging voltages and gas pressures are presented in Section 3.3.2.

3.3.1. Operating Characteristics of the Laser System.

Both contamination of, and reaction with the gas mixture affects laser operation dramatically. Initially, the system (mixing chamber, laser, etc.) is evacuated. Even with a clean system after evacuation, the HCl will react rapidly with the metallic components in the discharge. However, the reaction rate decreases with time as protective chlorides are formed (passivation). A properly passivated system will have negligible reaction with HCl. However, water vapour absorbed in or absorbed on the dielectrics will consume HCl.

After any exposure to the atmosphere, the system was evacuated, and then filled several times with a static mixture of 5%HCl/He for a period of time (15 minutes to several hours). After this initial passivation, the laser body was operated with a 5%HCl/He mixture at a low capacitor charging voltage. This procedure produced excellent passivation of the metallic surfaces, and greatly reduced residual H_2O concentration. As is well known, H_2O is probably the

most harmful species commonly present in XeCl lasers. When HCl is absorbed in water, it becomes a highly corrosive acid, thereby removing HCl from the gas mixture. Equally important, the resultant acid rapidly attacks and destroys the passivation. In addition to greatly decreasing the laser operating lifetime, H_2O and other contaminating molecules may absorb laser radiation, and consequently reduce the laser output energy and efficiency.

After adequate passivation, the laser could be operated reliably and continuously for periods in excess of 1 hour for each gas fill. Repetition rates in excess of 30 Hz were readily attainable. The pulse-to pulse variation in energy was better than $\pm 5\%$.

The laser resonant cavity was composed of two plane-parallel fused-silica substrates. An externally aluminized layer, providing a reflectance of $\approx 95\%$, was used for the "rear" reflector. The "front" reflector, used as the output coupler, was uncoated, and the effective reflectance is $\approx 7.5\%$. Careful alignment of the reflectors was necessary because both reflectors had plane surfaces. During laser operation, a deposit of metal halides slowly forms on the internal surfaces of the reflectors. When required, the reflector surfaces were cleaned using ethanol.

3.3.2. Laser Output Characteristics.

The laser output characteristics at 308-nm wavelength were investigated. The pulse waveform and energy were measured for various capacitor charging voltages, total gas pressures, and gas compositions. A fast-response vacuum photo-diode (risetime <200 ps), together with a 0.5-GHz bandwidth (0.6-ns risetime) oscilloscope (Tektronix 7834), was used for the measurement of the pulse waveforms. Output pulse energy was measured using a pyroelectric joulemeter (GenTec ED-200), with a stated accuracy of $\pm 10\%$, connected to a standard oscilloscope (Tektronix 547).

Table 3.1. Typical Laser System Parameters.

Discharge Volume	~ 1 cm^3
Discharge Length	10 cm
Discharge Width	0.2 cm
Electrode Separation	0.47 cm
Mirror Reflectance	~95% and 7.5%
Typical Operating Pressure (absolute)	~350-450 kPa
Charging Voltage	12-21 kV
Capacitance of Each Capacitor	1.56 nF
Inductance in Spark-Gap Circuit	27.6 nH
Inductance in Laser Circuit	6.0 nH
Peak Current	~10 kA
Current Pulse Duration	< 20 ns
Maximum E/N	~$40 \cdot 10^{-17}$ $V \cdot cm^2$
Gas Composition	0.8%Xe/0.3%HCl/He
Electrical Input Energy	~0.35 J
Optical Output Energy	~1 mJ
Overall Laser Efficiency	~0.3%
Optical Pulse Duration (FWHM)	< 2 ns

Only relative power can be observed with the waveform measurements. However, the numerical integrations of these waveforms are equal to the pulse output energies. Therefore, it is relatively easy to calibrate the waveforms in terms of instantous power as a function of time.

Figure 3.7 shows laser output waveforms for several capacitor charging voltages. The same gas mixture (0.8%Xe/0.3%HCl/He at a total pressure of 450 kPa) was employed for all of the measurements. The pulse durations are relatively constant in all cases. However, the peak powers are nearly proportional to the capacitor charging voltage. Below a voltage of 12 kV, the laser output energy decreases rapidly. Voltages above 21 kV were generally avoided in order to prevent damage to components (e.g., circuit-board breakdown). However, saturation of the output energy is expected (and has been observed) at higher capacitor charging voltages.

Figure 3.8 shows the variation of pulse shape with total gas pressure. A 0.8%Xe/0.3%HCl/He gas mixture and a charging voltage of 15 kV were used in all cases. Because the densities of the electrons and photons increase with gas pressure, the peak power increases with total pressure. The pulse durations also vary with pressures, but in a different manner. Longer pulse durations are observed at lower pressures because the quenching of the upper laser level ($XeCl^*$) by electrons is reduced. In addition, double peaks appear for pressures below 350 kPa, with the height of second peak increasing with decreasing pressure. The second peak is caused by gain produced in the second half cycle of the discharge current. At high pressures, the gain is quenched by the considerably higher electron densities which are now present.

The total pulse energy as a function of capacitor charging voltage is shown in Fig. 3.9(a) for a total gas pressure of 450 kPa. In the range investigated (12 kV to 20 kV), the energy is proportional to charging voltage, but the pulse duration does not change obviously with charging

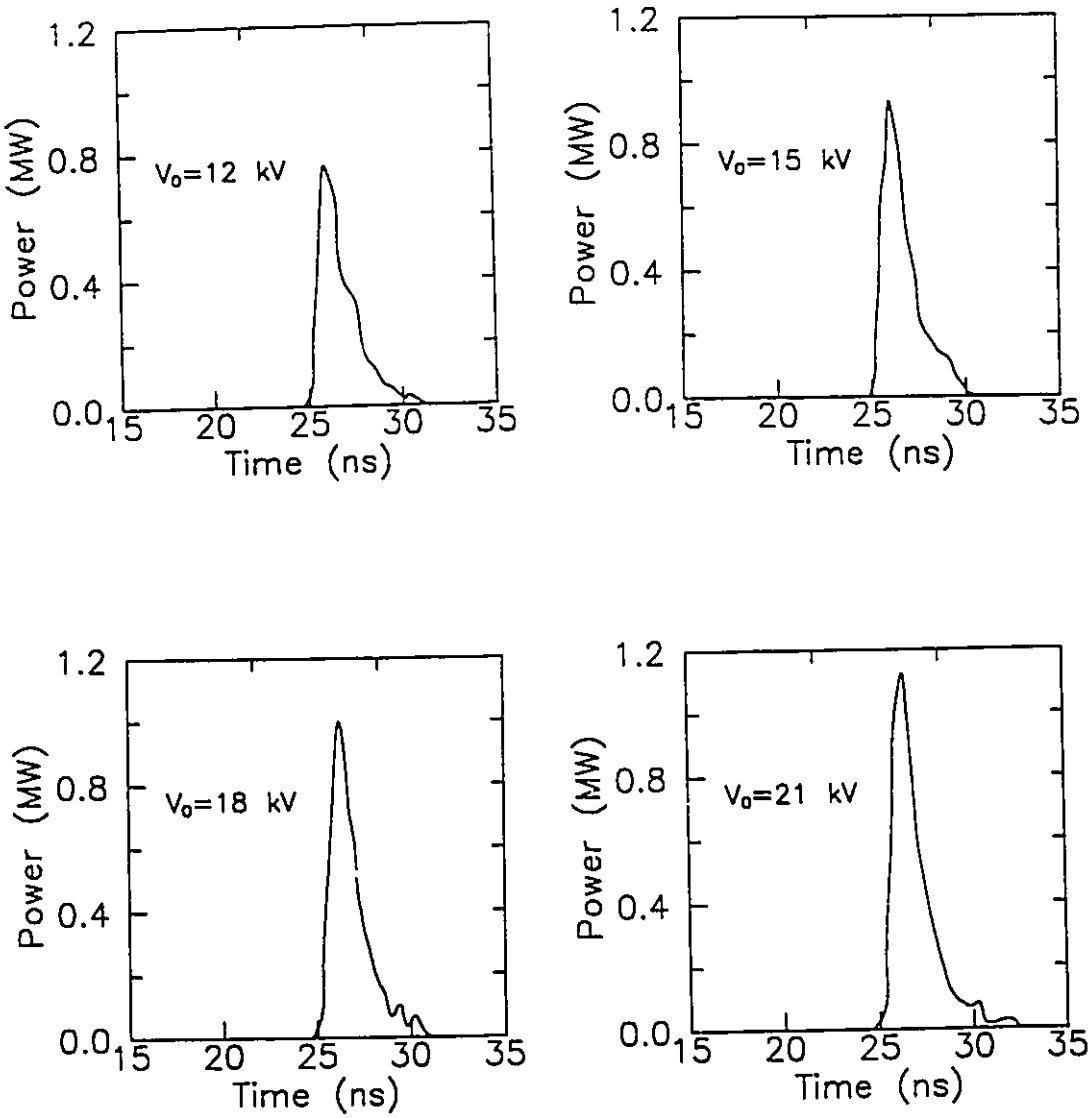

Fig. 3.7. The relationship between laser output power and applied voltage. The gas mixture is 0.8%Xe/0.3%HCl/He at 450-kPa absolute pressure. The structure in the waveform results from multiple reflection of the laser pulse within the resonant cavity, and not from the properties of the gain medium.

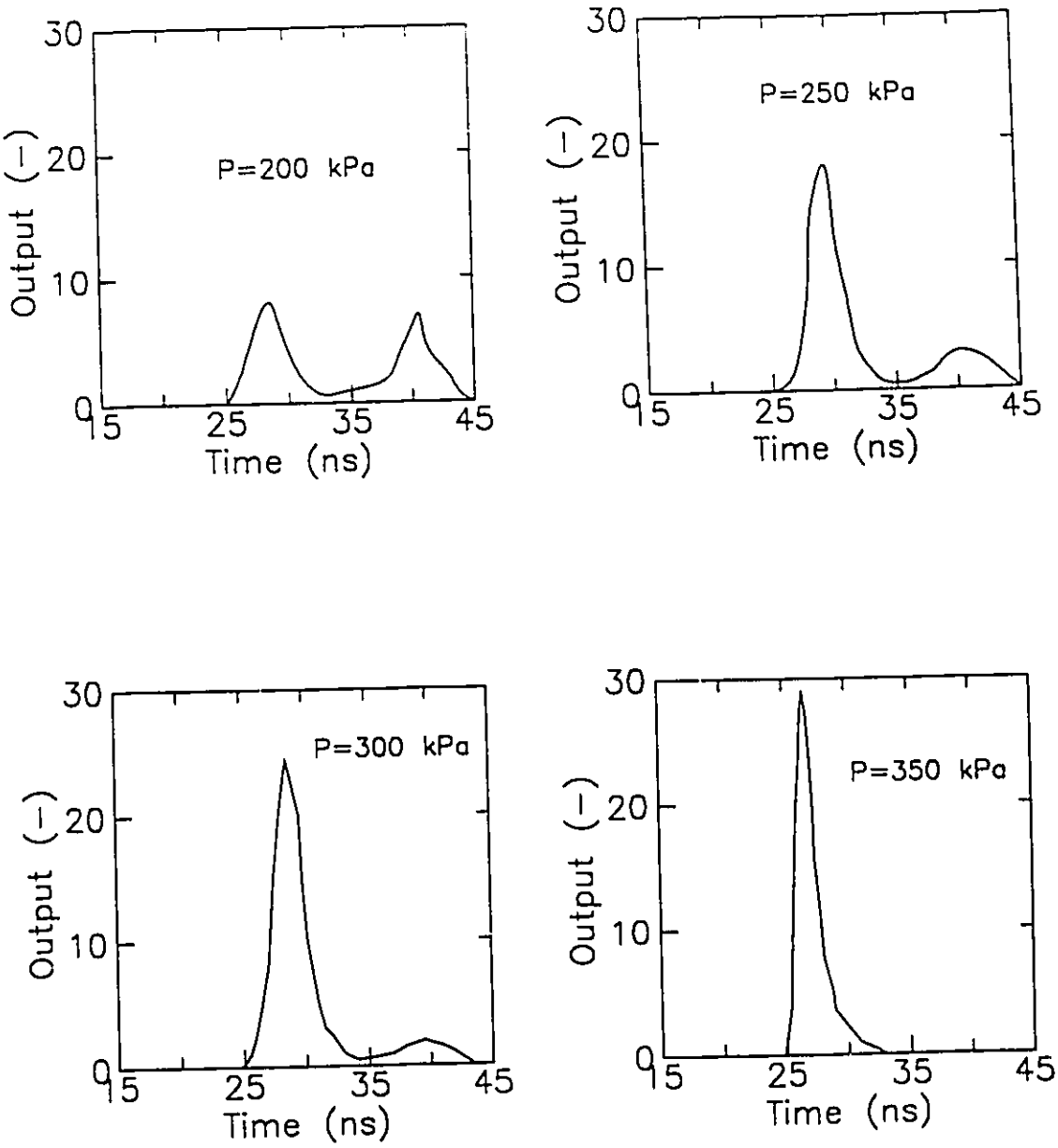

Fig. 3.8. The relationship between pulse shape and total gas pressure at a charging voltage of 15 kV. The laser outputs are given in arbitrary units.

voltage. At a fixed charging voltage, the output energy increases withincreasing pressure, but saturates at high pressures, as shown in Fig. 3.9(b). Figures 3.9(c) and 3.9(d) show the output energy as a function of the Xe and HCl pressures, respectively. For these data, the charging voltage, the total pressure and the other component (HCl or Xe) pressure are all kept constant. It was observed that pulse shape and duration are relatively independent of gas composition. However, the energy varies substantially with Xe or HCl content, as shown in Figs. 3.9(c) and 3.9(d), respectively. In both cases, a rapid increase of energy quickly reaches saturation as the partial gas pressure is increased.

Figure 3.10 compares the laser output waveform for two different buffer gases (He and Ne). In our compact laser, producing short-duration output pulses, the 1.06%Xe/0.24%HCl/Ne mixture behaves essentially similar to the 0.8%Xe/0.3%HCl/He mixture, in terms of pulse shape and duration. However, the 1.06%Xe/0.24%HCl/Ne mixture gives slightly lower energy. In the usual XeCl laser systems (>10 ns pulse duration), a Xe/HCl/Ne mixture produces lower peak powers and longer pulse durations than a Xe/HCl/He mixture (Maeda et al, 1982). Furthermore, the efficiency of energy deposition into the discharge are different for the two mixtures.

In order to find the optimum operating conditions for a laser, it is also necessary to consider the laser optical gain and efficiency together with the output, over a range of operating conditions. The operating characteristics for the compact XeCl laser are discussed in detail in Chapter 6. These characteristics include the optimum mixture and excitation, the optical gain and the laser efficiency.

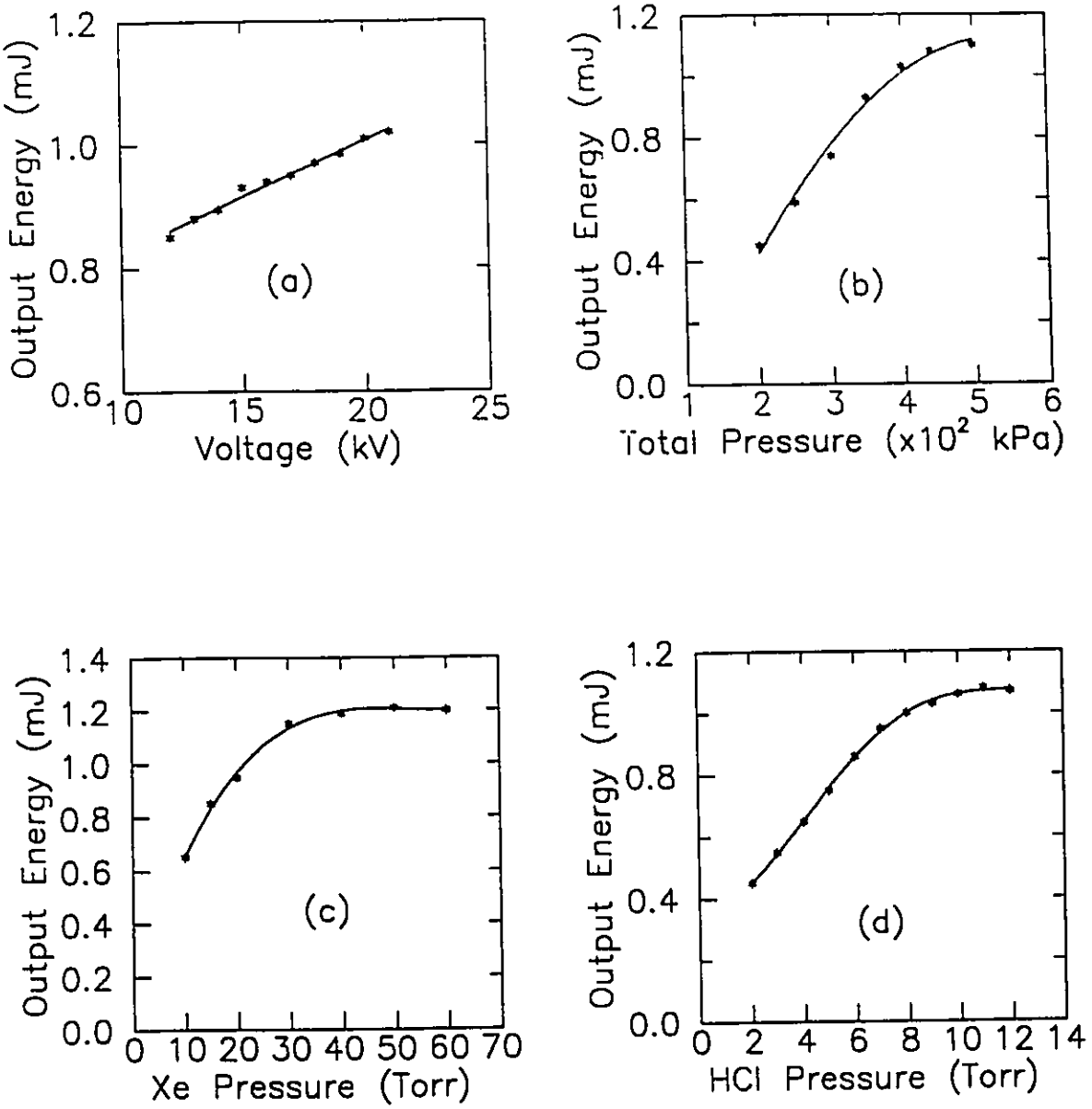

Fig. 3.9. (a) The variation of laser output energy with voltage. The gas mixture was 0.8%Xe/0.3%HCl/He at a 450-kPa absolute pressure (equivalent to 3380 Torr). (b) The variation of laser output energy with total gas pressure, employing the same mixture as (a) and a fixed charging voltage of 15 kV. (c) The variation of laser output energy with Xe partial pressure. The charging voltage was 15 kV, the He partial pressure was 450 kPa and the HCl partial pressure was 10 Torr. (d) The variation of laser output energy with the HCl partial pressure. The charging voltage was 15 kV, the He partial pressure was 450 kPa and the Xe partial pressure was 26.5 Torr.

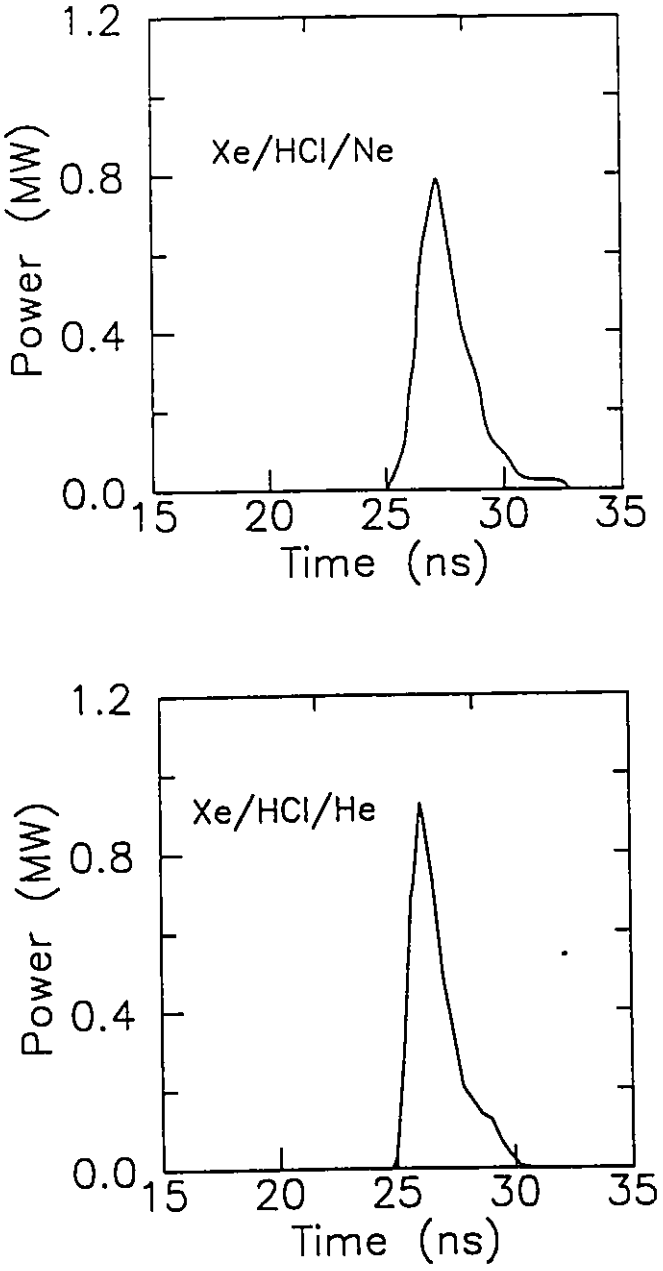

Fig. 3.10. Comparison of laser outputs for gas mixtures of 0.8%Xe/0.3%HCl/He and 1.06%Xe/0.24%HCl/Ne at total pressures of 450 kPa. The charging voltage was 15 kV.

Chapter 4

Investigations of the Discharge Voltage and Current Waveforms

Discharge voltage and current waveforms provide very important data in the study of gas lasers. The laser output energy is related to the energy deposition into the discharge, which can be calculated from the voltage and current waveforms. In addition, accurate measurements of these waveforms are used to verify the validity of the kinetic model for the discharge, as described later in Chapters 5 and 6.

The modelling of the discharge excitation circuit is described in Section 4.1. Measurements of the discharge voltage and current waveforms are described in Sections 4.2 and 4.3, respectively.

4.1. The Discharge Excitation Circuit.

In order to understand how electrical energy is transferred into the laser discharge medium, it is necessary to investigate the current and voltage waveforms for each component in the circuit. The equivalent circuit for the discharge excitation, shown in Fig. 3.4, can be expressed by the five differential equations

$$LSG\frac{dI_1}{dt} + RSG\ I_1 - \frac{Q_1}{C1} = 0 \quad , \tag{4.1}$$

$$LD\frac{dI_2}{dt} + RD(t)\ I_2 + \frac{Q_1}{C1} - \frac{Q_2}{C2} = 0 \quad , \tag{4.2}$$

$$I_2 = -\frac{dQ_2}{dt} \quad , \tag{4.3}$$

$$I_3 = -\frac{dQ_1}{dt} \tag{4.4}$$

and

$$I_3 = I_1 - I_2 \quad , \tag{4.5}$$

where Q_1 and Q_2 are the charge stored in capacitors C1 and C2, and I_1 and I_2 are the currents through the spark gap and laser discharge media, respectively. After the spark gap is triggered, resistance RSG quickly reaches a constant value of $\approx 1\ \Omega$ (see Section 4.3). The discharge resistance RD is initially an open circuit. When the voltage across the discharge medium reaches some critical value, an avalanche discharge begins, and the value of RD drops very rapidly. The measured voltage and current waveforms (see Sections 4.2 and 4.3) show that RD decreases to $< 1\ \Omega$ in a time < 2 ns, and then remains approximately constant during the duration that the laser operates. The time-dependent value of RD used in the Eq. (4.2) is evaluated from

$$RD(t) = \frac{d}{\mu_e(t) \cdot n_e(t) \cdot A \cdot e} \quad , \tag{4.6}$$

where μ_e is the electron mobility, n_e is the electron density, d is the distance between the electrodes, and $A = l \cdot h$ is the active discharge cross-sectional area. The length of the active discharge medium (l) is approximately the length of the electrodes. Dimensions d and h are determined from the cross-section of the laser output observed at the end of the laser cavity. Parameters μ_e and n_e are calculated from the rate equations describing the kinetic processes in the discharge (see Chapter 6).

The numerical solution of Eqs. (4.1) to (4.5) provide the voltage and current waveforms

for all of the circuit components. The voltages across capacitors C1 and C2 are given by

$$V_{C1} = V_0 - \frac{1}{C1}\int I_3 dt \qquad (4.7)$$

and

$$V_{C2} = V_0 - \frac{1}{C2}\int I_2 dt \quad , \qquad (4.8)$$

where V_0 is the capacitor charging voltage. The voltage between the laser electrodes is

$$V_{RD} = V_{C2} - V_{C1} \qquad (\textit{before breakdown})$$

or

$$V_{RD} = I_2 \cdot RD(t) \qquad (\textit{after breakdown}) \quad . \qquad (4.9)$$

All the relevant waveforms are shown in Fig. 4.1. The circuit component values are provided in Table 3.1. Discharge breakdown is assumed to commence when the voltage across the electrodes reaches 20 kV.

The energies stored in the capacitors are calculated from

$$E_C = \frac{1}{2} Ci \cdot V_{Ci}^2 \qquad (i=1,2) \quad . \qquad (4.10)$$

The time-dependent energies for C1 and C2 are given in Figs. 4.2(a) and 4.2(b), respectively. The powers deposited into the laser discharge and spark gap, calculated from $E_{RSG} = I_1^2 \cdot RSG$ and $E_{RD} = I_2^2 \cdot RD$, are given in Figs. 4.2(c) and 4.2(d), respectively. These waveforms show that the energy is initially stored in C1 and C2, and that the voltage across the discharge is zero. After the spark gap is triggered, the spark gap conducts, producing a series oscillatory circuit. Soon after the voltage across C1 is reversed, the voltages across C1 and C2

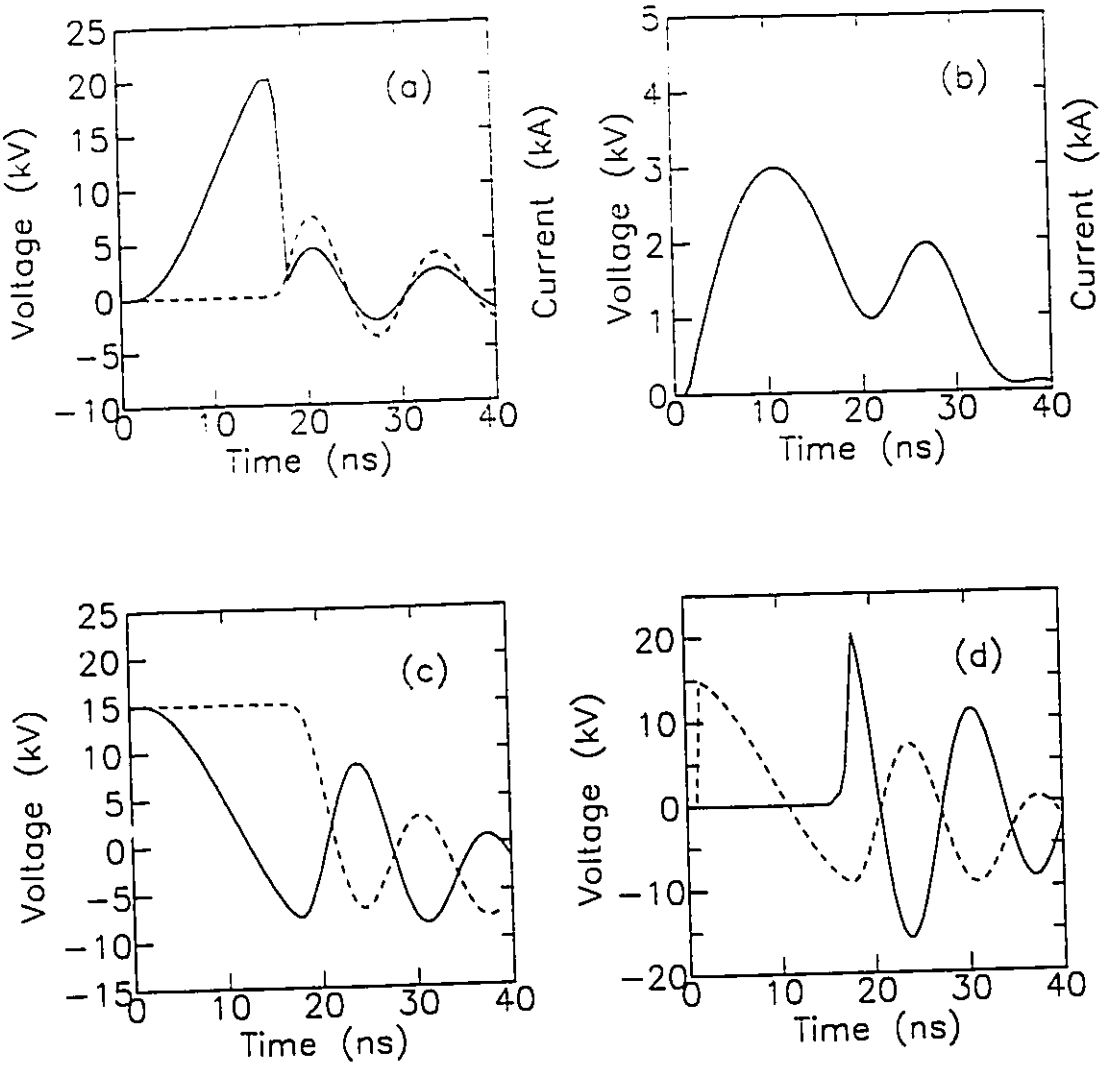

Fig. 4.1. Calculated voltage and current waveforms. (a) Voltage (solid) and current (dashed) waveforms for RD. (b) Voltage and current waveforms for RSG (both curves overlap). (c) Voltage waveforms across C1 (solid) and C2 (dashed). (d) Voltage waveforms across LD (solid) and LSG (dashed).

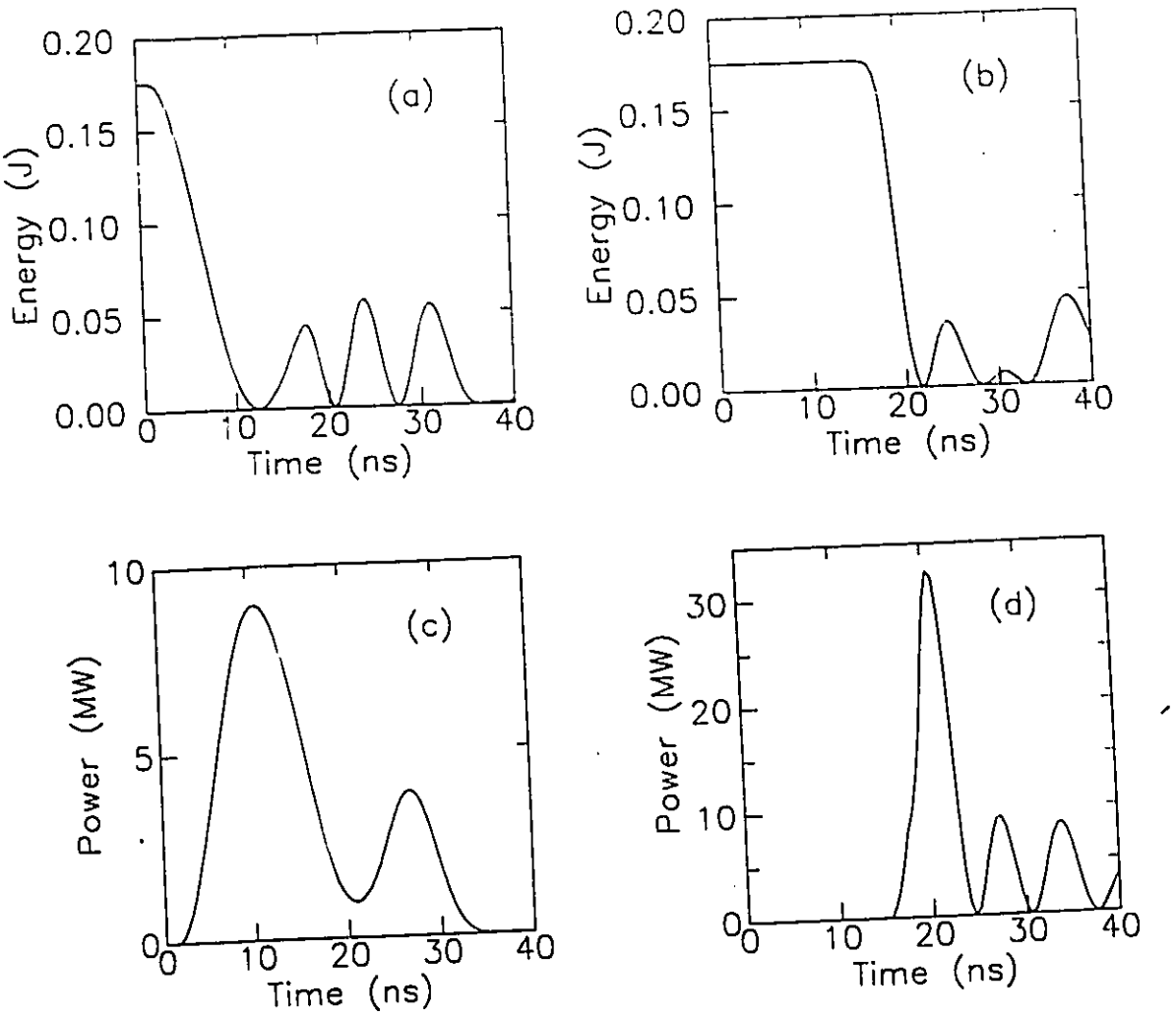

Fig. 4.2. (a) Energy stored in C1. (b) Energy stored in C2. (c) Power deposited into the spark-gap circuit. (d). Power deposited into the laser discharge.

add. When a critical voltage is reached, the laser discharge begins. The time delay between spark-gap breakdown and laser medium discharge is controlled mainly by the inductance LSG. After discharge breakdown, most of the energy stored in C1 and C2 is deposited into the discharge.

Discharge breakdown occurs approximately 15 ns after spark-gap breakdown. The laser emission is observed to peak approximately 10 ns after discharge breakdown (i.e., 25 ns after spark-gap breakdown). This time delay, which is controlled by the kinetic reactions in the discharge, is discussed in Chapter 6.

4.2. Measurements of Discharge Voltage Using an Electro-optic Technique.

Standard high voltage probes are unsuitable for measuring the voltage between the electrodes in the compact short-pulse laser used in the research. This laser has an avalanche voltage falltime of ≈ 1 ns and an effective discharge duration of < 15 ns. Furthermore, the electrodes are isolated from "ground". Optical techniques for measuring voltage provide the necessary isolation. In addition, the effects of electromagnetic noise on measurements can be greatly reduced in comparison to standard high voltage probes.

KDP Pockels cell has been employed for measuring the discharge voltage of a TE N_2 laser (Mitani and Nakaya, 1978). One disadvantage is that this material is hydroscopic. Measurements have also been carried out using Kerr cells (Bergmann and Kolleogy, 1977). However, these devices have greater nonlinearity than Pockels cells. A Pockels cell employing a quartz crystal provided a reliable and accurate method for measuring the voltage between the electrodes in our compact XeCl laser. Both the Pockels cell and the basic experimental arrangement used in this

thesis work are similar to those described in the paper by Ballik and Liu (1983), but with improved components to provide better time resolution and signal-to-noise (SNR) ratio.

4.2.1. Principle of the Voltage-Measurement Technique.

The measurement technique is based on voltage-induced polarization changes in the optical radiation passing through an appropriate crystal. In the present research, a quartz crystal was used. This material belongs to the 32-symmetry point group. If an external voltage V is applied across the crystal in the x-direction of the index ellipsoid, and the radiation propagates along the z-direction, then the phase retardation between the polarizations in the x- and y-directions is

$$\Delta\phi = \phi_y - \phi_x = \frac{2\pi}{\lambda} n_0^3 \gamma_{11} l \frac{V}{d} \quad , \tag{4.11}$$

where l is the crystal length in the z-direction, d is the crystal thickness in the x-direction, n_0 is the refractive index in the absent of applied voltage, γ_{11} is the first element in the electro-optic coefficient tensor, and λ is the radiation wavelength. The voltage required to produce a $\lambda/2$ retardation ($\Delta\phi = \pi$) can be calculated from

$$V_{1/2} = \lambda d / 2 n_0^3 l \gamma_{11} \quad . \tag{4.12}$$

The calculated value is in good agreement with the measured value given in Section 4.2.2.

A cross-sectional view of the XeCl laser body, the Pockels cell and the mounting assembly is shown in Fig. 4.3. The quartz bar has dimensions 1.0 x 2.1 x 14.0 cm^3 (x, y and z axes, respectively), and polished ends for the optical path. The voltage between the electrodes (i.e., the discharge voltage) is applied across the x surfaces of the bar by means of copper-foil electrodes connected to the laser electrodes.

The experimental arrangement for voltage measurements is shown schematically in

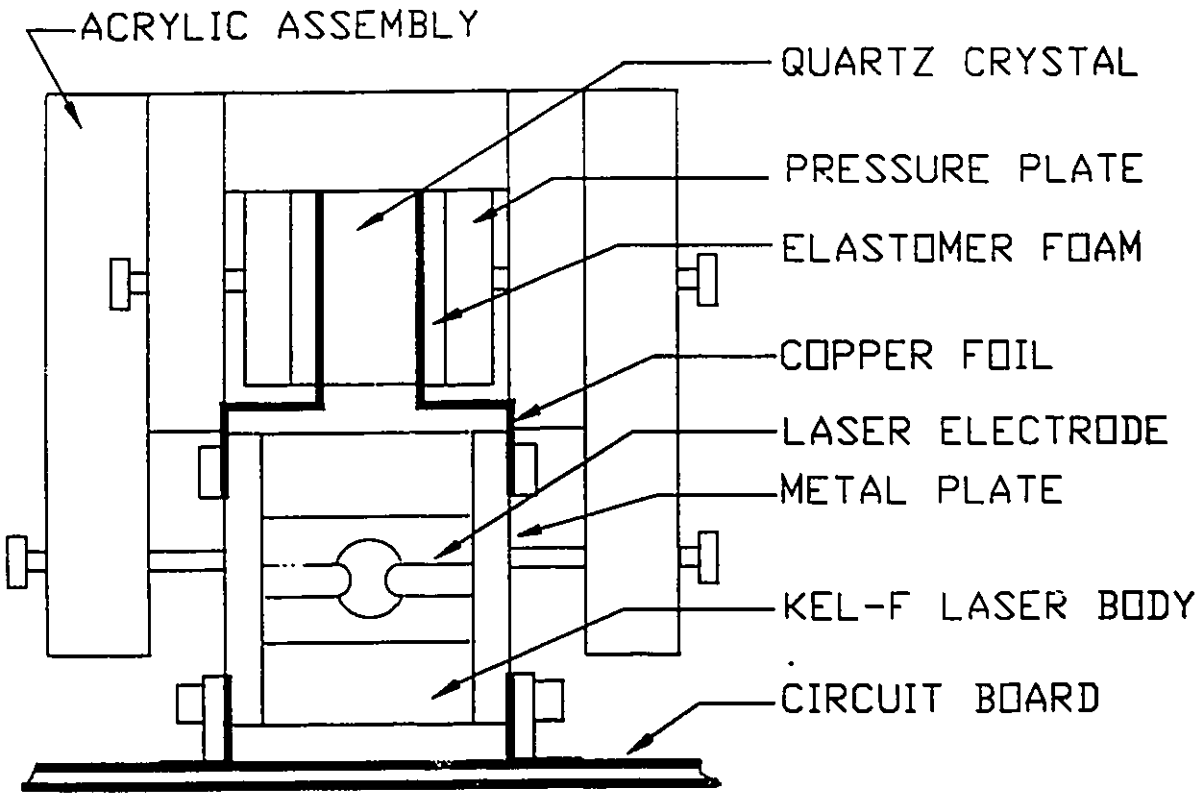

Fig. 4.3. Cross-sectional view of the laser body and the Pockels cell.

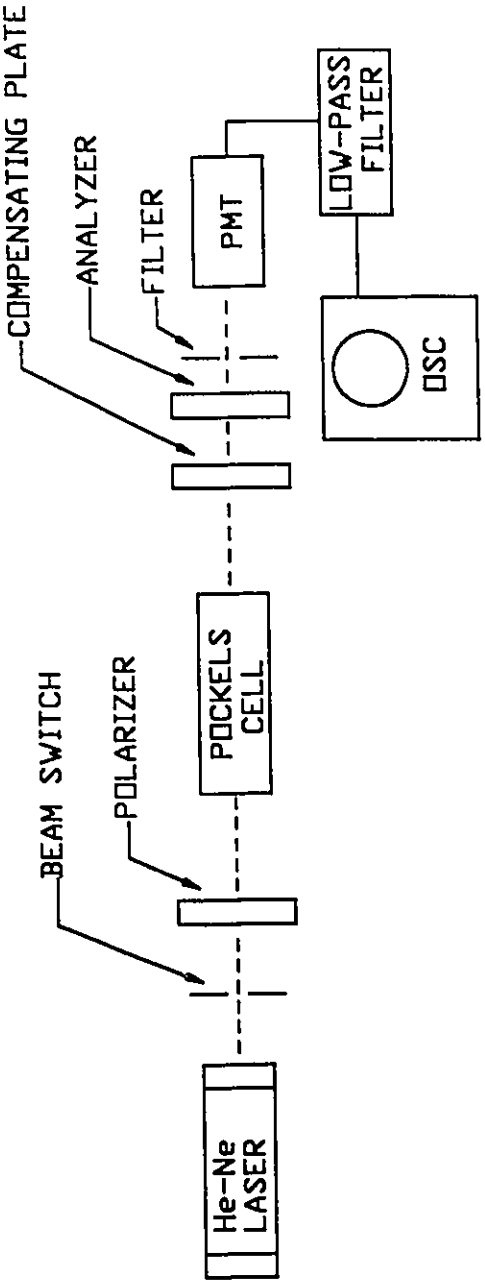

Fig. 4.4. Schematic of the experimental arrangement for voltage measurement.

Fig. 4.4. A 2-mW He-Ne laser (Melles Griot 05-LHR-121) was employed as the radiation source. All measurements were made after the laser output was stable (several minutes operation). The axes of the input and output (analyzer) polarizers are perpendicular to each other, and at 45° to the crystal x- and y-axes. The response time of the PMT (RCA C7151W) was improved by reducing the number of active dynode stages in the photomultiplier from 10 to 5 (dynodes 6 to 10 connected to the anode), and by PMT operation at high voltage (12 to 13 kV). The PMT output was recorded using a fast response (0.6-ns risetime) storage oscilloscope (Tektronix 7834). To reduce the electrical noise caused by discharge, the PMT and connecting cables were shielded.

A mechanical beam switch (1-mm diameter aperture) is used to pulse the He-Ne laser radiation in order to prevent damage to the photomultiplier. In pulsed input operation, the photocathode can tolerate much higher incident intensities than in continuous input operation. The higher intensities are required because of the reduced gain of the PMT resulting from the reduced number of dynodes. A schematic of the beam switch is shown in Fig. 4.5. The basic component of the switch is a relatively fast relay (Potter & Brumfield PRD5DYO) with an extension on the armature for the aperture. The assembly is adjusted to have one contact of the relay making contact at the instant that the aperture axis is coincident with the axis of the laser beam. When the relay is operated, the aperture assembly is attracted to the relay magnet. At the time that the radiation through the Pockels cell is a maximum, the relay contact closes and provides a trigger signal for the spark-gap circuit.

The PMT output current I is proportional to the intensity of the incident radiation on the photocathode. This intensity is determined by the analyzer axis. The normalized PMT output current is given by

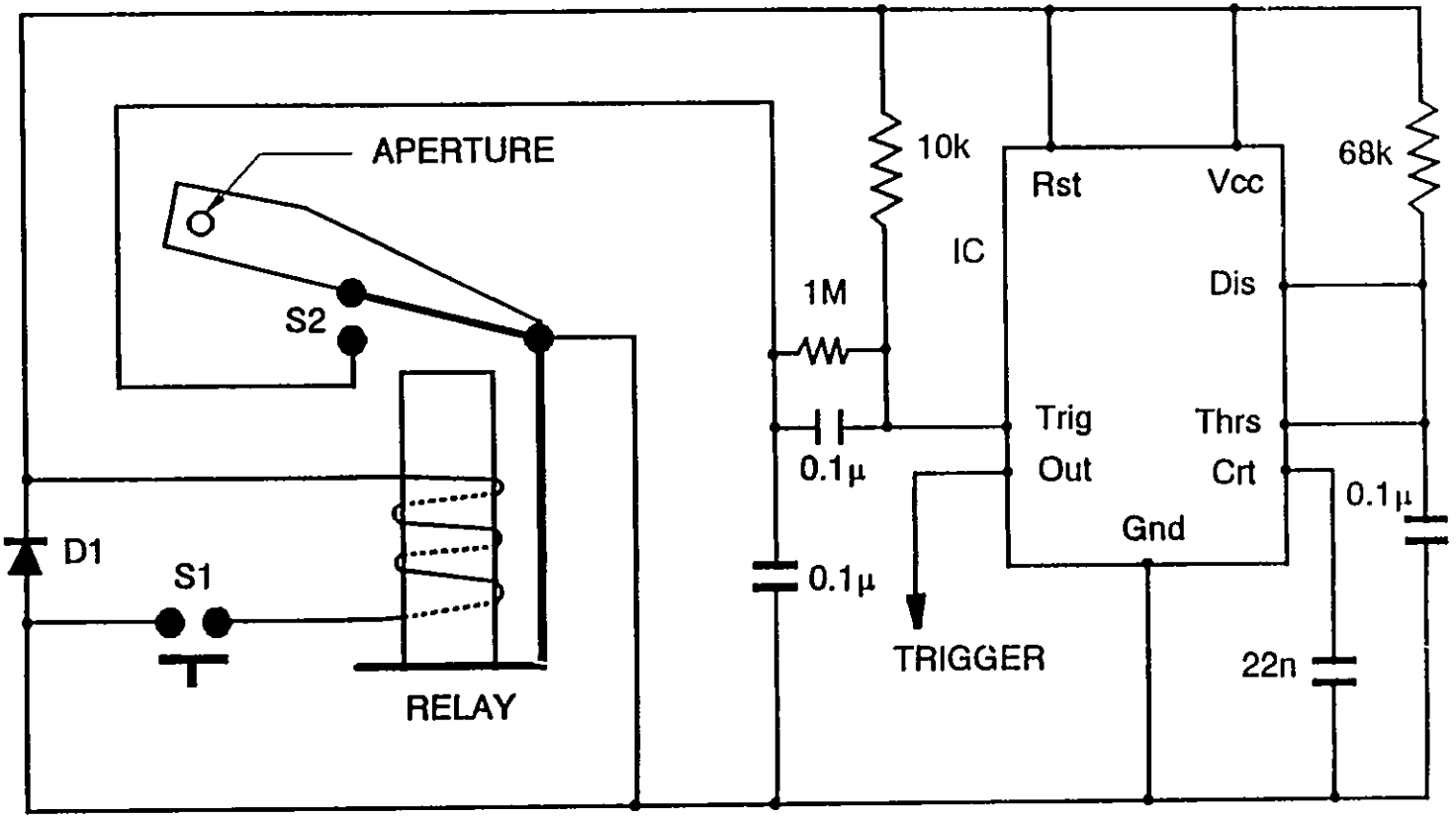

Fig. 4.5. Laser beam switch assembly and spark-gap trigger circuit. The IC is a LM555 timer which is connected to produce trigger pulse of 8 ms duration. Diode D1 is for surge protection. Switches S1 and S2 are the "trigger on" and relay contact, respectively.

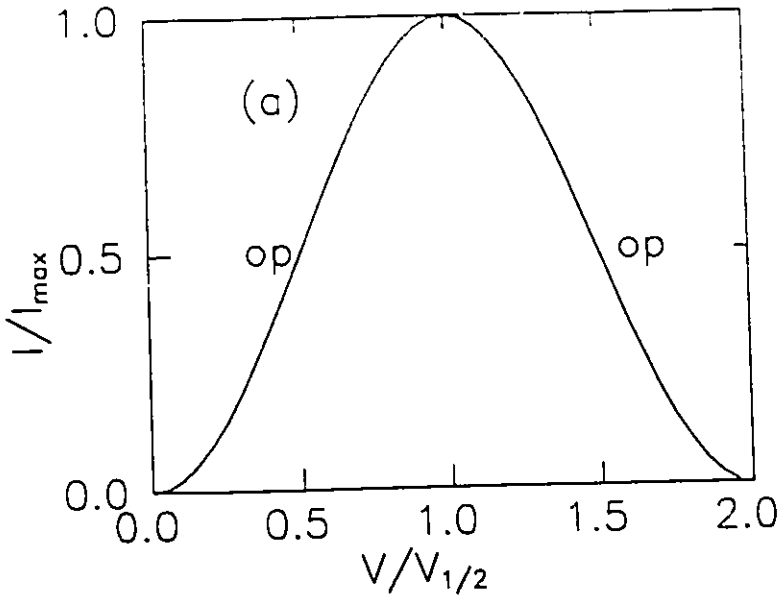

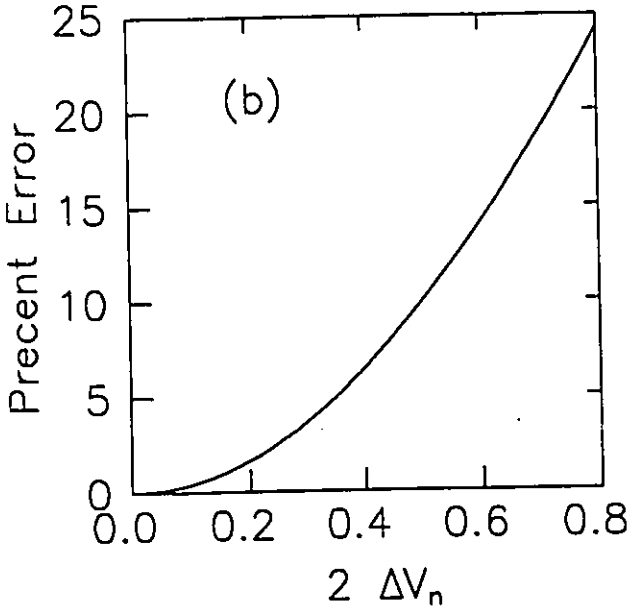

Fig. 4.6. (a) Normalized output current from a photomultiplier as a function of the normalized applied voltage across a Pockels cell. The operating point (op) is at I/I_{max}=0.5. (b) Percent error in the normalized peak-to-peak voltage operating symmetrically about V_n=0.5 or V_n=1.5.

$$I/I_{max} = \sin^2[\frac{\pi V_n}{2} + \theta] \quad , \tag{4.13}$$

where $V_n = V/V_{1/2}$, and θ is a phase shift which may be caused by imperfections or stress within the crystal. This phase shift can be changed or eliminated by use of a compensating plate. A curve of Eq. (4.13) for $\theta=0$ is provided in Fig. 4.6(a). An important parameter in the measurement of voltage waveforms is the linearity of the output signal. Let the initial phase shift θ be set at the operating point (op) as shown in Fig. 4.6(a). At this point, the output (I/I_{max}) is symmetrical with the applied voltage ($V/V_{1/2}$), and has the best linearity. The ratio of the observed voltage (V_m) to the applied voltage (V_a) is given by

$$V_m/V_a = [\sin(\pi\ \Delta V_n)]/(\pi\ \Delta V_n) \tag{4.14}$$

where $2\Delta V_n$ is the total normalized peak-to-peak voltage symmetrical about op in Fig. 4.6(a). Figure 4.6(b) shows the percent error as a function of $2\Delta V_n$. It can be seen that the error is acceptably small for relatively large values of ΔV_n. For this research, a linear relationship between V_m and V_a has been assumed because $2\Delta V_n$ was generally less than 0.3. If more accurate results were required, the correction could be carried out using Eq. (4.13). In addition, the absolute magnitudes of the voltages can always be calculated using Eq. (4.15) in the next section.

4.2.2. Experimental Results.

An approximate calibration of the quartz crystal can be made by applying dc voltages across the crystal. However, the static value of $V_{1/2}$ will always be considerably less that the fast response value. For the crystal used in the present measurements, the static value was found to be $V_{1/2}=28.6$ kV. This is considerably less than the fast response value obtained from Eq. (4.15).

The time response of the detection system was determined using a LED radiation source

with a pulse duration of approximately 0.1 ns. The pulse duration observed with the oscilloscope was 2 ns (FWHM) with a waveform which is approximately Gaussian in shape. This duration is limited primarily by the photomultiplier. The risetime for the quartz crystal and the oscilloscope are <0.5 ns and 0.6 ns, respectively.

Typical discharge voltage waveforms for capacitor charging voltages of 12, 15 and 18 kV are given in Figs. 4.7(a) to 4.7(c), respectively. These are taken from photographs of the waveforms obtained with the oscilloscope. The magnitude of the breakdown voltage can be calculated using

$$V_{br} = V_{C2} + V_{C1} = V_0[1-\cos(2\pi t/T)\exp(-At)] \quad , \tag{4.15}$$

where V_0 is the capacitor charging voltage and t is time from spark-gap breakdown to discharge breakdown. The period T and the decay constant A can be calculated from the measured current waveforms in the spark-gap circuit when the laser head is removed from the circuit board (see Section 4.3.2.). This corresponds to leaving switch SD in Fig. 3.4 always open. From Fig. 4.7 it can be seen that the time to discharge breakdown decreases with increasing charging voltage. However, both the observed and calculated breakdown voltages only increase slowly with increasing charging voltage.

The deconvolution of a Gaussian instrumentation response (2 ns FWHM) from the observed data shown in Fig. 4.8 (Curve A) results in Curve B. An interesting feature of Curve B is the dip appearing immediately after breakdown. This dip results from the inductance in the laser discharge circuit. At the moment of avalanche breakdown, the discharge current increases very rapidly, causing a rapid decrease in the voltage between the electrodes. The decrease is sufficiently fast that this voltage may approach zero. To observe such a low value would require much better instrumentation than was available for this research.

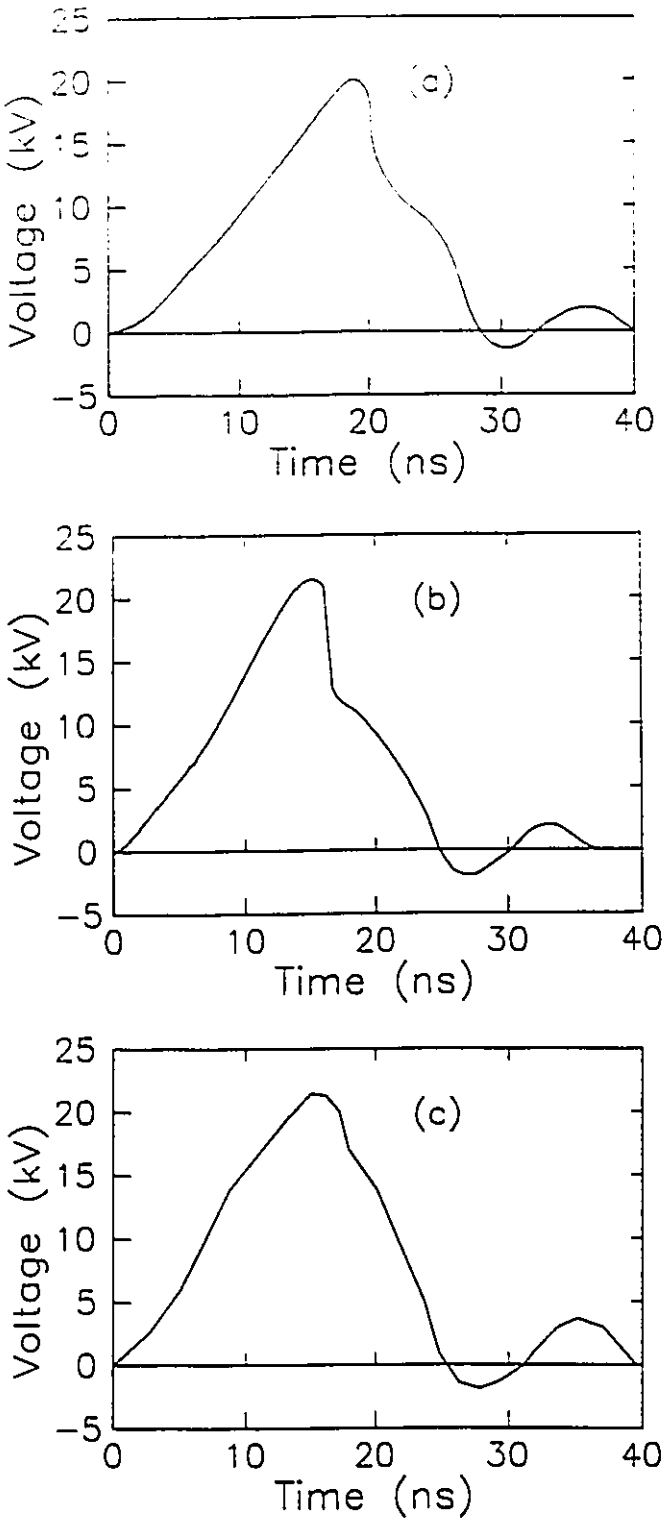

Fig. 4.7. Measured discharge-voltage waveforms for capacitor charging voltages of (a) 12 kV, (b) 15 kV and (c) 18 kV.

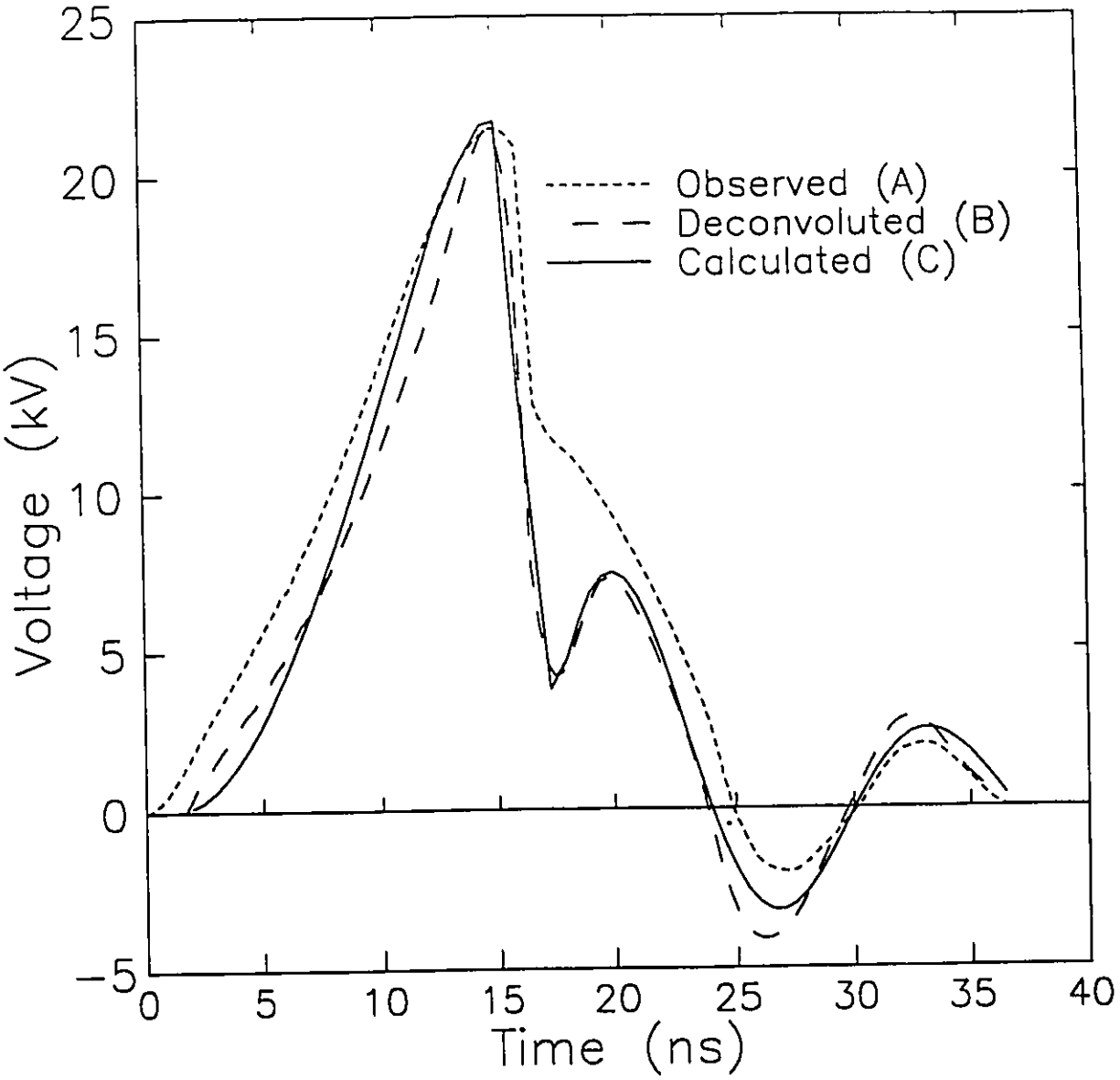

Fig. 4.8. Comparison of discharge voltage waveforms. Curve A is the waveform observed with the oscilloscope. Curve B is the result of deconvoluting the instrumentation response from Curve A. Curve C is calculated using the equivalent circuit in Fig. 3.4 and the parameters in Table 3.1.

After breakdown, the voltage is a damped oscillation with a period of ≈ 14 ns. This waveform has the same period, phase and exponential decay as the discharge current waveform. It follows that the impedance of the discharge is resistive and approximately constant in value during the duration of the main discharge.

4.3. Measurement of Discharge Current.

Current waveforms provide essential information on the characteristics of the laser gain medium. These waveforms are related to the electron density, the electron energy distribution and the conductivity of the discharge medium. Therefore, accurate current measurements help to establish the accuracy of the models for both the excitation circuit and the kinetic processes in the discharge plasma. This section describes a current probe employing a Rogowski coil which is capable of observing the short duration current waveforms present in our laser. Also included are data measured with this probe.

4.3.1. Current-Measurement Technique.

The Rogowski probe consists of a small copper coil wound at the end of a coaxial cable, as shown in Fig. 4.9(a). The shield is constructed using an insulated overlap in order to avoid a "shorted" turn around the coil. An additional flexible shield is placed over the full length of the coaxial cable. This provides a substantial reduction in electrical noise. During measurement, the probe and connecting cable are contained within a polycarbonate tube (0.5-in I.D.,0.12-in wall thickness), in order to insulate the probe from the capacitor plate. The probe output was recorded using a fast (0.6-ns risetime) storage oscilloscope (Tektronix 7834).

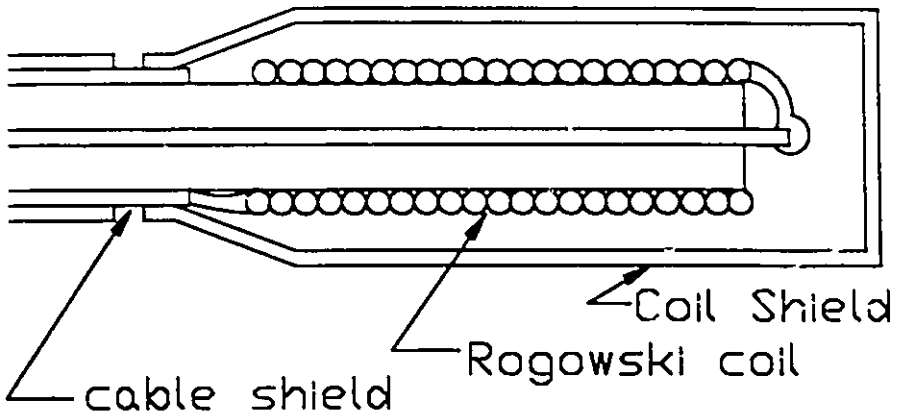

(a)

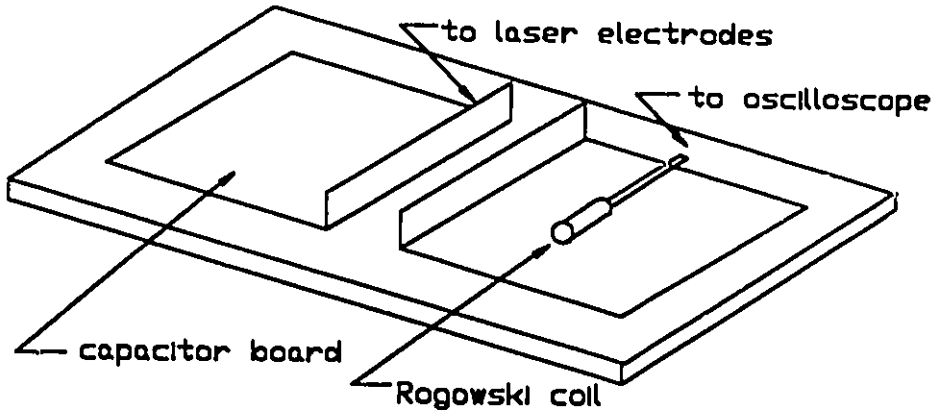

(b)

Fig. 4.9. (a) Cross-sectional view of the Rogowski-coil current probe. (b) Experimental arrangement for current measurements.

The measurement technique is based on Faraday's Induction Law. When a Rogowski coil is positioned near a time-varying current source, the resultant magnetic field induces a secondary current in the coil which is proportional to the source current. The equivalent circuit equation for the probe can be represented by

$$\frac{d\Phi}{dt} = L\frac{di_i}{dt} + i_i R \quad , \tag{4.16}$$

where i_i is the induced current in the coil, ϕ is the magnetic flux parallel to the coil axis, L is the coil inductance and R is the total resistance (including load). The Fourier-Transform solution of Eq. (4.16) is

$$I_i(\nu) = \frac{2\pi j\nu}{R+2\pi j\nu L}\Phi(\nu) \quad , \tag{4.17}$$

where $I_i(\nu)$ and $\phi(\nu)$ are the induced current and the magnetic flux, respectively, in the frequency domain. The relationship between the magnetic flux at the coil and the source current is

$$\phi(t) = M\, i_s(t) \quad , \tag{4.18}$$

where M is the mutual inductance between the source circuit and the Rogowski coil. In the frequency domain, Eq. (4.18) can be written

$$\Phi(\nu) = M\, I_s(\nu) \quad . \tag{4.19}$$

Substitution of Eq. (4.19) into Eq. (4.17) results in

$$I_i(\nu) = \frac{2\pi j\nu M}{R+2\pi j\nu L} I_s(\nu) \quad . \tag{4.20}$$

Therefore, the source current in the time domain is given by

$$i_s(t) = F^{-1}I_s(\nu) = F^{-1}\left[\frac{R+2\pi j\nu L}{2\pi j\nu M}I_i(\nu)\right] \quad . \tag{4.21}$$

Both R and L are relatively easy to determine from measurements of square-wave current sources. It can be seen from Eq. (4.21) that the time constant L/R can be an important factor. A reasonably large L/R is required if relatively-low-frequency components are present in the waveforms (i.e., L/R affects the low-frequency response).

In principle, the probe can be calibrated from the parameters of the system. The mutual inductance between the Rogowski coil and the Blumlein circuit board can be calculated with a reasonable degree of accuracy. However, it is much easier to calibrate the probe using a known current waveform, as described in Section 4.3.2.

4.3.2. Current-Waveform Measurements.

The basic experimental arrangement for the measurement of current waveforms in the spark-gap and laser-discharge circuits is shown in Fig. 4.9(b). For clarity, the insulating tube surrounding the probe and cable are not shown. The Rogowski coil assembly is placed directly on top of the circuit-board capacitor. The response time of the instrumentation is determined primarily by the oscilloscope. The induced current in the Rogowski coil can be calculated from the voltage observed with the oscilloscope, divided by the oscilloscope input impedance (R=50 Ω). The self-inductance L of the Rogowski-coil probe used for our measurements was approximately 10 μH. For the compact XeCl laser, ν in Eq. (4.21) is in the region of 100 MHz. Consequently, R in Eq. (4.21) can be taken as zero, and the equation put in the form

$$i_s = F^{-1}[\frac{L}{M} I_t(\nu)] = \frac{L}{M} i_s(t) \quad . \tag{4.22}$$

As mentioned previously, the current probe characteristics can be found by calculation of the mutual inductance M. In practice, this is a relatively difficult procedure. A more practical approach is to calibrate the probe by observation of the current in the spark-gap circuit alone (i.e., when the laser head is removed). This current is given by

$$I = I_0 \sin(2\pi t/T)\exp(-At) \quad , \tag{4.23}$$

where T is the period and A the decay constant of the observed waveform. The value of I_0 can be calculated from the energy stored in the capacitor.

Measured current waveforms for the spark-gap circuit, for different capacitor charging voltages, are given in Figs. 4.10(a) to 4.10(c). For these measurements, the current probe was located at the strip connecting the spark gap to the circuit board. The waveforms in Fig. 4.10 share a common oscillation period T=42 ns and damping factor $A=0.43 \cdot 10^9$. This damping factor is directly related to the impedance and inductance by A=R/2L. The period of oscillation in the spark-gap circuit is given by

$$T = 2\pi \sqrt{\frac{1}{LC} - (\frac{R}{2L})^2} \quad , \tag{4.24}$$

where, from Fig. 3.4, L=LSG, C=C1 and R=RSG. From Table 3.1, $C_1=1.56$ ns. Therefore, solution of Eq. (4.24), using A=R/2L (evaluated from Fig. 4.10), results in LSG=27 nH and RSG=1 Ω.

The discharge current waveforms for several capacitor charging voltages are shown in Figs. 4.11(a) to 4.11(c). All waveforms have the same period T=13.8 ns and the same damping

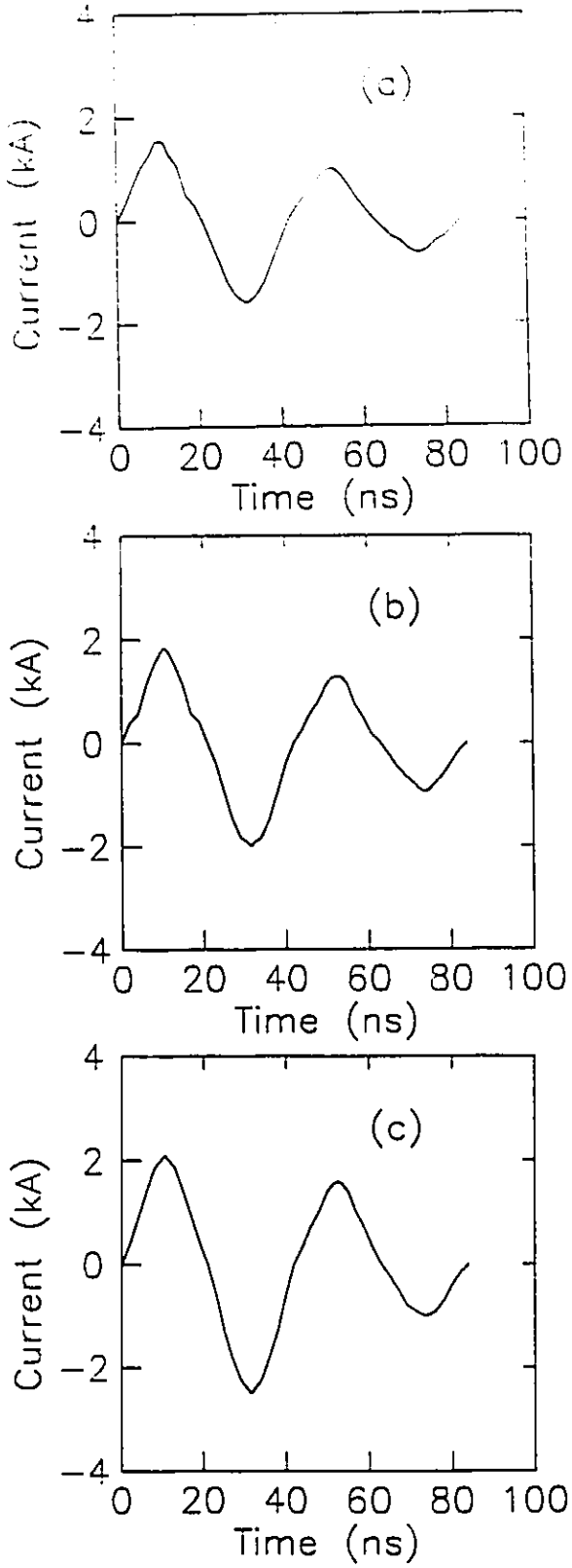

Fig. 4.10. Current waveforms for the spark-gap circuit only (laser head is removed), at applied voltages of (a) 12 kV, (b) 15 kV and (c) 18 kV.

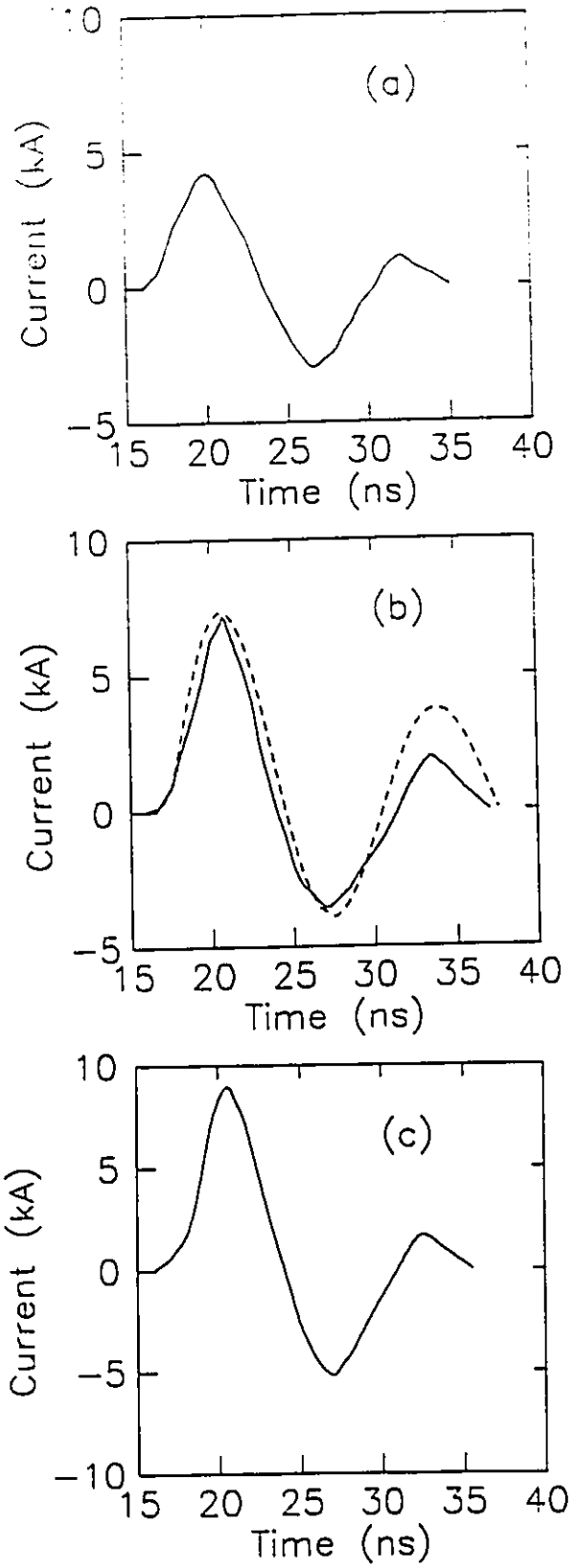

4.11. Current waveforms for the laser discharge, at applied voltages of (a) 12 kV, (b) 15 kV and (c) 18 kV.

factor $A=0.058\cdot10^{9}$. These waveforms can be represented by $I=I_0\sin(2\pi t/13.6)\exp(-0.058t)$, where t is in nanoseconds. The only major difference between the waveforms is the magnitude I_0, which is approximately proportional to the charging voltage. Using an analysis similar to that used for the spark gap circuit, the total inductance of the laser discharge circuit is LD=6.0 nH, and the total impedance is RD=0.8 Ω. A calculated current waveform is also included in Fig. 4.11(b), which is in good agreement with the measured curve.

Transmission line behavior may have a significant influence on a high frequency circuit when the sizes of circuit components are comparable to the wavelength of the electromagnetic signal. In the present system, the capacitors have length l=26.7cm, separated by a dielectric with a dielectric constant n=4.3. The discharge current has an oscillation period of 13.6 ns, with a corresponding wavelength of 95 cm. The round-trip time t_r of the electromagnetic wave in each capacitor board is 2nl/c=3.69 ns. The most simple transmission line approximation for the discharge circuit is shown in Fig. 4.12, where C11, C12, C21 and C22 each have half the value of either C1 or C2 in Fig. 3.4. The values of L1 (0.22 nH) and L2 (0.22 nH) are obtained from $T_r=(1/L1\cdot C1)^{1/2}$ and $T_r=(1/L2\cdot C2)^{1/2}$, respectively. Discharge current and voltage waveforms, calculated using lumped circuits and the transmission line approximation, are compared in Fig. 4.13. Both calculations give essentially similar results. Consequently, it is not necessary to consider the transmission line characteristics of the circuit-board capacitor employed in the present system. Similar results are obtained if several π-sections are used to represent each transmission line.

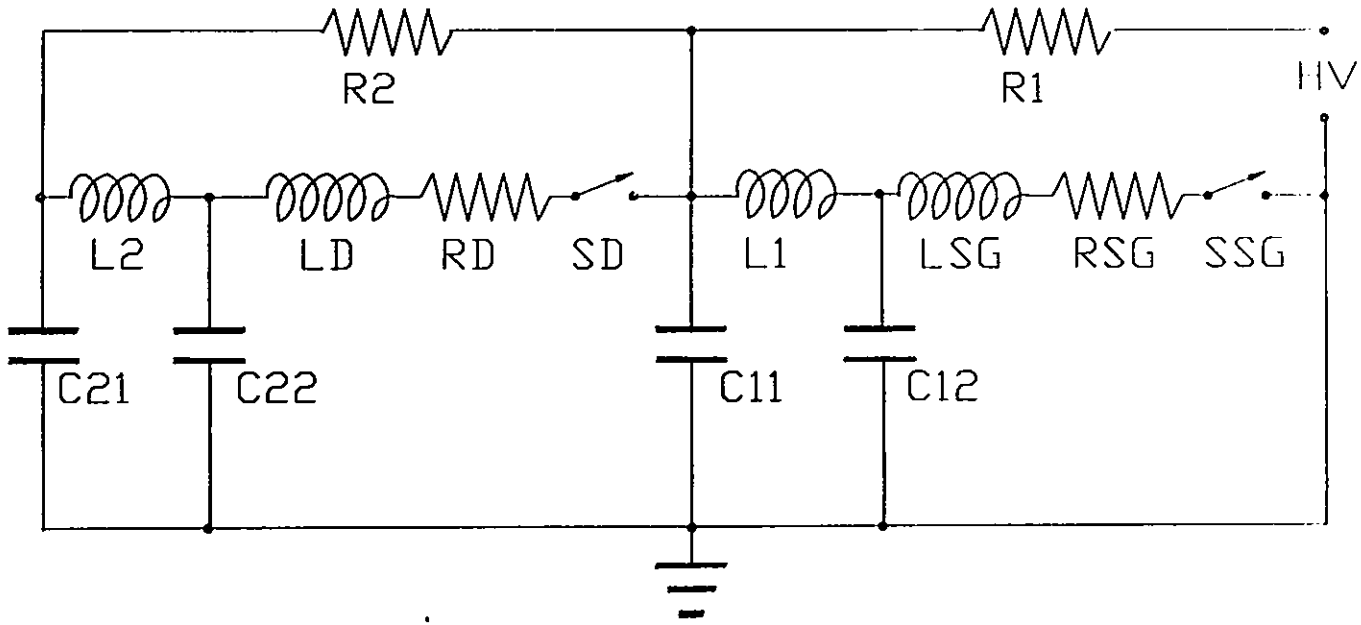

4.12. The equivalent circuit for the discharge circuit when the capacitors are replaced by simple transmission lines.

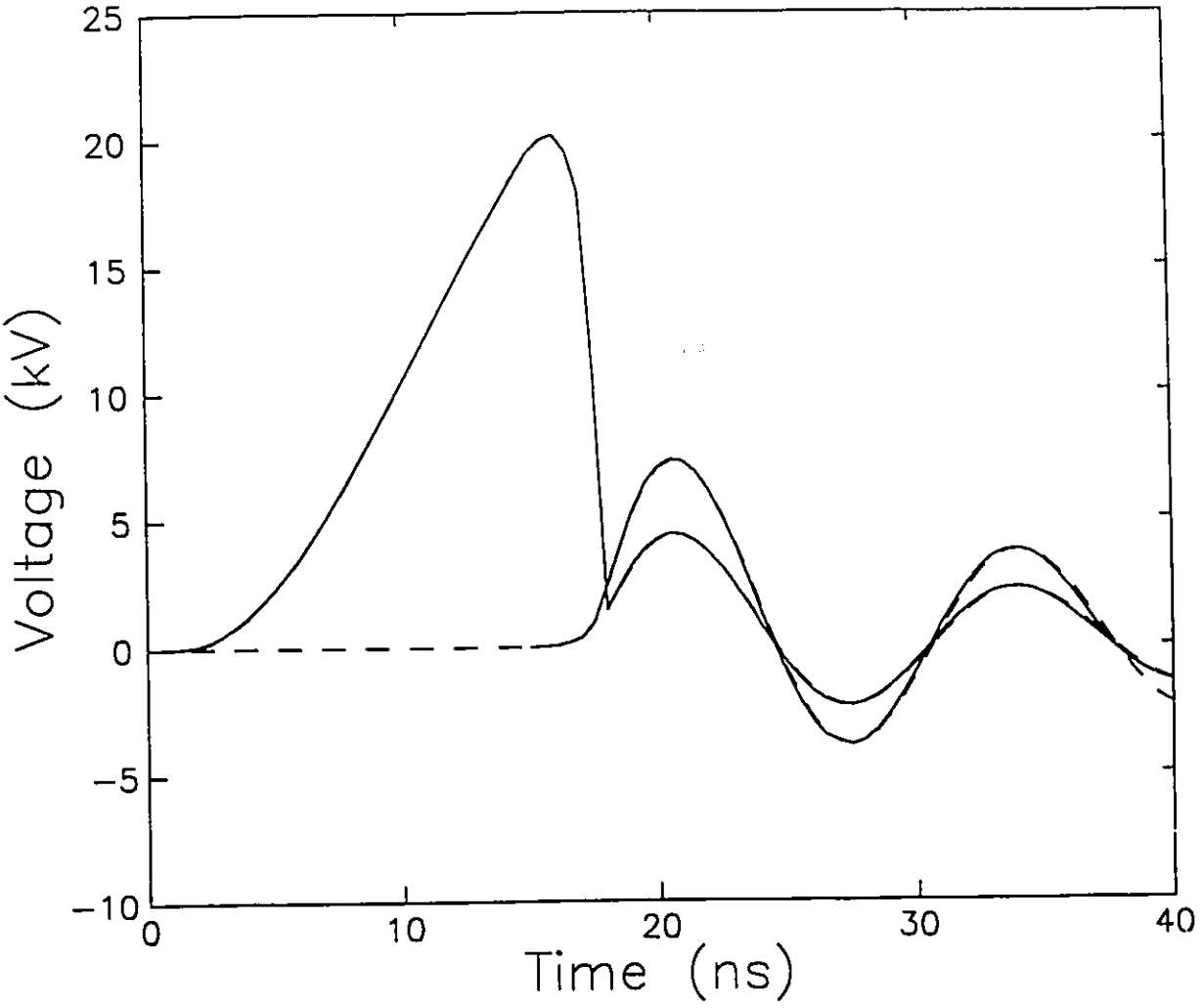

4.13. Comparison of discharge voltage and current waveforms when considered as a transmission line (dashed curves) and when considered as a lumped circuit (solid curves). Clearly, the dashed and solid curves co-incide.

Chapter 5

Electron Impact Collisions in Discharges

Electron impact collisions are one of the most important kinetic processes in a discharge. The rates of these collisions are determined mainly by the collision cross-sections and the electron energy distribution function.

Free electrons present in a discharge obtain their kinetic energy from the electric field applied between the electrodes. This kinetic energy is transferred to the various species present in the gas via elastic, inelastic, superelastic and dissociative-attachment collisions between the electrons and the species, as well as by electron-electron coulomb collisions. The electron energy distribution, which characterizes a statistical behavior of the electrons, is determined by the applied electric field and by all of the collision processes.

The electron impact collisions employed in our calculations of kinetic processes are listed in Table 5.1. The classical and quantum theories of elastic collisions are discussed in Section 5.1. Section 5.2 introduces inelastic, superelastic, and dissociative-attachment collisions. The Boltzmann equation for the electron energy distribution is presented in Section 5.3. In Section 5.4, the parameters which describe the properties of the discharge are calculated.

5.1. Elastic Collisions.

In an elastic collision, the total kinetic energy of the system of colliding particles is the same before and after the collision, and there are no permanent changes in the internal excitation

Table 5.1. Electron Impact Collisions in Xe/HCl/He(Ne).

No.	Collisions	Reference
1.	$e + Xe \longrightarrow Xe + e$	Hayashi (1983)
2.	$e + He \longrightarrow He + e$	Nesbet (1979), Crompton et al (1967)
3.	$e + Ne \longrightarrow Ne + e$	O'Malley and Crompton (1980), Fon and Berrington (1981)
4.	$e + HCl(v=0) \longrightarrow HCl(v=0) + e$	Padial et al (1983), Lee (1983)
5.	$e + Xe \longrightarrow Xe^* + e$	Schaper and Scheibner (1969), de Heer et al (1979)
6.	$e + He \longrightarrow He^* + e$	Schaper and Scheibner (1969), Borst (1974)
7.	$e + Ne \longrightarrow Ne^* + e$	Schaper and Scheibner (1969),
8.	$e + HCl(v=0) \longrightarrow HCl(v=1) + e$	Rohr and Linder (1976)
9.	$e + HCl(v=0) \longrightarrow HCl(v=2) + e$	Rohr and Linder (1976)
10.	$e + Xe \longrightarrow Xe^+ + e$	Rapp and Englander-Golden (1965)
11.	$e + Xe^* \longrightarrow Xe^+ + e$	Ton-That and Flannery (1977)
12.	$e + He \longrightarrow He^+ + e$	Rapp and Englander-Golden (1965)
13.	$e + He^* \longrightarrow He^+ + e$	Vriens (1964)
14.	$e + Ne \longrightarrow Ne^+ + e$	Rapp and Englander-Golden (1965)
15.	$e + Ne^* \longrightarrow Ne^+ + e$	Ton-That and Flannery (1977)
16.	$e + Xe^* \longrightarrow Xe + e$	
17.	$e + He^* \longrightarrow He + e$	
18.	$e + He^* \longrightarrow He + e$	
19.	$e + HCl(v=0) \longrightarrow H + Cl^-$	Orient and Srivastava (1985)
20.	$e + HCl(v=1) \longrightarrow H + Cl^-$	Domcke and Mündel (1985)

energies of the collision partners. Both linear and angular momentum are conserved at all the times throughout the collision. The differential elastic-scattering cross-section $\sigma_s(\theta,\phi)$ of a target particle is defined as the number of particles (N_s) scattered into a unit solid angle, divided by the number of incident particles (N_i) crossing a unit area per unit time, i.e.,

$$\sigma_s(\theta,\phi) = \frac{N_s(\theta,\phi)}{N_i} \quad . \tag{5.1}$$

The total elastic-scattering cross-section σ_s is given by the integral of the differential cross-section over all angles, i.e.,

$$\sigma_s = \int_0^{2\pi}\int_0^{\pi} \sigma_s(\theta,\phi)\sin\theta \; d\theta d\phi \quad . \tag{5.2}$$

Determining differential cross-sections is the basic problem in the study of collision processes. Both theoretical calculations and experimental measurements play important roles in the evaluation of the cross-sections.

5.1.1. Classical Theory and Momentum-Transfer Cross-Sections.

Consider two particles of masses m and M interacting with each other via a central potential V(r). To simplify calculations, the analysis is carried out in the center-of-mass (CM) coordinate system. The relationship between the scattering angles in the laboratory and CM systems is shown in Fig. 5.1, where θ_{lab} and Θ_{CM} are defined as the scattering angles of the mass m in the laboratory and CM systems, respectively. The scattering distribution is independent of the azimuth angle in a central potential interaction. Therefore, $\phi_{lab}=\phi_{CM}=\phi$, and

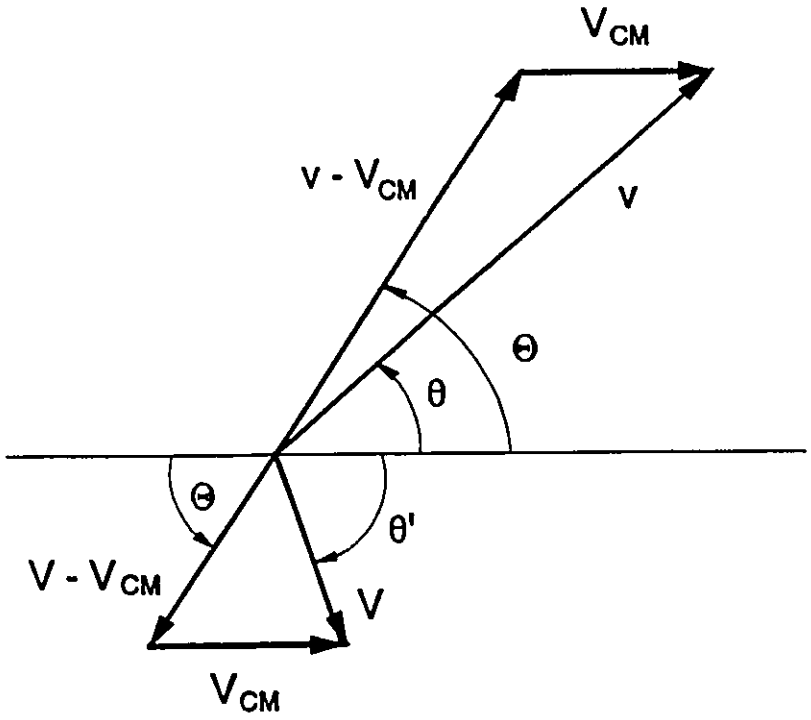

Fig. 5.1. Relationship between the scattering angles in the laboratory (θ) and CM (Θ) systems.

$$\sigma_s(\theta,\phi)d\Omega_{lab} = \sigma_s(\Theta,\phi)d\Omega_{CM} \quad . \tag{5.3}$$

The relationship between the cross-sections in the laboratory and CM systems is (McDaniel, 1964)

$$\sigma_s(\theta,\phi) = \frac{[(m/M)^2 + 2(m/M)\cos\Theta + 1]^{3/2}}{1 + (m/M)\cos\Theta}\sigma_s(\Theta,\phi) \quad . \tag{5.4}$$

Figure 5.2 shows the collision in the plane perpendicular to the direction of angular momentum. Masses m and M approach each other with an initial velocity v_0. Other important parameters are the impact parameter (b), the distance between m and M ($r=r_m+r_M$), the orientation angle of $\overline{r}$ (φ), and the value of φ at the smallest value of r (Φ at r_s). The conservation of energy and angular momentum for the collision system are expressed by

$$\frac{1}{2}M_r v_0^2 = \frac{1}{2}M_r(\dot{r}^2 + r^2\dot{\varphi}^2) + V(r) \tag{5.5}$$

and

$$M_r b v_0 = M_r r^2\dot{\varphi} \quad , \tag{5.6}$$

where $M_r=mM/(m+M)$ is the reduced mass of the system. From Eqs. (5.5) and (5.6),

$$\frac{dr}{d\varphi} = \frac{dr}{dt}/\frac{d\varphi}{dt} = \pm\frac{r^2}{b}[1 - \frac{V(r)}{M_r v_0^2/2} - \frac{b^2}{r^2}]^{1/2} \quad . \tag{5.7}$$

The negative and positive signs are for the incoming and outgoing branches of the trajectory, respectively. The angle Φ is given by

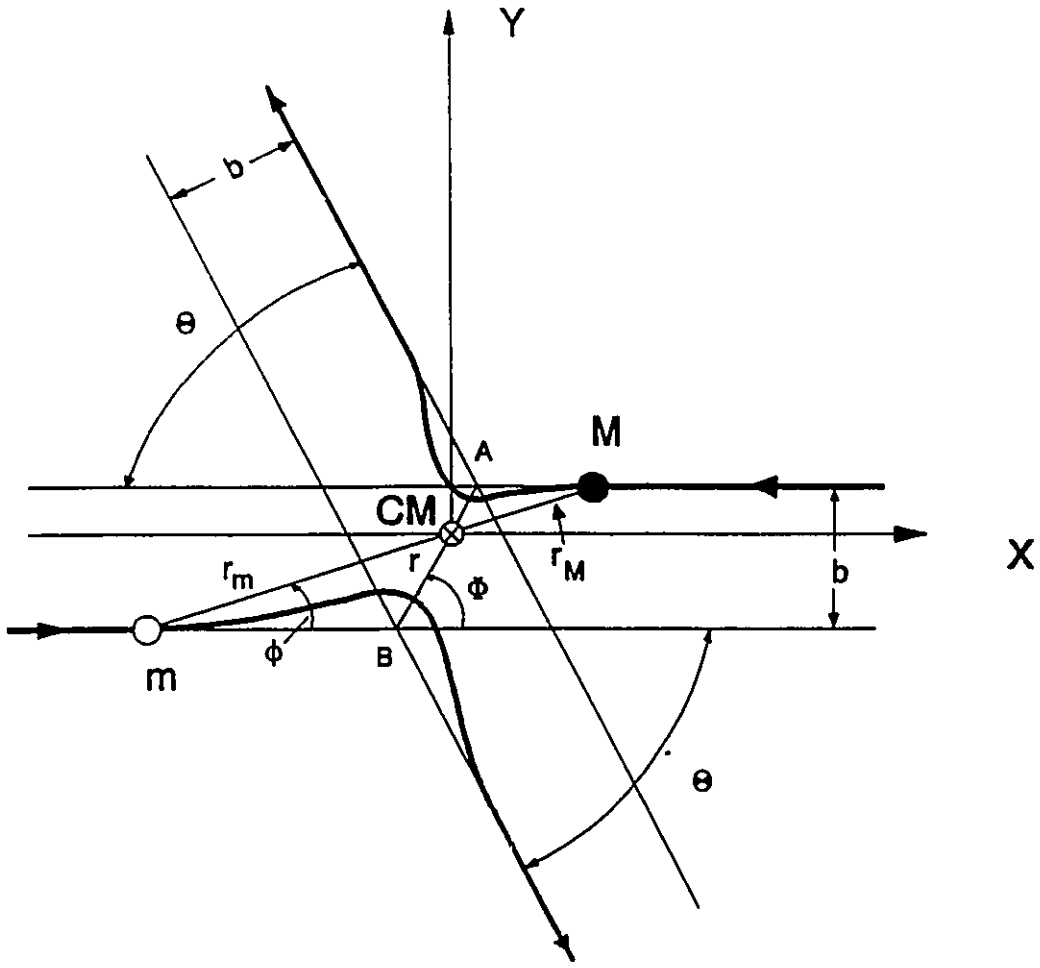

Fig. 5.2. A schematic of the collision between m and M, where b is the impact parameter, r is the distance between m and M ($r=r_m+r_M$), φ is the angle of orientation of r, and Φ is the value of φ at the smallest value of r (r_s). Note that r_s is located along AB in the figure.

$$\Phi = -\int_{\infty}^{r_a} \frac{d\varphi}{dr} dr = -\int_{\infty}^{r_a} [\frac{r^4}{b^2}(1 - \frac{V(r)}{M_r v_0^2/2}) - r^2]^{-1/2} dr \quad . \tag{5.8}$$

It can be shown that the trajectories for both m and M are symmetrical about r_a, at an angle Φ (McDaniel, 1964). Therefore, $\Theta = \pi - 2\Phi$ and

$$\Theta = \pi - 2b\int_{\infty}^{r_a} [r^4(1 - \frac{V(r)}{M_r v_0^2/2}) - b^2 r^2]^{-1/2} dr \quad . \tag{5.9}$$

Consider that a particle of initial velocity v_0 is scattered into a solid angle element $d\Omega_{CM} = 2\pi \sin\Theta \, d\Theta$. The necessary and sufficient condition for this to occur is that the particle is incident through an annular ring with inner radius b and outer radius b+db, i.e.,

$$|2\pi b \, db| = |\sigma_s(\Theta) \, 2\pi \, \sin\Theta \, d\Theta| \quad . \tag{5.10}$$

Equation (5.10), which is the differential cross-section, can be calculated using the expression for Θ in Eq. (5.9).

In the study of discharge kinetics, the momentum-transfer cross-sections are more important than elastic-collision cross-sections. The cross-sections for momentum transfer and kinetic-energy transfer must be weighed according to the corresponding momentum or kinetic-energy loss in each collision. For electron collisions with heavy species, the electron mass (m) is much less than the mass of the collision partner (M). Using the momentum and energy conservation equations for the system, it can be shown that the fractional momentum loss for the electron is

$$\delta_m \approx (1 - \cos\Theta) \tag{5.11}$$

and that the fractional kinetic energy loss is

$$\delta_c = \frac{2m}{M}(1 - \cos\Theta) \quad . \tag{5.12}$$

From Eqs. (5.3) and (5.11), the total cross-section for momentum transfer is

$$\sigma_m = \int(1 - \cos\Theta)\ \sigma_s(\Theta,\phi)d\Omega_{CM} \quad . \tag{5.13}$$

Equation (5.13) is a measure of the average momentum or kinetic-energy loss ($\delta_m \propto \delta_c$) for particles of mass m in collision with particles of mass M. The largest contribution to the cross-section is at large scattering angles.

5.1.2. Quantum Theory.

In classical collision theory, the orbits of the colliding partners are well-defined. According to the Heisenberg uncertainty principle, this theory is only a good approximation for the limiting cases of heavy particles or at high temperatures, where the uncertainty of particle location is relatively small. Furthermore, the classical theory doesn't explain the symmetrical exchange effect for identical particles. In quantum theory, the de Broglie wave function $\Psi(\overline{r},t)$ is introduced. Physically, $|\Psi(\overline{r},t)|^2 d^3\overline{r}$ is the probability that, at time t, the particle described by the wave-packet state $\Psi(\overline{r},t)$ is located inside the volume $d^3\overline{r}$ at position $\overline{r}$.

Consider elastic collisions in a long-range central potential, and in CM coordinates as in Fig. 5.2. The time-independent Schrodinger equation is

$$(\frac{\hbar^2}{2M_r}\nabla^2 + E_k)\Psi_{\bar{k}}(\bar{r}) = V(\bar{r})\Psi_{\bar{k}}(\bar{r}) \quad , \tag{5.14}$$

where $E_k = \hbar^2k^2/2M_r$, k is wave number, and

$$\nabla^2 = \frac{1}{r^2}\frac{\partial}{\partial r}(r^2\frac{\partial}{\partial r}) + \frac{1}{r^2\sin\Theta}\frac{\partial}{\partial\Theta}(\sin\Theta\frac{\partial}{\partial\Theta}) + \frac{1}{r^2\sin^2\Theta}\frac{\partial^2}{\partial\phi^2} \quad . \tag{5.15}$$

Note that only eigenstates in the form of an incident plane wave plus scattered wave, and with eigen energy $E_k > 0$, are needed for the solution of scattering problems. The asymptotic solution of Eq. (5.14), employing Green's function, is

$$\Psi = \Psi_{inc} + \Psi_{scatt} = e^{ikz} + \frac{e^{ikr}}{r}f(\Theta) \quad , \tag{5.16}$$

where $f(\Theta)$ is called the scattered amplitude. The differential scattering cross-section is defined as the scattering flux into an area dA, divided by the incident flux and $d\Omega$. Therefore,

$$\sigma_s(\Theta) = \frac{\hbar k}{m}\frac{|f(\Theta)|^2 dA}{r^2} / \frac{\hbar k}{m} d\Omega = |f(\Theta)|^2 \quad . \tag{5.17}$$

The partial wave method and the Born approximation are two approaches for solving Eq.(5.14). In the partial wave method, the wave function $\Psi(\overline{r},t)$ is separated into the product of R(r) and $Y(\Theta)$ (ϕ is omitted because there is no dependence on the azimuthal angle in central potential scattering). The wave equation, Eq. (5.14), becomes

$$\frac{1}{r^2}\frac{d}{dr}(r^2\frac{dR}{dr}) + [k^2 - \frac{2M_r V(r)}{\hbar^2} - \frac{l(l+1)}{r^2}]R = 0 \quad , \tag{5.18}$$

and

$$\frac{1}{\sin\Theta}\frac{d}{d\Theta}(\sin\Theta\frac{dY}{d\Theta}) + l(l+1)Y = 0 \quad , \tag{5.19}$$

where l is angular-momentum quantum number. The solutions of Eq. (5.19) are the Legendre polynomials $P_l(\cos\Theta)$, and the solutions of Eq.(5.18) have the asymptotic forms

$$R_l(r) = \frac{1}{kr}\sin(kr - \frac{l\pi}{2} + \eta_l) \quad , \tag{5.20}$$

where η_l is called the lth phase shift, which depends on both the wavenumber k and the potential V(r). Therefore, $\Psi(r,\Theta)$ can be written as an expansion of the angular-momentum eigenstates $P_l(\cos\Theta)$, i.e.,

$$\Psi(r,\Theta) = \sum_{l=0}^{\infty} A_l P_l(\cos\Theta) R_l(r) \quad , \tag{5.21}$$

where A_l are arbitrary constants. By comparing the scattered and incident wave functions, the scattered amplitude $f(\Theta)$ can be obtained from (McDaniel, 1964)

$$f(\Theta) = \frac{1}{2ik}\sum_{l=0}^{\infty}(2l+1)(e^{2i\eta_l} - 1)P_l(\cos\Theta) \quad . \tag{5.22}$$

Therefore, the differential elastic cross-section is

$$\sigma_s(\Theta) = |f(\Theta)|^2 = \frac{1}{k^2}\left|\sum_{l=0}^{\infty}(2l+1)e^{i\eta_l}\sin\eta_l\ P_l(\cos\Theta)\right|^2 \quad , \tag{5.23}$$

and the total elastic cross-section is

$$\sigma_s = \frac{4\pi}{k^2}\sum_{l=0}^{\infty}(2l+1)\sin^2\eta_l \quad . \tag{5.24}$$

Note that the partial wave method has an advantage only for small-energy scattering, where only a few η_l with low l make a significant contribution to the scattering cross-section σ_s. Otherwise, it would be a formidable task to calculate σ_s.

In contrast to the partial wave method, the Born approximation applies to the high energy case ($E_k >> V(r)$), where the effect of the scattering potential is small on partial waves of higher

quantum number l. Following Baym's approach (Baym, 1973), the expression for the first-order Born approximation for η_l is given by

$$\eta_l \approx - \frac{2mk}{\hbar^2}\int_0^\infty r^2 dr V(r)\,|j_l(kr)|^2 \quad , \tag{5.25}$$

where $j_l(kr)$ is the lth spherical Bessel function. If the scattering potential has a small effect on all partial waves, then the Born approximation for $f(\Theta)$ is

$$f(\Theta) = - \frac{m}{2\pi\hbar^2}\int d^3r' \; e^{i(\bar{k}-\bar{K}')\cdot\bar{r}'} V(\bar{r}') \quad . \tag{5.26}$$

The cross-section can be evaluated from Eqs. (5.26) and (5.17) provided that the interaction potential is known.

5.1.3. Cross-Sections Used in the Calculations.

Both experimental measurements and theoretical calculations are employed to study the momentum-transfer and elastic-scattering cross-sections. In general, the experimental methods include direct single-beam measurements (which are efficient for electron energies lower than the first excited level of the target gas molecule), diffusion methods (applicable at extremely low energies), microwave methods (cover the energy range from thermal to several eV), and crossed-beam methods (suitable for chemically unstable systems). Elastic-scattering cross-sections are relatively easier to measure for rare gases because these gases are chemically stable.

The momentum-transfer cross-sections used in our calculation are recently published data. The data for He are shown in Fig. 5.3(a). The data for the energy range from 0.1 to 12 eV are taken from Nesbet (1979). These are based on variational calculations for s- and p-wave shifts, and the partial-wave Born approximation for phase shifts $l > 1$. The Nesbet data are in good

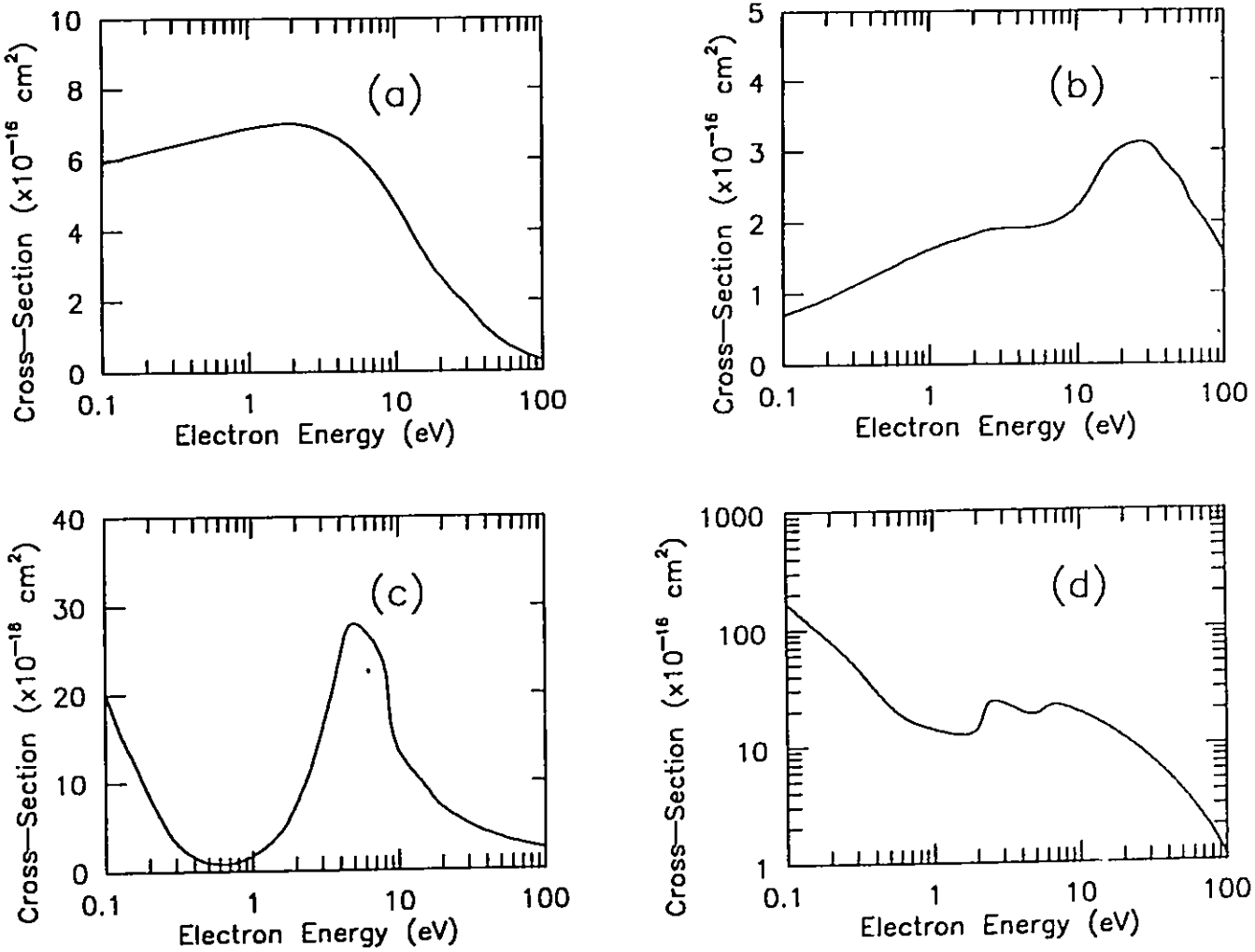

Fig. 5.3. Momentum-transfer cross-sections as a function of electron kinetic energy ε for (a) He, (b) Ne, (c) Xe and (d) HCl.

agreement (better than 1.5%) with those obtained by Crompton et al (1967) and by Milloy and Crompton (1977) from electron-swarm measurements. In addition, the difference between the Nesbet data and the data from the crossed-beam measurements of Andrich and Bitsch (1975) is $<4\%$. For the energy range from 12 to 100 eV, the data are taken from the R-matrix calculations of Fon et al (1981), which are in excellent agreement (better than 1%) with the data from Nesbet (1979) in the region where the calculations overlap (5 to 12 eV).

For energies below 2.17 eV, the cross-section data for Ne in Fig. 5.3(b) were obtained by O'Malley and Crompton (1980) from an analysis of the drift-velocity data taken from Robertson's measurements (1972). The data for the higher energy range (5 to 100 eV) were obtained by Fon and Berrington (1981) using R-matrix calculations. The reliability of these calculations is confirmed by the good agreement of the calculated total elastic cross-sections with previously measured data.

The Xe data used in Fig. 5.3(c) are from Hayashi's (1983) recommended data for the energy range $0 \text{ eV} < \varepsilon < 10^4 \text{ eV}$. These are based on the analysis of the experimental and theoretical data of Ramsauer and Kollath (1932), Frost and Phelps (1964), Braglia et al (1965), Schackert (1968), Williams and Crowe (1975), Riley et al (1975), Heindorff et al (1976), and Klewer et al (1980). The dip in the curve appearing at lower energies is due to the Ramsauer-Townsend effect for heavy rare-gas atoms.

It is difficult to measure the momentum-transfer cross-sections for HCl because of the large cross-sections for vibrational excitation and dissociative attachment at low energies. Theoretical values of the momentum-transfer cross-sections ($0 \text{ eV} < \varepsilon < 11 \text{ eV}$) for this polar molecule were determined by Padial et al (1983) using close-coupling calculations. The cross-sectional data for HCl are shown in Fig. 5.3(d). The data from Lee (1983) are used at energies >11 eV.

5.1.4. Electron-Electron Coulomb Collisions.

For scattering of identical particles, the wavefunction must be either symmetric or antisymmetric (with respect to the interchange of the particles), depending on whether the spin quantum number is integer or half-integer, respectively. The differential cross-sections for a system with even spin is (Landau and Lifshitz, 1977)

$$\sigma_{s\text{-}sym}(\Theta) = |f(\Theta) + f(\pi - \Theta)|^2 \quad , \tag{5.27}$$

and for odd spin is

$$\sigma_{s\text{-}anti}(\Theta) = |f(\Theta) - f(\pi - \Theta)|^2 \quad . \tag{5.28}$$

For each system, all of the spin states have equal probability. Therefore, the differential cross-section for each system must be the sum of the appropriately weighted symmetric and antisymmetric cross-sections. The differential cross section for half-integer s is

$$\sigma_s = \frac{s}{2s+1}\sigma_{s\text{-}sym} + \frac{s+1}{2s+1}\sigma_{s\text{-}anti} \quad , \tag{5.29}$$

where s is the spin number for a single particle. Similarly, the expression for integral s is

$$\sigma_s = \frac{s}{2s+1}\sigma_{s\text{-}anti} + \frac{s+1}{2s+1}\sigma_{s\text{-}sym} \quad . \tag{5.30}$$

Because electrons are particles with half integer s, the cross-sections are calculated using Eq. (5.29). Similar to the approach used for Eq. (5.23), the scattering cross-sections can be calculated by the phase shifts of partial waves, yielding

$$\sigma_{s\text{-}sym} = \frac{1}{2k^2}\left|\sum_{even\ l}(2l+1)(e^{2i\eta_l}-1)P_l(\cos\Theta)\right|^2 \tag{5.31}$$

and

$$\sigma_{s-anti} = \frac{1}{2k^2}\left|\sum_{odd\ l}(2l+1)(e^{2i\eta_l}-1)P_l(\cos\Theta)\right|^2 \quad . \tag{5.32}$$

The cross-sections for electron-electron Coulomb collisions can be calculated from (Rosenbluth et al 1957)

$$\sigma_{ee} = \frac{e^4}{4\pi\epsilon_0^2\varepsilon^2}\ln\left[\frac{4\pi\epsilon_0\varepsilon}{e^2}\left(\frac{2\epsilon_0\bar{\varepsilon}}{3ne^2}\right)^{1/2}\right] \quad . \tag{5.33}$$

where ϵ_0 is the vacuum permittivity, $\bar{\varepsilon}$ is average electron energy, and ε is electron energy in Joules. The calculated cross-sections, as a function of electron kinetic energy (ε in eV), are given in Fig. 5.4.

5.2. Electron-Impact Inelastic Collisions in a Discharge.

In contrast to elastic processes, the total kinetic energy of colliding particles changes after an inelastic collision. There is a permanent change in the internal energy of the collision partners. The important electron-impact inelastic collisions in our discharge plasma include excitations of atoms (Xe, He and Ne) to metastable electronic states, vibrational excitation of HCl molecules, ionization of atoms from the ground states (Xe, He and Ne) and from the metastable states (Xe^*, He^* and Ne^*), and electron attachment to the molecules HCl and HCl(v). The energy thresholds for all of these processes are given in Table 5.2. The cross-sections for these collisions, determined by experimental measurements or theoretical calculations, are discussed below.

Ionization produces charged residual heavy ions, and these ions can be easily detected by electric current measurements. This is used as a general method for the determination of

Table 5.2. Threshold Energies for Inelastic Collisions.

Scatterer	Product	Threshold (eV)
Xe	Xe^*	8.32
He	He^*	18.99
Ne	Ne^*	16.30
Xe	Xe^+	12.13
Xe^*	Xe^+	4.00
He	He^+	24.59
He^*	He^+	5.48
Ne	Ne^+	21.50
Ne^*	Ne^+	4.95
HCl(v=0)	HCl(v=1)	0.33
HCl(v=0)	HCl(v=2)	0.70
HCl(v=0)	Cl^-	0.24
HCl(v=1)	Cl^-	0.45

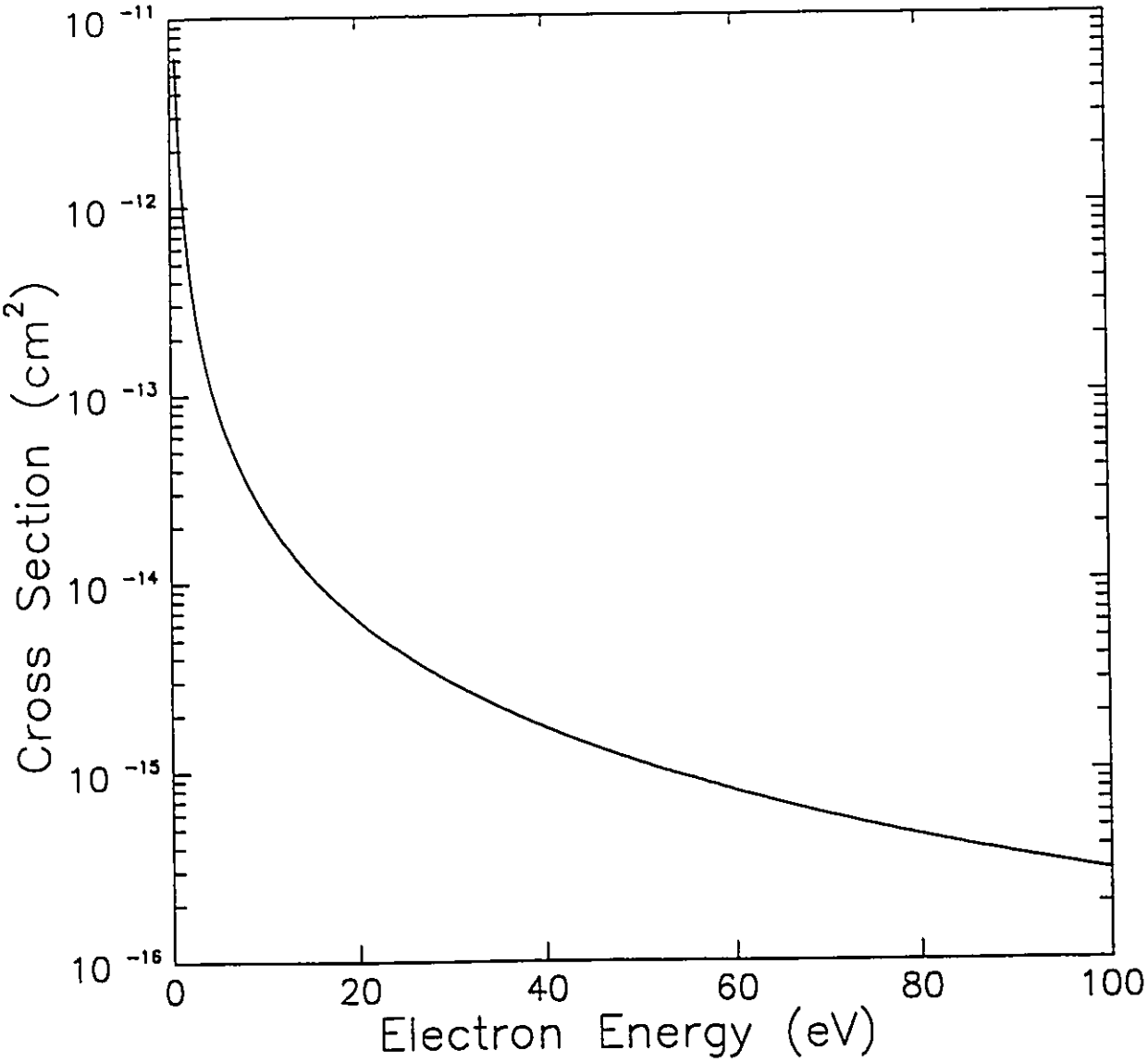

Fig. 5.4. Cross-sections for electron-electron Coulomb collisions as a function of the electron energy (ε). For this data, the electron density is 10^{16} cm^{-3} and the average electron energy is 4 eV.

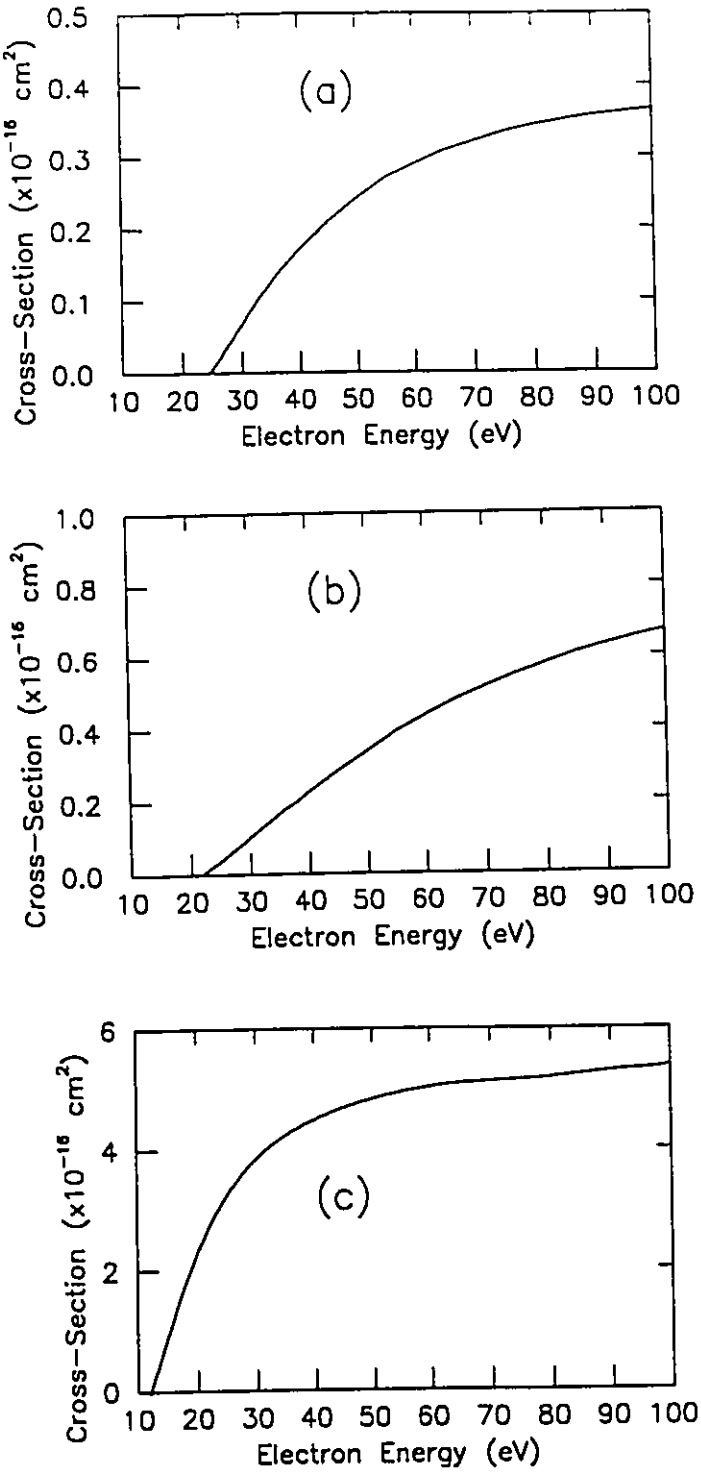

Fig. 5.5. Ionization cross-sections for (a) He, (b) Ne and (c) Xe, as a function of the electron kinetic energy (ε).

ionization cross-sections. Rapp and Englander-Golden (1965) give reliable experimental results for the total ionization cross-sections of He, Ne, Xe, and other rare gas atoms, at electron energies ranging from their ionization thresholds to 1 keV. Results for electron energies < 100 eV are given in Fig. 5.5. The data for He are in excellent agreement with the early measurements of Smith (1930) employing electrons with energies < 80 eV. The validity of the data for Ne is confirmed by the results of de Heer et al (1979). There is also good agreement (better than 1%) between the Xe data of Rapp and Englander-Golden and those of Schram et al (1965).

Measurements of excitation cross-sections are more difficult than those for ionization because excitation is not directly related to electric current flow. The conventional, but difficult method for determining excitation cross-sections is based on measuring the spectral profile of the emission from the excited states. Data for the excitation cross-sections are shown in Fig. 5.6. The excitation of He, Ne and Xe to their corresponding metastable states $He^*(2^3S, 2^1S$ and $2^3P)$, $Ne^*(3^3S, 3^1S$ and $3^3P)$ and $Xe^*(6^3S, 6^1S$ and $6^3P)$ were measured by Schaper and Scheibner (1969) at the lower electron-energy regions. Higher energy (>25 eV) data for He are taken from the measurements of Borst (1974), which are consistent with the measurements of Schaper and Scheibner in the overlapping energy range (19.8 to 25 eV). For Ne at energies greater than 22 eV, the data from de Heer et al (1979) are used. The semi-empirical of de Heer et al (1979) is also used for Xe at energies >30 eV. A linear approximation is used between these two groups of data because data for energies in the range from 22 to 30 eV are not available.

The cross-sections for ionization from the metastable states of He^*, Ne^* and Xe^* are shown in Fig. 5.7. The data for He^* are those calculated by Vriens (1964). The data for Ne^* and Xe^* are taken from the results of Ton-That and Flannery (1977), which were calculated using the

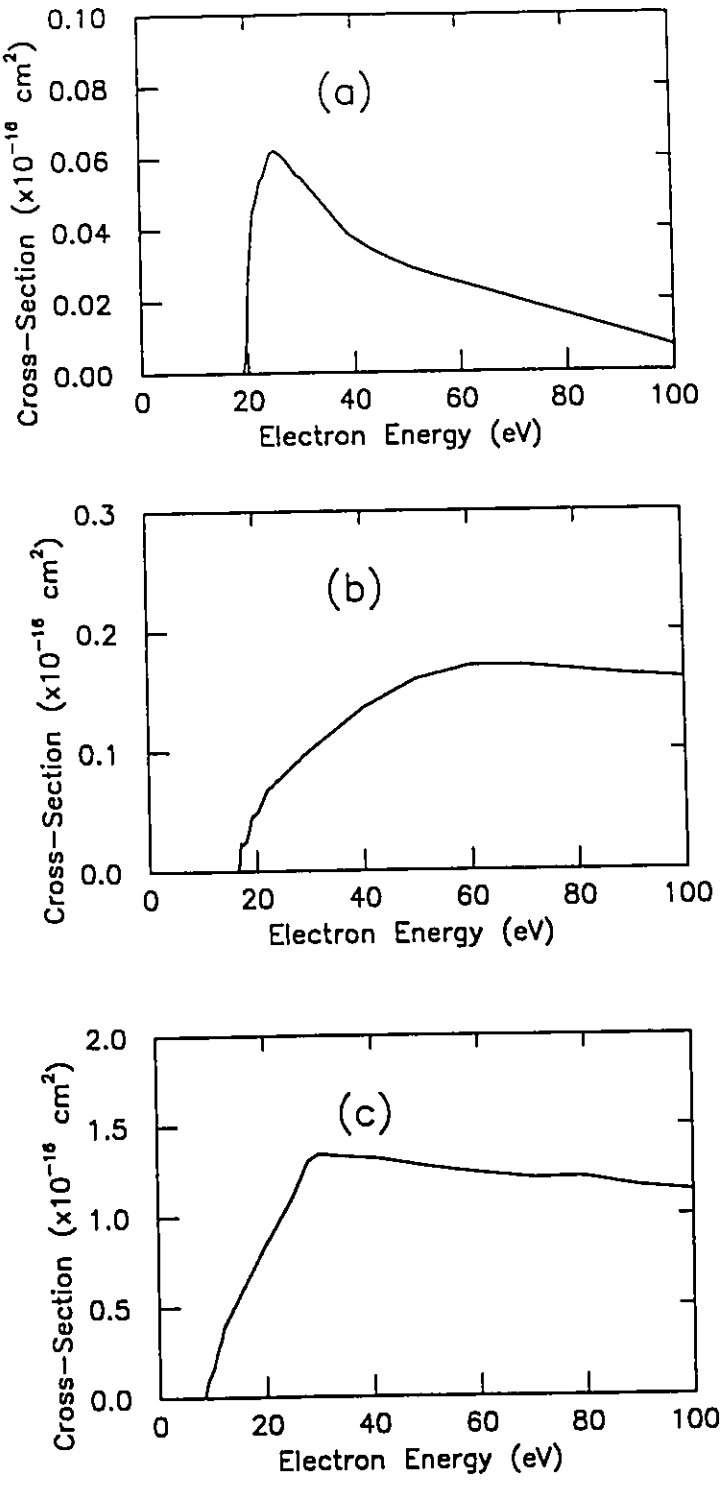

Fig. 5.6. Cross-sections for the excitation of (a) He, (b) Ne and (c) Xe to their metastable states, as a function of the electron kinetic energy (ε).

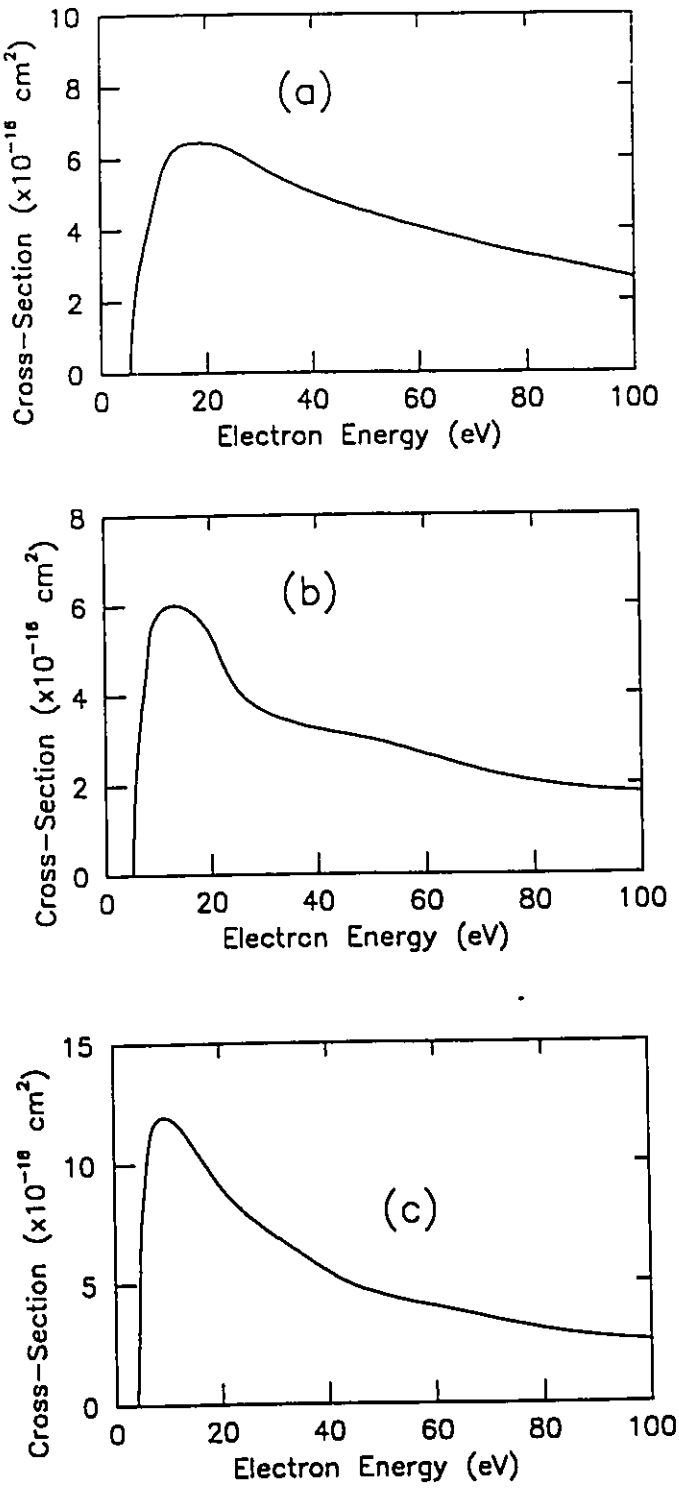

Fig. 5.7. Ionization cross-sections for metastable (a) He^*, (b) Ne^* and (c) Xe^*, as a function of the electron kinetic energy (ε).

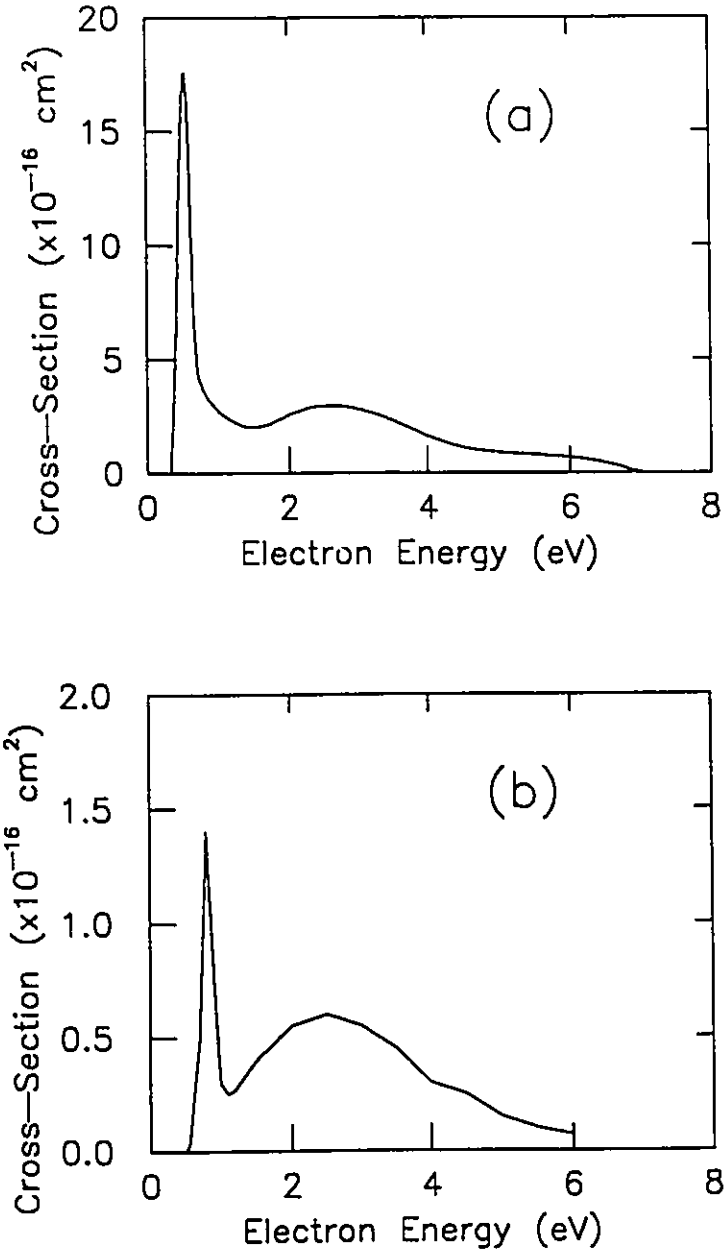

Fig. 5.8. Cross-sections for the vibrational excitation of HCl(v=0) to (a) HCl(v=1) and (b) HCl(v=2).

Born half-range theory. All of these data are in excellent agreement (better than 5%) with the calculations of Hyman (1979).

Vibrational excitation of HCl(v=0) to HCl(v=1,2) and the electron dissociative attachment of these molecules are low-energy scattering processes. The cross-sections for excitation from v=0 to v=1,2, shown in Fig. 5.8, are based on the experimental data of Rohr and Linder (1976). The reliability of these data is confirmed by the calculations of Domcke and Mündel (1985). Figure 5.9 shows the cross-sections for electron dissociative attachment. These data, also from Domcke and Mündel (1985), are in good agreement with the measurements of Orient and Srivastava (1985), and with those of Abouaf and Teillet-Billy (1977).

5.3. The Boltzmann Equation and the Electron Energy Distribution.

The energy distribution of electrons plays an important role in determining the properties of a gas or plasma. For a system in thermodynamic equilibrium (no externally-applied electric field and only elastic collisions), the free-electron energy distribution function is a Maxwellian distribution. In a discharge plasma, where an applied electric field always exists, free electrons encounter both elastic and inelastic collisions with the various chemical species present in the plasma. Consequently, the electron energy distribution is no longer Maxwellian.

The Boltzmann equation is a continuity equation in six-dimensional position and velocity $(\overline{r},\overline{v})$ phase space. This equation describes the change of the distribution function $f(\overline{r},\overline{v},t)$ under the influences of applied fields, diffusion and various collisions. In general, the Boltzmann equation is expressed as

$$\frac{\partial f}{\partial t} + \bar{v} \cdot \nabla_r f + \frac{\bar{F}}{m} \cdot \nabla_v f = \left(\frac{\delta f}{\delta t}\right)_c \quad , \tag{5.34}$$

where $(\delta f/\delta t)_c$ gives the rate of change of the electron energy distribution function caused by collisions with various species in the discharge plasma. For electrons in an electric discharge, the applied force $\overline{F}$ is $-e\overline{E}$.

A spatially-homogeneous model is used for the analyses of our laser discharge plasma. This is a reasonable assumption for our laser because the discharge is observed to have good uniformity in all of the active region. Spatial homogeneity implies that the electric field E, the current density J, and the densities of all the species are coordinate independent. Therefore, the term with the spatial gradient in the Boltzmann equation vanishes, and the equation becomes

$$\frac{\partial f}{\partial t} - \frac{e\overline{E}}{m} \cdot \nabla_v f = \left(\frac{\delta f}{\delta t}\right)_c \quad . \tag{5.35}$$

Elastic collisions are the dominant collision processes in our laser discharge. Furthermore, the average velocity gained by the electrons between collisions (due to the external field) is much less than the average thermal velocity. Therefore, the distribution function can be expressed as isotropic term f_0 plus a small anisotropic perturbation f_1 in a first-order Legendre polynomial, i.e.,

$$f(\bar{v},t) = f_0(v,t) + \cos\theta_1 f_1(v,t) \quad , \tag{5.36}$$

where θ_1 is the angle between $\overline{v}$ and $\overline{E}$. Following the procedure of Cherrington (1979), Eq. (5.36) is substituted into Eq. (5.35). Applying the orthogonality properties of the Legendre polynomials results in the two coupled equations

$$\frac{\partial f_0}{\partial t} - \frac{eE}{3m}\left(\frac{\partial f_1}{\partial v}\right) - \frac{eEf_1}{3mv} = \frac{1}{4\pi}\int \left(\frac{\delta f}{\delta t}\right)_c d\Omega \tag{5.37}$$

and

$$\frac{\partial f_1}{\partial t} - \frac{eE}{m}\left(\frac{\partial f_0}{\partial v}\right) = \frac{3}{4\pi}\int \cos\theta_1 \left(\frac{\delta f}{\delta t}\right)_c \, d\Omega \quad , \tag{5.38}$$

where the integrations are over the total 4π solid angle.

It would require a formidable effort to evaluate completely the collision integrals. However, when elastic collisions of electrons with heavy particles are assumed to be the dominant processes, Cherrington (1979) showed that collision integral in Eq. (5.38) is given by

$$\frac{3}{4\pi}\int \cos\theta_1 \left(\frac{\partial f}{\partial t}\right)_c \, d\Omega = -\nu_m(v)\, f_1(v) = -\sum_j N_j \, \sigma_m^j(v) v f_1(v) \quad , \tag{5.39}$$

where $\sigma_m^j(v)$ (cm^2) is the momentum-transfer cross-section, $\nu_m(v)$ (s^{-1}) is the elastic electron-molecule collision frequency, and N_j (cm^{-3}) is the neutral gas density.

When the electric field is strong, the electrons become more energetic. Therefore, the energy and momentum transfer between electrons and heavy particles during an elastic collision must be taken into account. Ginzburg and Qurevich's (1960) solution for the collision integral in Eq. (5.37), influenced only by elastic collisions, is

$$\frac{1}{4\pi}\int \left(\frac{\partial f}{\partial t}\right)_c \, d\Omega = \frac{1}{2v^2}\frac{\partial}{\partial v}\left[v^2 \delta \nu_m \left(\frac{kT}{m}\frac{\partial f_0}{\partial v} + v f_0\right)\right] \quad , \tag{5.40}$$

where $\delta = 2m/M$ is the average fractional energy transferred in an elastic collision. The neutral particles are assumed to have a Maxwellian distribution characterized by the gas temperature T.

After substitution of Eqs. (5.39) and (5.40) into Eqs. (5.37) and (5.38), the coupled equations become

$$\frac{\partial f_0}{\partial t} - \frac{1}{mv^2}\frac{\partial}{\partial v}\left(\frac{ev^2}{3} E f_1 + \frac{m}{2}\nu_m \delta v^3 f_0 + kT 2 \nu_m \delta v^2 \frac{\partial f_0}{\partial v}\right) = \left(\frac{\partial f_0}{\partial t}\right)_c \tag{5.41}$$

and

$$\frac{\partial f_1}{\partial t} - \frac{eE}{m}\left(\frac{\partial f_0}{\partial v}\right) = -\nu_m f_1 \quad , \tag{5.42}$$

where the subscript $\bar{c}$ on the differential indicates the collision integral in the absence of elastic collisions. The electric-field term varies slowly compared to the elastic collision term in Eq. (5.42). For example, in our laser the reversal frequency of the electric field is approximately 10^8 Hz, but the collision frequency is approximately 10^{11} Hz. Therefore, $\partial f_1/\partial t$ in Eq. (5.42) can be neglected to give the quasi steady-state solution

$$f_1 = \frac{eE(\partial f_0/\partial v)}{m\nu_m} \quad . \tag{5.43}$$

Substituting f_1 from Eq. (5.43) into Eq. (5.41), and changing to energy as a variable using $f_0(\varepsilon)$, where $\varepsilon = mv^2/2$, results in

$$\frac{\partial f_0}{\partial t} - \sqrt{\frac{m}{2\varepsilon}}\frac{\partial}{\partial \varepsilon}\left(\frac{2\varepsilon e^2 E}{3mN_j\sigma_m^j}\left(\frac{\partial f_0}{\partial \varepsilon}\right) + \frac{4N_j}{M}\sigma_m^j \varepsilon^2 f_0 + \frac{4kT}{M}N_j\sigma_m^j\varepsilon^2\frac{\partial f_0}{\partial \varepsilon}\right) = \left(\frac{\delta f_0}{\delta t}\right)_{\bar{c}} \quad , \quad (5.44)$$

where $f_0(\varepsilon)$ is the electron energy distribution function, with normalized value

$$\int_0^\infty \varepsilon^{1/2} f_0(\varepsilon)\, d\varepsilon = 1 \quad . \tag{5.45}$$

Following the procedure of Smith and Thomson (1978), consider the net change of the density of electrons in the six-dimensional volume element $(\bar{r}, \bar{v})$ at time δt. Assume that the molecular and atomic velocities are negligible compared to the electron velocities because the atomic and molecular masses are much heavier. The contribution to $(\delta f_0/\delta t)_{\bar{c}}$ from the excitation and ionization processes (i.e., inelastic collisions) is

$$(\frac{\delta f_0}{\delta t})_{c\text{-}inel} = \sum_j N_j[f_0(\varepsilon+\varepsilon_j)\sigma_j(\varepsilon+\varepsilon_j)(\varepsilon+\varepsilon_j) - f_0(\varepsilon)\sigma_j(\varepsilon)\varepsilon]\sqrt{\frac{2}{m\varepsilon}} \quad , \qquad (5.46)$$

where the electrons lose energy ε_j in these collisions. In the case of superelastic collisions, the electrons gain energy ε_j from molecules in the excited states. Therefore,

$$(\frac{\delta f_0}{\delta t})_{c\text{-}supel} = \sum_j N_j^*[f_0(\varepsilon-\varepsilon_j)\sigma_{-j}(\varepsilon-\varepsilon_j)(\varepsilon-\varepsilon_j) - f_0(\varepsilon)\sigma_{-j}(\varepsilon)\varepsilon]\sqrt{\frac{2}{m\varepsilon}} \quad , \qquad (5.47)$$

where N_j^* are the number of molecules and atoms in the excited states. The cross-sections for superelastic collisions, $\sigma_{-j}(\varepsilon)$, are related to those of the relevant excitation collisions, $\sigma_j(\varepsilon+\varepsilon_j)$, by (Mitchell and Zemansky, 1971)

$$\sigma_{-j}(\varepsilon) = \frac{\varepsilon+\varepsilon_j}{\varepsilon}\sigma_j(\varepsilon+\varepsilon_j) \quad . \qquad (5.48)$$

For convenience of numerical calculations, the Boltzmann equation can be written in terms of the electron number density $n(\varepsilon)=n_e\varepsilon^{1/2}f(\varepsilon)$ (n_e is the electron density), yielding

$$\frac{\partial n}{\partial t} = -\frac{\partial}{\partial \varepsilon}[\frac{2Ne^2(E/N)^2\varepsilon}{3m(\nu/N)}(\frac{n}{2\varepsilon}-\frac{\partial n}{\partial \varepsilon})] - \frac{\partial}{\partial \varepsilon}[\bar{\nu}(n(\frac{kT}{2}-\varepsilon) - kT\varepsilon\frac{\partial n}{\partial \varepsilon})] +$$

$$+ \sum_j N_j[R_j(\varepsilon+\varepsilon_j)n(\varepsilon+\varepsilon_j) - R_j(\varepsilon)n(\varepsilon)] +$$

$$+ \sum_j N_j^*[R_j'(\varepsilon-\varepsilon_j)n(\varepsilon-\varepsilon_j) - R_j'(\varepsilon)n(\varepsilon)] \quad , \qquad (5.49)$$

where

$$\frac{\nu}{N} = \left(\frac{2\varepsilon}{m}\right)^{1/2} \sum_s \delta_s \sigma_m^s(\varepsilon) \quad , \tag{5.50a}$$

$$\bar{\nu} = 2mN\left(\frac{2\varepsilon}{m}\right)^{1/2} \sum_s \frac{\delta_s \sigma_m^s(\varepsilon)}{M_s} \quad , \tag{5.50b}$$

and where $N=\Sigma N_j$, R_j *and* R_j' are the inelastic and the superelastic collision rates, respectively, which are the products of cross-section and electron velocity $v(\varepsilon)$, i.e.,

$$R_j(\varepsilon) = \sigma_j(\varepsilon)\nu(\varepsilon) \tag{5.51a}$$

and

$$R_j'(\varepsilon) = \left(\frac{\varepsilon+\varepsilon_j}{\varepsilon}\right)\sigma_j(\varepsilon+\varepsilon_j)\nu(\varepsilon) = \sigma_{-j}(\varepsilon)\nu(\varepsilon) \quad . \tag{5.51b}$$

The effects of electron-electron collisions are only significant in a highly-ionized gas. When electron-electron collision are included, Eq. (4.49) requires the additional terms (Rosenbluth et al 1957)

$$\left(\frac{\partial n}{\partial t}\right)_{e-e} = \frac{\varepsilon}{6}\left(\frac{2}{m}\right)^{\frac{1}{2}}\sigma_{ee}\left[3\varepsilon^{-\frac{1}{2}}n^2 + 2\varepsilon^{\frac{3}{2}}\frac{\partial Q}{\partial \varepsilon}\frac{\partial}{\partial \varepsilon}\left(\frac{\partial n}{\partial \varepsilon} - \frac{n}{2\varepsilon}\right) + \varepsilon^{-\frac{1}{2}}Q\left(\frac{\partial n}{\partial \varepsilon} - \frac{n}{2\varepsilon}\right)\right] \quad , \tag{5.52}$$

where

$$Q(\varepsilon,t) = 3\int_0^{\varepsilon} n dx - \frac{1}{\varepsilon}\int_0^{\varepsilon} x n dx + 2\varepsilon^{\frac{1}{2}}\int_{\varepsilon}^{\infty} x^{-\frac{1}{2}} n dx \tag{5.53}$$

An algorithm developed by Rockwood (1973) was used for the numerical solution of Eq. (5.49). The electron-energy axis is first partitioned into K cells of width $\Delta\varepsilon$ using the finite difference method. Parameter n_k is defined as the number density of electrons with energy between $\varepsilon_k=(k-1)\Delta\varepsilon$ and $\varepsilon_k^+=k\Delta\varepsilon$. Equation (5.49) is then converted into the set of k-coupled

ordinary differential equations

$$\frac{\partial n_k}{\partial t} = a_{k-1}n_{k-1}+b_{k+1}n_{k+1}-(a_k+b_k)n_k+a'_{k-1}n_{k-1}+b'_{k+1}n_{k+1}-(a'_k+b'_k)n_k +$$

$$+\sum_j N_j(R_{j,k+m_j}n_{j,k+m_j}-R_{j,k}n_k)+\sum_j N_j^*(R'_{j,k-m_j}n_{k-m_j}-R'_{j,k}n_k) \quad , \qquad (5.54)$$

where m_j is the nearest integer to $\varepsilon_j/\Delta\varepsilon$. Parameters a, b are related to momentum-transfer collisions, and a′, b′ to electron-electron collisions by

$$a_k = \frac{2Ne^2}{3m}\left(\frac{E}{N}\right)^2\frac{1}{(\nu_k^*/N)(\Delta\varepsilon)^2}\left(\varepsilon_k^*+\frac{\Delta\varepsilon}{4}\right)+\frac{\bar{\nu}_k^*}{2\Delta\varepsilon}\left[\left(\frac{kT}{2}-\varepsilon_k^*\right)+\frac{2kT\varepsilon_k^*}{\Delta\varepsilon}\right] \quad , \qquad (5.55)$$

$$b_k = \frac{2Ne^2}{3m}\left(\frac{E}{N}\right)^2\frac{1}{(\nu_k/N)(\Delta\varepsilon)^2}\left(\varepsilon_k-\frac{\Delta\varepsilon}{4}\right)+\frac{\bar{\nu}_k}{2\Delta\varepsilon}\left[\varepsilon_k-\frac{kT}{2}+\frac{2kT\varepsilon_k}{\Delta\varepsilon}\right] \quad , \qquad (5.56)$$

$$a'_k = \sum_l A_{kl}n_l \quad , \qquad (5.57)$$

and

$$b'_k = \sum_l B_{kl}n_l \quad , \qquad (5.58)$$

respectively, where

$$A_{k,l} = \frac{\varepsilon}{6}\left(\frac{2}{m}\right)^{\frac{1}{2}}\sigma_{ee}[(\varepsilon_{k+1}^{-\frac{1}{2}}H_{k+1,l}+\varepsilon_k^{-\frac{1}{2}}H_{k,l})(\varepsilon_l\mu_k^*-0.75) +$$

$$+((1-H_{k,l})\varepsilon_{k+1}+(1-H_{k-1,l})\varepsilon_k)(\varepsilon_k^{-\frac{1}{2}}u_k^*)] \quad , \qquad (5.59)$$

$$B_{k,l} = \frac{\varepsilon}{6}(\frac{2}{m})^{\frac{1}{2}}\sigma_{ee}[(\varepsilon_{k+1}^{-\frac{1}{2}}H_{k+1,l}+\varepsilon_k^{-\frac{1}{2}}H_{k,l})(\varepsilon_l u_k^{-}+0.75) +$$

$$+((1-H_{k,l})\varepsilon_{k+1}+(1-H_{k-1,l})\varepsilon_k)(\varepsilon_k^{-\frac{1}{2}}u_k^{-})] \quad , \tag{5.60}$$

$$u_k^{\pm} = (\frac{1}{\Delta\varepsilon} \pm \frac{0.25}{\varepsilon_{k+1/2}}) \; , \quad H_{k,l} = 0 \;\; (k<l),\; 1 \;\; (k\geq l) \quad . \tag{5.61}$$

Parameters a_k and a_k' are interpreted as the rate at which electrons having energy ε_k are increased to energy ε_{k+1}. Similarly, b_k and b_k' are the rates for a decrease of energy from ε_{k+1} to ε_k. Note that Eq.(5.54) can be expressed in matrix notation by

$$\frac{\partial n_k}{\partial t} = \sum_l C_{kl}n_l + \sum_l T_{kl}n_l \quad , \tag{5.62}$$

where the elements of the matrix C_{kl} are related to a_k, b_k, R_j and R_j'. The elements of T_{kl} are related to a_k' and b_k', which are functions of electron density n_k. Both C_{kl} and T_{kl} are matrices with elements forming a band along the diagonal. Applying an implicit Euler algorithm (Rockwood, 1973), Eq. (5.62) becomes the set of algebraic equations

$$(I_{kl}-C_{kl}h)\cdot n_l(t+h) = [I_{kl}+hT_{kl}(n(t))]n_l(t) \quad , \tag{5.63}$$

where $I_{kl}=\delta_{kl}$ is the unity matrix, and h is the duration of the integration time step.

At time step t, $n_l(t)$, C_{kl} and T_{kl} are all known parameters. Therefore, the electron energy distribution $n_l(t+h)$ at time t+h can be solved from Eq. (5.63) using the Gaussian elimination method (Ralston, 1965) for the matrix equation system [A]X=[B]. The calculated distribution functions, with and without electron-electron collisions, are shown in Fig. 5.10 at time t=22.5 ns after spark-gap breakdown. At this time, both the electron density and the effects of electron-electron collisions reach the maximum values within the laser discharge. The electron-electron

collisions tend to drive the distribution towards a Maxwellian distribution. In our laser discharge (see Chapter 6), the degree of ionization is less than 10^{-4}. As can be seen from Fig. 5.10, the effects of electron-electron collisions can be neglected in the calculations of the kinetic processes in our laser.

5.4. Collision Rates and Transport Coefficients.

The collision rate-coefficients of the various reactions, R_j (cm^3/s), can be determined from the collision cross-sections and the isotropic part of the electron-energy distribution. In our laser, the anisotropic part of the distribution is negligible in comparison to the isotropic part. Coefficient R_j can be put in the form $R_j = <\sigma_j v>$, where v is the relative velocity of the collision particles. This is usually taken as the electron velocity for electron-species collisions, because the velocities of the heavy species are much smaller than those of the electrons. Applying the numerical code presented in Section 5.3, R_j is calculated using

$$R_j = \frac{\int \sigma_j(\varepsilon) v(\varepsilon) n(\varepsilon) d\varepsilon}{\int n(\varepsilon) d\varepsilon} \quad , \tag{5.64}$$

where $n(\varepsilon)$ is electron density distribution obtained from the solution of Eq. (5.63). The calculated rate-coefficients (constants) for the various collisions in the discharge (excitation, ionization, dissociative attachment, and superelastic collisions) are shown in Fig. 5.11 as a function of E/N (ratio of the electric field to the gas density).

The average energy of the electrons (ε_c) and the electron temperature (T_c) are two characteristic quantities determined from the isotropic part of the electron distribution. The energy ε_c is calculated from

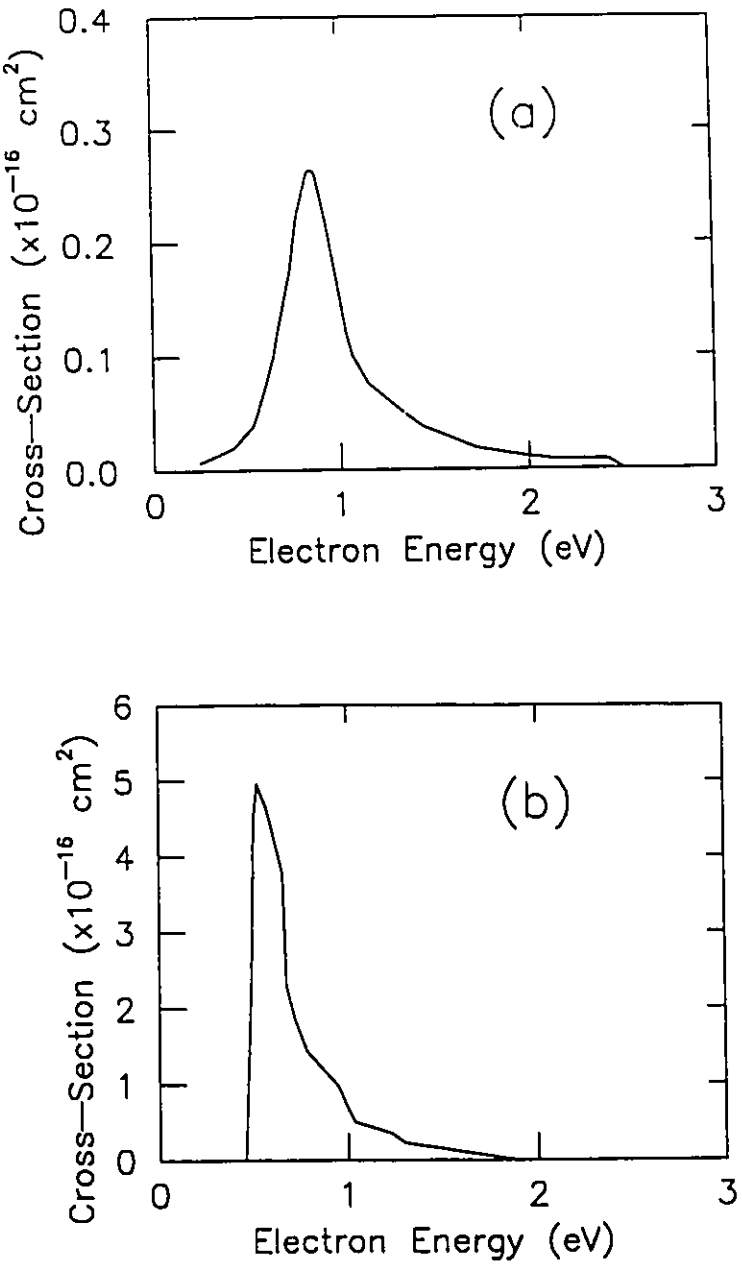

Fig. 5.9. Cross-sections for electron dissociative attachment to (a) HCl(v=0) and (b) HCl(v=1).

$$\varepsilon_e(t) = \frac{\int \varepsilon\ n(\varepsilon,t)d\varepsilon}{\int n(\varepsilon,t)d\varepsilon} \quad . \tag{5.65}$$

Figure 5.12 shows the calculated time-dependent average electron energy. The electron temperature is defined by the average translational electron energy corresponding to a Maxwell-Boltzmann distribution of electron energies, i.e.,

$$\frac{3}{2}kT_e = \frac{\int \varepsilon\ n(\varepsilon,t)d\varepsilon}{\int n(\varepsilon,t)d\varepsilon} \quad . \tag{5.66}$$

Transport coefficients of a discharge system are of particular interest because these are measurable parameters. By definition, the isotropic part of electron distribution function has no direct contribution to the transport properties. Only the anisotopic part makes a nonzero contribution to the electron conductivity, mobility and diffusion. This is shown by the calculation of free-electron flow in a discharge. Consider that an external dc electric field E_z is applied along the z-axis. Therefore, the drift velocity of the electrons (v_z) is also in the z-axis direction. The current density is

$$J_z = -n_e e\langle V_z\rangle = n_e e\frac{\int v_z\, f\, d\Omega_v}{\int f\, d\Omega_v}$$

$$= -n_e e\frac{\int_0^\infty \int_0^\pi (v\cos\theta_1)(f_0 + f_1\cos\theta_1)2\pi v^2\sin\theta_1 d\theta_1 dv}{\int_0^\infty \int_0^\pi (f_0 + f_1\cos\theta_1)2\pi v^2\sin\theta_1 d\theta_1 dv} = -\frac{1}{3}n_e e\ \frac{\int_0^\infty v^3 f_1\ dv}{\int_0^\infty f_0 v^2 dv} \quad . \tag{5.67}$$

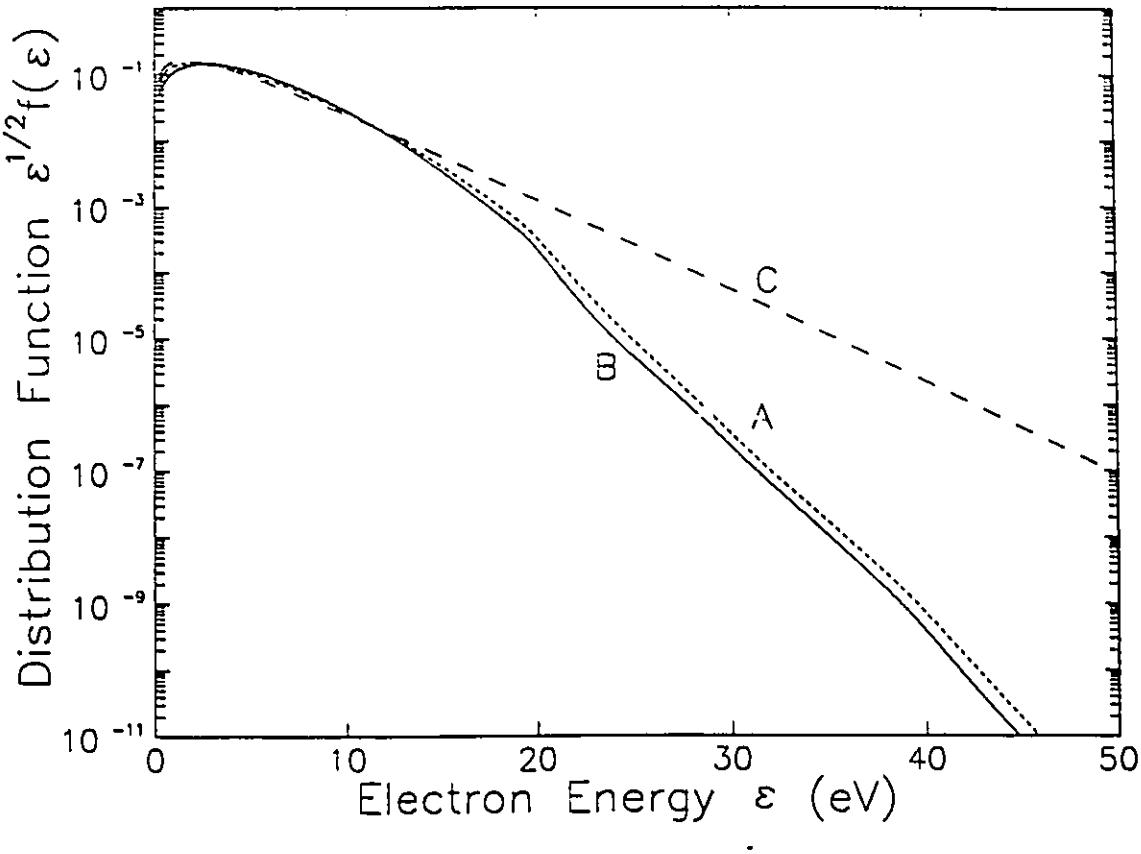

Fig. 5.10. Electron-energy distribution function at time t=22.5 ns after the spark-gap breakdown. At this time the electron density is a maximum. Curves A (solid) and B are the distribution functions with and without electron-electron collisions, respectively. Curve C is the Maxwellian distribution assuming the same average electron energy as Curves A and B. For this data, the gas mixture is 0.8%Xe/0.3%HCl/He at a pressure of 350 kPa and a charging voltage of V_0=15 kV.

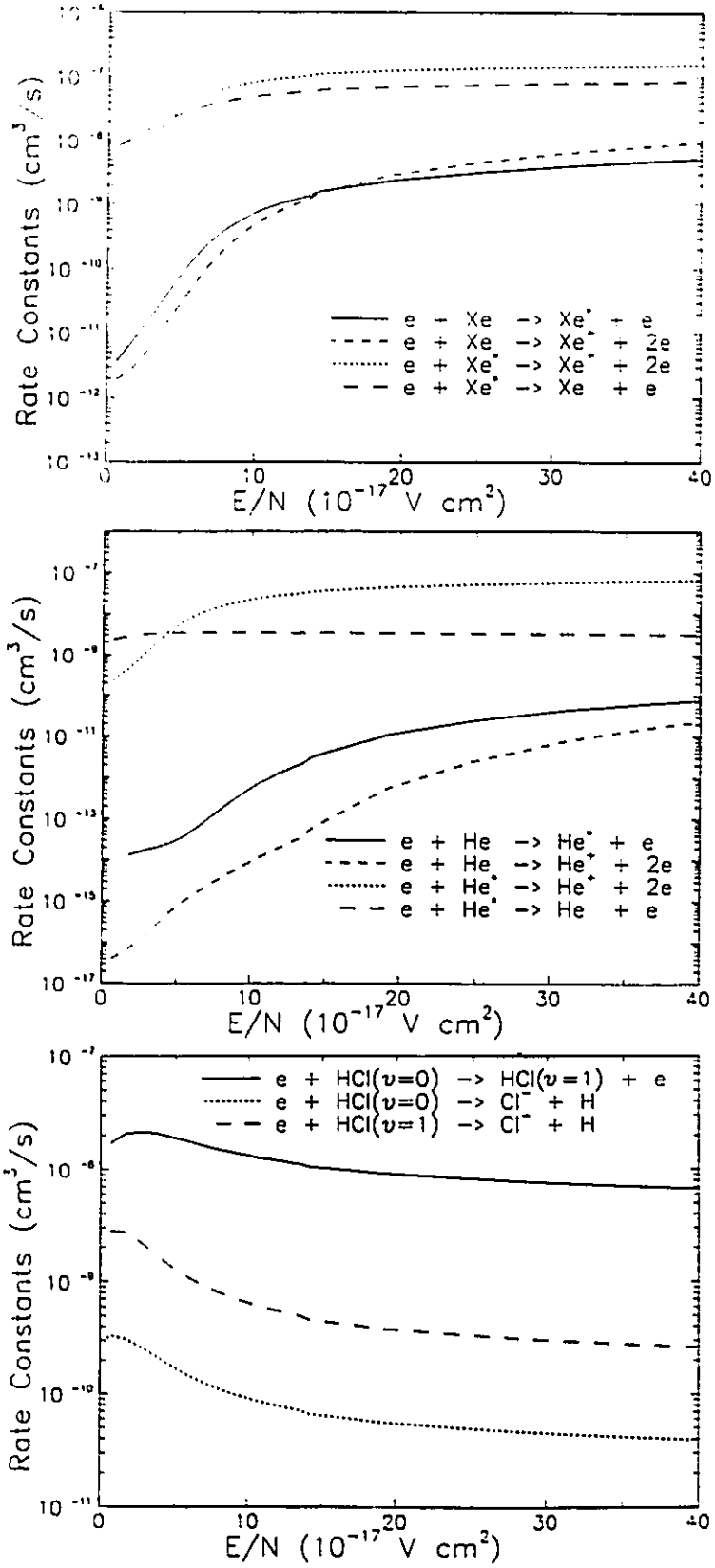

Fig. 5.11. Calculated rate-coefficients (rate-constants) for the various collision processes in the discharge as a function of E/N (ratio of electric field to gas density). The discharge parameters are the same as those for Fig. 5.10.

The variable v in Eq. (5.67) can be replaced by the electron energy $\varepsilon = mv^2/2$, and the distribution function f_0 normalized using Eq. (5.45). Therefore, the current flow, as an integral of f_1, is

$$J_z = -\frac{n_e e}{3}\left(\frac{2}{m}\right)^{1/2}\int_0^{\infty} \varepsilon\, f_1\, d\varepsilon \quad . \tag{5.68}$$

From Eq. (5.43), f_1 can be expressed as a differential of f_0. By definition, the conductivity σ is given by $J_z = \sigma E_z$. Therefore,

$$\sigma = -\frac{n_e e^2}{3}\left(\frac{2}{m}\right)^{1/2}\int_0^{\infty} \frac{\varepsilon\, \partial f_0/\partial\varepsilon}{\sum_j N_j \sigma_m^j(\varepsilon)}\, d\varepsilon \quad , \tag{5.69}$$

where σ_m is the momentum-transfer collision cross-section, and N_j is the density of the heavy species involved in momentum-transfer collisions.

The electron mobility μ is another transport parameter. When the potential energy between the electrons and ions is negligible in comparison to the electron kinetic energy (both thermal and electric field induced), the electron drift velocity in the field direction (v_d) is proportional to the electric field E ($v_d = \mu_e E$). The proportionality constant, which is the mobility μ_e, is directly related to the conductivity σ by

$$\vec{J} = \sigma\vec{E} = -n_e e\bar{v} = n_e e \mu_e \vec{E} \quad . \tag{5.70}$$

After substitution of Eq. (5.69),

$$\mu_e = -\frac{e}{3}\left(\frac{2}{m}\right)^{1/2}\int_0^{\infty} \frac{\varepsilon}{\sum_j N_j \sigma_m^j(\varepsilon)} \frac{\partial f}{\partial \varepsilon}\, d\varepsilon \quad . \tag{5.71}$$

The mobility μ_e decreases with increasing gas pressure, and with decreasing electron temperature.

For calculations, use is made of the relationship between μ_e and the rate at which the electrons gain energy. This relationship can be written in the numerical form (Rockwood, 1973)

$$\mu_e = \sum_k \frac{(a_k^{\cdot} - b_k^{\cdot}) n_k \Delta\varepsilon}{E^2 \sum_k n_k} \quad , \tag{5.72}$$

where

$$a_k^{\cdot} = \frac{2Ne^2}{3m}\left(\frac{E}{N}\right)^2 \frac{1}{(\nu_k^{\cdot}/N)(\Delta\varepsilon)^2}\left(\varepsilon_k^{\cdot} + \frac{\Delta\varepsilon}{4}\right)$$

and

$$b_k^{\cdot} = \frac{2Ne^2}{3m}\left(\frac{E}{N}\right)^2 \frac{1}{(\nu_k/N)(\Delta\varepsilon)^2}\left(\varepsilon_k - \frac{\Delta\varepsilon}{4}\right) \quad .$$

The discharge impedance is given by

$$R = \frac{d}{Ae\mu_e n_e} \quad , \tag{5.73}$$

where A is the cross-sectional area of the active discharge region, d is the distance between the electrodes, and n_e is the electron density evaluated from solutions of the rate equations for kinetic processes (discussed in Chapter 6). The calculated and measured impedances are compared in Fig. 5.13.

5.5. Summary.

In this chapter, various electron-impact collisions in a discharge are discussed. The

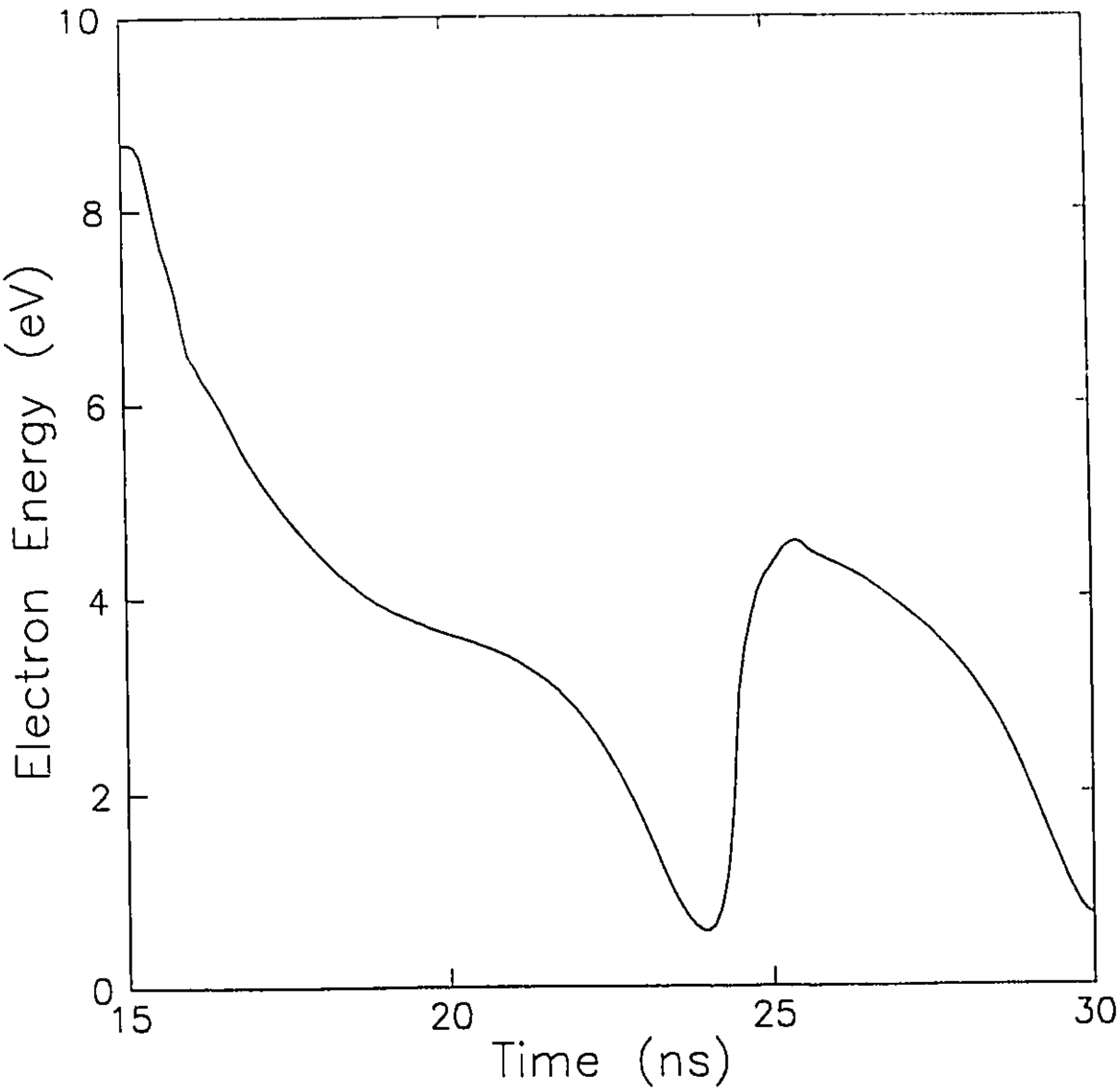

Fig. 5.12. Calculated time-dependent average electron energy. The discharge parameters are the same as those for Fig. 5.10.

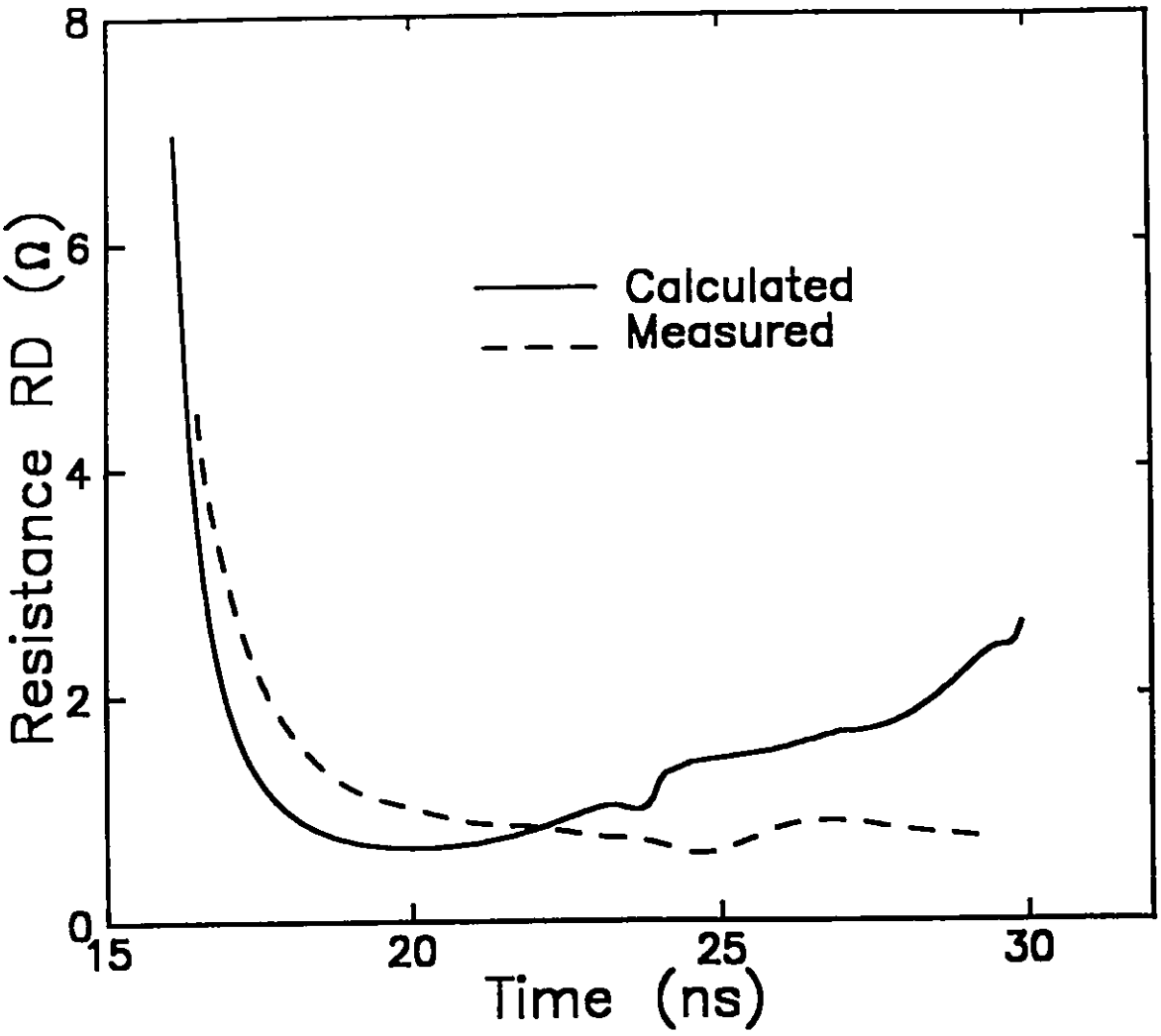

Fig. 5.13. Comparison of measured and calculated time-dependent discharge impedance. The discharge parameters are the same as those for Fig. 5.10.

reliability of the data for collision cross-sections is confirmed by comparison of data from a variety of sources. The most reliable data are used in the calculations.

The statistical electron-energy distribution is determined from the Boltzmann equation for spatially-homogeneous medium. A numerical code based on the finite difference algorithm by Roodwood (1973) is developed to determine this distribution function. The rate-coefficients and transport parameters calculated from the electron distribution are very important in the study of kinetic processes within a laser discharge.

Chapter 6

Reaction Kinetics

Kinetic reactions in rare-gas halide lasers are very complicated processes. Generally, these kinetic processes involve several ground-state atomic and molecular species, several ionic species, and a large number of excited atomic and molecular states. The kinetics in the most common types of rare-gas-halide lasers (>50-ns discharge pulse duration) are incredibly complicated processes which are still not understood completely. However, our compact laser assists in providing a much better understanding than has been attained previously of the fast laser excitation processes. The short-duration (< 10 ns) discharge makes it possible to develop a new and concise kinetic model which only involves a small number (15) of discharge species (chemical species, electrons and photons), and 40 important fast-reaction processes. The calculations indicated that these processes are sufficient to describe the performance of our compact laser.

The typical rare-gas-halide gas mixture used in our laser is 0.8%Xe/0.3%HCl/He. The species concerned in our model are Xe, Xe^*, Xe^+, He, He^*, He^+, HCl, HCl(v), Cl^-, $XeCl^*$, XeCl, Cl, Xe_2^+ the free-electron density n_e, and the photon density N_p. In addition to the electron-species collision processes discussed in the previous chapter, the model developed in this chapter also includes the chemical reactions which influence directly or indirectly the formation and quenching of the upper laser level $XeCl^*$, and the photon emission and absorption processes.

The kinetic reactions are discussed in detail in Section 6.1, with particular emphasis on the formation and quenching mechanisms of $XeCl^*$. Section 6.2 describes the rate equations used to

calculate the time-dependent densities of the various species and the laser radiation. Investigation of the laser output power, energy and efficiency are presented in Section 6.3. Finally, in Section 6.4, comparisons are made between the use of different buffer gases for the laser medium.

The kinetic model, together with the model for the discharge excitation circuit, form a self-consistent model which is capable of evaluating the laser performance. The validity of this self-consistent model is demonstrated by the good agreement between the calculated and measured data for discharge voltage, current and resistance, and for the pulse shape and energy of the laser output.

6.1. Kinetic Reactions.

All of the kinetic reactions and the corresponding reaction rates used in the model are listed in Table 6.1. Most of the discharge energy results in the production of the excited atoms and ions (Reactions 1 to 7 in Table 6.1). Although the excited atoms are initially formed in many excited states, at high gas pressures most of these states are rapidly quenched to lower excited states via collisions. Therefore, only metastable states of the various individual atoms (Rhodes, 1974) are considered in our model.

6.1.1. Kinetics in a Rare-Gas-Halide Mixture.

If the excited species are sufficiently energetic, these may form ions through Penning or association ionization reactions of the type

Table 6.1. Chemical reactions used in the model.

No.	Reaction[a]	Rate constant[b]	Reference
1.	$e + Xe \longrightarrow Xe^* + e$	R_1	Schaper and Scheibner (1974) de Heer et al (1979)
2.	$e + He \longrightarrow He^* + e$	R_2	Borst (1974)
3.	$e + HCl \longrightarrow HCl(v) + e$	R_3	Rohr and Linder (1976)
4.	$e + Xe \longrightarrow Xe^+ + e$	R_4	Rapp and Englander-Golden (1965)
5.	$e + Xe^* \longrightarrow Xe^+ + e$	R_5	Ton-That and Flannery (1977)
6.	$e + He \longrightarrow He^+ + e$	R_6	Rapp and Englander-Golden (1965)
7.	$e + He^* \longrightarrow He^+ + e$	R_7	Vriens (1964)
8.	$e + Xe^* \longrightarrow Xe + e$	R_8	
9.	$e + He^* \longrightarrow He + e$	R_9	
10.	$e + HCl \longrightarrow H + Cl^-$	R_{10}	Orient and Srivastava (1985)
11.	$e + HCl(v) \longrightarrow H + Cl^-$	R_{11}	Domcke and Mündel (1985)
12.	$Xe^* + Xe^* \longrightarrow Xe^+ + Xe + e$	$5.0 \cdot 10^{-10}$ cm^3/s	Maeda et al (1982)
13.	$He^* + Xe \longrightarrow He + Xe^+ + e$	$1.2 \cdot 10^{-10}$ cm^3/s	Kubota et al (1975)
14.	$Xe^+ + Cl^- + He \longrightarrow XeCl^* + He$	$3.7 \cdot 10^{-27}$ cm^6/s	Flannery and Yang (1978) Hokazono et al (1984)
15.	$Xe^* + HCl(v) \longrightarrow XeCl^* + H$	$2.0 \cdot 10^{-10}$ cm^3/s	Chang (1982)
16.	$Xe^* + HCl \longrightarrow Xe + H + Cl$	$5.6 \cdot 10^{-10}$ cm^3/s	Kolts et al (1979)
17.	$Xe^* + HCl(v) \longrightarrow Xe + H + Cl$	$5.6 \cdot 10^{-10}$ cm^3/s	Mihkelsoo et al (1989)

(continued)

18.	$Xe^* + Xe + He \longrightarrow Xe_2^* + He$	$1.4 \cdot 10^{-32}$ cm^6/s	Brau (1984)
19.	$Xe^* + 2Xe \longrightarrow Xe_2^* + Xe$	$4 \cdot 10^{-32}$ cm^6/s	Brau (1984)
20.	$Xe' + Xe + He \longrightarrow Xe_2' + He$	$1.1 \cdot 10^{-31}$ cm^6/s	Brau (1984)
21.	$Xe' + 2Xe \longrightarrow Xe_2' + Xe$	$2 \cdot 10^{-31}$ cm^6/s	Brau (1984)
22.	$Xe_2^* + Cl^- \longrightarrow XeCl^* + Xe$	$1.1 \cdot 10^{-7}$ cm^3/s	Flannery and Yang (1978)
23.	$Xe^* + Cl + He \longrightarrow XeCl^* + He$		Lee et al (1993)
24.	$XeCl^* + e \longrightarrow Xe + Cl + e$	$3.0 \cdot 10^{-7}$ cm^3/s	Wang (1982)
25.	$XeCl^* + HCl \longrightarrow Xe + HCl + Cl$	$7.7 \cdot 10^{-10}$ cm^3/s	Levin et al (1981)
26.	$XeCl^* + HCl(v) \longrightarrow Xe + HCl + Cl$	$6.3 \cdot 10^{-10}$ cm^3/s	Mihkelsoo et al (1989)
27.	$XeCl^* + Xe \longrightarrow 2Xe + Cl$	$2.3 \cdot 10^{-11}$ cm^3/s	Inoue et al (1984)
28.	$XeCl^* + He \longrightarrow Cl + Xe + He$	$5.0 \cdot 10^{-13}$ cm^3/s	Hokazono et al (1984)
29.	$Xe_2^* + e \longrightarrow 2Xe + e$	$1.0 \cdot 10^{-9}$ cm^3/s	Kannari et al (1984)
30.	$Xe_2^* \longrightarrow 2Xe + h\nu'$	$5.0 \cdot 10^{7}$ 1/s	Maeda et al (1982)
31.	$Xe_2' + e \longrightarrow Xe^* + Xe$	$2.3 \cdot 10^{-6}$ (T_e /300)$^{-0.6}$ cm^3/s [c]	Biondi (1982)
32.	$XeCl + He \longrightarrow Xe + Cl + He$	$3.0 \cdot 10^{-12}$ cm^3/s	Lee (1983) Krause and Kleinschmidt (1991)
33.	$XeCl + HCl \longrightarrow Xe + Cl + HCl$	$2.2 \cdot 10^{-11}$ cm^3/s	Waynant and Eden (1980)
34.	$XeCl + Xe \longrightarrow 2Xe + Cl$	$5.6 \cdot 10^{-12}$ cm^3/s	Waynant and Eden (1980)

[a] HCl and HCl(υ) in the Table represent HCl(υ=0) and HCl(υ=1,2), respectively.

[b] Rate constants for reaction 1 to 11 were calculated from the Boltzmann equation. These values are dependent on the electron energy.

[c] T_e is the average electron energy over the distribution in K.

$$Xe^* + Xe^* \rightarrow Xe^+ + Xe + e \qquad (6.1a)$$

and

$$He^* + Xe \rightarrow He + Xe^+ + e \quad . \qquad (6.1b)$$

These types of reactions are very fast processes, almost proceeding at every collision if there is sufficient energy.

The excited Xe atoms can also be quenched rapidly to the ground state by collisions with the halide donors HCl and HCl(v) via the processes (Kolts et al, 1979; Mihkelsoo et al, 1989)

$$Xe^* + HCl \rightarrow Xe + H + Cl \qquad (6.2a)$$

and

$$Xe^* + HCl(v) \rightarrow Xe + H + Cl \quad . \qquad (6.2b)$$

In these reactions, the energy necessary for dissociation of the halide donors is provided by the excited states of the rare-gas atoms. The extra energy between the excited state (8.32 eV) and the dissociation energy of HCl (4.62 eV) is converted to kinetic energy in the reaction products Xe, H and Cl.

The excited rare-gas atoms and ions may dimerize via the fast three-body recombination processes (Brau, 1984)

$$Xe^* + Xe + He \rightarrow Xe_2^* + He \quad , \qquad (6.3a)$$

$$Xe^* + 2Xe \rightarrow Xe_2^* + Xe \quad , \qquad (6.3b)$$

$$Xe^+ + Xe + He \rightarrow Xe_2^+ + He \qquad (6.3c)$$

and

$$Xe^+ + 2Xe \rightarrow Xe_2^+ + Xe \quad . \qquad (6.3d)$$

In each reaction, one of the ground state atoms functions as a "buffer" atom which converts the energy difference between the excited atom (ion) and the dimer into kinetic energy. This allows the reactions to proceed rapidly in the direction of the arrows. Other possible dimers (He_2^*, He_2^+, $HeXe^*$ and $HeXe^+$) and related reactions are not considered in our model. For the short-duration discharge present in our laser, the densities of these dimers are very low. Inclusion of these

species only changes laser output by less than 1%.

The dimer molecule can be dissociated to ground-state atoms by a collision with a free electron (Kannari et al, 1984), i.e.,

$$Xe_2^* + e \rightarrow 2Xe + e \quad . \tag{6.4a}$$

or via the spontaneous emission process (Maeda et al, 1982)

$$Xe_2^* \rightarrow 2Xe + h\nu' \quad . \tag{6.4b}$$

A Xe_2^+ dimer ion can recombine with an electron to form an excited atom in the dissociative recombination reaction

$$Xe_2^+ + e \rightarrow Xe^* + Xe \quad . \tag{6.5a}$$

In addition, this ion can make a small contribution to the formation of the excited rare-gas halide ($XeCl^*$) via the two-ion recombination process (Biondi, 1982)

$$Xe_2^+ + Cl^- \rightarrow XeCl^* + Xe \quad . \tag{6.5b}$$

6.1.2. Formation and Quenching Mechanisms of $XeCl^*$.

A single upper laser level ($XeCl^*$) is considered in our concise model, based on the assumption that there is fast collisional mixing of the $XeCl^*(B)$ and $XeCl^*(C)$ states and virtually instantaneous relaxation of the vibrational levels in the $XeCl^*(B)$ state. This is a reasonable assumption for a discharge using a He buffer at a high gas pressure (Hokazono et al, 1984). In this case, the most important mixing and relaxation processes for $XeCl^*(B)$ and $XeCl^*(C)$ are collisions with He buffer atoms. This collision rate is $\approx 2.9 \cdot 10^{-11}$ cm^3s^{-1} (Dreiling and Setser, 1981), which is much faster than the quenching rate of $5.0 \cdot 10^{-13}$ cm^3s^{-1} (Reaction 6 in Table 6.1) for the same states (Hokazono et al, 1984).

Extensive initial calculations were performed for our short-pulse laser employing both a

single upper laser level and multiple upper laser levels. Essentially identical results were obtained for both cases. In order to reduce computational complexity, the model containing a single upper laser level was used solely for our final calculations. Only the results of these calculations are included in the thesis.

In some recent models for XeCl laser discharges using a Ne buffer, the multi-levels $XeCl^*(B,v=0)$, $XeCl^*(B,v\neq 0)$ and $XeCl^*(C)$ are considered (Ohwa and Kushner, 1989; Kannari et al, 1990). The rate for collisional mixing in a Ne buffer is $\approx 4.8\cdot 10^{-12}$ cm^3s^{-1} (Dreiling and Setser, 1981), which is comparable to the quenching rate of $3.3\cdot 10^{-13}$ cm^3s^{-1} (Fisher et al, 1979).

A schematic diagram for $XeCl^*$ formation is shown in Fig. 6.1. During the discharge, substantial densities of excited Xe atoms and ions are produced by electron-impact collisions. Both of these species contribute to the formation of $XeCl^*$. The dominant channel is the three-body ionic recombination process

$$Xe^+ + Cl^- + He \rightarrow XeCl^* + He \quad . \tag{6.6}$$

When a positive ion is formed in discharge, a slow secondary electron is also produced. This low-energy electron may attach to a halide donor HCl or HCl(v), which then dissociates to form Cl^-, i.e.,

$$HCl + e \rightarrow H + Cl^- \tag{6.7a}$$

and

$$HCl(v) + e \rightarrow H + Cl^- \quad . \tag{6.7b}$$

Reactions (6.7a) and (6.7b) have large rate coefficients ($\approx 10^{-7}$ cm^3s^{-1}) at room temperature, However, these rates decrease dramatically with increasing electron temperature. In contrast to the excitation and ionization of Xe atoms, which occur primarily in the early stages of the discharge when the average electron energy is high. Reactions (6.7a) and (6.7b) become significant at relatively later stages when the average electron energy decreases.

Reaction (6.6) is a very rapid process with a rate coefficient in the order of 10^{-7} cm^3s^{-1}. This rate has not been measured directly. However, theoretical results from previous models (Flannery, 1972, 1982) and from the electron-jump model described in Section 2.4 provide reliable estimates.

Another major channel for $XeCl^*$ formation from Xe^* is the reaction

$$Xe^* + HCl(v) \rightarrow XeCl^* + H \quad , \tag{6.8}$$

where the Xe^* transfers its outermost electron to the halogen at some small internuclear separation (5 to 10 Å). This reaction is named a two-body electron "harpooning" process. In a typical XeCl laser gain medium at a total pressure of 450 kPa, the rate coefficient is in the order of 10^{-10} cm^3s^{-1} (Chang, 1982), which is three orders of magnitude less than the value for the ionic-recombination rate given by Reaction (6.6).

Reaction (6.8) is able to proceed because the energy of Xe^* is slightly greater than the total energy required to dissociate HCl(v) and then to form the exciplex $XeCl^*$ (i.e., the process is exothermic). However, the reaction between metastable $Xe(^3P_2)$ and ground state HCl is endothermic, and therefore not allowed. Although reactions between HCl and other metastable Xe^* species ($^3P_1$ and $^3P_0$) are energetically allowed, these can also be neglected due to the very low formation rates.

The exciplex $XeCl^*$ can decay to its ground state by either photon emission or collisions with species in the discharge. Most dominant of the quenching (decay) processes are collisions with neutral species and electrons. Of these, the collision with the halogen-bearing species,

$$XeCl^* + HCl \rightarrow Xe + Cl + HCl \tag{6.9a}$$

and

$$XeCl^* + HCl(v) \rightarrow Xe + Cl + HCl \quad , \tag{6.9b}$$

have the largest rate coefficients ($\approx 10^{-9}$ cm^3s^{-1}). These processes are usually important for low

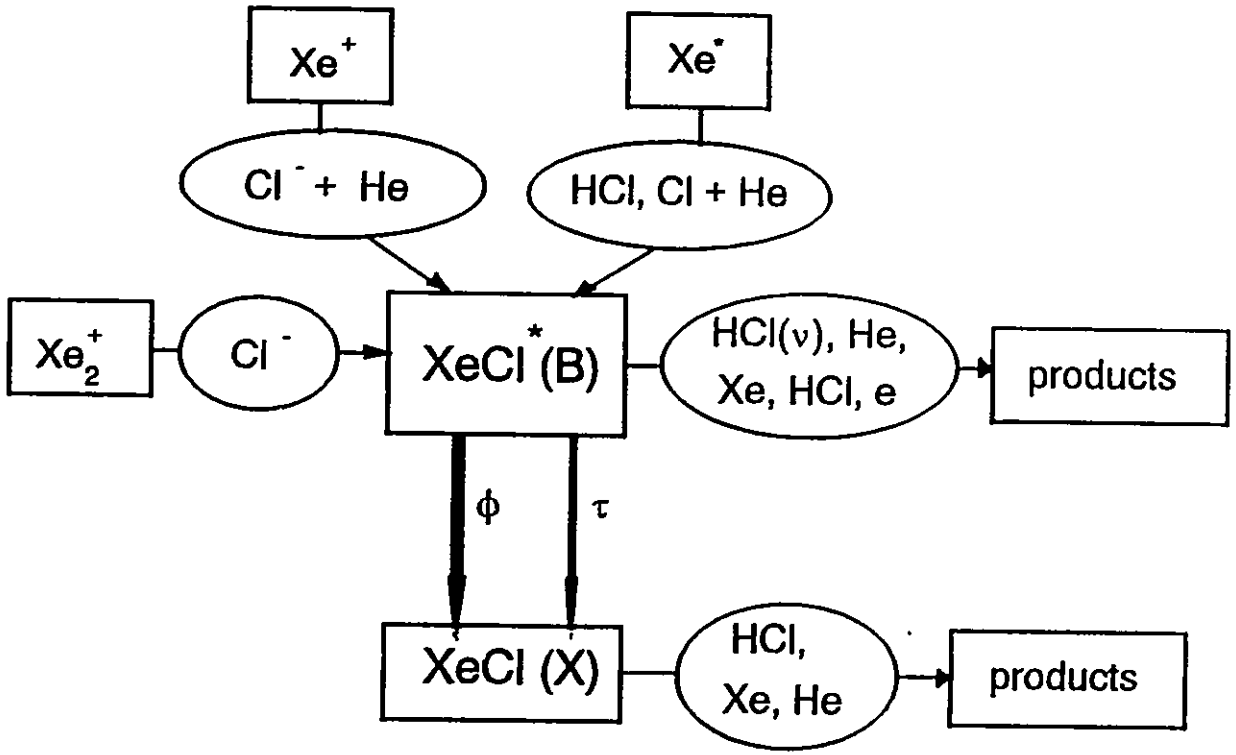

Fig. 6.1. A schematic diagram of the important formation and quenching channels for XeCl*.

pressure laser mixtures where a high proportion of halogen donor is used. However, in the typical gas mixture (0.8%Xe/0.3%HCl/He) at high pressures (several hundreds of kPa), the quenching processes by rare-gas atoms (especially He),

$$XeCl^* + Xe \rightarrow 2Xe + Cl \qquad (6.10a)$$

and

$$XeCl^* + He \rightarrow Xe + He + Cl \quad , \qquad (6.10b)$$

become relatively important. The rate coefficients for these reactions are in the order of 10^{-10} and 10^{-12} cm^3s^{-1}, respectively.

In our short-pulse laser discharge, the degree of ionization for the gas mixture is relatively high (10^{-5} to 10^{-4}). The quenching of $XeCl^*$ by electrons,

$$XeCl^* + e \rightarrow Xe + Cl + e \quad , \qquad (6.11)$$

is the most dominant quenching process because of the high density of electrons and the correspondingly large rate coefficient ($\approx 10^{-7}$ cm^3s^{-1}). Consequently, this process is one of the major factors which limits the peak power of the laser output pulse.

At high gas pressures, three-body reactions can also quench $XeCl^*$ by forming triatomic species in reactions of the type

$$XeCl^* + Xe + He \rightarrow Xe_2Cl^* + He \quad . \qquad (6.12)$$

The existence of Xe_2Cl^* is confirmed by observation of its fluorescence in a long-pulse (> 50 ns) discharge (Marowsky et al, 1981). However, in our laser, the effects of Xe_2Cl^* and Reaction (6.12) are negligible because the discharge duration is small (< 10 ns).

6.1.3. Dissociation of Ground State XeCl.

Spectral studies (Tellinghuisen et al, 1976; Shostak and Strong, 1979) indicate that the ground state XeCl(X) has a shallow potential well containing 20 vibrational levels and a

dissociation energy of 281 cm^{-1}. As a consequence of the shallow potential well, the dissociation of XeCl by collisions has a significant effect on laser performance. In our laser mixture, the important dissociative collisions involving XeCl are those with neutral HCl and rare-gas atoms, i.e.,

$$XeCl + HCl \rightarrow Xe + Cl + HCl \quad , \tag{6.13a}$$

$$XeCl + He \rightarrow Xe + Cl + He \tag{6.13b}$$

and

$$XeCl + Xe \rightarrow 2Xe + Cl \quad . \tag{6.13c}$$

At 300 K, the dissociation rates for Reactions (6.13a) and (6.13c) are 2.2×10^{-11} cm^3s^{-1} and 5.6×10^{-12} cm^3s^{-1} respectively, as determined by Waynant and Eden (1980) from observations of the absorption from the vibrational levels in the shallow potential well of XeCl. Krause and Kleinschmidt (1991) estimate that the dissociation rate using He buffer is 3.0×10^{-12} cm^3s^{-1}. This rate increases with gas temperature because the density distribution of vibrational states in XeCl, and the kinetic energies of the neutral species, both increase with gas temperature. However, these temperature changes can be neglected in a short-pulse-duration discharge.

Collisions with He is the major channel for XeCl dissociation because the population of He is three orders of magnitude higher than those of Xe and HCl. For a total gas pressure of 450 kPa (i.e., He density $\approx 10^{21}$ cm^3s^{-1}), the lifetime of the ground state XeCl is ≈ 0.3 ns, which is nearly two orders of magnitude less than the lifetime of $XeCl^*$ (≈ 10 ns). This lifetime difference contributes to the potential for high efficiency XeCl laser operation using discharge excitation.

6.1.4. Photon Emission and Absorption.

As discussed in Chapter 2, the B → X emission at 308 nm is the most dominant emission

at high gas pressures. The radiative lifetime of the $XeCl^*(B)$ state is 11 ns (Hay and Dunning, 1978; Inoue et al, 1984), which is equivalent to a transition rate of $9 \cdot 10^7$ s^{-1} for the spontaneous emission transition

$$XeCl^* \rightarrow XeCl + h\nu \quad . \tag{6.14}$$

The stimulated-emission cross-section for the B → X transition,

$$XeCl^* + h\nu \rightarrow XeCl + 2h\nu \quad , \tag{6.15}$$

is $4.5 \cdot 10^{-16}$ cm^2. This cross-section was determined from the product $\sigma\tau = 50$ $Å^2 \cdot ns$ reported by Brau and Ewing (1975) and the radiation lifetime $\tau = 11$ ns for $XeCl^*(B)$ reported by Hay and Dunning (1978).

The important photo-absorption processes are listed in Table 6.2. These include the photo-detachment of negative ions formed in the discharge via

$$Cl^- + h\nu \rightarrow Cl + e \quad , \tag{6.16}$$

and the photo-ionization of excited rare-gas atoms, such as

$$Xe^* + h\nu \rightarrow Xe^+ + e \tag{6.17a}$$

and

$$He^* + h\nu \rightarrow He^+ + e \quad . \tag{6.17b}$$

The major absorber in our laser mixture is Cl^- because of the large absorption cross-section. Photo-ionization of dimer molecules and dimer ions can also occur in the discharge. Although photon processes involving dimers have cross-sections comparable to Processes (6.16), (6.17a) and (6.17b), these are much less important because the dimer population is relatively low in a short-duration discharge. From our calculations, the absorption processes have a significant effect only when the photon density approaches the maximum value of 10^{15} cm^{-3} in our laser. At this maximum value, approximately 10% of the laser radiation is absorbed. The XeCl population becomes relatively large only after the laser output ceases. At these times, absorption by XeCl

Table 6.2. Photon processes used in the model.

No.	Reaction	Cross-Section	Rate	Reference
1.	$XeCl^* + h\nu \longrightarrow XeCl + 2h\nu$	$4.5 \cdot 10^{-16}$ cm^2		Brau and Ewing (1975)
2.	$XeCl^* \longrightarrow XeCl + h\nu$		$9.0 \cdot 10^7$ s^{-1}	Hay and Dunning (1978) Inoue et al (1984)
3.	$XeCl + h\nu \longrightarrow XeCl^*$	$4.5 \cdot 10^{-16}$ cm^2		Brau and Ewing (1975)
4.	$Cl^- + h\nu \longrightarrow Cl + e$	$2.1 \cdot 10^{-17}$ cm^2		Rothe (1969)
5.	$Xe^* + h\nu \longrightarrow Xe^+ + e$	$6.0 \cdot 10^{-20}$ cm^2		Dozy and Hyman (1980) McCann and Flannery (1977)
6.	$He^* + h\nu \longrightarrow He^+ + e$	$2.8 \cdot 10^{-18}$ cm^2		McCann and Flannery (1977)

can be neglected. However, any absorption by XeCl that does occur will increase the population of $XeCl^*$.

6.2. Rate Equations and Densities of Species.

A set of 14 kinetic equations and a charge conservation equation are set up to include all of the processes listed in Tables 6.1 and 6.2. These equations are used for solving the time history of the densities of 13 chemical species, and of electrons and photons in the discharge. Some typical rate equations are given in Table 6.3, where k_j is the rate coefficient. For example, the rate equation for the photon density N_p, and the charge conservation equation for electron density n_e are

$$\frac{dN_p}{dt} = \frac{1}{\tau}\rho[XeCl^*] + (\sigma_1([XeCl^*] - [XeCl]) - \sigma_2[Xe^*]$$

$$-\sigma_3[Cl^-] - \sigma_4[He^*])\frac{L_1}{L_2}cN_p + \ln(R)cN_p/L_2 \qquad (6.18)$$

and

$$\frac{dn_e}{dt} = \frac{d[Xe^*]}{dt} + \frac{d[He^*]}{dt} + \frac{d[Xe_2^*]}{dt} - \frac{d[Cl^-]}{dt} \quad , \qquad (6.19)$$

where c is the velocity of light, σ_i is the photon emission or absorption cross-section, τ is the spontaneous emission lifetime, L_1 and L_2 are the lengths of the active medium and laser cavity, respectively, R is the effective reflectance of the mirrors ($R^2=R_1 \cdot R_2$), and ρ is the fraction of spontaneous emission which is amplified ($\approx 5 \cdot 10^{-5}$).

The rate equations appear as first-order nonlinear differential equations with a stiff

numerical property. This set of equations is solved using Gear's method (Ralston, 1965) with automatic time steps. The rate-coefficients used in the rate equations are obtained from the solution of the Boltzmann equation. Both the electric field in the discharge and the densities of the species change with time. Therefore, the code for the Boltzmann equation (discussed in Chapter 5) is called at each time step to calculate the rate-coefficients and the discharge resistance at that time. This calculated resistance is used in the next step as an input for the circuit equation. The solution of the circuit equation at the new step gives the voltage and current in the discharge. In addition, the electric field, $E(t)=V(t)/d$, is used as the input parameter for the Boltzmann equation at this new step.

In order to save computing time, only the circuit equation is solved before discharge breakdown. When the voltage across the discharge increases to a value which is slightly smaller than the breakdown voltage, then the complete code is operative. At this moment, a small initial discharge current is assumed in order to avoid numerical instability resulting from a sudden transient change in the resistance.

In the model, the effect of the UV preionization is treated as a volume source of electrons. With the rate for electron attachment to the halogen donor in order of 10^{-9} $cm^{-3}s^{-1}$, the initial electron density for the calculations is assumed to be $\approx 5 \cdot 10^{8}$ cm^{-3}. However, the numerical results are insensitive to variations in this initial density.

Figures 6.2(a) and 6.2(b) provide the calculated time-dependent densities of several important chemical species in the discharge. The laser system is operated under typical conditions (i.e., 0.8%Xe/0.3%HCl/He gas mixture at a total pressure of 350 kPa and a capacitor charging voltage of 15 kV). Because Xe and He have large cross-sections for excitation and ionization at high electron energies, the densities of Xe^{*}, Xe^{+}, He^{*} and He^{+} build up rapidly at the beginning

Table 6.3 Rate Equations

$$\frac{d[XeCl^*]}{dt} = -\left(R_{24}[n_e] - R_{25}[HCl] + R_{26}[HCl(v)] + R_{27}[Xe] + R_{28}[He]\right)\cdot[XeCl^*]$$
$$- \sigma_1 \cdot c[N_p]([XeCl^*] - [XeCl]) - \frac{1}{\tau}[XeCl^*]$$
$$+ R_{14}[Xe^+][Cl^-] + R_{15}[Xe^*][HCl(v)] + R_{22}[Xe^*][Cl^-] + R_{23}[Xe^*][Cl]$$

$$\frac{d[XeCl]}{dt} = \frac{1}{\tau}[XeCl^*] + \sigma_1 \cdot c[N_p]([XeCl^*] - [XeCl]) - (R_{32}[He] + R_{33}[HCl]$$
$$+ R_{34}[Xe])\cdot[XeCl]$$

$$\frac{d[N_p]}{dt} = \frac{1}{\tau}\rho\,[XeCl^*] - \left(\sigma_1\cdot([XeCl^*] - [XeCl]) - \sigma_2[Xe^*] - \sigma_3[Cl^-]\right.$$
$$\left. - \sigma_4[He^*]\right)\cdot\frac{L_1}{L_2}\cdot c\,[N_p] + \ln(R)\cdot c\cdot[N_p]/L_2$$

$$\frac{d[Xe^*]}{dt} = -\left(R_5[n_e] + R_8[n_e] + R_{12}[Xe^*] + R_{15}[HCl(v)] + R_{16}[HCl] + R_{17}[HCl(v)]\right.$$
$$\left. + (R_{18} + R_{19})[Xe] + R_{23}[Cl] + c\cdot\sigma_2[N_p]\right][Xe^*]$$
$$+ R_1[n_e][Xe] + R_{31}[Xe_2^+][n_e]$$

$$\frac{d[Xe^+]}{dt} = -\left(R_{14}[Cl^-] + R_{20}[Xe] + R_{21}[Xe]\right)[Xe^+] + R_4[Xe][n_e] + R_5[Xe^*][n_e]$$
$$+ R_{12}[Xe^*][Xe^*] + R_{13}[He^*][Xe] + c\cdot\sigma_2[N_p][Xe^*]$$

$$\frac{d[Cl^-]}{dt} = -\left(R_{14}[Xe^+] + R_{22}[Xe^+] + c\cdot\sigma_3[N_p]\right)[Cl^-] + R_{10}[n_e][HCl] +$$
$$+ R_{11}[n_e][HCl(v)]$$

$$\frac{d[HCl(v)]}{dt} = -\left(R_{11}[n_e] + R_{15}[Xe^*] + R_{17}[Xe^*] + R_{26}[XeCl^*]\right)[HCl(v)]$$
$$+ R_3[n_e][HCl]$$

$$\frac{d[He^*]}{dt} = -\left(R_7[n_e] + R_9[n_e] + c\cdot\sigma_4[N_p]\right)[He^*] + R_2[n_e][He]$$

$$\frac{d[He^+]}{dt} = R_6[n_e][He] + \left(R_7[n_e] + c\cdot\sigma_4[N_p]\right)[He^*]$$

of the discharge, when the average energy of the electrons is high. The densities of Xe^+ and Xe^* are much higher than those of He^+ and He^*. Therefore, the dominant processes are direct ionization and excitation of Xe followed by ionization of Xe^* (shown schematically in Fig. 6.3). Cl^- is formed rapidly later in the discharge because the electron attachment processes have relatively large cross-sections at low electron energies. The densities of the secondary products $XeCl^*$ and XeCl peak after a small time delay.

The electron density is controlled primarily by the ionization of Xe and by the attachment of HCl. This density has two peaks corresponding to the two half cycles of the discharge current, as shown in Fig. 6.4. The maximum magnitude is almost one order higher than that in long pulse laser discharges. It's difficult to obtain long-duration stable discharge with this electron density.

The laser output pulse is an important characteristic of the laser performance. The output power is calculated from

$$P_L(t) = \frac{h \cdot \nu \cdot V}{T_c} N_p(t) \quad , \tag{6.20}$$

where $h\nu$ is the photon energy, V is the active discharge volume, $N_p(t)$ is the photon density, and T_c is the cavity lifetime (≈ 0.7 ns). The measured and calculated output waveforms are in good agreement with each other, as shown in Fig. 6.5. The output pulse has a duration of ≈ 1 ns (FWHM) and a peak power of ≈ 1 MW. Note that the secondary peak of the measured waveform, which is delayed by the round-trip time of the resonator, results from the reflection of the main peak at the output reflector. This effect has not been included in the calculations. To do so would have greatly increased computational complexity while providing little additional information.

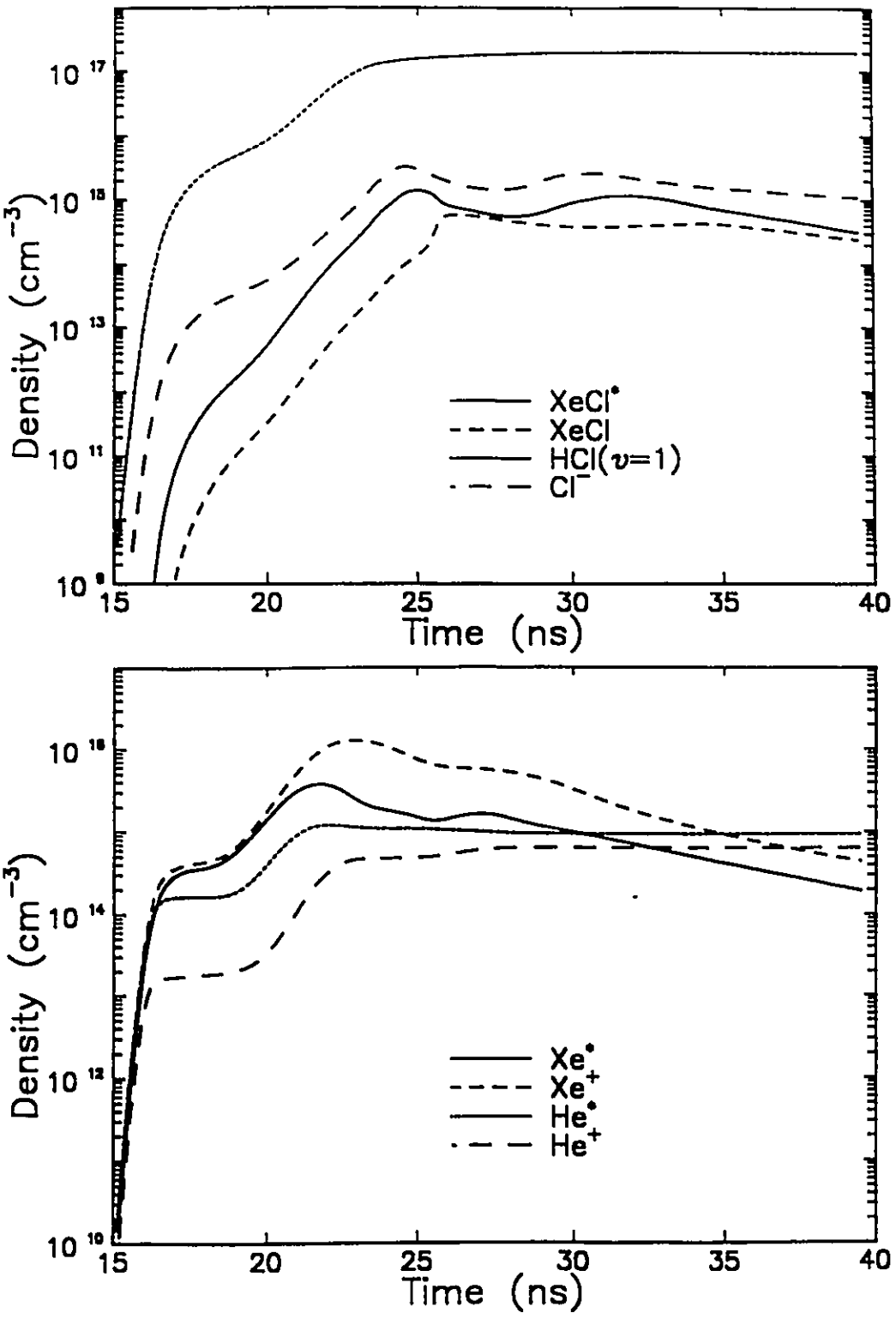

Fig. 6.2. Calculated time-dependent densities of several important chemical species in the discharge at normal operating conditions (0.8%Xe/0.3%HCl/He, total pressure P=350 kPa, charging voltage V_0=15 kV). The time scale is relative to the initiation of spark-gap breakdown.

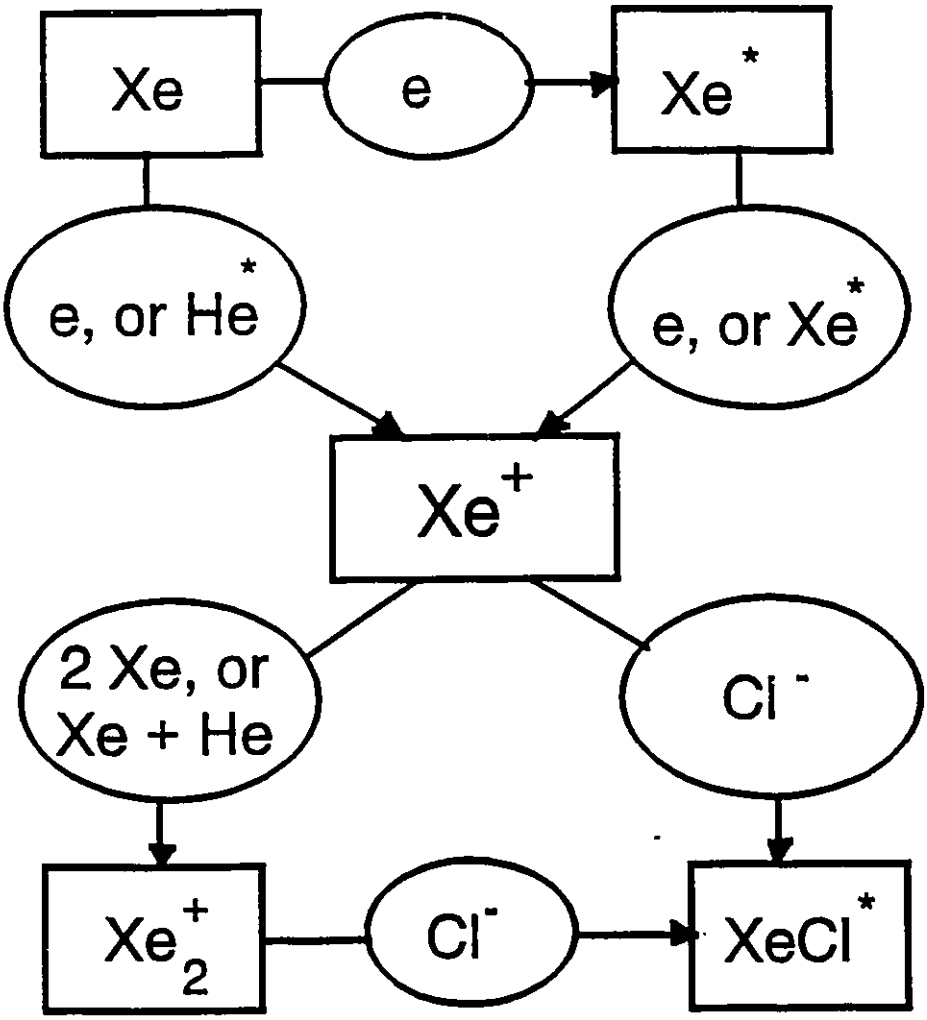

Fig. 6.3. A schematic diagram for the reactions involving Xe.

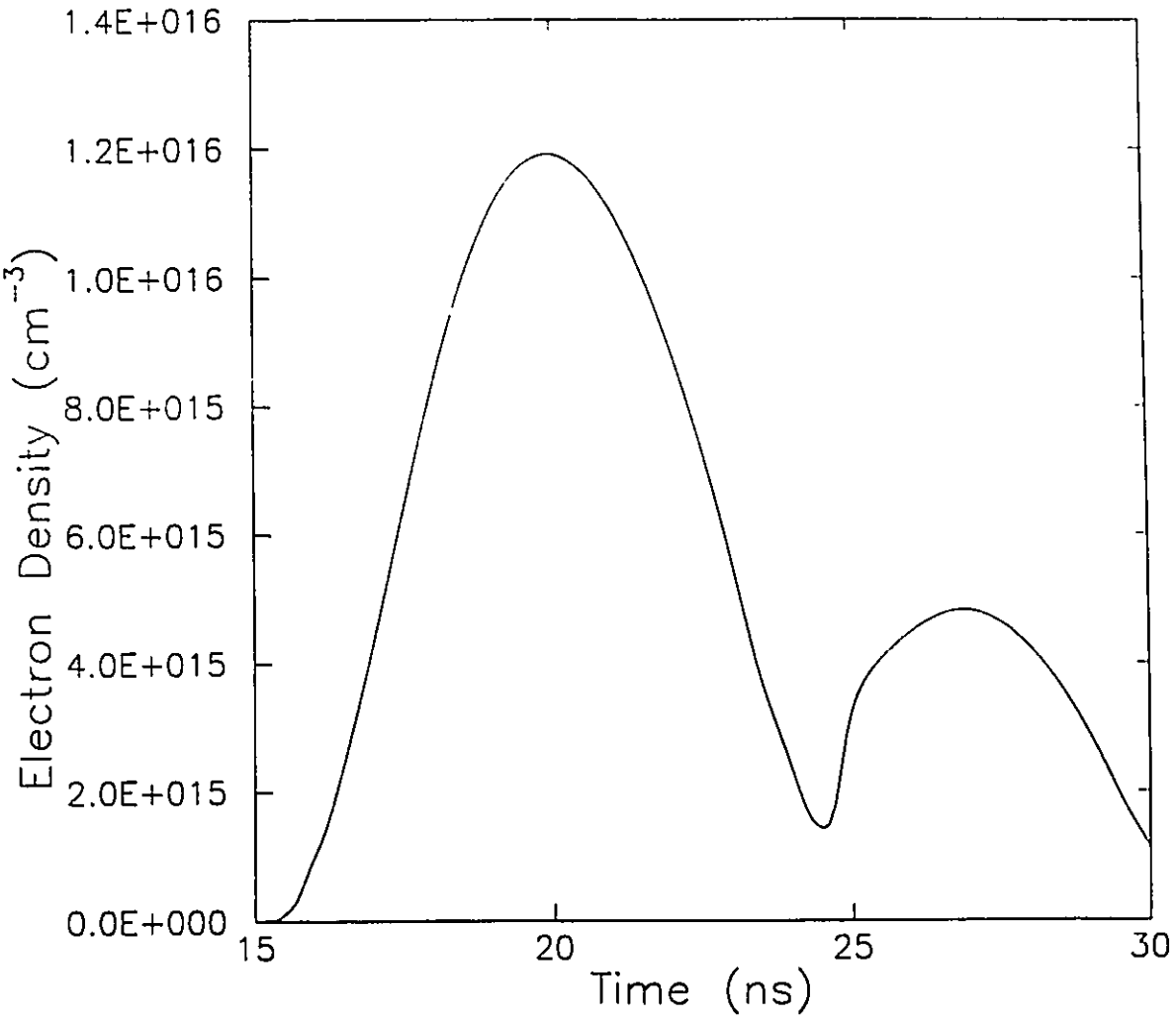

Fig. 6.4. Calculated time-dependent density of electrons in discharge at the normal operating conditions (see Fig. 6.2). The time scale is relative to the initiation of spark-gap breakdown.

6.3. Laser Output Parameters.

The laser output energy per pulse is the integral of Eq. (6.20) over the pulse duration. This energy, as a function of capacitor charging voltage, and using a typical gas mixture, is shown in Fig. 6.6. The results from both measurements and calculations indicate that the output energy is approximately proportional to the charging voltage in the voltage range from 12 kV to 21 kV. Below 12 kV, this energy begins to drop rapidly with deceasing charging voltage. From the calculations, the output energies are expected to saturate at voltages higher than 21 kV, for the following reason. The electron density in the discharge increases with capacitor charging voltage. Consequently, the discharge impedance deceases. The result is that the proportion of energy expended in the first half-cycle of the discharge current (the portion providing the main gain production) decreases. Experiments for higher voltages were not carried out because of the potential for component damage (e.g., circuit-board breakdown).

The quantum efficiency (η_q) is defined by

$$\eta_q = \frac{laser\ output\ energy}{E^*} \quad , \tag{6.21}$$

where E* is the energy absorbed by inelastic reactions in the discharge. The efficiency of energy deposition into the discharge (η_p) is defined by

$$\eta_p = \int I_2^2 \cdot RD \cdot dt / [\frac{1}{2}(C1 + C2) \cdot V_0^2] \quad , \tag{6.22}$$

where I_2 and RD are discharge current and impedance, respectively.

The laser output energy and efficiency as a function of a single-component gas pressure (other partial pressures are kept constant) are shown in Figs. 6.7, 6.8 and 6.9. For this data, the

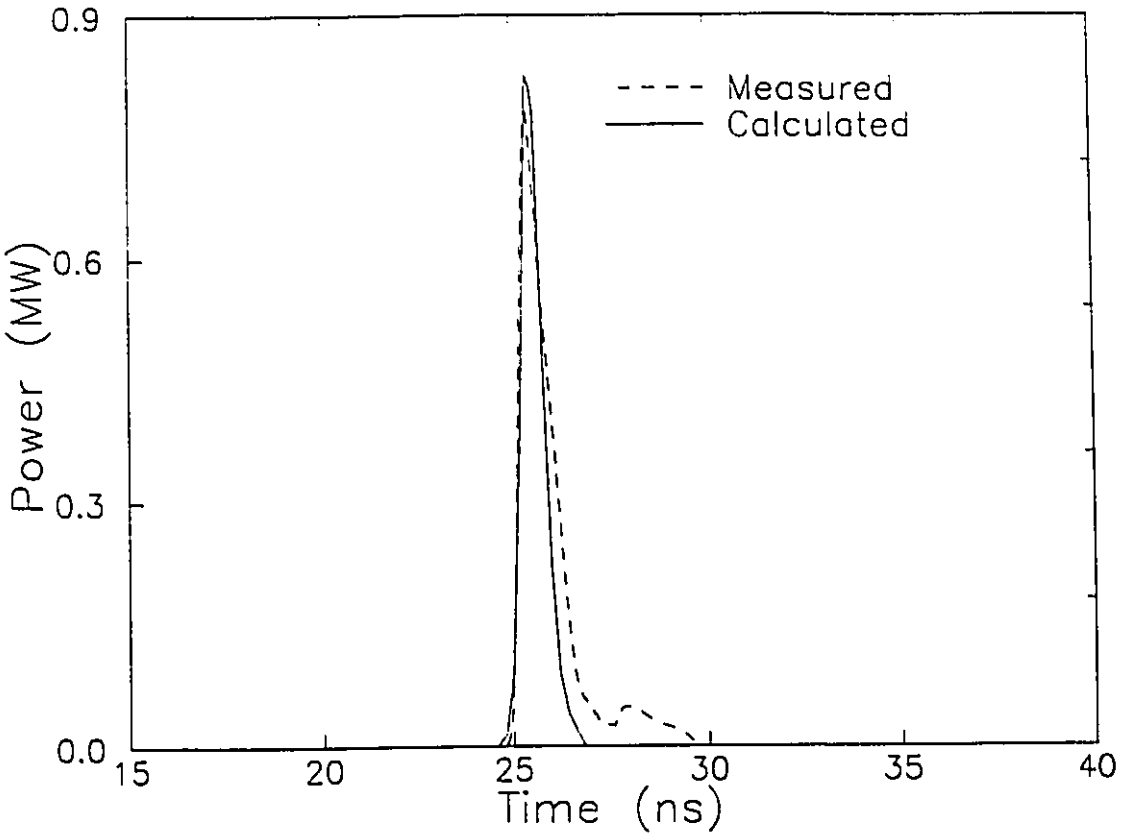

Fig. 6.5. Measured and calculated laser-output waveforms at normal operating conditions (see Fig. 6.2). The time scale is relative to the initiation of spark-gap breakdown.

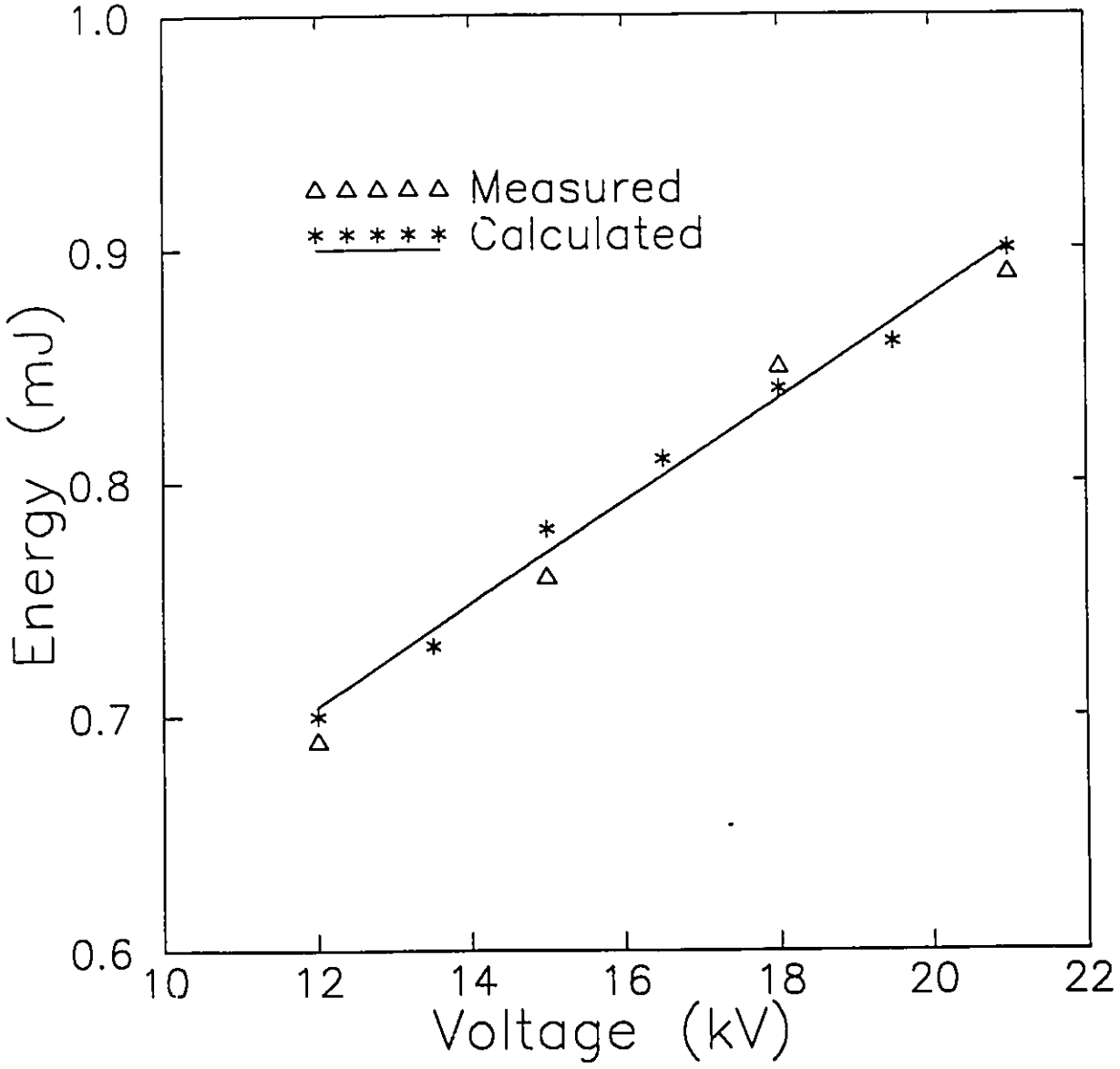

Fig. 6.6. Calculated and measured laser output energies as a function of the capacitor charging voltage (0.8%Xe/0.3%HCl/He, total pressure P=350 kPa).

charging voltage is kept constant at 15 kV. In all these cases, the output energy increases with increasing gas pressure, and saturates at the higher pressures. However, the increases in each case occurs for different reasons, which can be explained by considering the efficiencies.

For the data represented by Fig. 6.7(b), when the density of He increases, the electron mobility decreases, resulting in an increase of the discharge impedance. Consequently, the total energy deposited into the discharge increases. Therefore, η_p is almost proportional to He pressure in the region of interest. However, He doesn't contribute directly to the formation of the upper laser level. The quantum efficiency η_q decreases at the higher pressures because a larger proportion of the discharge energy is used to excite the He.

As can be seen from Figs. 6.8(b) and 6.9(b), the Xe and HCl densities have only a small effect on η_p. The reason is that the proportions of Xe and HCl are very small compared to that of He. Consequently, the energy deposited into the discharge is determined primarily by the He pressure. In the cases of Xe and HCl, the quantum efficiency η_q is influenced more by the pressures of these gases than by the He pressure. The densities of Xe^+ and Cl^- produced in a discharge increases with the Xe and HCl densities. Recombination of Xe^+ and Cl^- is the main channel for $XeCl^*$ formation.

Figures 6.10(a) and 6.10(b) show the calculated time development of the total discharge excitation power density, and the power density absorbed from the discharge for several electron-impact processes. The waveforms have two peaks which correspond to the two half-cycles of the discharge current. Most of excitation energy is deposited into the discharge during the first full cycle of the discharge current. The main energy deposition results from the excitation and ionization of Xe and He, which occur at the beginning of discharge, when the electric field is large. Vibrational excitation of HCl(v=0) and the ionization of metastable Xe^* and He^* occur

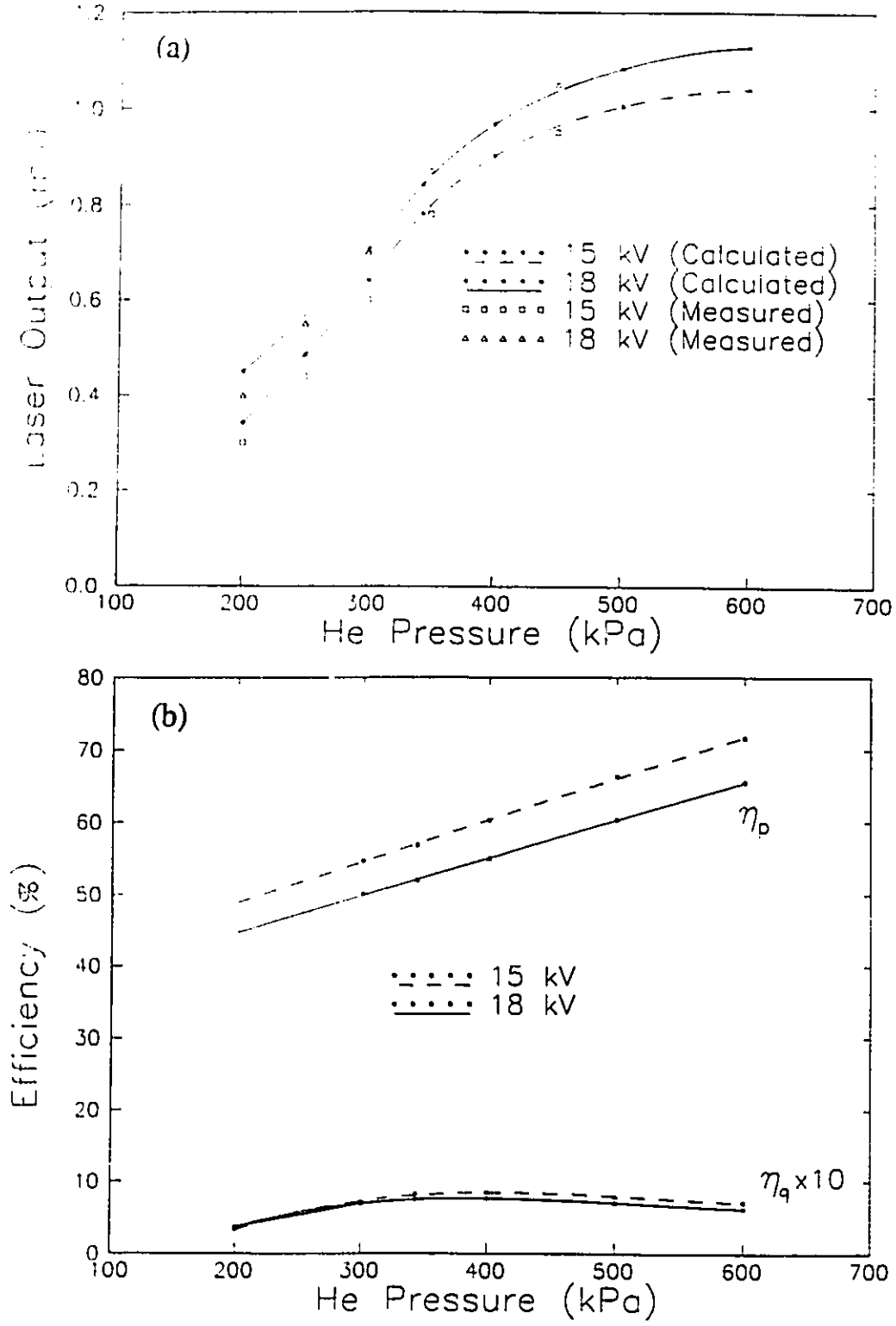

Fig. 6.7. (a) Laser output energy as a function of the He pressure. (b) Calculated efficiencies η_q and η_p as a function of He pressure. The Xe and HCl pressures were kept constant at 20.8 Torr and 7.8 Torr, respectively.

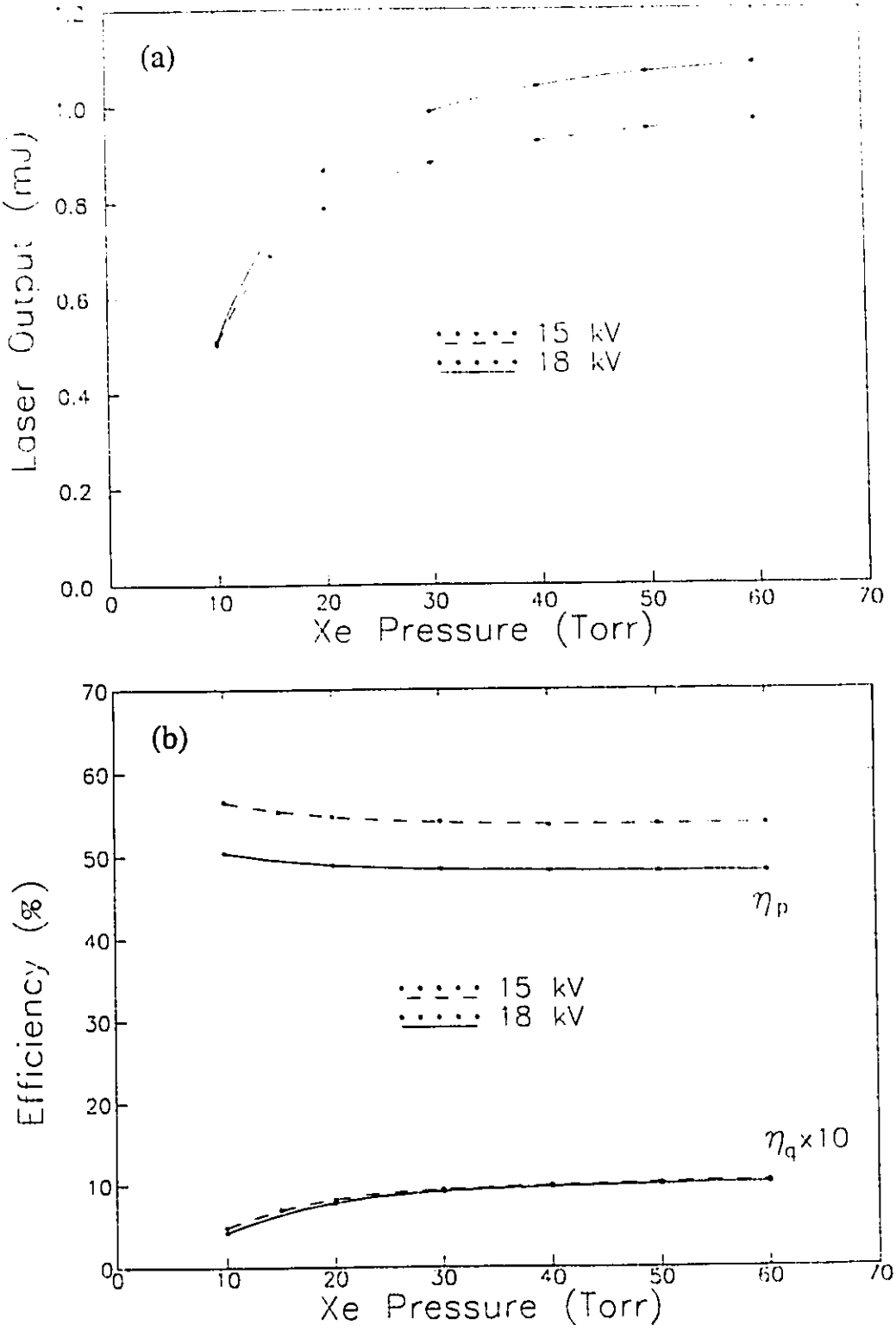

Fig. 6.8. (a) Laser output energy as a function of Xe pressure. (b) Calculated efficiencies η_q and η_p as a function of Xe pressure. The He and HCl pressures were kept constant at 350 kPa and 7.8 Torr, respectively.

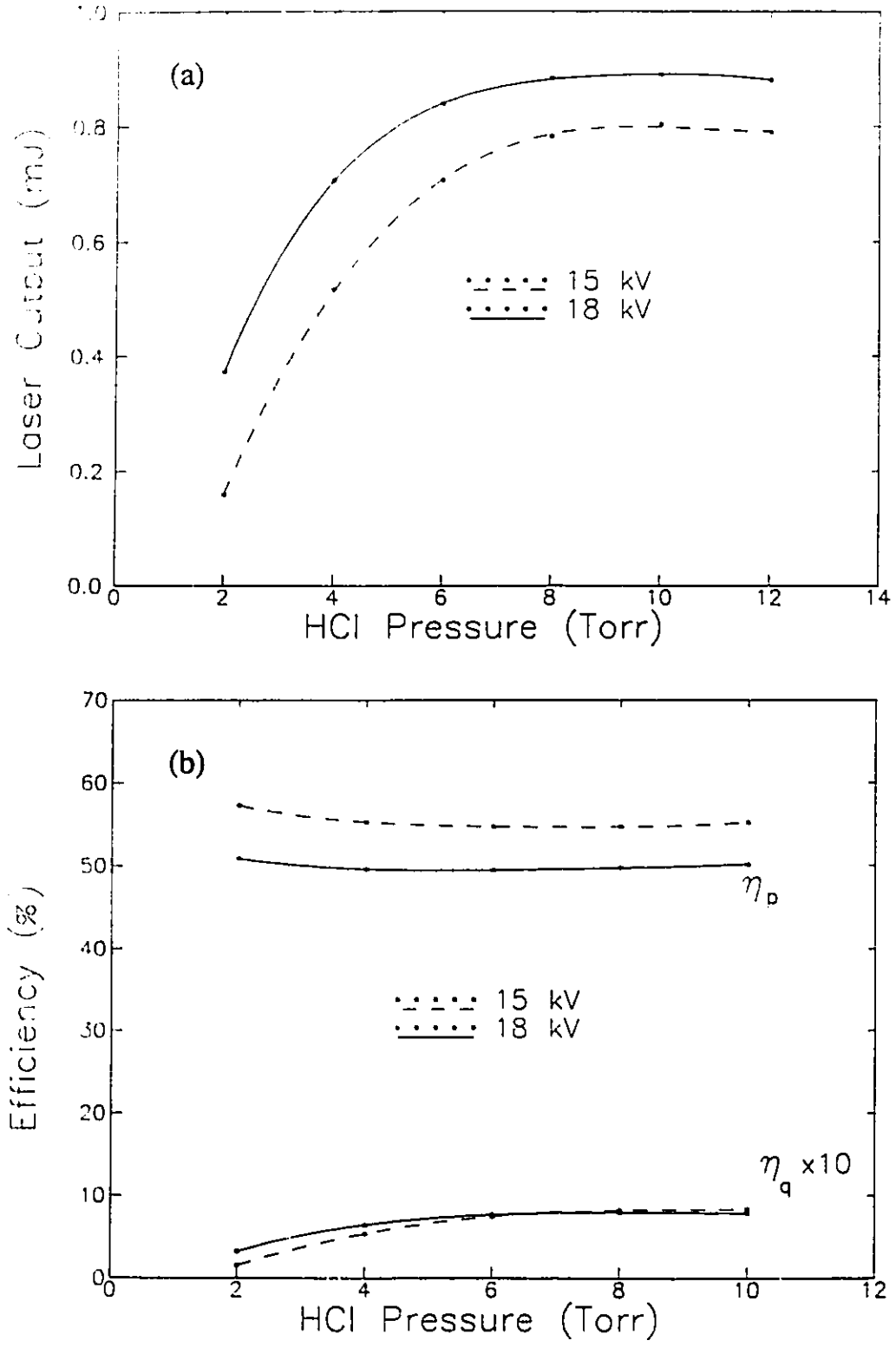

Fig. 6.9. (a) Laser output energy as a function of HCl pressure. (b) Calculated efficiencies η_q and η_p as a function of HCl pressure. The He and Xe pressures were kept constant at 350 kPa and 20.8 Torr, respectively.

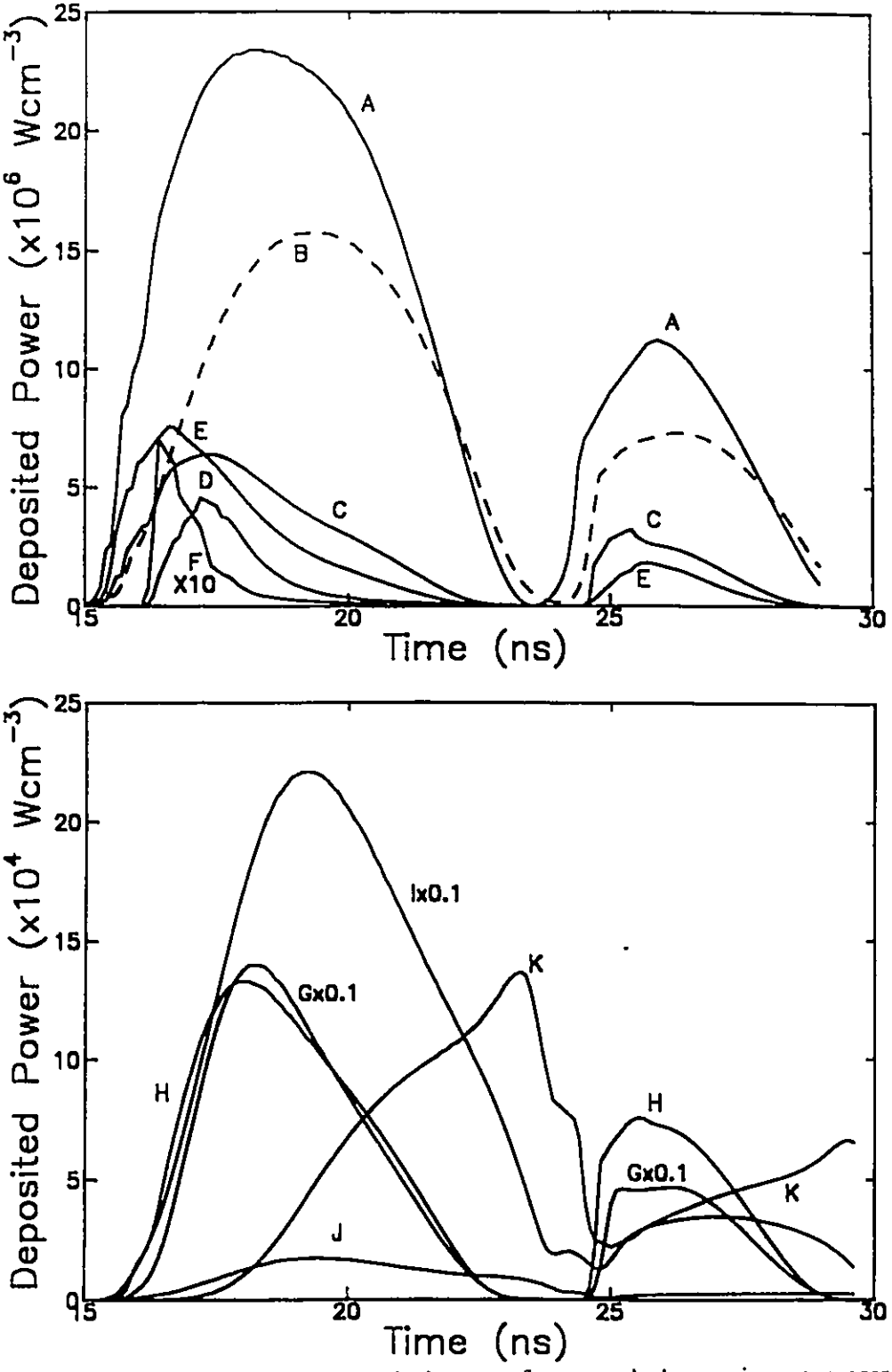

Fig. 6.10. Time development of deposited power for several electron-impact processes. The normal operating condition apply (see Fig. 6.2). For Fig. 6.10(a): A. Total deposited power, B. Loss due to elastic collisions, C. Excitation of Xe, D. Excitation of He, E. Ionization of Xe, and F. Ionization of He. For Fig. 6.10(b): G. Ionization of Xe^*, H. Ionization of He^*, I. Vibrational excitation of HCl(v=0), J. Electron attachment to HClv=0), and K. Electron attachment to HCl(v=1).

near the maximum of the discharge power deposition. However, efficient electron attachment to HCl(v=0) and HCl(v=1) occurs at the smaller electric fields present in the later stages of the discharge, when the electron energies are reduced.

To assist in understanding the discharge excitation processes, an energy flow diagram is shown in Fig. 6.11. The energies obtained from the model are also shown in the figure. The circuit loss is primarily in the spark-gap circuit.

The nonlinear gain and absorption characteristics of the XeCl laser system are investigated with the aid of the kinetic model. Macroscopic parameters, such as the unsaturated gain g_0, the absorption coefficients α_0 and the saturation irradiance ϕ_s, are evaluated in terms of the microscopic kinetic properties of the discharge. The calculations are carried out by assuming a quasi-steady state condition at each time step. Using the rate equations for $XeCl^*$ and XeCl listed in Table 6.3, results in

$$([XeCl^*]-[XeCl])\sigma_l\phi - [XeCl]Q'' + \frac{1}{\tau}[XeCl^*] + F'' = 0 \qquad (6.23)$$

and

$$([XeCl^*]-[XeCl])\sigma_l\phi + [XeCl^*]Q' + \frac{1}{\tau}[XeCl^*] - F' = 0 \quad , \qquad (6.24)$$

where σ_l is the stimulated-emission cross-section, $\phi = c \cdot N_p$ is the irradiance flux, Q" and F" are the total quenching frequency and formation rate, respectively, for the ground state XeCl, and Q' and F' are the corresponding values for the exciplex state $XeCl^*$. The inverted density is evaluated using

$$\Delta N = \frac{(Q''-\frac{1}{\tau})F' - (Q'+\frac{1}{\tau})F''}{Q''(Q'+\frac{1}{\tau}) + \sigma_1\phi(Q'+Q'')} \quad . \tag{6.25}$$

The laser gain, defined by $g = \sigma_1 \cdot \Delta N$, can be put in the form

$$g = \frac{g_0}{1+\phi/\phi_s} \quad . \tag{6.26}$$

Consequently, the unsaturated gain, and the saturation irradiance are

$$g_0 = (\frac{Q''-1/\tau}{Q'+1/\tau})\frac{F'}{Q''} - \frac{F''}{Q''} \tag{6.27}$$

and

$$\phi_s = \frac{Q'+1/\tau}{\sigma_1(1+Q'/Q'')} \quad , \tag{6.28}$$

respectively. If the absorption from all photoabsorbers is considered, then the absorption coefficient α_0 is

$$\alpha_0 = \sigma_2[Xe^*] + \sigma_3[Cl^-] + \sigma_4[He^*] \quad , \tag{6.29}$$

and the net optical gain is

$$g_{net} = g - \alpha_0 \quad . \tag{6.30}$$

The calculated parameters g, g_0, α_0 and ϕ, as functions of time are given in Fig. 6.12. While the saturation irradiance is determined only by the quenching frequencies, the unsaturated gain depends primarily on the formation rate of $XeCl^*$. Because this formation rate is determined predominantly by ionization and excitation of Xe, both the gain duration and the laser output pulse can be controlled by the duration of the discharge excitation. In our laser system, the short duration output pulse is determined solely by the short-duration discharge.

6.4. Comparison of the Xe/HCl/He and Xe/HCl/Ne Systems.

Investigations have been carried out using different buffer gases (He and Ne) for the XeCl laser. For our short-pulse discharge system, both measurements and calculations show that the laser pulse duration is approximately the same with the different buffer gases. However, the peak laser output power and total energy per pulse for the Xe/HCl/He system is ≈ 1 MW and ≈ 1 mJ, respectively, for the normal discharge conditions (i.e., 0.8%Xe/0.3%HCl/He at a total pressure 450 kPa and a charging voltage 15 kV). These are at least 20% higher than the corresponding values for the 1.06%Xe/0.24%HCl/Ne system under the same conditions.

The electron-energy distributions for the 0.8%Xe/0.3%HCl/He and 1.06%Xe/0.24%HCl/Ne systems, for the same E/N ratio, are shown in Fig. 6.13. The peak of the distribution function is broadened and shifted towards higher energies when Ne is used as the buffer in place of the He. This results from a smaller kinetic-energy loss in the momentum-transfer involving collisions of electrons with the heavier Ne atom. In addition, and in comparison with He, less energy is required to ionize and excite Ne.

The laser outputs are affected not only by formation of $XeCl^*$, but also by the amount of energy deposited into discharge. As shown in Fig. 2.12, the rate of three-body ionic recombination for $XeCl^*$ is higher with Ne than with He. In both cases, the buffer gases provide a mechanism for efficient energy transformation of the reaction. However, the average electron energy in a Ne system is higher than in a He system, and the ionization rates of rare-gas atoms increase with increased electron energy. As a result, the electron density produced in a Ne system is considerably higher than in a He system. This higher electron density and a correspondingly higher electron mobility provides a smaller discharge impedance when using a Ne buffer.

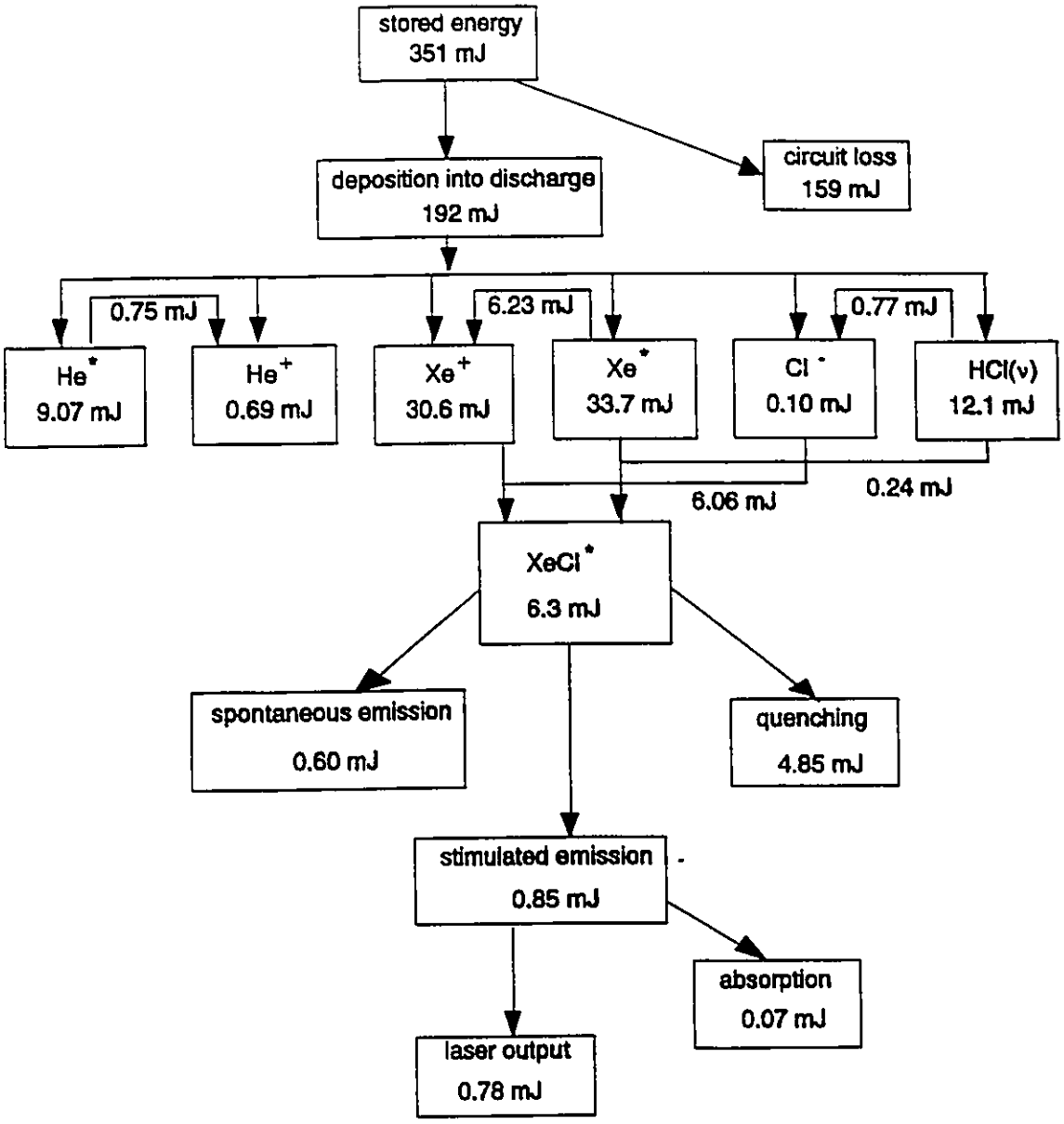

Fig. 6.11. A schematic diagram of energy flow in the XeCl laser system. (0.8%Xe/0.3%HCl/He, total pressure P=350 kPa).

Therefore, compared to a He system, less energy is deposited into a Ne system during the first half-cycle of discharge, resulting in a lower laser output energy.

The discharge impedances for both buffer gases are shown in Fig. 6.14. The minimum value of the discharge impedance is 0.2 Ω using the Ne buffer, and 0.6 Ω using the He buffer. In order to achieve maximum energy deposition, the minimum discharge impedance, RD_m, should be the value for which the circuit Q is equal to 1. Therefore,

$$RD_{min} = \sqrt{LD/C3} \quad , \tag{6.31}$$

where

$$C3 = \frac{C1 \cdot C2}{C1 + C2} \quad . \tag{6.32}$$

In our laser excitation circuit, the inductance LD is 6 nH and the equivalent capacitance C3 is 0.78 nF, which requires that $RD_m \approx 2.8$ Ω for maximum energy deposition. Therefore, the energy deposited in the He system ($RD_m \approx 0.6$ Ω) is higher than in the Ne system ($RD_m \approx 0.2$ Ω). It should be noted that, in larger system with longer output pulse durations, the laser efficiency and energy per pulse are usually higher with Ne buffer than with He buffer.

6.5. Summary

Investigations of the physics of the kinetic processes in a discharge plasma are discussed thoroughly in this chapter. A self-consistent model is developed for the laser processes and the discharge circuit. This model allows calculation of the laser output pulse waveform, energy, gain coefficients, and the efficiency of various energy transfer processes. The validity of this model is confirmed by good agreement between the calculated and measured data. This model can be

used for the optimization of laser performance.

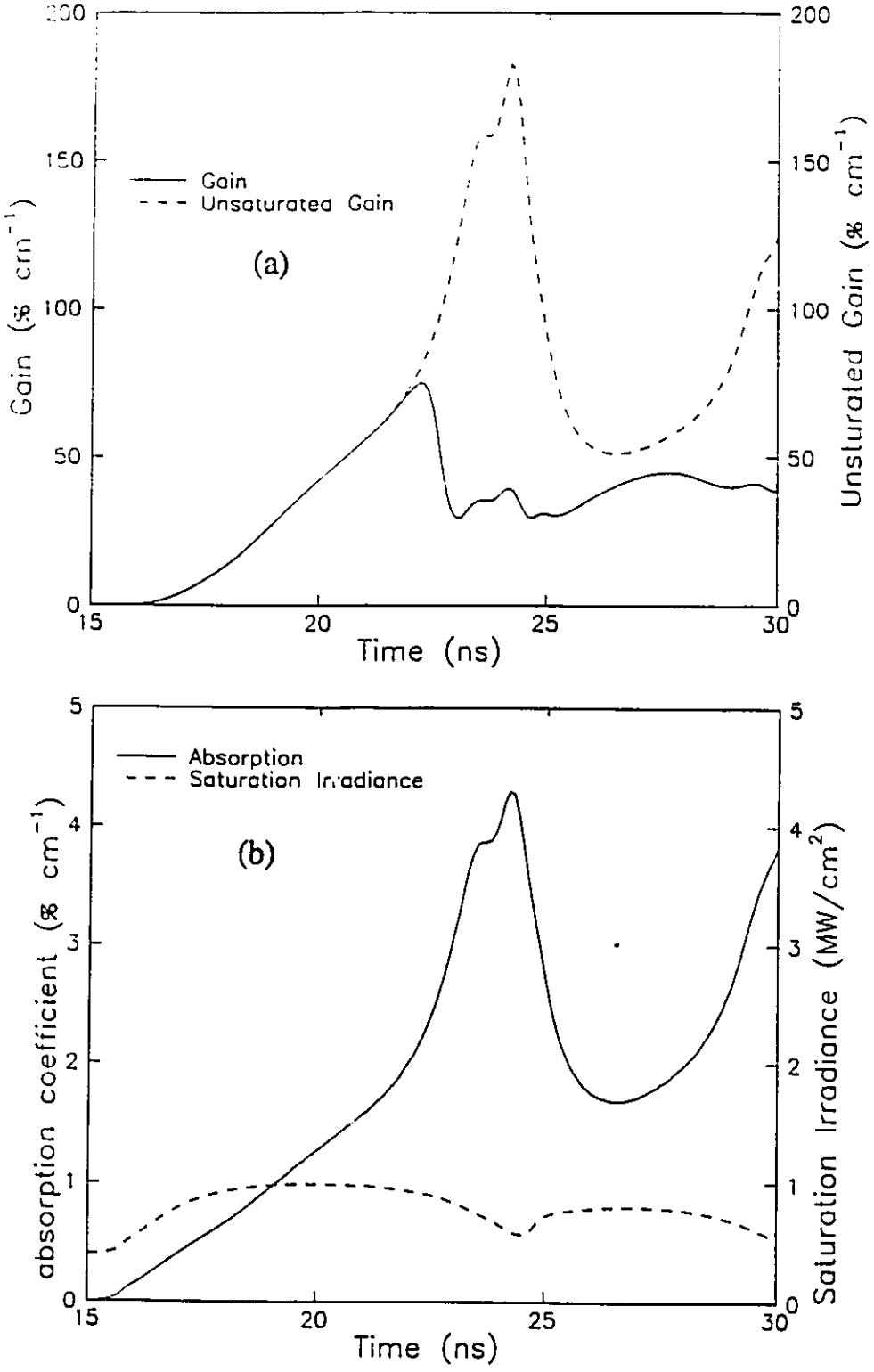

Fig. 6.12. (a) Calculated gain and unsaturated gain coefficients, and (b) absorption coefficient and saturation irradiance as a function of time, at normal operating conditions (see Fig. 6.2).

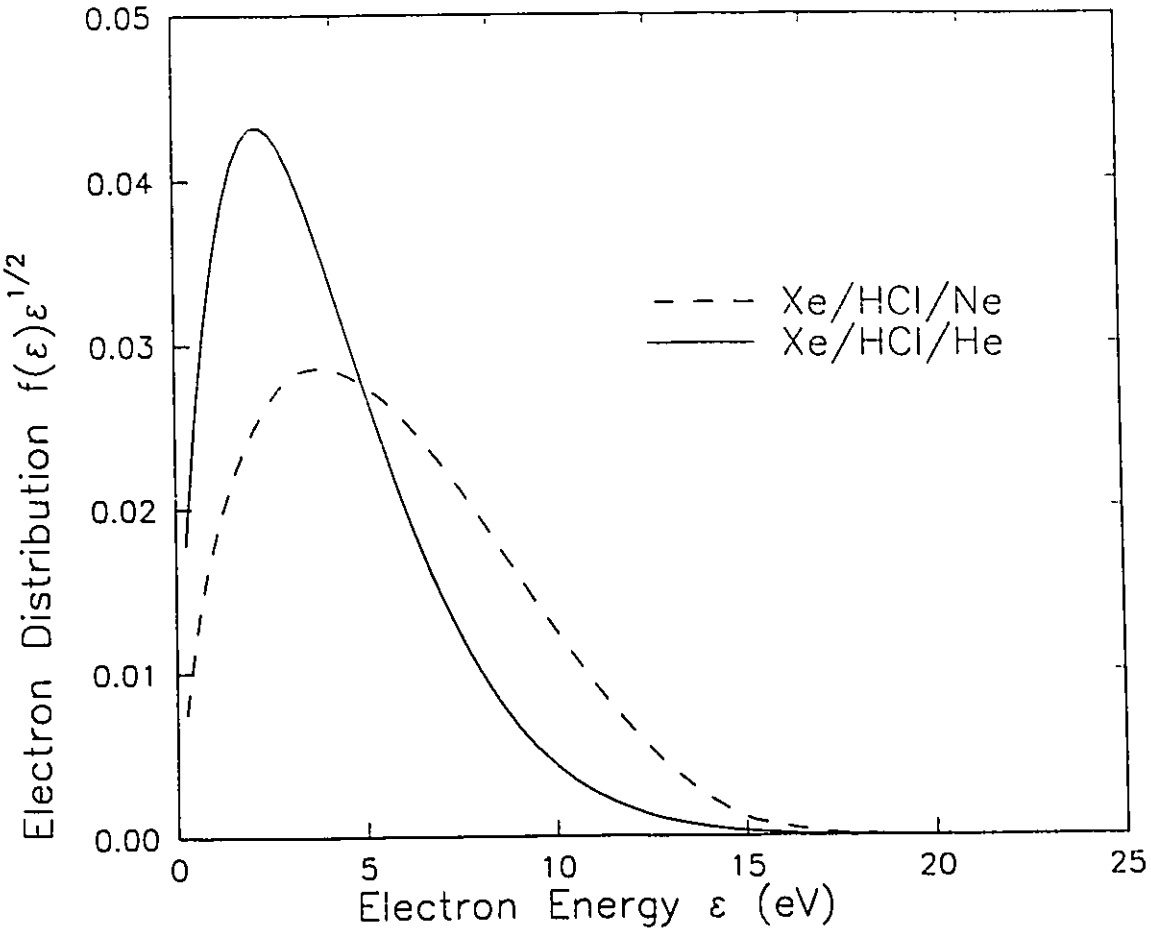

Fig. 6.13. Electron energy distribution for Xe/HCl/He and Xe/HCl/Ne systems using the same E/N ratio (1.76×10^{-17} Vcm^2).

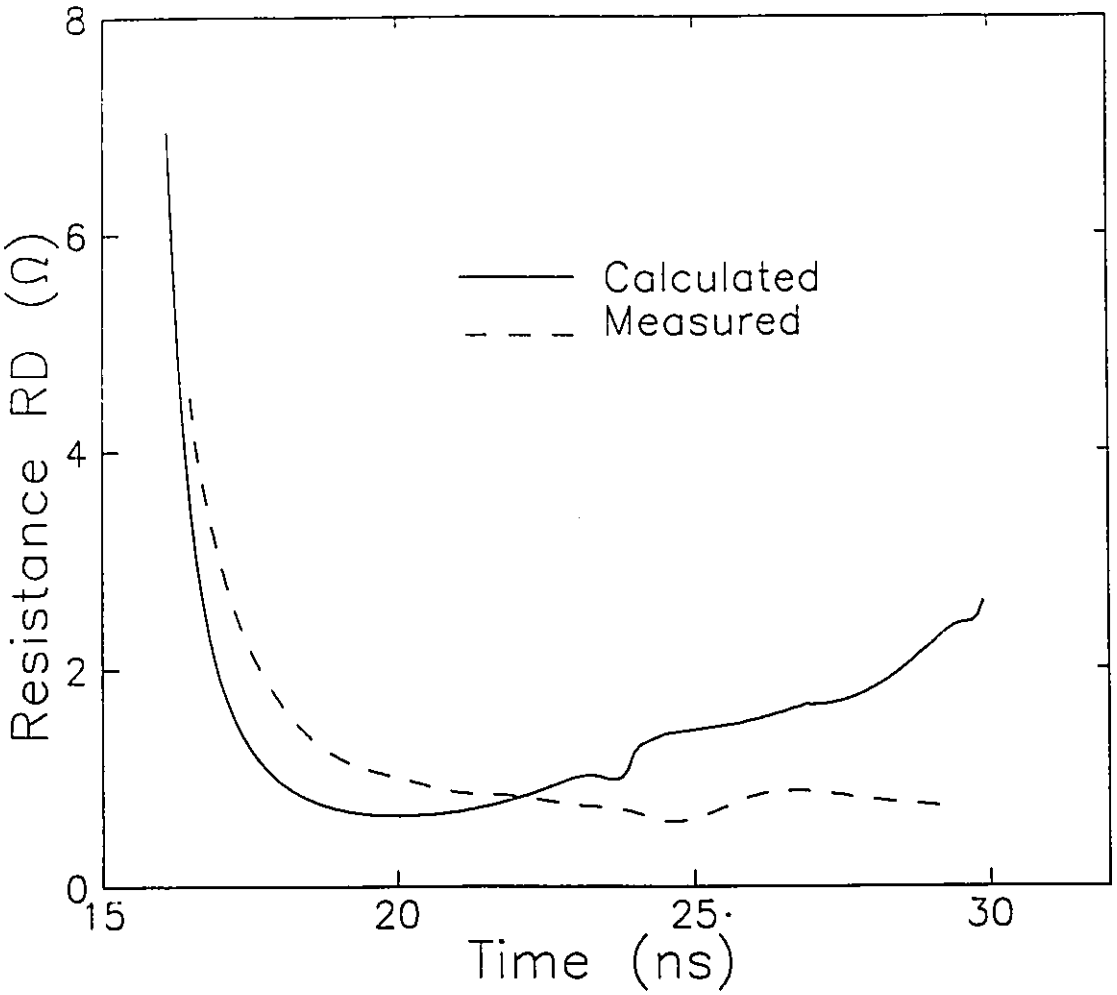

Fig. 6.14. Time-dependent discharge impedance for the Xe/HCl/He and Xe/HCl/Ne systems. In both cases, $V_0 = 15$ kV and P=350 kPa. The time scale is relative to the initiation of spark-gap breakdown.

Chapter 7

Conclusions and Recommendations

7.1. Conclusions.

This thesis reports on a comprehensive investigation of a compact, UV-preionized, discharge-excited, short-pulse XeCl laser. The investigation includes the following main areas:

(1) Theoretical studies of the molecular states and potential-energy curves of XeCl, and possible radiative transitions for this molecule.

(2) Development of an electron-jump model for the calculation of the formation rate for the exciplex $XeCl^*$.

(3) Measurements of the laser output over a range of discharge conditions.

(4) Measurements of the discharge voltage and current waveforms employing fast-response instrumentation, and modelling of the excitation circuit.

(5) Detailed investigations of the laser kinetics, including numerical solution of the Boltzmann equation for the electron energy distribution.

(6) Application of the kinetic model to the evaluation of laser performance.

A basic description of the molecular structure of rare-gas monohalides is provided. All of these molecules have a structure configuration similar to that of the XeCl molecule. It is expected that the ground state of XeCl ($X^2\Sigma^+_{1/2}$) is essentially repulsive because of the weak interaction between the closed shell of $Xe(^1S_0)$ and open shell of $Cl(^2P_{3/2})$. However, spectral measurements reported in the literature show that a shallow potential-energy well (281-cm^{-1} deep) exists for the

$X^2\Sigma^+_{1/2}$ state, which contains 20 vibrational levels. The weak bond of the $X^2\Sigma^+_{1/2}$ state is explained as a van der Waals attraction induced by charge-transfer mixing of the ground state with the ionic-bound excited states.

Three strongly-bound ionic excited states ($B^2\Sigma^+_{1/2}$, $C^2\Pi_{3/2}$ and $D^2\Pi_{1/2}$) of the XeCl molecule are formed from the ions $Xe^+(^2P_{3/2})$, $Xe^+(^2P_{1/2})$ and $Cl^-(^1S_0)$. The higher excited states are the covalent Rydberg states formed from Cl atoms and metastable Xe atoms. Employing the selection rules for electric-dipole transitions, there are five radiative transitions from the ionic excited states ($B^2\Sigma^+_{1/2}$, $C^2\Pi_{3/2}$ and $D^2\Pi_{1/2}$) to the ground states ($X^2\Sigma^+_{1/2}$, $A^2\Pi_{3/2}$ and $A^2\Pi_{1/2}$). Using experimental data from various sources, it is concluded that the bound-bound transition B → X (308 nm) has the strongest intensity at high gas pressures. At these pressures the ionic states $C^2\Pi_{3/2}$ and $D^2\Pi_{1/2}$ are quenched very rapidly. Therefore, efficient B → X laser operation is also expected to occur at high gas pressures. The lifetimes and stimulated-emission cross-sections for the B → X and D → X transitions were calculated using the Franck-Condon factors. The accuracy of our calculations is dependent on the accuracy of the dipole moments reported by Hay and Dunning (1978).

An electron-jump (harpoon) model is developed to calculate the formation rate-coefficient of the exciplex $XeCl^*$. This model, based on the pseudo-crossings of the potential-energy curves of the ionic states and Rydberg states, confirms that three-body ionic recombination of Xe^+ and Cl^- is the most important channel for $XeCl^*$ exciplex formation. Good agreement is achieved between the data from our model and those from previous models, at low and intermediate gas pressures. The other models predict that, at high pressures, there is a decrease in the rate coefficients with increasing pressure. However, the rate-coefficients from our calculations "saturate" to a constant value in this pressure range. In addition, our model provides important

new information. It is shown that two additional channels, involving metastable Xe^* and Cl atoms, are also efficient paths for the formation of $XeCl^*$ in the presence of a third light body (i.e., He). Furthermore, our model is able to evaluate the rate-coefficients for each individual dissociative channel for $XeCl^*$.

The compact laser system employed for the research has an active discharge volume of 1 cm^3, providing ≈ 1 mJ output energy in a pulse duration of ≈ 1 ns. This corresponds to a peak output power of ≈ 1 MW. Elsewhere, only recently have comparable short-duration output pulses been produced directly in a discharge-excited excimer laser. In order to obtain high-energy short-duration laser output pulses, a high density of excitation energy must be deposited in a short time interval. Therefore, care was taken to reduce the oscillation period of the excitation circuit, in particular to minimize the circuit inductance. The maximum discharge-current risetime is $\approx 0.3 \cdot 10^{13}$ A/s. With the type of UV preionization employed, the discharge is observed to be reasonably uniform. The cavity length is 16.5 cm, corresponding to a cavity round-trip time of 1.1 ns, which is longer than the usual duration of the laser output.

Experimental investigations indicate that the best performance with our laser is achieved using a 0.8%Xe/0.3%HCl/He gas mixture at a total gas pressure in the range from 350 kPa to 450 kPa. This provides a small excess of HCl, which improves laser operating lifetime. A charging voltage of 15 kV provides good output energy and reliability. In addition, the output pulse duration is nearly independent of the charging voltage and the gas composition and pressure. However, increasing the excitation-circuit inductance increases the pulse duration by a small amount. The peak power and the energy per pulse are found to be approximately proportional to the charging voltage in the range from 12 kV to 21 kV. Initially, the laser energy increases with the total gas pressure, and with the partial gas pressures of Xe and HCl, until the

optimum values are achieved (≈450 kPa total pressure, ≈0.8% Xe and ≈0.2% HCl). At gas pressures below 350 kPa, a second peak is observed. This peak is caused by gain production in the second half-cycle of the discharge current.

The discharge voltage and current waveforms provide very important data concerning the energy deposition into the discharge. Accurate measurements of these waveforms are also required for comparison with the results of the model for the discharge kinetics. An optical technique employing a fast-response Pockels cell was used for the measurement of discharge voltages. This technique provides good linearity for the range of high voltages employed. The time-response of the measurement system was limited by the photomultiplier (≈2 ns). However, deconvolution of the known instrumentation response from the measured waveform extended the response to considerably better than 1 ns. Overall, the optical technique is the most reliable and accurate method available for measuring the discharge voltage of devices such as the compact XeCl laser.

Discharge current waveforms were measured using a fast-response Rogowski coil. After discharge breakdown, the voltage and current waveforms are very similar to each other in terms of relative amplitude, period and phase. This indicates that the discharge behaves approximately like a resistance of constant value (≈ 1 Ω). From an analysis of the periods and damping factors of the waveforms, the values of the components in the excitation circuit can be determined. These values are then used in the model for the circuit. The circuit model, combined with the kinetic model, results in a self-consistent model for the XeCl laser. Good agreement is achieved between the measured and calculated waveforms.

Electron-impact collision processes are very important in the kinetics of gas lasers. A comprehensive description of classical and quantum theories for elastic collisions is provided in

the thesis. The Boltzmann equation for a spatially-homogeneous medium is employed to investigate electron transport in a discharge within either a Xe/HCl/He or Xe/HCl/Ne mixture. In addition to the elastic collisions with neutral species, the calculations also include the excitation, ionization and superelastic collisions with various other species, as well as electron-electron Coulomb collisions. A numerical code using a finite difference method was developed to solve the Boltzmann equation. The electron energy distribution, obtained from the solution of Boltzmann equation, is used to determine the rate-coefficients for the electron-impact collisions. These rate-coefficients are then used in the kinetic model. In addition, the parameters, such as electron mobility, discharge impedance, discharge current and average electron energy, are calculated on the basis of the microscopic collision processes.

Our concise kinetic model requires only 40 kinetic processes involving 13 chemical species, plus photons and electrons. These 40 processes, chosen from a much larger number of possible processes, all have relatively large rate-coefficients and thus have a significant influence in a short-duration discharge. All of the eliminated processes have relatively small rate-coefficients. The model was developed using the criterion that good agreement should exist between the calculated and measured laser output in terms of waveforms, peak power, total energy, and delay time to the onset of laser emission. The validity of the model is also confirmed by the good agreement between the measured and calculated discharge voltage, current and impedance waveforms. The important results from the model are summarized below.

(a) At high pressures, the formation of the upper laser level $XeCl^*$ via three-body ionic recombination of Xe^+ and Cl^- is dominant to the harpooning (electron-jump) process involving Xe^* and HCl(v). For the typical gas mixture containing 0.8%Xe/0.3%HCl/He at 350 kPa pressure, less that 5% of $XeCl^*$ is formed through the harpooning process.

(b) The exciplex $XeCl^*$ is depleted primarily via quenching collisions with neutral species (He, Xe, HCl and HCl(v)) and via superelastic collisions with electrons. It is found that quenching by electrons is the dominant loss mechanism for $XeCl^*$ at the degree of ionization existing in our laser discharge (10^{-5} to 10^{-4}). Consequently, this latter quenching process is the major factor limiting the laser peak power. Quenching by He is the second most important loss channel because of the large population of He.

(c) The lower laser level XeCl(X) has a finite lifetime, resulting from dissociation of XeCl, primarily by collisions with He atoms. For a collision rate of $3.0 \cdot 10^{-12}$ cm^3/s and a He density of $\approx 1.0 \cdot 10^{21}$ cm^{-3}, the lifetime is ≈ 0.3 ns.

(d) Photon absorption by Cl^-, Xe^* and He^* is considered in the calculations. The major absorber in our gas mixture is Cl^- because of its large absorption cross-section. This photon absorption is not too important for our short-pulse laser. The calculations indicate that $< 10\%$ of the laser emission is absorbed. However, photon absorption may be significantly greater in XeCl lasers having longer-duration output pulses.

(e) Studies of the energy flow in the discharge show that the excitation energy is deposited into the discharge mostly via electron-impact ionization and excitation of Xe atoms. Free electrons are produced primarily by ionization of Xe and Xe^*. However, the density of He in the gas mixture affects the electron energy distribution, and consequently the discharge impedance. In the usual range of pressures employed in our laser, the efficiency of energy deposition increases with He pressure. Initially, the quantum efficiency of the laser increases with Xe and HCl, but is relatively independent of the He pressure in the region when a stable discharge exists. The quantum efficiency reaches a maximum near the usual operating mixture (0.8%Xe/0.3%HCl/He). There is a small increase in efficiency when the HCl is reduced to

0.2%, but at a reduced laser operating lifetime.

(f) The nonlinear gain and absorption coefficients, and the saturation irradiance of the XeCl laser are calculated using the kinetic model. These macroscopic parameters are determined solely by the microscopic processes. While the saturation irradiance is controlled by the quenching frequencies of XeCl and $XeCl^*$, the unsaturated gain depends mainly on the formation rate of $XeCl^*$.

In conclusion, a self-consistent model has been developed which combines the models for the kinetic processes and for the excitation circuit. The validity of this model is demonstrated by the good agreement between the calculated and measured data for discharge voltage, current and resistance, and for laser output. This model is very useful for the analysis of the kinetics for XeCl lasers having a short-duration output pulse, and for the optimization of the laser performance.

7.2. Recommendations.

The research covered by this thesis provides an excellent basis for a continuing effort related to compact XeCl lasers, and to the extension of the research to larger and more complex systems. Future work should cover the following topics:

(a) Other gas mixtures should be investigated. It appears that laser operating lifetime may be substantially improved by replacing the Xe/HCl/He mixture with $Xe/BCl_3/He$ (Peet et al 1991), where BCl_3 in the halogen donor. In the event that trace amounts of H_2O are present, the reaction

$$BCl_3 + 3H_2O \rightarrow H_3BO_3 + 3HCl \qquad (7.1)$$

produces another halogen donor, HCl, which has a positive influence on laser performance.

With the usual HCl donor, trace amounts of H_2O can significantly reduce the laser gain.

(b) Additional research should be carried concerning the kinetic processes. In particular, the model should be extended to include XeCl lasers producing longer duration output pulses. This would require the inclusion of the slow kinetic processes into the model. For a more accurate solution of the electron energy distribution, the Boltzmann equation should be solved to a higher order approximation than was used for this thesis. In addition, the effects of spatial non-uniformity, which may be present in the discharge and induce discharge instability, should also be investigated experimentally and considered in the model.

(c) Although good agreement is achieved between the calculated and measured parameters, the validity of the kinetic model should also be confirmed by direct measurement of the time-dependent densities of the various species in the discharge. Many of these densities have been measured using absorption spectra for long-pulse XeCl laser discharges (Treshchalov et al, 1986; Hammer and Botticher, 1989). The electron densities, which are the most important parameters in the discharge, have also been measured by Mochizuki et al (1989) and Meyer and Elezzabi (1990) using Mach-Zehnder interferometers. However, the resources are not available to carry out comparable measurements with our compact short-pulse laser.

Appendix

Derivation of Transition Probabilities

Let R_b and R_c represent the internuclear separation at pseudo-crossing points b and c (these are the intersections of the dotted lines in Fig. 6.3). According to McDaniel (1964), if atomic or ionic species A and B (in states $A^{**} + B$, $A^{*} + B$, or $A^{+} + B^{-}$) come together adiabatically (i.e., infinitely slowly), then there is no change in the states via the pseudo-crossings. However, the species approach each other with a finite relative kinetic energy. Therefore, there is a corresponding finite probability for a jump from curve I to curve II at R_c, and from curve II to curve III at R_b. Let P_b and P_c be the probabilities (at R_b and R_c, respectively) for the atoms or ions (A and B) to jump from one potential curve to the other. Therefore, the probabilities for A and B to approach each other without a jump are $1 - P_b$ and $1 - P_c$, respectively.

To a good approximation, P_b and P_c can be obtained by application of Thomson's treatment (1924). Within a critical internuclear separation R ($R_T = 2e^2/3KT$), the probability for a single ion-neutral encounter within R_T is (Bates and Moffett, 1966)

$$w(x_i) = 1 - [1 - (1 + 2x_i)\exp(-2x_i)]/(2x_i^2) \quad , \tag{A.1}$$

where

$$x = \lambda_i/R_T \quad , \tag{A.2}$$

and where λ_i (i=1,2) are the mean free paths of the positive and negative ions in the neutral buffer gas. The total probability that both ions collide with a neutral atom is

$$P(R_T) = w(x_1) + w(x_2) - w(x_1)w(x_2) \quad . \tag{A.3}$$

Because the crossing points R_b and R_c are at large internuclear distances, the potential energies at R_b and R_c are essentially the same as those at R_T. To a good approximation, the probabilities at R_b and R_c are given by

$$P_b(R_b) = w(R_b/\lambda_1) + w(R_b/\lambda_2) - w(R_b/\lambda_1)w(R_b/\lambda_2) \quad (A.4)$$

and

$$P_c(R_c) = w(R_c/\lambda_1) + w(R_c/\lambda_2) - w(R_c/\lambda_1)w(R_c/\lambda_2) \quad (A.5)$$

For this system, ΔE_{mn} is the energy difference between states m and n at the dissociation limit, and D is the depth of the potential-energy well of state 0 with respect to state 2. The maximum quantum numbers for the various transitions can be determined from the energy conservation conditions for kinetic, potential and rotational energies. Because the quantum number l_{max} is usually a large number, $l(l+1)$ is approximately equal to l^2. Furthermore, R_b and R_c are relatively large, and therefore the potential energies at R_b and R_c can assume the values at the dissociation limits. Consequently, l_{max} can be approximated by

$$l_{0b} = R_b [H (E - D)]^{1/2} \quad , \quad (A.6)$$

$$l_{0c} = R_c [H (E - (D + \Delta E_{32}))]^{1/2} \quad , \quad (A.7)$$

$$l_{1b} = R_b [H (E + \Delta E_{12})]^{1/2} \quad , \quad (A.8)$$

$$l_{1c} = R_c [H (E + \Delta E_{13})]^{1/2} \quad , \quad (A.9)$$

$$l_{2b} = R_b [H E]^{1/2} \quad , \quad (A.10)$$

$$l_{2c} = R_c [H (E + \Delta E_{32})]^{1/2} \quad , \quad (A.11)$$

$$l_{3b} = R_b [H (E + \Delta E_{32})]^{1/2} \quad , \quad (A.12)$$

and

$$l_{3c} = R_c [H E]^{1/2} \quad , \quad (A.13)$$

where $H = 2\mu/\hbar^2$. Introducing

$$E_0 = \Delta E_{32} R_b^2 / (R_c^2 - R_b^2) \quad (A.14)$$

and

$$E_0' = E_0 + \Delta E_{32} \quad , \quad (A.15)$$

the probabilities for transitions, $P_l(m,n)$, involving the molecular states shown in Fig. 6.3, can be expressed in terms of the crossing probabilities

$$P_l(1,0) = P_b P_c \quad , \quad l < l_{1b} \tag{A.16}$$

$$P_l(0,1) = \left\{ \begin{array}{ll} P_b P_c & , \; l < l_{0b} \text{ and } E > (D+\Delta E_{12}) \\ P_c & , \; l_{0b} < l < l_{0c} \text{ and } E > \Delta E_{12} \end{array} \right\} \tag{A.17}$$

$$P_l(1,2) = P_b(1-P_b)P_c \quad , \quad l < l_{1b} \tag{A.18}$$

$$P_l(2,1) = P_b(1-P_b)P_c \quad , \quad l < l_{2b} \text{ and } E > \Delta E_{12} \tag{A.19}$$

$$P_l(1,3) = \left\{ \begin{array}{ll} (2-2P_b+P_b^2)P_c(1-P_c) & , \; l < l_{1b} \\ 2P_c(1-P_c) & , \; l_{1b} < l < l_{1c} \end{array} \right\} \tag{A.20}$$

$$P_l(3,1) = \left\{ \begin{array}{ll} (2-2P_b+P_b^2)P_c(1-P_c) & , \; l < l_{3b} \text{ and } E > \Delta E_{13} \\ 2P_c(1-P_c) & , \; l_{3b} < l < l_{3c} \text{ and } E > \Delta E_{13} \end{array} \right\} \tag{A.21}$$

$$P_l(2,0) = \left\{ \begin{array}{ll} (1-P_b) & , \; \left\{ \begin{array}{l} l < l_{2b} \text{ and } E > \Delta E_{12} \\ \text{or } l_{2c} < l < l_{2b} \text{ and } E_0' > E > \Delta E_{32} \end{array} \right. \\ (1-P_b)/(1-(P_bP_c)^2) & , \; \left\{ \begin{array}{l} l < l_{2b} \text{ and } \Delta E_{12} > E > E_0' \\ \text{or } l < l_{2c} \text{ and } E_0' > E > \Delta E_{32} \end{array} \right. \\ 2(1-P_b)/(2-P_b) & , \; l < l_{2b} \text{ and } \Delta E_{32} > E \end{array} \right\} \tag{A.22}$$

$$P_l(0,2) = \left\{ \begin{array}{ll} (1-P_b) & , \; l < l_{0b} \text{ and } E > (D+\Delta E_{12}) \\ \dfrac{2(1-P_b)(1-P_c+P_bP_c)}{2-(2-2P_b+P_b^2)P_c} & , \; \left\{ \begin{array}{l} l < l_{0b} \text{ and } (D+\Delta E_{12}) > E > (D+E_0') \\ \text{or } l < l_{0c} \text{ and } (D+E_0') > E > (D+\Delta E_{32}) \end{array} \right. \\ 2(1-P_b)/(2-P_b) & , \; l < l_{0b} \text{ and } (D+\Delta E_{32}) > E > D \end{array} \right\} \tag{A.23}$$

$$P_l(2,3) = \left\{ \begin{array}{ll} P_b(1-P_b)(1-P_c) & , \; l < l_{2b} \text{ and } E > \Delta E_{12} \\ \dfrac{P_b(1-P_b)(1-P_c)}{1-(2-2P_b+P_b^2)P_c^2} & , \; \left\{ \begin{array}{l} l < l_{2b} \text{ and } \Delta E_{12} > E > E_0' \\ \text{or } l < l_{2c} \text{ and } E_0' > E > \Delta E_{32} \end{array} \right. \end{array} \right\} \tag{A.24}$$

$$P_l(3,2) = \left\{ \begin{array}{ll} P_b(1-P_b)(1-P_c) & , \; l < l_{3b} \text{ and } E > \Delta E_{13} \\ \dfrac{P_b(1-P_b)(1-P_c)}{1-(2-2P_b+P_b^2)P_c^2} & , \; \left\{ \begin{array}{l} l < l_{3b} \text{ and } \Delta E_{13} > E > E_0 \\ \text{or } l < l_{3c} \text{ and } E_0 > E \end{array} \right. \end{array} \right\} \tag{A.25}$$

$$P_l(3,0) = \left\{ \begin{array}{ll} P_b(1-P_c) \ , & l < l_{3b} \text{ and } E > \Delta E_{13} \\ \dfrac{P_b(1-P_c)}{1-(2-2P_b+P_b^2)P_c^2} \ , & \left\{ \begin{array}{l} l < l_{3b} \text{ and } \Delta E_{13} > E > E_0 \\ \text{or } l < l_{3c} \text{ and } E_0 > E \end{array} \right. \end{array} \right\} \tag{A.26}$$

$$P_l(0,3) = \left\{ \begin{array}{ll} P_b(1-P_c) \ , & l < l_{0b} \text{ and } E > (D+\Delta E_{12}) \\ (1-P_c) \ , & l_{0b} < l < l_{0c} \text{ and } E > (D+\Delta E_{12}) \\ \dfrac{2P_b(1-P_c)}{2-(2-2P_b+P_b^2)P_c} \ , & \left\{ \begin{array}{l} l < l_{0b} \text{ and } (D+\Delta E_{12}) > E > (D+E_0') \\ \text{or } l < l_{0c} \text{ and } (D+E_0') > E > (D+\Delta E_{12}) \end{array} \right. \\ 2(1-P_c)/(2-P_c) \ , & l_{0b} < l < l_{0c} \text{ and } (D+\Delta E_{12}) > E > (D+E_0') \end{array} \right\} \tag{A.27}$$

References

Abouaf, R. and Teillet-Billy, D., J. Phys. B **10**, 2261 (1977).

Armandillo, E., Grasso, G., and Salvetti, G., Rev. Sci. Instrum. **56**, 674 (1985).

Andrich, D. and Bitsch, A., J. Phys. B **8**, 393 (1975).

Ault, E.R., Bradford, R.S. Jr., Bhaumik, M.L., Appl. Phys. Lett. **27**, 413 (1975).

Ballik, E.A., Final Report for PRAI Grant, McMaster University (1981).

Ballik, E.A. and Liu, D.W., IEEE J. Quant. Electronics **19**, 1166 (1983).

Bardsley, J.N. and Wadehra, J.M., Chem. Phys. Lett. **72**, 477 (1980).

Bates, D.R. and Flannery, M.R., Proc. Roy. Soc. (London), A**69**, 910 (1968).

Bates, D.R., Chem. Phys. Lett. **75**, 409 (1980).

Bates, D.R. and Moffett, R.J., Proc. Roy. Soc. (London), A **291**, 1 (1966).

Baym, G., "Lectures on Quantum Mecahnics", (The Benjamin/Cummings Publishing Company, Inc., 1973).

Bergmann, E.E. and Kolleogy, G.P., Rev. Sci. Instrum. **48**, 1641 (1977).

Bhaumik, M.L., Bradford, R.S. Jr., and Ault, E.R., Appl. Phys. Lett. **28**, 23 (1976).

Biondi, M.A., in Applied Atomic Collision Physics Vol. **3**, (Academic Press 1982).

Borst, W.Z., Phys. Rev. **9**, 1195 (1974).

Braglia, G.L., G.M. de'Munari and G. Mambriani, Comitato Nazionale Energia Nucleare RT/F1 (65) 60 (1965)

Brau, C.A. and Ewing, J.J., J. Chem. Phys. **63**, 4640-4647 (1975).

Brau, Ch., in "Excimer Lasers", Ch.K. Rhodes ed., (Springer-Verlag, 1984).

Brumer, P. and Kapplus, M., J. Chem. Phys. **58**, 3903-3915 (1973).

Burnham, R., Opt. Comm. **24**, 161 (1978).

Burnham, R., Harris, N.W., and Djeu, N., Appl. Phys. Lett. **28**, 86 (1976).

Bychkov, Yu.I., Kostin, M.N., Tarasenko, V.F., and Fedorov, A.I., Sov. J. Quant. Electron. **8**, 668 (1978).

Bychkov, Yu.I., Vinnik, M.L., and Losev, V.F., Sov. J. Quant. Electron. **17**, 1002 (1987).

Champagne, L.F., Dudas, A.J., and Harris, N.W., J. Appl. Phys. **62**, 1576 (1987).

Champagne, L.F., Appl. Phys. Lett. **33**, 523 (1978).

Chang, R.S.F., J. Chem. Phys. **76**, 2943 (1982).

Cherrington, B.E., "Gaseous Electronics and Gas Lasers", (Pergamon Press, 1979).

Christensen, C.P., Braverman, L.W., Steier, W.H., and Wittig, C., Appl. Phys. Lett. **29**, 424 (1976).

Crompton, R.W., Elford, M.T., and Jory, R.L., Aust. J. Phys. **20**, 369 (1967).

de Heer, F.J., Jansen, R.H.J., and van der Kaay, W., J. Phys. B **12**, 979 (1979).

Daugherty, J.D., Mangano, J.A., and Jacob, J.H., Appl. Phys. Lett. **28**, 581 (1976).

Domcke, W. and Mündel, C., J. Phys. B **18**, 4491 (1985).

Dreiling, T.D. and Setser, D.W., J. Chem. Phys. **75**, 4360 (1981).

Dunning, T.H. Jr. and Hay, P.J., J. Chem. Phys. **69**, 134, (1978).

Duzy, C. and Hyman, H.A., Phys. Rev. A **22**, 1878 (1980).

Ewing, J.J. and Brau, C.A., Appl. Phys. Lett. **27**, 350, (1975).

Fisher, C.H., Center, R.E., and McDaniel, J.J., presented at the 32nd Annual Gaseous Electronics Conference, Pittsburgh, P.A. Oct. (1979).

Flannery, M.R. and Yang, T.P., Appl. Phys. Lett. **32**, 327 (1978).

Flannery, M.R., in "Case Studies in Atomic Collision Physics", Vol. **2** (North-Holland, Amsterdam 1972).

Flannery, M.R., in "Applied Atomic Collision Physics", Vol. **3** (Academic Press 1982).

Fon, W.C., Berrington, K.A., and Hibbert, A., J. Phys. B **14**, 318 (1981).

Fon, W.C. and Berrington, K.A., J. Phys. B **14**, 323 (1981).

Fraga, S., Saxena, K.M.S., and Lo, B.W.N., At. Data **3**, 323 (1971).

Frost, L.S. and Phelps, A.V., Phys. Rev. A **136**, 1538 (1964).

Forestier, B.M., Fontaine, B.L., and Solenne, T., J. Phys. Lett. **42**, L221 (1981).

Gerritsen, J.W., Keet, A.L., Ernst, G.L., and Witteman, W.J., J. Appl. Phys. **67**, 3517 (1990).

Ginzburg, V.L. and Qurevich, A.V., Sov. Phys. Uspekhi **3**, 115 (1960).

Glownia, J.H., Misewich, J., and Sorokin, P.P., J. Opt. Soc. Am. B **4**, 1061 (1987).

Gower, M.C., Kearsley, A.J., and Webb, C.E., IEEE J. Quant. Electron. **16**, 231 (1980).

Hammer, Th. and Bötticher, W., Appl. Phys. B **48**, 73 (1989).

Hasama, T., Miyazaki, K., Yamada, K., and Sato, T., IEEE J. Quant. Electron. **25**, 113 (1989).

Hassal, S.B., Ph.D. Dissertation, McMaster University, (1991).

Hay, P.J. and Dunning, T.H. Jr., J. Chem. Phys. **69**, 2209, (1978).

Hayashi, M., J. Phys. D **16**, 581 (1983).

Heindorff, T., Hofft, J., and Dabkiewicz, P., J. Phys. B **9**, 89 (1976).

Herzberg, G., "Molecular Spectra and Molecular Structure.I. Spectra of Diatomic molecules", (Van Nostrand, Princeton, 1950).

Hiramatsu, M. and Goto, T., Rev. Sci. Instrum. **57**, 534 (1986).

Hokazono, H., Midorikawa, K., Obara, M., and Fujioka, T., J. Appl. Phys. **56**, 680 (1984).

Huestis, D.L., Marowsky, G., and Tittel, F.K., in "Excimer Lasers", p184, (Ck.K. Rhodes, ed., Springer Verlag, 1984).

Hyman, H.A., Phys. Rev. A **20**, 855 (1979).

Inoue, G., Ku, J.K., and Setser, D.W., J. Chem. Phys. **80**, 6006 (1984).

Ishchenko, V.N., Lisitsyn, V.N., and Razhev, A.M., Opt. Comm. **21**, 30 (1977).

Kannari, F., Kimura, W.D., and Ewing, J.J., J. Appl. Phys. **68**, 2615 (1990).

Kannari, F., Suda, A., Obara, M., and Fujioka, T., J. Appl. Phys. **56**, 680 (1984).

Klewer, M., Beerlage, M.J.M. and van der Wiel, M.J., J. Phys. B **13**, 571 (1980).

Koehler, H.A., Ferderber, L.J., Redhead, D.L., and Ebert, P.J., Phys. Rew. Lett. **21**, 198 (1972).

Kolts, J.H., Velazco, J.E., and Setser, D.W., J. Chem. Phys. **71**, 1247 (1979).

Krause, U. and Kleinschmidt, J., Contrib. Plasma Phys. **31**, 101 (1991).

Kubota, S., Davies, C., and King, T.A., Phys. Rev. A **11**, 1200 (1975).

Kudryavtsev, Yu.A. and Kuz'mina, N.P., Sov. J. Quant. Electron. **7**, 131 (1977).

Landau, L.D. and Lifshitz, E.M., "Quantum Mechanics", (Pergamon Press 1977).

Langevin, P., Ann. Chem. Phys. **48**, 433 (1903).

Lee, J.W.Y., Ph.D. Dissertation, McMaster University (1983).

Lee, W.Y., Xia, Z.M., and Ballik, E.A., "Formation of XeCl(B) exciplex via double crossings of potential-energy curves", in preparation.

LeRoy, R.J, in "Specialist Periodical Report on Electronic Spectroscopy", R.F. Barrow, ed., Vol.1, p.113, Chemical Society, London, 1973.

Letardi, T., Fang, H., and Fu, S., IEEE J. Quant. Electron. **28**, 1647 (1992).

Levin, L.A., Moody, S.E., Klosterman, E.L., Center, R.E., and Ewing, J.J., IEEE J. Quant. Electron. **17**, 2282 (1981).

Lin, S.-C. and Levatter, J.I., Appl. Phys. Lett. **34**, 505 (1979).

Long, W.H. Jr., Plummer, M.J., and Stappaerts, E.A., Appl. Phys. Lett. **43**, 735 (1983).

Maeda, M., Takahashi, A., Mizunami, T. and Miyazoe, Y., Japaness J. Appl. Phys. **21**, 1161 (1982).

Marowsky, G., Glass, G.P., Smayling, M., Tittel, F.K., and Wilson, W.L., J. Chem. Phys. **75**, 1153 (1981).

Mathias, L.E.S., and Parker, J.T., Appl. Phys. Lett., **3**, 16 (1963).

McCann, K.J. and Flannery, M.R., Appl. Phys. Lett. **31**, 599 (1977).

McDaniel, E.W., "Collision Phenomena in Ionized Gases", (John Willey & Sons, 1964).

McKee, T.J., Stoicheff, B.P., Wallace, S.C., Appl. Phys. Lett. **30**, 278 (1977).

Meyer, J. and Elezzabi, A.Y., J. Appl. Phys. **68**, 3838 (1990).

Mies, F.H., Mol. Phys. **26**, 1233, 1973.

Mihkelsoo, V., Miidla, P., Peet, V., Sherman, Q., Sorkina, R., Tamme, E., and Treshchalov, A., J. Phys. B **22**, 1489 (1989).

Milloy, H.B. and Crompton, R.W., Phys. Rev. A **15**, 1847 (1977).

Mitani, T. and Nakaya, T., J. Phys. D: Appl. Phys. **11**, 2071 (1978).

Mitchell, A.C.G. and Zemansky, M.W., "Resonance Radiation and Excited Atoms", (Cambridge University Press, 1971).

Miyazaki, K., Toda, Y. Hasama, T., and Sato, T., Rev. Sci. Instrum. **56**, 201 (1985).

Mochizuki, T., Hirata, K., Ninomiya, H., Nakamura, K., Maeda, K., Horiguchi, S., and Fujiwara, Y., Optics Communications **72**, 302 (1989).

Moore, C.E., "Atomic Energy Levels", (U.S. Nat'l Bur. Stand. Circ **467** Vol. I, 1949; Vol. II, 1952; and Vol. III, 1958).

Nassisi, V. and Perrone, M.R., Appl. Phys. B **51**, 254 (1990).

Natanson, G.L., Sov. Phys.-Tech. Phys. **4**, 1263 (1959).

Nesbet, R.K., Phys. Rev. A **20**, 58-69 (1979).

Ohwa, M. and Kushner, M.J., J. Appl. Phys. **65**, 4138 (1989).

O'Malley, T.F. and Crompton, R.W., J. Phys. B **13**, 3451 (1980).

Orient, O.J. and Srivastava, S.K., Phys. Rev. A **32**, 2678 (1985).

Osborne, M.R. and Hutchinson, M.H.R., J. Appl. Phys. **59**, 711 (1986).

Padial, N.T., Norcross, D.W., and Collins, L.A., Phys. Rew. A **27**, 141 (1983).

Peet, V.E., Treshchalov, A.B., and Slivinskij, E.V., Appl. Phys. B **52**, 234 (1991).

Raffenetti, R.C., J. Chem. Phys. **58**, 4452 (1973).

Ralston, A., "A First Course in Numerical Analysis", (McGraw-Hill, 1965).

Ramsauer, C. and and Kollath, R., Ann. Phys. Lpz. **12**, 529 (1932).

Rapp, D. and Englander-Golden, P., J. Chem. Phys. **43**, 1464 (1965).

Rhodes, C.K., IEEE J. Quant. Electron., **10**, 153 (1974).

Riley M.E., MacCallum, C.J. and Biggs, F., Atomic Data and Nucl. Data Tables **15**, 443 (1975)

Robertson, A.G., J. Phys. B **5**, 648 (1972)

Rockwood, S.D., Phys. Rev. A **8**, 2348 (1973).

Rohr, K. and Linder, L., J. Phys. B **9**, No 14, 2521 (1976).

Rosenbluth, M.N., MacDonald, W.M., and Judd, D.L., Phys. Rev. **107**, 1 (1957).

Rothe, D.E., Phys. Rev. **177**, 93 (1969).

Rácz, B., Patócs, A., Szabó, G., Bor, Zs., and Ignácz, F., Appl. Phys. B **54**, 513 (1992).

Schackert, K., Z. Phys. **213**, 316 (1968)

Schaper, M. and Scheibner, H., Beitr. Plasmaphys. **9**, 45 (1969).

Schram, B.L., de Heer, F.L., van der Wiel, M.J., and Kistemaker, J., Physica **31**, 94 (1965).

Searles, S.K. and Hart, G.A., Appl. Phys. Lett. **27**, 243 (1975).

Shay, T.M., Sze, R.C., Maloney, M., and Figneira, J.F., J. Appl. Phys. **64**, 375 (1988).

Shostak, S.L. and Strong, R.L., Chem. Phys. Lett. **63**, 370 (1979).

Smith, P.T., Phys. Rev. **36**, 1293 (1930).

Smith, K. and Thomson, R.M., "Computer Modelling of Gas Lasers", (Plenum Press, 1978).

Sorkina, R., J. Phys. D **23**, 806 (1990).

Stevens, W.J. and Krauss, M., Paper Tu-A2, presented at IEEE/OSA Topical Meeting on Excimer Lasers, Charleston, South Carolina (1979).

Stielow, G., Hammer, Th., and Bötticher, W., Appl. Phys. B **47**, 333 (1987).

Steyer, M. and Voges, H., Appl. Phys. B **42**, 155 (1987).

Steyer, M., Stankov, K.A., Mizoguchi, H., Ouyang, B., and Schafer, F.P., Appl. Phys. B **49**, 331 (1989).

Sur, A., Hui, A.K., and Tellinghuisen, J., J. Molecular Spectroscopy **74**, 465-479 (1979).

Sze, R.C. and Seegmiller, E., IEEE J. Quant. Electron. **17**, 81 (1981).

Taylor, R.S. and Leopold, K.E., J. Appl. Phys. **65**, 22 (1989).

Tellinghuisen, J., Hoffman, J.M., Tisone, G.C., and Hays, A.K., J. Chem. Phys. **64**, 2484 (1976).

Thomson, J.J., Phil. Mag. **47**, 337 (1924).

Ton-That, D. and Flannery, M.R., Phys. Rev. A **15**, 517 (1977).

Treshchalov, A., Peet, V., and Mihkelsoo, V., IEEE J. Quant. Electron. **22**, 51 (1986).

Turner, M.M. and Smith, P.W., IEEE Trans. Plasma Sci. **19**, 350 (1991).

Varshni, Y.P. and Shulka, R.C., J. Phys. Chem. Ref. Data **4**, 539 (1975).

Varshni, Y.P. and Shulka, R.C., J. Mol. Spectrosc. **16**, 63 (1965).

Vriens, L., Phys. Lett. **8**, 260 (1964).

Wang, Yuh-Shu, Ph.D. Dissertation, University of California (San Diego 1982).

Waynant, R.W. and Eden, J.G., Appl. Phys. Lett. **36**, 262 (1980).

Wigner, E. and Witmer, E.E., Z. Physik **51**, 883 (1928).

Williams, J.F. and Crowe, A., J. Phys. B **8**, 2233 (1975).

Xia, Z.M. and Ballik, E.A., Optics Communications **98**, 172 (1993).